UNIVERSITY OF SOUTHAMPTON

A theoretical study into the fundamental design limits of devices based on one- and two-dimensional structured fibres

by

Vittoria Finazzi

Thesis for the degree of Doctor of Philosophy

in the
Faculty of Engineering, Science and Mathematics
Optoelectronics Research Centre

September 2003

UNIVERSITY OF SOUTHAMPTON

ABSTRACT

FACULTY OF ENGINEERING, SCIENCE AND MATHEMATICS
OPTOELECTRONICS RESEARCH CENTRE

Doctor of Philosophy

A theoretical study into the fundamental design limits of devices based on one- and two-dimensional structured fibres

by Vittoria Finazzi

The sub-wavelength perturbation of an originally uniform material in order to manipulate light is the basis of two of the latest key technologies used to produce optical fibre devices for telecommunication system applications. The first technology (fibre Bragg gratings) concerns the 1-dimensional perturbation of the refractive index of an optical fibre (i.e. along the propagation axis of the fibre), whereas the second technology (microstructured optical fibres) concerns a 2-dimensional perturbation of the refractive index (i.e. in the transverse plane of the fibre).

This thesis concerns the modelling of different fibre structures that exploit these two technologies, in order to improve the performance of existing devices, give a clearer insight and understanding of the physical mechanisms on which the devices are based and open the route to new studies and ideas for novel fibres and fibre components.

Regarding the fibre Bragg gratings, the effect of background losses on uniform gratings and of cladding mode losses on linearly chirped gratings have been studied by means of two extended versions of coupled-mode theory. The possibility of compensating the cladding mode losses acting on the chirped grating profile is also analysed. Considering the microstructured optical fibres, an extensive study of highly nonlinear, small-core, silica holey fibres has been performed with the implementation of the multipole method, which was chosen after a careful consideration of other available modelling techniques. Guidelines were produced for optimising the design of holey fibres for particular device applications especially when trade-offs between small effective mode area and low confinement loss are important. The work on modelling highly nonlinear holey fibres was extended to include a preliminary study of the use of higher refractive index glasses and their future device applications.

Contents

Acknowledgements

I first would like to thank the people that have supervised me and my work during the course of my PhD studies: Dr. Tanya Monro, Prof. Dave Richardson and Prof. Michalis Zervas. I'm particular in debt to Tanya for all the enthusiasm she always conveys, for all the expertise she is always able to pass onto me, and also for being so patient and helpful when giving me useful guidelines in not so secondary matters such as the writing of papers and reports and the preparation of presentations.

I also would like to thank all the people that were able to help me on several occasions, never hesitating to share their knowledge with me: Kentaro Furusawa, Dr. Gilberto Brambilla, Joanne Baggett, Marco Petrovich amongst others. I want especially to thank Fabio Ghiringhelli for patiently listening to me about any mathematical, physical and "general knowledge" doubt, and for being almost always able to point me on the right direction towards the solution of the problem.

I wouldn't have started this adventure if it wasn't for the student grant awarded to me by Pirelli Cavi e Sistemi S.p.A. (Milan, Italy), in particular for the continuous support that Dr. Marco Romagnoli has given to me since the last part of my graduate studies back in Italy. Sincere and warm thanks goes to Dr. Eleanor Tarbox for the careful proof-reading of this thesis, and for, more importantly, always being there to encourage me during any inevitable ups and downs of the life of a PhD student.

I wouldn't have finished this adventure if it wasn't for all the thoughts of love and appreciation of my family (yes *sorellina*, I'm referring to you too) and old friends back in Italy, not to mention Mrs. Brenda Henderson and the rest of the "step-family" I gained here in England. I can't forget all the friends I met since I moved to England: too many to name, but if I refer to the people of the "House of the People" I'm sure I won't leave any of them out.

Finally, I really have to thank all the people that have given me the strength of enduring the endless amount of hours I spent in front of this "white box": Janis Joplin, Nina Simone, Jeff Buckley, Sonic Youth, the Breeders, Michael Stipe and the R.E.M., Maria Callas, Free Kitten, Thom Yorke and the Radiohead, Coldplay, the White Stripes, The Strokes, Eddie Vedder and the Pearl Jam, Ludwig Van Beethoven, Pink Floyd, Kurt Cobain and Nirvana, Vinicio Capossela, Muse, Giuseppe Verdi and "La Traviata", Carmen Consoli, Sigur Ros, Johann Sebastian Bach, the Blonde Redhead, Lou Reed, Jacqueline du Pré, the Marmoset, Supergrass, Giacomo Puccini and "Tosca", the Pixies,

Cakes, Billie Holiday, Jim Morrison and The Doors, Abba, The Velvet Underground & Nico, "The Adventure of Priscilla Queen of the Desert" soundtrack, Sergei Rachmaninov, Tricky, Goran Bregović, Glenn Gould, Patty Pravo, Zbigniew Preisner and all his Krzysztof Kieslowski's movie soundtracks, the Jon Spencer Blues Explosion, P. J. Harvey, Madredeus, the Jefferson Airplaine, Jacques Loussier, and Gloria Gaynor for her unique and marvellous way of singing *I will survive...*

Those who can, do.
Those who can't, simulate.

Chapter 1

Introduction

Optical fibres have assumed a dominant role in telecommunication systems over the last 20 years, allowing low-loss transmission of a huge amount of data over many kilometres. The erbium-doped fibre amplifier (EDFA) has in particular opened the route towards a wide range of new optical devices, and has been used to replace traditional electronic devices such as repeaters. A fully-optical telecommunication system is preferable in order to avoid the penalties and bandwidth restrictions related to electronic-to-optical and optical-to-electronic conversions of the signal. A large number of optical devices are now available, however the means of improving the performance and cost of such devices are still required in many instances.

This thesis deals with what can be called "microstructured materials". Specifically I have studied two technologies that exploit the sub-wavelength perturbation of an originally uniform material in order to manipulate the light. The first technology, fibre Bragg gratings (FBGs), concerns the 1-dimensional perturbation of the refractive index of an optical fibre (i.e. along the propagation axis of the fibre). The second technology, microstructured optical fibres (MOFs), concerns a 2-dimensional perturbation of the refractive index (i.e. in the transverse plane of the fibre). The fabrication challenges involved in both these technologies have been largely overcome in the past few years, allowing the realisation of novel and innovative devices. The cost of implementing novel technologies can however be very high, thus having the possibility of studying and reliably targeting the design and performances of novel devices *a priori* is always highly desirable.

Theoretical modelling is *de facto* an important part of scientific research, especially when dealing with complex and expensive technologies. Modelling can be used not only to design new devices or improve the performance of existing devices, but it is also useful in giving a clearer insight and understanding of the physical mechanisms on which the devices are based, and therefore in opening the route to new studies and ideas for new devices. Of course one has to keep in mind that every model is only an approximation

of the "real world" and that the only proof that the model is right is when the resulting predictions match (within the model assumptions) the experimental results.

1.1 Thesis outline

This work started in September 1999. I was first involved in the fibre Bragg gratings project under the supervision of Prof. Michalis Zervas. However, in January 2001 Prof. Zervas moved to a position within a local spin-off company along with most of the other senior members of the ORC's grating team. Consequently I had to change my research focus. Since January 2001 I have been involved in the microstructured optical fibres project supervised by Dr. Tanya Monro and Prof. David Richardson. This thesis thus contains work in two distinct areas as outlined below.

1.1.1 Part I: Fibre Bragg gratings

Part I of this thesis deals with the effect of losses on Fibre Bragg gratings (FBGs). Two kinds of losses only are considered: the background loss and the loss due to coupling to cladding modes.

In Chapter 2 the interaction between a uniform refractive index and a uniform loss grating with the same spatial periodicity is analysed. The loss pattern affects the features and symmetry of the FBG reflection, transmission and loss spectra according to the value of the de-phasing between the index and loss patterns. An extension of the coupled mode theory [1], already developed for studying distributed feedback structures [2], has been used to achieve this analysis. The resultant spectral asymmetry has been successfully explained by considering the overlap between the standing-wave intensity distribution and the periodic loss pattern. The latter approach has then been used in the appendix, at the end of the chapter, to give physical insight into the effective index medium picture often used to address some of the FBGs properties associated with the band-gap region.

In Chapter 3 the interaction between cladding and core propagating modes is analysed in linearly chirped FBGs (which are often used as dispersion compensators). The chirping of the FBG results in a spectral overlap of the resonant coupling of the forward-propagating core mode to a particular backward-propagating cladding mode. A new extension of the standard coupled-mode theory has been developed to study the resultant mode dynamics. Coupling of light into cladding modes results in a loss on the short-wavelength side of the reflection spectrum that affects the performance of the dispersion compensator. A technique to equalise the spectrum by means of a properly designed apodisation profile is analysed here, and the fundamental limitations of this approach are also derived.

1.1.2 Part II: Microstructured optical fibres

Part II of this thesis deals with microstructured optical fibres (MOFs) and the modelling of their properties. Most of this study is centred on highly-nonlinear small-core silica holey fibres (HFs). This class of fibre can be used to improve the performance of devices for many nonlinear applications previously demonstrated with standard fibre types and also opens up new device possibilities.

Chapter 4 of the thesis presents a background on MOFs and on the varieties of model that can be used to predict their optical properties. Chapter 5 explains the Multipole Method which has been chosen to model MOFs in the remainder of this work. The choice has been made bearing in mind that the majority of this study will concern small-core HFs. The implementation of the multipole method is first addressed, the accuracy and convergence of the solutions found by applying the method are analysed in detail, and the advantages and disadvantages of this choice of method are then discussed.

In Chapter 6 and 7 a novel study on highly nonlinear small-core silica HFs is presented. In single-material HFs the core has the same refractive index as the material beyond the finite holey cladding region, and so every propagating mode is therefore intrinsically leaky. This loss, named confinement loss, is determined by the geometry of the structure. As the scale structure of the HF is reduced compared to the optical wavelength, the confinement loss penalties can become significant. Chapter 6 illustrates several guidelines for the optimisation of practical HF designs, in terms of achieving high values of nonlinearity and the desired dispersive properties, and reducing the confinement loss penalties. As the scale structure of the HF is reduced compared to the optical wavelength, also the efficiency with which light can be coupled into these extreme fibres degrades. Chapter 7 investigates the fundamental limitations of this regime of HFs, in terms of mode coupling and polarisation properties of the fundamental mode. Chapter 6 also presents a preliminary study on the effective nonlinearities theoretically achievable when glasses with a higher refractive index (thus a higher intrinsic nonlinearity) than silica are considered, although this analysis concerns air-suspended rod structures only.

In Chapter 8 the multipole method is successfully validated against previous results predicted by the multipole method present in the literature, experimental results relative to several fabricated HF structures (including small-core silica HFs) and results predicted by other techniques. In this chapter the multipole method is also applied to the analysis of a number of other MOF designs, including applications within structural design regimes different from the small-core regime, and to the study of the single-modality of finite cladding HFs.

Finally, Chapter 9 summarises the main findings of the thesis and illustrates possible future works.

Part I

Fibre Bragg gratings

Chapter 2

Effect of periodic background loss on grating spectra

2.1 Fibre Bragg gratings: an introduction

Fibre Bragg gratings (FBGs) are optical fibres in which the refractive index in the core has been (quasi)-periodically perturbed. Every index perturbation can scatter light guided in the fibre, and part of the light is thus back-reflected. Since in an FBG the index modulation profile is periodic, the maximum reflection is achieved when the different contributions from each grating plane are in phase with each other, i.e. when the Bragg condition is fulfilled. The light wavelength λ is then equal to the Bragg wavelength $\lambda_B = 2n_{eff}\Lambda$ where n_{eff} is the effective index of the propagating mode and Λ is the perturbation period. Although the scattering from an individual grating plane is weak and broadband the resultant back-reflection from a grating containing many thousands of planes can be very strong over a narrow bandwidth, and the precise shape and strength of this reflection can be modified by a correct design of the (quasi)-periodic index perturbation.

The formation of permanent gratings, by photosensitivity, in an optical fiber was first demonstrated by Hill *et al.* [3]. The photosensitivity is characteristic of some of the glasses used to dope fibre cores. These glasses experience an increase in their refractive index after exposure to UV light. The index change magnitude usually ranges between 10^{-5} to 10^{-3}, but can be enhanced up to 10^{-2} using techniques such as hydrogen loading [4] and flame brushing [5]. Despite a vast number of studies on photosensitivity, its physical mechanism is not yet fully understood.

Bragg gratings were first fabricated using the internal writing technique [3]. The latest holographic technique [6] introduced the concept of UV side-exposure of the fibre and this is the basis of all the different grating writing techniques in use nowadays. The

phase-mask approach was then introduced [7] and improved into a phase-mask scanning technique [8]. A technique for fabricating truly continuous fibre gratings was developed at the ORC [9]. This versatile system involves the translation of the fibre through a phase-mask generated UV field pattern and an appropriate de-phasing of sequential exposures (the UV laser is strobed on and off as the fibre is moved). The capability to write structures of arbitrary length and profile has been achieved whilst maintaining a high level of positional and induced index change accuracy.

The FBGs unique filtering properties and versatility as an in-fibre device is illustrated by their use in wavelength-stabilised lasers, fibre lasers, remotely pump amplifiers, Raman amplifiers, phase conjugators, wavelength converters, passive optical networks, wavelength division multiplexers (WDMs), demultiplexers, add/drop multiplexers, dispersion compensators, and gain equalisers [10]. Moreover FBGs have also become popular as sensing devices, ranging in use from structural monitoring to chemical sensing [11].

2.2 Background losses

Background losses, intrinsically present in various optical devices, are generally considered to be a parasitic effect that degrades the device performance. In optical waveguides, background losses result simply in uniform attenuation of the transmitted power. In more complex structures, such as interferometric optical devices, however, the effect of background losses on the device performance is more complicated. For example, when the background loss is the same in both waveguides of an optical coupler, although the total transmitted power is attenuated, the cross-coupling efficiency is not affected. When, on the other hand, the losses are present in one of the waveguides only, in addition to total power attenuation, the cross-coupling efficiency is also affected [12].

Fibre Bragg gratings (FBGs) are wavelength selective devices that find extensive use throughout the field of optical technology [13]. The most evident effect of uniformly distributed background losses on gratings is the uniform decrease of the reflectivity spectrum, in particular of the reflectivity saturation value at the Bragg wavelength, and the increase of the out-of-band transmission (insertion) loss [14]. Also, uniform background loss disturbs the destructive multiple interference at the edges of the stop-band resulting in non-zero reflectivity at these wavelengths, broadening of the reflectivity spectrum and decreasing the device wavelength selectivity [14].

However, a quite different response is observed when the loss, instead of being uniformly distributed, is localised inside the grating structure. It has been shown [15] that in this case the effect of loss on the grating performance depends on the relative position of the localised loss. In addition, the grating loss spectrum also changes significantly with the loss position. This is due to the dispersive nature of the grating and the wavelength dependence of the detailed power distribution inside the grating [16]. This effect has

been proposed as a method of discriminating between the two otherwise degenerate spatial modes in distributed-feedback (DFB) lasers [17]. In addition to introducing $\pi/2$ phase shifts in uniform gain structures [2], DFB laser single-mode operation can be achieved by combining dephased index- and gain-grating structures [18], which rely on the differential electric-field/gain-medium overlap to reduce the gain threshold of one of the spatial modes.

The FBG writing process involves side-illumination of the fibre with a periodic UV radiation pattern [6]. In addition to the induced refractive index changes, UV illumination increases the propagation mode background losses around 1550 nm. The level of background losses depends on the fibre type, photosensitisation process and writing conditions.

For a hydrogen-loaded fibre (3mol% H_2) exposed to uniform UV light at 244 nm, the measured average background loss at 1550nm was 0.2 dB/cm [19]. This average loss is known to scale with the UV fluence and therefore with the induced refractive change [20]. It is, therefore, expected that exposure to periodically varying UV intensity, in addition to periodic refractive index change, will result in a periodic modulation of the induced background loss. It should also be stressed that depending on the way it is introduced, the periodic loss can be in-phase or anti-phase with the periodic refractive index pattern.

Combined metal/dielectric periodic layers are also used as photonic band gap structures to produce optical filters with enhanced transmissivity at various wavelength ranges [21, 22]. These filters rely again on the presence of the periodic loss to selectively suppress certain transmission windows.

Refractive index (photorefractive) gratings and loss (photochromic) gratings are also known to coexist in various photorefractive materials [23, 24, 25, 26]. Photorefractive and photochromic gratings are spatially separated by some spatial phase ϕ, which depends on the physical mechanisms of charge transport and charge trapping, the grating writing conditions and material properties. The spatial phase ϕ affects the overall coupling process and diffraction data and may lead to erroneous conclusions.

In the following sections, the effect of the periodic modulated background loss on the spectral response of FBGs is considered and analysed thoroughly. The theoretical study is achieved by extending the standard coupled-mode theory (CMT) to include the effect of periodic loss. It is shown that, as in the case of the localised scattering centre [15], the grating spectrum is affected non-uniformly by the presence of the periodic loss. In Section 2.3, the extended CMT equations are developed. In Section 2.4, numerical calculations of grating spectra and internal power distributions under different loss conditions are presented. In Section 2.5, the final conclusions are presented.

2.3 Coupled-wave Model

In the following analysis, a coexisting refractive-index and background-loss perturbation of period Λ [1, 18] (shown schematically in Figure 2.1 it is assumed, expressed by

$$n(z) = n + n_1 \cos 2\beta_B z \tag{2.1a}$$

$$\alpha(z) = \alpha + \alpha_1 \cos(2\beta_B z + \phi) \tag{2.1b}$$

where $\beta_B = \pi/\Lambda$. The Bragg wavelength is given by $\lambda_B = 2n\Lambda$. The parameters n and $\alpha(> 0)$ represent the background effective refractive index and propagation loss, respectively. n_1 and $\alpha_1(> 0)$, on the other hand, give the amplitudes of the refractive index and loss gratings, respectively. A phase difference ϕ has been introduced between the index and loss grating structures. This is to allow for the refractive-index grating to be in phase ($\phi = 0$) or in anti-phase ($\phi = \pi$) with the loss grating. The former occurs when UV exposure increases both refractive index and loss. The latter, on the other hand, can correspond to the case where UV exposure has opposite effects on refractive index and loss modulation (e.g., negative index gratings [27]). The spatially varying propagation constant is then given by

$$K(z) = k_0 n(z) + j\alpha(z) \tag{2.2}$$

with $k_0 = \omega_0/c = 2\pi/\lambda_0$ (λ_0 is the free space wavelength). Note that the loss wavelength dependence has been neglected. The substitution of (2.1) into (2.2), with the following small-perturbation assumptions [1]

$$n_1 \ll n \qquad \alpha \ll \beta_0 = k_0 n \qquad \alpha_1 \ll \beta_0 \tag{2.3}$$

allows us to write $K^2(z)$ in the form

$$K^2(z) \approx \beta_0^2 + j2\beta_0\alpha + 4\beta_0(\kappa_c \cos 2\beta_B z - \kappa_s \sin 2\beta_B z) \tag{2.4}$$

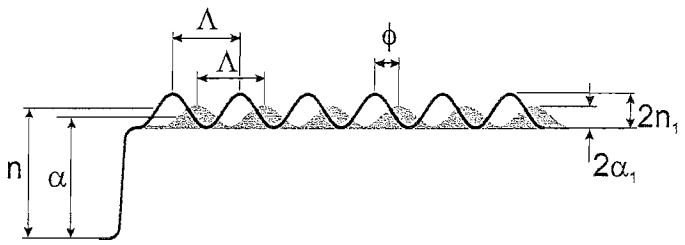

FIGURE 2.1: Schematic illustration of the refractive-index and back- ground-loss Λ-periodic perturbation patterns discussed in the text.

where $\beta_0 = k_0 n$ and

$$\kappa_c = \frac{\pi}{\lambda} n_1 + j\frac{\alpha_1}{2}\cos\phi \tag{2.5a}$$

$$\kappa_s = j\frac{\alpha_1}{2}\sin\phi \tag{2.5b}$$

are the expressions of the extended coupling constants. When the Bragg scattering dominates ($\beta_0 \approx \beta_B$), the wave equation

$$\nabla^2 E + K^2(z)E(z) = 0 \tag{2.6}$$

can be analytically solved, because only two of the infinite set of diffraction orders are in phase and have significant amplitude. So the total electric field can be written as the sum of two counter-propagating waves of complex amplitudes $A(z)$ and $B(z)$, respectively, namely

$$E(z) = E_f(z) + E_b(z) = A(z)e^{j\beta z} + B(z)e^{-j\beta z} \tag{2.7}$$

where β is the propagation constant of the uncoupled waves ($n_1, \alpha_1 = 0$) defined as

$$\beta^2 = (\beta_0 + j\alpha)^2 \approx \beta_0^2 + j2\beta_0\alpha. \tag{2.8}$$

Substituting (2.7) into the wave equation (2.6), equating synchronous terms and using the slowly-varying envelope approximation [1], the following pair of coupled-wave equations can be obtained:

$$\begin{cases} \dfrac{dA}{dz} = j(\kappa_c + j\kappa_s)e^{j2\Delta z}B \\ \\ \dfrac{dB}{dz} = -j(\kappa_c - j\kappa_s)e^{-j2\Delta z}A \end{cases} \tag{2.9}$$

with $\Delta \equiv \beta_B - \beta = \beta_B - \beta_0 - j\alpha$. The integration of the system (2.9), with boundary conditions $E_b(L) = 0$ and $E_f(0) = E_{inc}$, leads to the following expressions for the forward and backward components of the electric field

$$E_f(z) = E_{inc}\frac{p\cosh(p(z-L)) - j\Delta\sinh(p(z-L))}{p\cosh(pL) + j\Delta\sinh(pL)}e^{j\beta_B z} \tag{2.10a}$$

$$E_b(z) = -jE_{inc}\frac{(\kappa_c - j\kappa_s)\sinh(p(z-L))}{p\cosh(pL) + j\Delta\sinh(pL)}e^{-j\beta_B z}. \tag{2.10b}$$

with $p = \sqrt{\kappa_c^2 + \kappa_s^2 - \Delta^2}$. The reflection and transmission coefficients are then given by

$$r = \frac{E_b(0)}{E_f(0)} = \frac{j(\kappa_c - j\kappa_s)\sinh(pL)}{p\cosh(pL) + j\Delta\sinh(pL)} \tag{2.11a}$$

$$t = \frac{E_f(L)}{E_f(0)} = \frac{pe^{j\beta_B L}}{p\cosh(pL) + j\Delta\sinh(pL)} \tag{2.11b}$$

with which the reflectivity and the transmissivity can be obtained as

$$R = |r|^2 \tag{2.12a}$$

$$T = |t|^2. \tag{2.12b}$$

The total loss, calculated in dB as 10 times the base 10 logarithm of the ratio between the input and output power, is equal to

$$\alpha_{\text{loss}} = -10\log_{10}(T + R). \tag{2.13}$$

The reflection and transmission phase-time delays are calculated by using the expression [28]:

$$\tau_{r,t} = -\frac{\lambda^2}{2\pi c}\frac{\mathrm{d}\theta_{r,t}}{\mathrm{d}\lambda} \tag{2.14}$$

where $\theta_{r,t}$ is the phase of the reflection and transmission coefficient, respectively.

It is worth noticing that the coupling coefficients appearing in the coupled-wave equations (2.9) are equivalent to

$$\kappa_f = \kappa_c + j\kappa_s = \frac{\pi}{\lambda}n_1 + j\frac{\alpha_1}{2}e^{j\phi} \tag{2.15a}$$

$$\kappa_b = \kappa_c - j\kappa_s = \frac{\pi}{\lambda}n_1 + j\frac{\alpha_1}{2}e^{-j\phi}. \tag{2.15b}$$

The two coefficients κ_f and κ_b are basically equal to the sum of the coupling coefficient due to the refractive index grating ($\pi n_1/\lambda$) and to loss grating ($j\alpha_1/2$) only, taking into account the phase difference (ϕ) between the two patterns.

2.4 Numerical Results

The reflection and transmission coefficient formulae, developed in the previous section, are now employed to calculate the mixed refractive-index/loss grating response. The effect of the amplitude and relative spatial phase of the loss grating on the obtained reflectivity and loss spectra is studied in detail. The physical insight into the resulting spectra is also provided.

Figure 2.2 shows the spectral characteristics of a uniform-loss grating with $n = 1.45$,

$n_1 = 10^{-4}$, $L = 2$ cm, $\lambda_B = 1550$ nm, $\alpha = 0.023$ cm^{-1} and $\alpha_1 = 0$. This value of α corresponds to the power loss coefficient $\alpha_p = 0.2$ dB/cm that has been experimentally measured in [19], for an hydrogen loaded germanosilicate fibre (3mol% H_2), through the relation $\alpha[\text{cm}^{-1}] = \ln 10/20 \cdot \alpha_p[\text{dB/cm}]$. All the curves are plotted as a function of the wavelength detuning $\Delta\lambda = \lambda - \lambda_B$. The lossless case ($\alpha = 0$, dashed line) is also plotted for comparison. Figures 2.2(a) and (b) show the reflectivity and transmissivity spectra. It is confirmed that the uniform background loss reduces both the grating reflectivity and transmissivity. The latter results in an increased device insertion loss. The effect is most severe around the wavelengths of maximum transmission at the edges of the stop-band. Figures 2.2(c) and (d) show the spectra of the phase-time delay of the reflected and transmitted light, calculated by using (2.14). It is shown that the presence of uniform background loss breaks the time-delay degeneracy between reflected and transmitted light that otherwise exists in lossless one-dimensional band gap structures. The phase-time delay (especially of the transmitted light) is reduced considerably around the stop-band edges, as marked in Figure 2.2(d). This is equivalent to the reduction of the Q factor of resonant cavities, e.g. Fabry-Perot interferometer, in the presence of intra-cavity losses (after all, Bragg gratings *are* distributed resonant cavities). Figure 2.2(e) shows the corresponding grating total-loss spectrum in the presence of uniform propagation background loss.

It is shown that the loss spectrum is quite non-uniform across the grating bandwidth. The minimum loss occurs at the Bragg wavelength ($\Delta\lambda = 0$), since at this wavelength the incident light is predominantly reflected ($R \gg T$) without penetrating deep into the lossy grating structure. The penetration depth is inversely proportional to the grating strength [29] and, therefore, the minimum loss decreases with the grating reflectivity. The maximum loss, on the other hand, is shown to occur at the edges of the stop-band. At these wavelengths, the reflectivity is almost zero and the incident light is predominantly transmitted ($T \gg R$). However, transmission at these wavelengths is a resonant effect that involves many round-trips inside the grating (as demonstrated by the corresponding increased phase-time delay – see Figure 2.2(d)), which inevitably results in increased transmission losses. The dotted line represents the average single-pass loss level given by $\alpha_p L$ (dB). The further from the Bragg wavelength, the smaller the grating (i.e. multi-reflection) effect is, and the total loss converges to this average value. Finally, it should be pointed out that, due to spatial symmetry, the response of a grating with uniform background loss, including its loss spectrum, remains symmetric with respect to wavelength detuning.

Next, the effect of periodic background losses on the grating response is considered. Figure 2.3 shows the spectral characteristics of a similar grating but with fully modulated periodic loss ($\alpha = \alpha_1 = 0.023$ cm^{-1}). The refractive index and loss modulations are considered to be in phase (i.e. $\phi = 0$). The presence of a fully modulated loss not only decreases the amplitude R, but also modifies the spectral shape. Figures 2.3(a), (b)

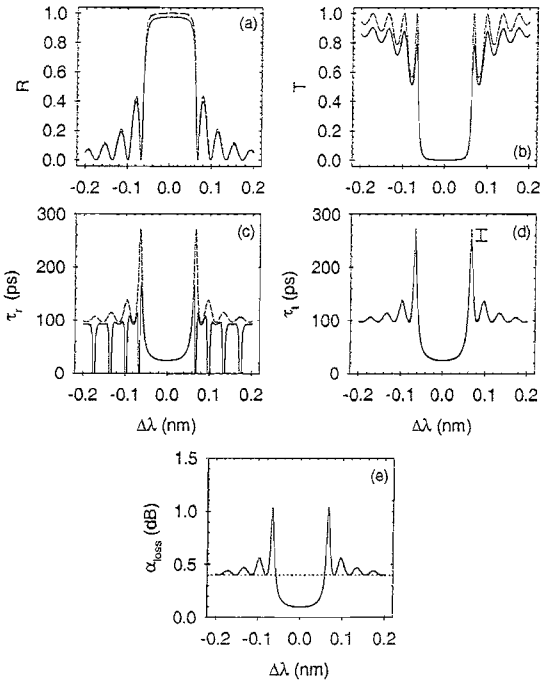

FIGURE 2.2: Spectral characteristics of a uniform-loss grating (solid lines) with $n = 1.45$, $n_1 = 10^{-4}$, $L = 2$ cm, $\lambda_B = 1550$ nm, $\alpha = 0.023$ cm^{-1} and $\alpha_1 = 0$: (a) reflectivity, (b) transmissivity, (c) reflection time delay (ps), (d) transmission time delay (ps), (e) loss (dB), the straight dotted line represents the average single-pass loss level; the lossless case is reported in dashed line for comparison; all plots are expressed as a function of the wavelength detuning $\Delta\lambda = \lambda - \lambda_B$ (nm).

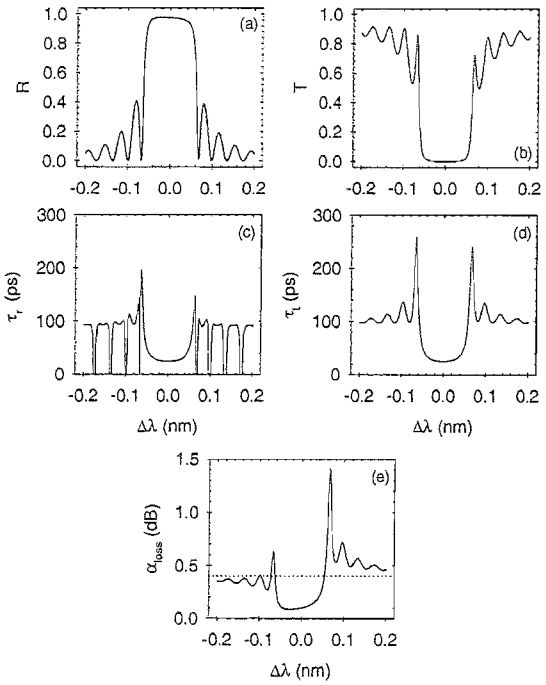

FIGURE 2.3: Spectral characteristics of a fully-modulated loss uniform grating, with the same specifications as the previous figure, but $\alpha = \alpha_1 = 0.023$ cm^{-1} and $\phi = 0$: (a) reflectivity, (b) transmissivity, (c) reflection time delay (ps), (d) transmission time delay (ps), (e) loss (dB), average single-pass loss level in dotted line; all plots are expressed as a function of the wavelength detuning $\Delta\lambda = \lambda - \lambda_B$ (nm).

and (e) show that the reflection and transmission spectra, and consequently the total-loss spectrum, are asymmetric with respect to Bragg wavelength ($\Delta\lambda = 0$), with the long-wavelength side ($\Delta\lambda > 0$) experiencing larger losses than the short-wavelength one ($\Delta\lambda < 0$). Surprisingly, in the short-wavelength side, the total loss becomes gradually smaller than the average single-pass loss. This is in clear disparity with the case of similar uniform background loss, where, although the grating total loss undulates, it always remains larger than the single-pass value (c.f., Figure 2.2(e)). As it will be explained later, this total-loss asymmetry (see Figures 2.7 and 2.8) is due to the wavelength dependence of the overlap between the total field intensity and the periodic loss pattern inside the grating. Figures 2.3(c) and (d) show that the phase-time delay spectra are also asymmetric, with the long-wavelength side showing smaller peak values than the short-wavelength one. Using similar arguments as in Figure 2.2, it can be easily seen that the presence of higher losses at the long-wavelength side (see Figure 2.3(e)) results in effective cavities with lower-Q, which translates into fewer round-trips and, there-

fore, smaller phase-time delays. Finally, it should be stressed that, in the case that the background-loss modulation is *in phase* with the refractive-index modulation, despite the spatial symmetry, the response of a grating is clearly *asymmetric*.

This asymmetry is further demonstrated in Figure 2.4 where the differences in reflectivity (a), equivalent time delay (b) and total loss (c), between the periodic (with ϕ=0) and uniform background loss cases, are plotted as a function of the wavelength detuning. The grating parameters are the same as the ones in Figures 2.2 and 2.3. Despite the fact that the average propagation loss coefficient is equal in both cases ($\alpha = 0.023$ cm^{-1}), the total loss in the periodic case is larger ($\Delta\alpha_{\text{loss}} > 0$) than the uniform one at the long-wavelength side ($\Delta\lambda > 0$). The opposite is true at the short-wavelength side ($\Delta\lambda < 0$). It is also shown that the part of the spectrum experiencing higher (lower) losses is also associated with lower (higher) reflectivity as well as equivalent time delay.

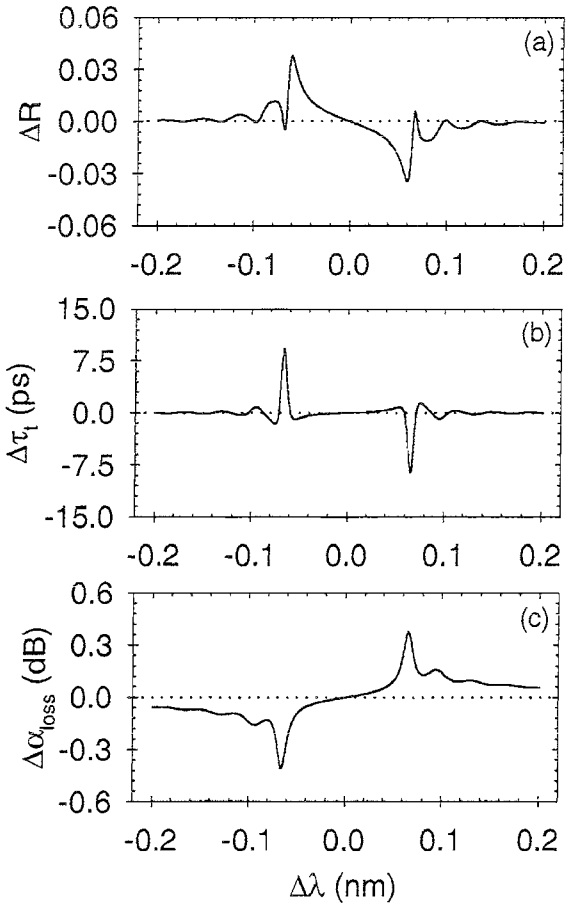

FIGURE 2.4: Comparison between the periodic (p) and uniform (u) loss case: (a) $\Delta R = R^p - R^u$, (b) $\Delta\tau_t = \tau_t^p - \tau_t^u$ and (c) $\Delta\alpha_{\text{loss}} = \alpha_{\text{loss}}^p - \alpha_{\text{loss}}^u$ are plotted as a function of the wavelength detuning $\Delta\lambda$ (in the case of periodic loss, $\phi = 0$).

The origin of the asymmetry in the grating response, in the presence of periodic loss, can be understood by considering the dispersive nature of the grating structure and its effect on the total field intensity distribution along the grating. Figure 2.5 shows the total electric-field intensity distribution (solid line) for five different wavelengths in

five different grating regions. The shaded area shows the corresponding refractive-index modulation in each region. To better visualise the spatial dephasing between the two patterns, the total field intensity in each region is expressed in arbitrary units. Each column corresponds to the same location along the grating, specified by the z-coordinate shown on the top, while each row corresponds to the same wavelength, indicated at the far left. λ_B is the Bragg wavelength, while λ_I^+ and λ_{II}^+ correspond to the resonant wavelengths at the first and second reflectivity zero ($R = 0$, $T = 1$), respectively, at the long-wavelength side of the spectrum (the superscript $(-)$ denotes the corresponding wavelengths at the short-wavelength side). Each grating subregion is 5-periods long.

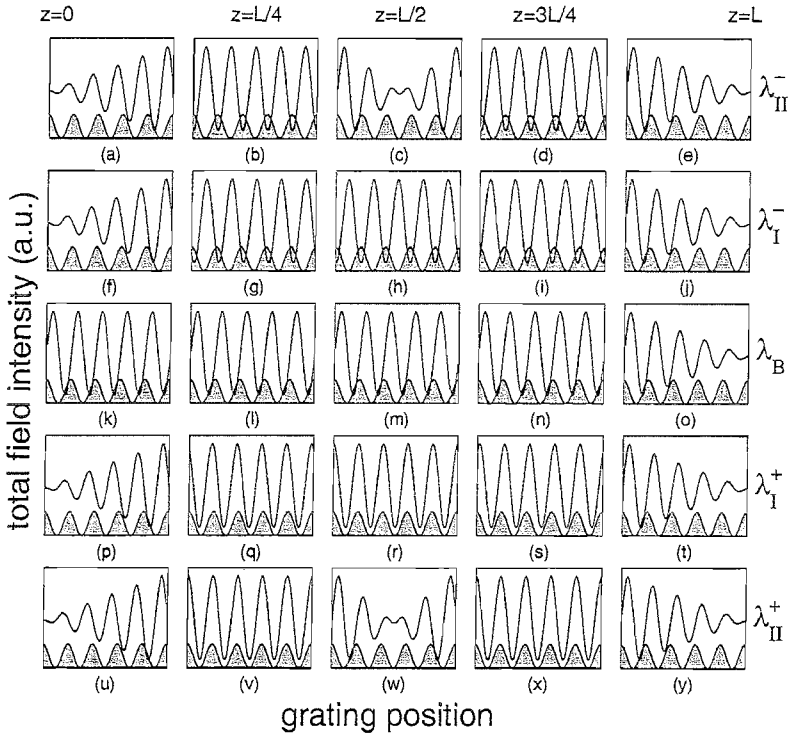

FIGURE 2.5: Total intensity field (black line) and refractive index pattern (gray area) versus grating length in five different zones (specified by the z coordinate on the top of each column) at the five wavelengths: λ_{II}^- (a-e), λ_I^- (f-j), λ_B (k-o), λ_I^+ (p-t) and λ_{II}^+ (u-y); the intensity field is expressed in arbitrary units, to indicate the de-phasing between the total-field-intensity and refractive-index patterns.

For all wavelengths, the spatial dephasing at the grating far end ($z = L$) is equal to $-\pi/2$ (see Section 2.6). This is due to the boundary condition at $z = L$ and the nature of the elementary partial standing-wave pattern formed by the last refractive-index-modulation fringe. Inside the grating, however, the spatial dephasing depends strongly on the wavelength and the relative grating position. For example, the total-field-intensity periodic pattern at the first resonant wavelength λ_I^+ on the long-wavelength side, around the grating centre ($z = L/2$), is *in-phase* with the refractive index periodic perturbation, i.e. intensity maxima coincide with refractive-index maxima (see Figure 2.5(r)). However, for the symmetric first resonant wavelength λ_I^- in the short-wavelength side, at the same position ($z = L/2$), the total-field-intensity and refractive-index patterns are

in *anti-phase*, with the intensity maxima aligned with the refractive-index minima (see Figure 2.5(h)). Similar spatial phase relations are observed between the second resonant wavelengths λ_{II}^{+} and λ_{II}^{-} around the grating positions $z = L/4$ and $3L/4$ (c.f. Figs. 2.5(v), (x) and (b), (d)). For the resonant wavelengths, the spatial dephasing shows a π discontinuity at the points corresponding to the standing wave nodes. This is due to the fact that, at these points, the backward propagating field is zero and the spatial dephasing acquires a different limiting value ($\pm\pi/2$), depending on whether the node is approached from the right or left side (see Section 2.6 for a full discussion). For all these wavelengths, the spatial dephasing varies along the grating length. At the Bragg wavelength, however, the spatial dephasing remains constant and equal to $-\pi/2$ throughout the grating length.

The full spatial dephasing dependence on position, in the lossless case, for the wavelengths λ_B, $\lambda_I^{\pm}$ and $\lambda_{II}^{\pm}$ is summarised in Figures 2.6(a), (b) and (c), respectively. The bottom of each figure shows the corresponding total field intensity envelope (normalised to the input field intensity). In Figures 2.6(b) and (c), the solid lines correspond to wavelengths λ_I^{+} and λ_{II}^{+}, respectively, while dashed lines correspond to λ_I^{-} and λ_{II}^{-}, respectively. The total-field-intensity envelopes at wavelengths λ_I^{+} and λ_{II}^{+} are identical to the ones at λ_I^{-} and λ_{II}^{-}, respectively.

Figures 2.5 and 2.6 clearly show that the total overlap between the intensity periodic pattern and refractive index modulation will vary with wavelength. Therefore, the loss spectrum, in the case of periodic loss, is expected to depend on the relative phase ϕ between the two periodic patterns. In the case where the modulated background loss is in phase with the refractive-index modulation ($\phi = 0$), the total loss spectrum asymmetry can be explained by considering Figures 2.5 and 2.6. On the long-wavelength side (c.f., λ_I^{+} and λ_{II}^{+}) the high-intensity fringes are predominantly aligned with the high-loss ones and it is expected to impart maximum loss. On the short-wavelength side (c.f., λ_I^{-} and λ_{II}^{-}) the high-intensity fringes are predominantly aligned with the low-loss ones and it is, therefore, expected to impart minimum loss. This also explains why the short-wavelength total loss for the modulated case is even lower than the corresponding value for the equivalent uniform one (see Figure 2.4(c)).

The effect of the dephasing factor ϕ between the refractive index and loss modulation on the total loss spectrum is illustrated in Figure 2.7. The grating parameters are similar to the ones in Figure 2.3 and $\phi = 0$, $\pi/2$, π and $3\pi/2$. The corresponding reflectivity spectra are shown in Figure 2.8, where the peak has been magnified in the inset. It is first shown that the $\phi = \pi$ case (dashed line) is a mirror image of the corresponding $\phi = 0$ one (solid line). This is due to the fact that by shifting the modulated loss pattern by π with respect to the modulated index pattern, the overlaps between the intensity pattern (which remains unchanged with respect to index modulation) and the loss pattern is now maximised in the short wavelength side. At the Bragg wavelength, due to resulting spatial symmetry, the $\phi = 0$ and $\phi = \pi$ cases give the same response

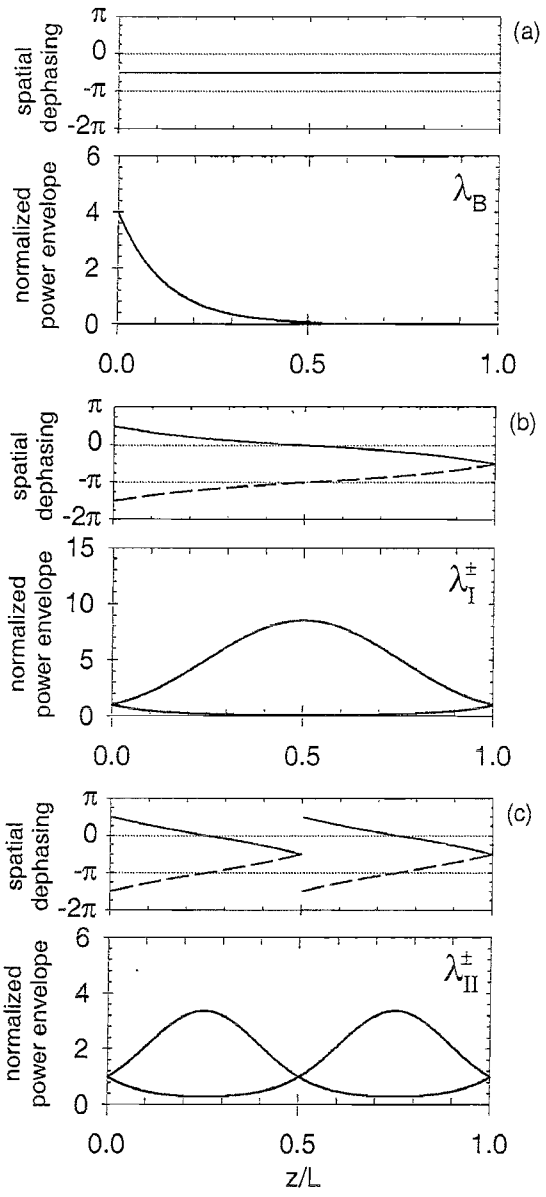

FIGURE 2.6: Spatial dephasing dependence on grating position, for the wavelengths: (a) λ_B, (b) λ_I^- in dashed and λ_I^+ in solid line, (c) λ_{II}^- in dashed and λ_{II}^+ in solid line; the corresponding normalised power envelope is plotted below each case.

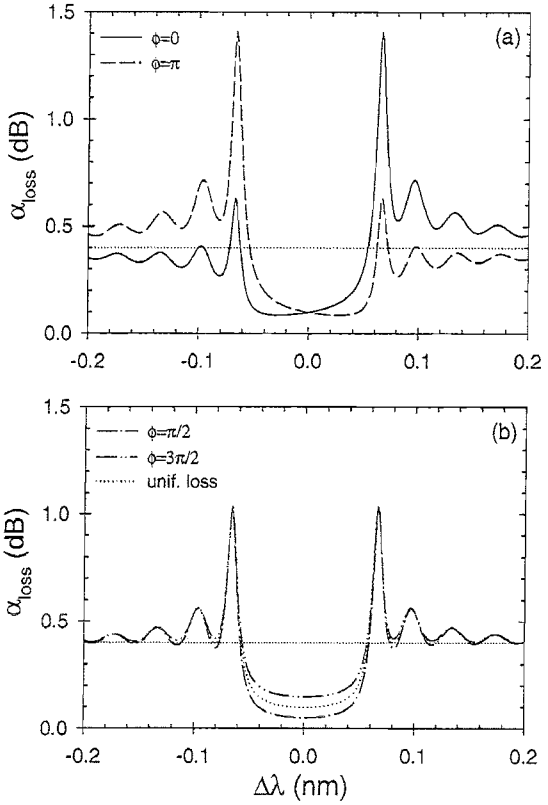

FIGURE 2.7: Spectral loss (dB) as a function of the wavelength detuning (nm) for different dephasing factor values: (a) $\phi = 0$ in solid and $\phi = \pi$ in dashed line; (b) $\phi = \pi/2$ in dot-dashed and $\phi = 3\pi/2$ in dot-dot-dashed line; the uniform-loss case is also shown in dotted line. All the other parameters are as in Fig 2.3. The straight dotted line, that appears in both (a) and (b), represents the average single-pass loss level.

(equal to the uniform loss case). This is further demonstrated in Figure 2.9, where the total intensity distribution at the Bragg wavelength (thick solid line), refractive index variation (thin solid line) and loss modulation (shaded area) are plotted over five grating periods, for $\phi = 0$, $\pi/2$, π and $3\pi/2$. For $\phi = \pi/2$ and $3\pi/2$, although the reflectivity and loss spectra become symmetric with respect to wavelength detuning, they acquire different peak values at the Bragg wavelength. In fact in Figure 2.7, the $\phi = \pi/2$ case (dot-dashed line) shows smaller loss and higher reflectivity compared to $\phi = 3\pi/2$ case (dot-dot-dashed line). It also appears that the uniform-loss case (dotted

line) performance corresponds to the average of the $\phi = \pi/2$ and $3\pi/2$ cases. This is again related to the spatial relation between the corresponding field-intensity and modulated-loss patterns (c.f., Figures 2.9(b) and (d)). Spatial shifts of $\phi = \pi/2$ and $3\pi/2$ align the field-intensity maxima with the modulated-loss minima and maxima, respectively.

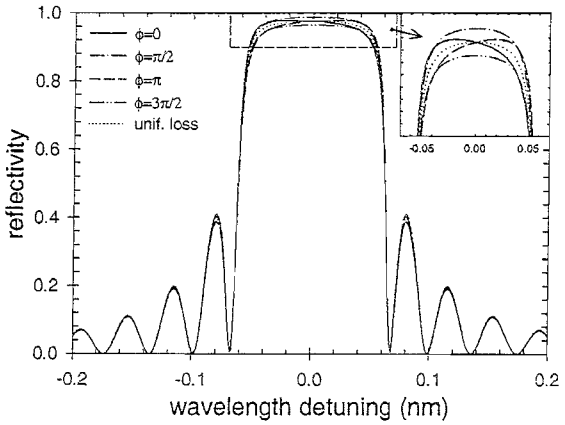

FIGURE 2.8: Reflectivity spectra versus wavelength detuning corresponding to the four full modulated-loss and the uniform-loss cases illustrated in Figure 2.7. The reflectivity peak has been magnified in the inset.

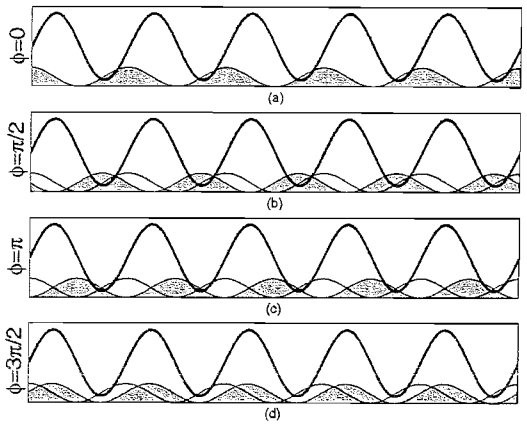

FIGURE 2.9: Intensity distribution (thick line) refractive index pattern (thin line) and background loss pattern (shaded area) versus grating length over five periods, at the Bragg wavelength and for a dephasing factor equal to: (a) $\phi = 0$, (b) $\phi = \pi/2$, (c) $\phi = \pi$, (d) $\phi = 3\pi/2$ (the three quantities are expressed in arbitrary units).

Background loss (uniform or modulated) not only affects the reflectivity and time-delay spectra, but also limits the maximum attainable (saturated) peak reflectivity. Figure 2.10 shows the Bragg wavelength reflectivity variation as a function of the grating length, for refractive-index modulation amplitudes $n_1 = 10^{-3}$, 10^{-4} and 10^{-5}, and a fixed uniform background loss of 0.2 dB/cm. It is shown that for the same uniform background loss, the gratings with smaller refractive-index modulation acquire lower saturated reflectivity, due to the longer physical lengths required. Figure 2.11 shows the Bragg wavelength reflectivity variation as a function of the grating length, for refractive-index modulation amplitude $n_1 = 10^{-5}$, fully modulated background loss of $\alpha_p = 0.2$ dB/cm and for $\phi = 0$, $\pi/2$, π and $3\pi/2$. The lossless case (dotted line) is also shown for comparison. Under the same conditions, $\phi = \pi/2$ and $3\pi/2$ result in the maximum and minimum saturated reflectivity, respectively. The corresponding values for $\phi = 0$ and π are identical and appear to be equal to the average of the $\phi = \pi/2$ and $3\pi/2$ values. This is in accordance with the findings of Figure 2.8.

The loss-spectrum asymmetry can be quantified by considering the difference of the loss peaks at the two first-order resonant wavelengths ($\lambda_I^{\pm}$), $\Delta\alpha_{peaks} = |\alpha(\lambda_I^+) - \alpha(\lambda_I^-)|$. The parameter is shown schematically in the inset of Figure 2.12, together with the difference

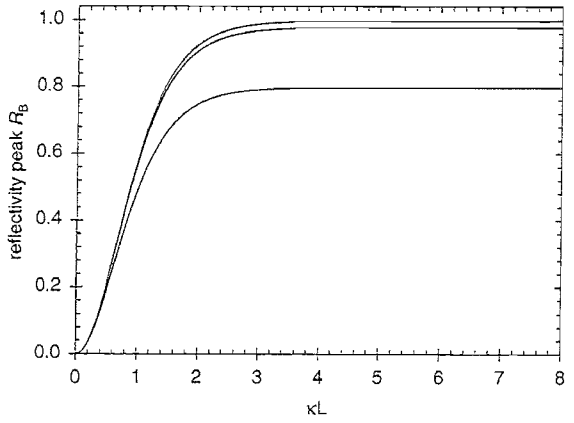

FIGURE 2.10: Reflectivity peak R_B versus κL for: $n_1 = 10^{-3}$ (upper curve), $n_1 = 10^{-4}$ (middle curve), $n_1 = 10^{-5}$ (lower curve); $\alpha_p = 0.2$ dB/cm, $\alpha_1 = 0$ (uniform loss); κ is the real part of κ_c.

$\Delta\lambda_{\text{peaks}} = \left|\lambda_I^+ - \lambda_I^-\right|$. The dependence of $\Delta\alpha_{\text{peaks}}$ with respect to the refractive index modulation amplitude is analysed in two different cases.

Firstly, the performance of gratings with fixed loss α_p (fully modulated) as n_1 increases is considered. The reflectivity at the Bragg wavelength is always kept constant by adjusting the grating length appropriately. Figure 2.12 shows the variation of $\Delta\alpha_{\text{peaks}}$ as a function of the refractive index modulation amplitude, for a peak reflectivity of 0.999 (in the absence of loss). The background loss is fully modulated with $\phi = 0$ and amplitude 0.1 dB/cm (solid line), 0.2 dB/cm (long dashed line), 0.3 dB/cm (medium dashed line) and 0.4 dB/cm (short dashed line). It is shown that, for each loss-modulation amplitude, the loss asymmetry peaks at a different refractive index modulation amplitude. The maximum is due to the fact that by increasing n_1 the effect of the index grating overcomes that of the loss grating (c.f. equations (2.15)), while by decreasing n_1 the effect of the loss grating dominates that of the index grating. Moreover, for very weak gratings the resonance effects at the edges of the stop band are very small and the loss peaks diminish.

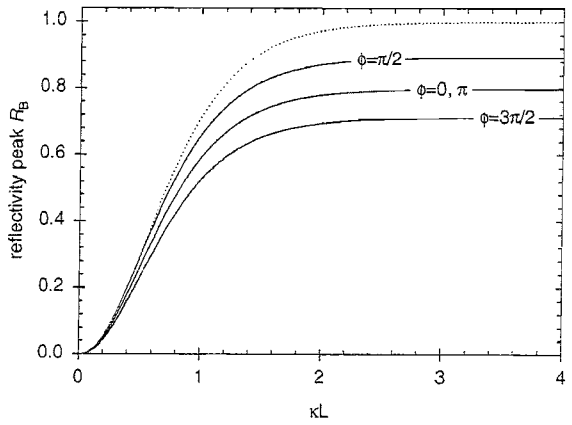

FIGURE 2.11: Reflectivity peak R_B versus κL for four ϕ values (solid lines), with $n_1 = 10^{-5}$, $\alpha_p = 0.2$ dB/cm, $\alpha_1 = \alpha$ (fully modulated loss); the dotted line corresponds to the lossless case ($\alpha = 0$); κ is the real part of κ_c.

For this reason the four plots have different starting points. As the value of the loss α_p is increased, the maximum position shifts to a higher n_1 value because a stronger value of the index coupling coefficient is required to overcome that particular loss grating.

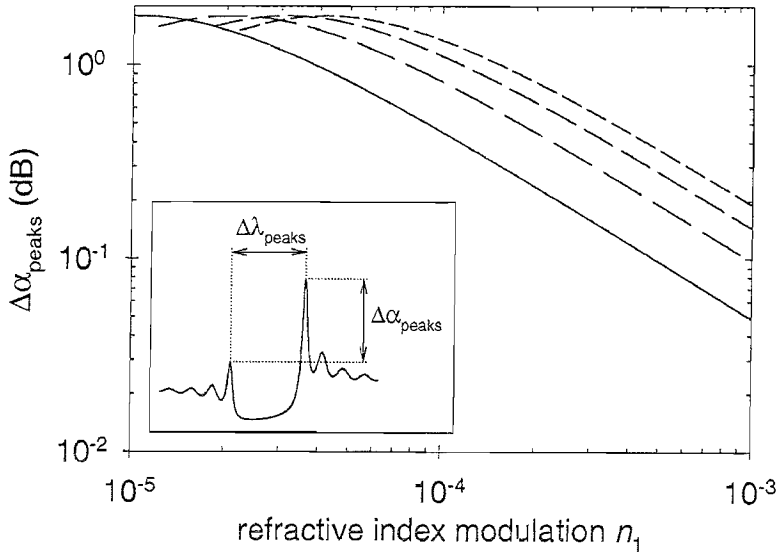

FIGURE 2.12: Amplitude difference $\Delta\alpha_{\text{peaks}}$ of the two loss peaks (shown in the inset) as a function of the refractive index modulation, for a (lossless) grating reflectivity of 0.999, $\phi = 0$ and for four different values of the power loss coefficient: $\alpha_p = 0.1$ dB/cm (solid line), $\alpha_p = 0.2$ dB/cm (long dashed line), $\alpha_p = 0.3$ dB/cm (medium dashed line), $\alpha_p = 0.4$ dB/cm (short dashed line).

Secondly, the performance of gratings with fixed length when both the refractive index modulation and loss modulation amplitudes increase proportionally (fixed α/n_1 ratio) is considered. This is a situation most likely to be encountered in practice when the UV writing process introduces additional losses [20]. Figure 2.13(a) shows the variation of $\Delta\alpha_{\text{peaks}}$ as a function of the refractive index modulation amplitude, and for $L = 2$ cm, a fully modulated background loss with $\phi = 0$ and five different values of the ratio α/n_1. The value of α_p at $n_1 = 3{\cdot}10^{-4}$ is equal to 0.3 dB/cm (solid line), 0.2 dB/cm (long dashed line), 0.1 dB/cm (medium dashed line), 0.05 dB/cm (short dashed line) and 0.01 dB/cm (dotted line). As the index modulation increases, the function $\Delta\alpha_{\text{peaks}}$, after an initial increase, decreases again. Now the index/loss coupling coefficients grow proportionally, but the average value of the loss is always increased. Due to the spectrum asymmetry the reflectivity peak shifts to a wavelength λ_p shorter than λ_B. The wavelength shift $\Delta\lambda_{\text{shift}} = |\lambda_p - \lambda_B|$ is plotted in Figure 2.13(b), while in Figure 2.13(c) the shift $\Delta\lambda_{\text{shift}}$ has been normalised to the peaks difference $\Delta\lambda_{\text{peaks}}$, proportional to the grating spectral bandwidth. However, this shift is a very small proportion of the total band gap.

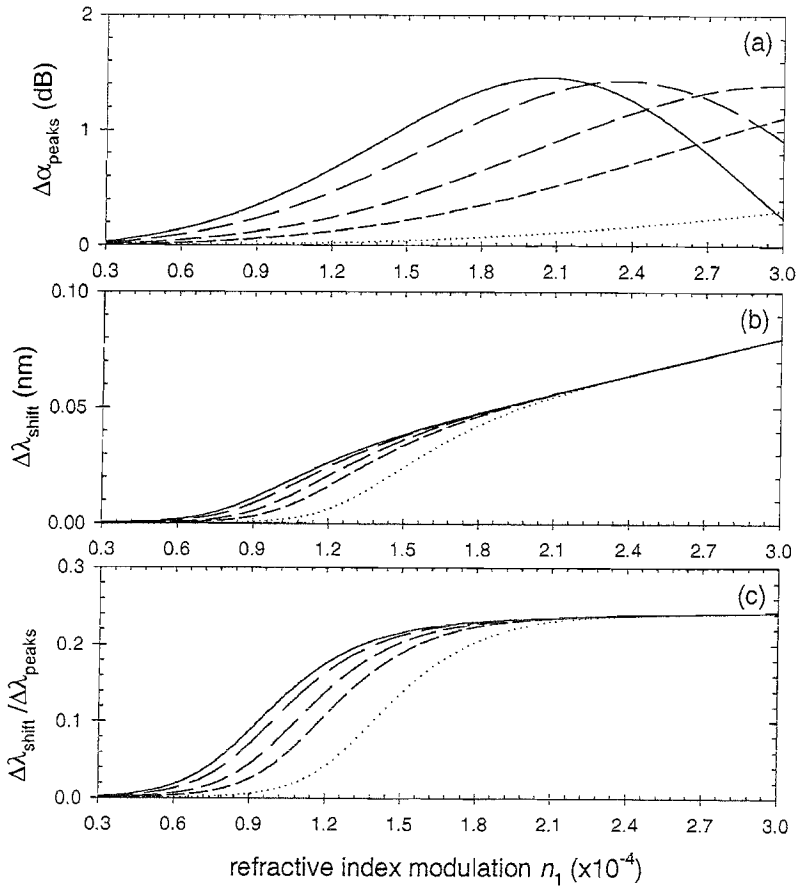

FIGURE 2.13: (a) Amplitude difference $\Delta\alpha_{peaks}$, (b) peak wavelength shift $\Delta\lambda_{shift} = |\lambda_p - \lambda_B|$ and (c) normalised peak wavelength shift $\Delta\lambda_{shift}/\Delta\lambda_{peaks}$ as a function of the refractive index modulation amplitude, for $L = 2$cm and five different values of the ratio $R_n = \alpha/n_1$ .The value of α_p at $n_1 = 3 \cdot 10^{-4}$ is equal to 0.3 dB/cm (solid line), 0.2 dB/cm (long dashed line), 0.1 dB/cm (medium dashed line), 0.05 dB/cm (short dashed line) and 0.01 dB/cm (dotted line).

2.5 Conclusions

In all cases so far reported, the total loss was calculated by using equation (2.13) and the resulting spectral asymmetries were explained physically by considering the spatial relation and overlap (O_{IL}) between field intensities and loss modulation at specific wavelengths and certain positions along the grating. To further endorse the idea that the loss spectra details are due to the exact overlap O_{IL}, a perturbation approach (outlined in Section 2.7) that gives identical results has been adopted. However, it should be stressed that the perturbation technique only applies to small background-loss modulation. When the loss is large and the effect of the loss grating (see equation (2.15)) is comparable to the refractive-index one, the simple perturbation technique becomes inaccurate. In Section 2.3, the analytical solution of the wave equation, considering a loss medium with a periodic modulation of both the real and imaginary part of the refractive index, was reported. For the sake of generality a dephasing factor ϕ has been considered between the two patterns. The expressions for the field distributions along the grating length and for the reflection and transmission coefficients have been deter-

mined. In Section 2.4, the simulation results obtained with the help of these expressions are reported. The comparison between the lossless and the lossy cases has shown an asymmetric spectral behaviour in the latter case. An explanation of this asymmetry in terms of overlap between the total field intensity and the loss zones, strongly dependent on the wavelength, has been developed. Moreover the importance of taking into account the periodicity of the background loss, in those cases in which the dephasing factor value results in a usual symmetric spectral shape, has been underlined.

2.6 Appendix A: Grating standing-wave patterns

In the following only the lossless case is considered with $\alpha = \alpha_1 = 0$ and, therefore, $\kappa_c = \kappa = n_1\pi/\lambda$, $\kappa_s = 0$. The total electric-field intensity inside the grating is given by:

$$I(z) = |E(z)|^2 = |E_f(z) + E_b(z)|^2 \tag{2.16}$$

where $E_f(z)$ and $E_b(z)$ are the forward- and backward-propagating electric fields, respectively. Taking into account equation (2.7), and substituting the slowly-varying amplitudes $A(z) = |A(z)|\exp[j\phi_A(z)]$ and $B(z) = |B(z)|\exp[j\phi_B(z)]$, the total field intensity is expressed as:

$$I(z) = |E(z)|^2 = |A(z)|^2 + |B(z)|^2 + 2\,|A(z)|\,|B(z)|\cos\big(2\beta z + \Delta\phi_{AB}(z)\big) \tag{2.17}$$

where $\beta = \beta_0 = nk_0 = n(2\pi/\lambda)$ is the propagation constant in the unperturbed lossless waveguide and $\Delta\phi_{AB}(z) = \phi_A(z) - \phi_B(z)$. It should be emphasised that under the slowly-varying envelope approximation (SVEA), both the moduli and phases of $A(z)$ and $B(z)$ are slow-varying parameters (i.e., they show infinitesimal changes over a grating period). Equation (2.17) describes a generalised standing-wave pattern with local fringe contrast:

$$F(z) = \frac{2\,|A(z)|\,|B(z)|}{|A(z)|^2 + |B(z)|^2} = \frac{2\,|E_f(z)|\,|E_b(z)|}{|E_f(z)|^2 + |E_b(z)|^2}. \tag{2.18}$$

The fringe contrast will vary along the grating length. The local period of the standing wave (Λ_{sw}) is determined by the total spatial phase of equation (2.17) as follows:

$$\Phi(z) = 2\beta z + \Delta\phi_{AB} = \int_0^z \frac{2\pi}{\Lambda_{sw}(\zeta)}d\zeta \tag{2.19}$$

from which it is obtained:

$$\frac{2\pi}{\Lambda_{sw}(z)} = \frac{d\Phi(z)}{dz} = 2\beta + \frac{d\phi_A(z)}{dz} - \frac{d\phi_B(z)}{dz}. \tag{2.20}$$

Under the SVEA, $d\phi_A/dz \approx d\phi_B/dz \approx 0$ and, therefore,

$$\Lambda_{sw} = \frac{\lambda}{2n} = \frac{\lambda_n}{2} \tag{2.21}$$

where $\lambda_n = \lambda/n$ is the optical wavelength in the propagation medium with refractive index n. The standing wave period is constant along the entire grating length and is proportional to the optical wavelength of the incident wave. It is, therefore, expected that there will be a spatial dephasing between the standing-wave and refractive-index periodic patterns that depends on the incident optical wavelength.

The spatial dephasing can be determined by starting from the full expressions for $E_f(z)$ and $E_b(z)$ given by equations 2.10(a) and (b). Expressing the forward- and backward-

propagating electric fields as $E_f(z) = |E_f(z)| \exp[j\phi_f(z)] \exp(j\beta_B z)$ and $E_b(z) = |E_b(z)| \exp[j\phi_b(z)] \exp(-j\beta_B z)$, the total electric-field intensity can be re-written as:

$$I(z) = |E(z)|^2 = |E_f(z)|^2 + |E_b(z)|^2 + 2\,|E_f(z)|\,|E_b(z)| \cos\big(2\beta_B z + \Delta\phi_{fb}(z)\big). \quad (2.22)$$

The standing-wave pattern is now expressed in terms of the grating spatial phase $2\beta_B z$ (c.f. equation 2.1(a)). The term $\Delta\phi_{fb} = \phi_f(z) - \phi_b(z)$ gives, therefore, directly the spatial dephasing between the total field intensity and the fixed periodic refractive-index modulation, at any point within the grating.

The spectral region outside the band-gap is firstly considered, where $\Delta^2 > \kappa^2$ and $p = j\sqrt{\Delta^2 - \kappa^2} = j\overline{p}$ is imaginary. The expressions for ϕ_f and ϕ_b are

$$\phi_f(z) = \arctan\left(\frac{-\overline{p}\Delta \sin \overline{p}z}{\Delta^2 \cos \overline{p}z - \kappa^2 \cos \overline{p}L \cos \overline{p}(z-L)}\right) + \pi\hat{\delta}(\Delta^2 \cos \overline{p}z - \kappa^2 \cos \overline{p}L \cos \overline{p}(z-L) < 0) \quad (2.23a)$$

$$\phi_b(z) = \arctan\left(\frac{\overline{p}}{\Delta} \cot \overline{p}L\right) + \pi\hat{\delta}(\Delta\kappa \sin \overline{p}L \sin \overline{p}(z-L) > 0) \quad (2.23b)$$

where $\hat{\delta}(y)$ is equal to 1 when the condition y is verified, otherwise it is zero. Using the low reflectivity approximation (i.e. $\overline{p} \approx |\Delta|$), the equation (2.23) can be simplified as

$$\phi_f^{\pm}(z) \approx \mp \overline{p}z \quad (2.24a)$$

$$\phi_b^{\pm}(z) \approx \pm\left(\frac{\pi}{2} - \overline{p}L\right) + \pi\hat{\delta}(\pm \sin \overline{p}L \sin \overline{p}(z-L) > 0) \quad (2.24b)$$

where the superscript $(\pm)$ denotes $\lambda = \lambda^{\pm}$. The low reflectivity approximation affects mainly the expression of ϕ_f that at higher reflectivity, due to the multi-reflections, is no longer a linear function of z. From equation (2.24a) is appears that ϕ_f is a continuous function of z and that $\phi_f^+ = -\phi_f^-$. This is anyway also verified by equation (2.23a). In both the expressions (2.23b) and (2.24b), ϕ_b is composed of two terms. The first one is z-independent, while the second consists of a π shift added to the grating sections where $\hat{\delta}(z) = 1$. From (2.23b) and (2.24b) it is in addition evident that $\phi_b^+ = -\phi_b^- + \pi$, so $\Delta\phi_{fb}^+ = -\Delta\phi_{fb}^- + \pi$.

The π phase discontinuities in $\Delta\phi_{fb}$ are due to ϕ_b only. The π shift condition of ϕ_b, argument of $\hat{\delta}$ in (2.24b), depends on z through $\sin \overline{p}(z-L)$, so when $\sin \overline{p}(z-L)$ changes sign there is a discontinuity. Moreover $|E_b(z)| \propto \sin \overline{p}(z-L)$, so each π phase discontinuity is localised in the z-coordinate, denoted by z_m, where the backward-propagating electric field goes to zero. From the condition $\sin \overline{p}(z_m - L) = 0$ it follows that $z_m = L - m\pi/\overline{p}$, where m is a whole positive number. With this notation, the boundary condition is placed at the "first node" $z_0 = L$. Depending on whether z_m is approached from the

higher (z_m^+) or the lower (z_m^-) values, from (2.24) it is derived that

$$\phi_f^{\pm}(z_m^+) = \mp\overline{p}L + m\pi \tag{2.25a}$$

$$\phi_b^{\pm}(z_m^+) = \mp\frac{\pi}{2} \mp \overline{p}L + \binom{m+1}{m}\pi \tag{2.25b}$$

and

$$\phi_f^{\pm}(z_m^-) = \mp\overline{p}L + m\pi \tag{2.25c}$$

$$\phi_b^{\pm}(z_m^-) = \mp\frac{\pi}{2} \mp \overline{p}L + \binom{m}{m+1}\pi \tag{2.25d}$$

where the upper (lower) part is valid for the long (short) wavelength side. It is now easily deduced that $\Delta\phi_{fb}(z_m^+) = +\pi/2$ and $\Delta\phi_{fb}(z_m^-) = -\pi/2$. So at z_m precisely, the local dephasing shows a π phase discontinuity.

Considering a grating made by a positive whole number of periods M (i.e. $L = M\Lambda$) the resonance wavelengths are expressed by

$$\lambda_w = \frac{\lambda_B}{1 - \frac{w}{M}} \tag{2.26}$$

where the integer w denotes the order (i.e. $\lambda_I^{\pm} = \lambda_{\pm 1}$, $\lambda_{II}^{\pm} = \lambda_{\pm 2}$, etc.). According to the low reflectivity approximation $\overline{p}_w = \pi\,|w|\,/L$. For each resonance wavelength, given two consecutive field nodes z_m and z_{m+1}, the value of the local dephasing at $\bar{z}_m = (z_m + z_{m+1})/2 = L - (2m+1)\pi/2\overline{p}$ is calculated, starting from

$$\phi_f^{\pm}(\bar{z}_m) = \mp\overline{p}L \pm \frac{(2m+1)\pi}{2} \tag{2.27a}$$

$$\phi_b^{\pm}(\bar{z}_m) = \pm\left(\frac{\pi}{2} - \overline{p}L\right) + \binom{m}{m+1}\pi. \tag{2.27b}$$

Therefore, for the short-wavelength side $\Delta\phi_{fb}^-(\bar{z}_m) = \pi$, while for the long-wavelength one $\Delta\phi_{fb}^+(\bar{z}_m) = 0$.

The spectral region inside the band-gap is now considered, where $\Delta^2 < \kappa^2$ and $p = \sqrt{\kappa^2 - \Delta^2}$ is real. The following expressions for ϕ_f and ϕ_b are obtained

$$\phi_f(z) = \arctan\left(\frac{-2p\Delta\sinh pz}{(p^2 - \Delta^2)\cosh pz + \kappa^2\cosh p(z-2L)}\right) \tag{2.28a}$$

$$\phi_b(z) = \arctan\left(\frac{p}{\Delta}\coth pL\right) + \pi\hat{\delta}(\Delta < 0). \tag{2.28b}$$

Since the denominator of the arctangent argument of ϕ_f is always positive, its sign is determined by the numerator, so that $\phi_f^+ = -\phi_f^-$ is verified. For ϕ_b the justification used for (2.23b) can be repeated, so $\phi_b^+ = -\phi_b^- + \pi$ and $\Delta\phi_{fb}^+ = -\Delta\phi_{fb}^- + \pi$. Moreover, the π shift condition of ϕ_b is z-independent, so inside the band-gap ϕ_b is constant along

the grating length.

At the Bragg wavelength $\Delta = 0$, so $\phi_f = 0$ and $\phi_b = \pi/2$ from which the spatial dephasing is equal to $\Delta\phi_{fb} = -\pi/2$ at any position along the grating length.

For all the wavelengths, both inside and outside the band-gap, at a point infinitesimally close to the grating far end ($z \to L$) $\Delta\phi_{fb} = -\pi/2$. Outside the band-gap it has already been demonstrated that $\Delta\phi_{fb}(z_0^-) = -\pi/2$, where $z_0 = L$. Inside the band-gap, at $z \to L$ the equations 2.28(a) and (b) can be approximated as:

$$\phi_f(L^-) = -\arctan\left(\frac{\Delta}{p}\tanh pL\right) \tag{2.29a}$$

$$\phi_b(L^-) = \arctan\left(\frac{p}{\Delta}\frac{1}{\tanh pL}\right) + \pi\hat{\delta}(\Delta < 0) \tag{2.29b}$$

that lead to $\Delta\phi_{fb}(L^-) = -\pi/2$.

2.7 Appendix B: Loss perturbation calculation

In case of a weakly absorbing medium, the fraction of the dissipated power can be calculated by considering the spatial overlap between the loss profile and the power distribution corresponding to the lossless case (therefore, $\kappa_c = \kappa = n_1\pi/\lambda$, $\kappa_s = 0$). This approach is quite accurate provided that the presence of loss constitutes only a weak perturbation and does not change considerably the final power distribution. In this case, the local intensity change over an infinitesimal section dz is given by:

$$dI_{\text{loss}}(\lambda) = 2\alpha(z)\frac{I(z,\lambda)}{I_{\text{inc}}(\lambda)}dz. \tag{2.30}$$

where $\alpha(z)$ is the local field absorption coefficient, $I_{\text{inc}}(\lambda) = |E_f(0,\lambda)|^2 = |E_{\text{inc}}|^2$ the incident field intensity and $I(z,\lambda)$ the local field intensity, corresponding to the lossless case [30]. The fraction of the input power, dissipated due to losses along the entire structure, is then given by:

$$I_{\text{loss}}(\lambda) = \frac{2}{|E_{\text{inc}}|^2}\int_0^L \alpha(z)\,|E(z,\lambda)|^2\,dz \tag{2.31}$$

where the background-loss perturbation is given by equation (2.1b).

Expressing the total electric-field intensity as in equation (2.22), under the SVEA the integral (2.31) can be simplified as

$$I_{\text{loss}}(\lambda) \approx \frac{2\alpha}{|E_{\text{inc}}|^2}\int_0^L (|E_f(z,\lambda)|^2 + |E_b(z,\lambda)|^2)dz + \frac{2\alpha_1}{|E_{\text{inc}}|^2}\int_0^L |E_f(z,\lambda)|\,|E_b(z,\lambda)|\cos(\phi - \Delta\phi_{fb}(z,\lambda))dz. \tag{2.32}$$

In the cases considered in this work, the integral (2.32) gives the loss spectrum as obtained from $I_{\text{loss}} = 1 - R - T$. Studying the wavelength dependence of $|E_f(z,\lambda)|$, $|E_b(z,\lambda)|$, and $\Delta\phi_{fb}(z,\lambda)$, it is possible to justify the symmetrical/anti-symmetrical behaviour of the grating loss spectrum according to the value of the dephasing factor ϕ. Since the moduli of the forward- and backward-propagating fields are symmetrical with respect to the Bragg wavelength, the first term in (2.32), that is ϕ-independent, is also symmetrical with respect to λ_B. The asymmetry observed for $\phi = 0$ and π is then due to the second term in (2.32), and particularly due to the fact that $\Delta\phi_{fb}(z,\lambda^+) = -\Delta\phi_{fb}(z,\lambda^-) + \pi$, as demonstrated in Section 2.6.

2.8 Appendix C: Effective index medium

In a uniform grating the maximum reflection occurs when the Bragg condition is fulfilled, i.e. at $\lambda_B = 2n_{eff}\Lambda$, where $n_{eff} = n$ if the refractive index perturbation is $n(z) = n + n_1 \cos 2\beta_B z$ (c.f. equation (2.1)). Considering the analogy of propagation in a homogeneous medium of refractive index n_{eff}, the wavelength of the light in the medium (λ/n_{eff}) equals twice the grating periodicity Λ.

Increasing the strength of a 100% reflectivity grating at λ_B broadens and squares off the grating spectral response (c.f. Figure 2.15). The reflection is maximum and equal to 1 over a band centred on the Bragg wavelength, here called saturation band. Does this mean that the Bragg condition is satisfied not only at the Bragg wavelength, but also at all the wavelengths included in the saturation band?

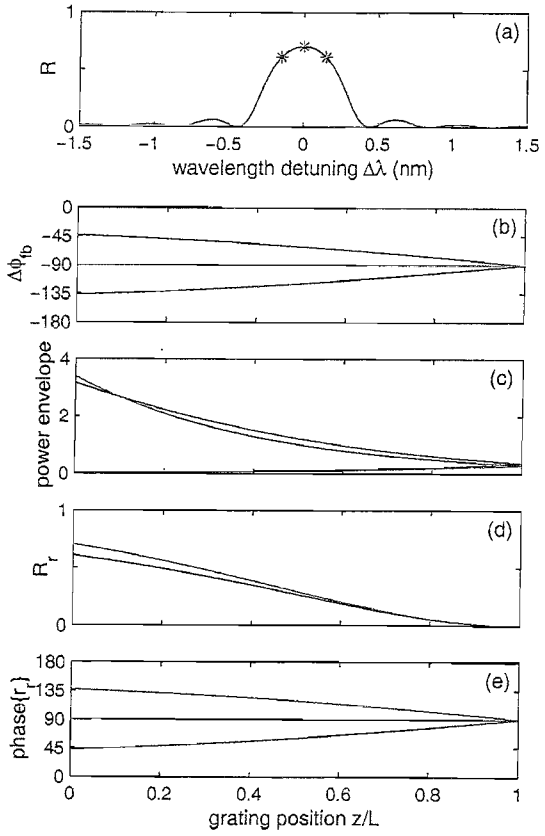

FIGURE 2.14: Not-saturated grating ($\sim$ 5 dB): (a) reflectivity R as a function of the wavelength detuning $\Delta\lambda$; (b) spatial dephasing $\Delta\phi_{fb}$, (c) normalised power envelope, (d) reflectivity of the "right grating" R_r and (e) phase of the reflection coefficient for the "right grating" as a function of the position along the grating length (z/L) at the three wavelengths marked in (a) by the asterisks.

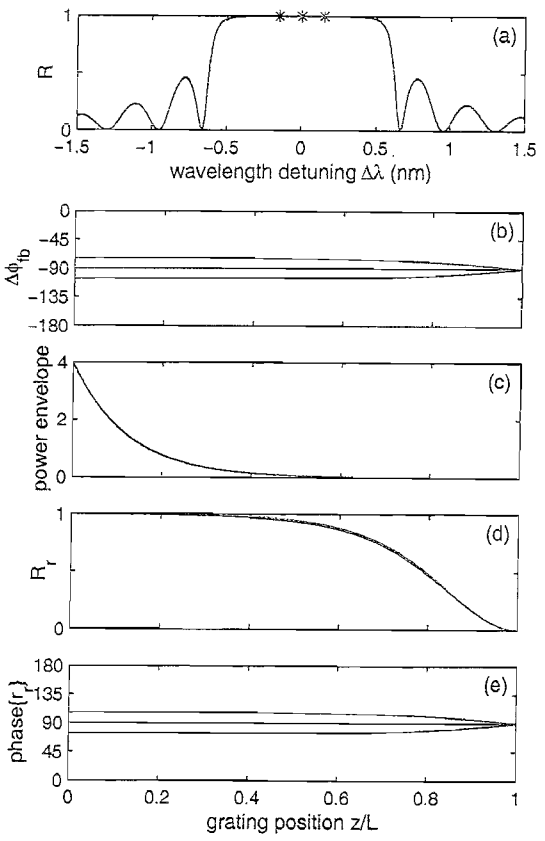

FIGURE 2.15: Saturated grating ($\sim$ 31 dB): (a) reflectivity as a function of the wavelength detuning $\Delta\lambda$; (b) spatial dephasing $\Delta\phi_{fb}$, (c) normalised power envelope, (d) reflectivity of the "right grating" R_r and (e) phase of the reflection coefficient for the "right grating" as a function of the position along the grating length (z/L) at the three wavelengths marked in (a) by the asterisks.

As already pointed out in Section 2.6, the grating standing-wave pattern can be expressed in terms of the grating spatial phase $2\beta_B z$ as:

$$I(z) = |E(z)|^2 = |E_f(z)|^2 + |E_b(z)|^2 + 2\,|E_f(z)|\,|E_b(z)|\cos\big(2\beta_B z + \Delta\phi_{fb}(z)\big) \quad (2.33)$$

where the term $\Delta\phi_{fb} = \phi_f(z) - \phi_b(z)$ gives directly the spatial dephasing between the total field intensity and the fixed periodic refractive-index modulation, at any point within the grating. It is worth noticing that at $\lambda \neq \lambda_B$ this is an "equivalent" standing-wave pattern, since the real one has a periodicity equal to $2\beta z$.

As shown in Figure 2.9, at λ_B the field intensity pattern is locked at $\pi/2$-dephasing with respect to the refractive index pattern, independently from the grating strength. This is confirmed by the green lines in Figures 2.14(b) (not-saturated grating) and 2.15(b) (saturated grating).

For the not-saturated grating (Figure 2.14) at wavelengths nearby λ_B (red and blue) the spatial dephasing is never constant in any position along the grating length. The grating seen by a forward-propagating wave as it propagates deeper into the structure, here called "right grating" (R_r), is always below 100% reflectivity (Figure 2.14(d)). The grating strength is not sufficient to completely reflect the forward-propagating wave, and results in an intensity pattern always travelling along the index one. The spatial dephasing $\Delta\phi_{fb}$ is anyway fully determined by the reflection phase of the "right grating" (Figure 2.14(e)).

In the saturated grating (Figure 2.15), the "right grating" reaches 100% reflectivity at a wavelength belonging to the saturation band (red and blue in Figure 2.15(d)). This results in the creation of a real standing-wave pattern localised in the first part of the grating (Figure 2.15(b)), where the total power that is rapidly decaying to zero is still present (Figure 2.15(c)). In this zone the spatial dephasing $\Delta\phi_{fb}$ is locked to a value different from $\pi/2$, still determined by the reflection phase of the "right grating" (Figure 2.14(e)). The spatial dephasing is smaller (bigger) than $\pi/2$ at wavelengths bigger (smaller) than λ_B, resulting in a bigger (smaller) overlap of the intensity pattern on the index pattern. This picture can be analytically verified by calculating the overlap between the index $n(z)$ and intensity $I(z)$ patterns with the following expression:

$$n_{eff,ov}(\lambda) = \frac{\int_0^L n(z)\,|E(z,\lambda)|^2\,dz}{\int_0^L |E(z,\lambda)|^2\,dz} \quad (2.34)$$

that truly represents the effective index experienced by $I(z)$, so called $n_{eff,ov}$. Under the slow-varying envelope approximation $n_{eff,ov}$ results in:

$$n_{eff,ov}(\lambda) \approx n + n_1 \frac{\int_0^L |E_f|\,|E_b|\cos(\Delta\phi_{fb})dz}{\int_0^L (|E_f|^2 + |E_b|^2)dz}. \quad (2.35)$$

Figure 2.16 shows the plot of $n_{eff,ov}$ for the not-saturated (n_{ns}) and saturated (n_s) grating (thick solid lines). The effective index resulting from the Bragg condition $n_{eff} = \lambda/2\Lambda$ is also plotted (thin solid line). While n_{ns} coincides with n_{eff} at λ_B only, n_s coincides with it all over the saturation band and the Bragg condition is clearly satisfied all over the saturation band.

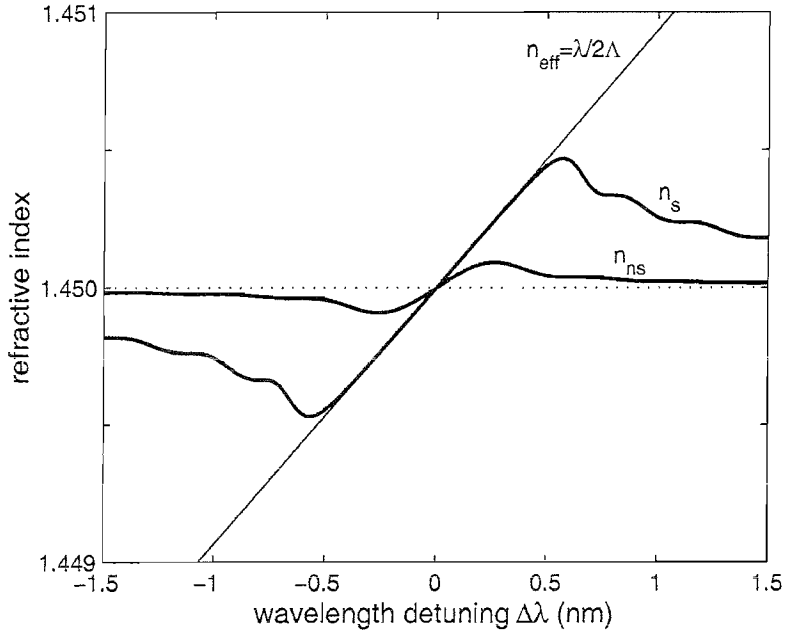

FIGURE 2.16: Effective refractive index as a function of the wavelength detuning (nm) for the not-saturated (n_{ns}) and saturated (n_s) grating (thick solid lines); the thin solid line is the effective index derived from the Bragg condition (n_{eff}).

It is worth noticing that with the help of the local fringe contrast expression (c.f. equation (2.18)) $n_{eff,ov}$ can be re-written as:

$$n_{eff,ov}(\lambda) \approx n + n_1 \frac{\int_0^L F(z)(|E_f|^2 + |E_b|^2)\cos(\Delta\phi_{fb})dz}{2\int_0^L (|E_f|^2 + |E_b|^2)dz}. \tag{2.36}$$

In the case of finite one-dimensional photonic band-gap structures another method has been developed to calculate the effective refractive index [31, 32]. In the analogy of propagation in a homogeneous medium, the total phase associated with the transmitted field can be expressed by:

$$\phi_t = k(\omega)L = \frac{\omega}{c} n_{eff,\phi}(\omega)L \tag{2.37}$$

where $k(\omega)$ is the effective wave-vector and consequently $n_{eff,\phi}$ is the effective refractive index attributed to the layered structure of length L. Applying the same approach to the gratings considered in this section results in a graph that doesn't coincide with $n_{eff,ov}$ (and with n_{eff} in the saturated case). $n_{eff,ov}$ and $n_{eff,\phi}$ are superimposed, in the saturation band, only when the length of the grating is increased to simulate an infinite grating. In the case of propagation in periodic stratified media, the effective index can

be derived by the Bloch mode theory as

$$n_{eff,BM}(\omega) = c\frac{K(\omega)}{\omega} \tag{2.38}$$

where $K(\omega))$ is the Bloch wave number [33, 34]. It is worth noticing that in the bandgap $n_{eff,BM}$ equals n_{eff}.

Chapter 3

Cladding mode losses in chirped fibre Bragg gratings

3.1 Chirped FBGs for dispersion compensation

Chirped FBGs can be used to compensate the dispersion of fibres used in fibre transmission lines, including SMF-28 the most commonly used. Transmission fibres have a dispersion zero at 1300 nm at wavelengths in the erbium-doped fibre amplifier (EDFA) gain bandwidth, which is centre at $\sim$ 1550 nm [35]. Chirped gratings "refocus" the spectral components of a chirped incident pulse directly by reflecting the longest wavelength at the start of the grating and shorter wavelengths at position progressively deeper into the grating. The continuous writing technique [9] allows long gratings to be written, therefore providing the possibility to compensate the dispersion resulting from the transmission along long lengths of fibre. As well as having a dispersion profile matched to the fibre to be compensated (i.e. the right phase response) it is also important that the reflection spectrum (amplitude response) of the device is flat. In the following, cladding mode losses which can affect the reflection spectrum of such devices are analysed. It is shown also how to design the chirped FBGs in order to counteract this loss.

3.2 Cladding mode losses

Cladding mode losses in fibre Bragg gratings (FGBs) have been addressed in several papers [28, 36, 37, 38] and shown to limit the performance of FBG devices. In unchirped gratings the resonant coupling of the forward-propagating core mode to a particular backward-propagating cladding mode is considered independently and the effect on the total transmissivity spectrum is obtained by simply multiplying the individual responses. The presence of cladding mode losses in chirped gratings affects the grating performance

in a much more complicated manner. Cladding mode losses interfere with the core mode within the main reflection band and introduce additional transmission loss on the short-wavelength side. This effect is independent of the grating input side. The corresponding effect on the reflection spectrum, however, depends on the grating input side. Entering the chirped grating from the "red" end (longer local period) results in a pronounced reflection spectrum slope, while entry from the "blue" end (shorter local period) leaves it unaffected. An experimental demonstration of this effect has been presented for broad-band chirped gratings in [39].

Several techniques can be used in order to minimise the overlap between core and cladding modes. Observe that increasing the extent (outer diameter) of the cladding results in reducing the confinement of the cladding modes, thus decreasing the cladding mode coupling strength. Ideally a fibre with an infinite cladding cannot guide cladding modes. However, due to integration with the standard fibre system, it is not possible to increase the cladding outer diameter over the extent needed to suppress all the cladding modes. Another approach consists of using high numerical aperture (high-NA) fibres [40]. The high-NA does not substantially affect the cladding modes, but allows the confinement of the core mode into a smaller area. Thus the overlap between core and cladding modes is reduced. The spectral distance between the first cladding mode and the core is also increased due to the higher refractive index in the core region with respect to the cladding region. The operation band is therefore larger than that achieved using standard fibres, but not wide enough for most applications. An alternative approach consists of extending the photosensitivity to the cladding region [41]. From the orthogonality principle of the modes, the overlap of the modal fields and the grating index would be zero in this case. Thus the core mode will not couple into any of the cladding modes. It is however very difficult to obtain the same photosensitivity over both cladding and core. Depressed cladding fibres reduce the cladding mode field strength over the core region and therefore reduce the coupling strength between the core mode and the cladding modes [42]. In [43] the resonant excitation of cladding modes is damped by introducing a propagation loss into the cladding modes. This is achieved by depositing a thin lossy layer on the cladding surface: a layer which does not affect the propagation of the core mode but only that of the cladding modes. All these approaches can also be combined for total elimination of cladding mode losses. However they require the fibre design to be properly modified.

In [39] the possibility of equalising the reflection spectrum of chirped FBGs, affected by cladding mode losses, with the help of a proper apodisation profile has been shown. This can be directly applied to standard fibre types. This chapter present a study of the interaction and power exchange between core-cladding and cladding-cladding fibre modes due to the grating chirp. To account for the complex effect of cladding modes on the performance of chirped FBGs, the basic coupled mode theory [1] should be extended to properly consider the mode interaction. The model is then used to study

the equalisation of the reflection spectrum by means of a proper apodisation profile, defining also the limitation of this approach.

3.3 Theoretical model

The refractive index perturbation of a linearly chirped fibre Bragg grating can be expressed by

$$n(z) = n_{eff} + \Delta n_{eff} = n_{eff} + \delta n_{eff}\{1 + v(z)\cos[K_0 z + \phi(z)]\} \tag{3.1}$$

where n_{eff} is the background effective refractive index of the fibre core, δn_{eff} and $v(z)$ are respectively the effective amplitude and the slowly varying envelop function of the induced change in index Δn_{eff}, $K_0 = 2\pi/\Lambda_0$ is the reference Bragg wavevector (Λ_0 is the reference Bragg period), $\phi(z)$ is the slowly varying grating phase. In order to have a linear chirp, the grating phase is defined as:

$$\phi(z) = -\frac{K_0 C_R}{2\lambda_0} z^2 \tag{3.2}$$

where C_R (in nm/cm) is the chirp rate. Note that the values of n_{eff} and δn_{eff} are both related to the propagating mode characteristics. In the following it is assumed that the induced index change δn_{co} is uniformly distributed across the core of a step-index profile fibre. For a propagating mode with a core power confinement factor Γ, $\delta n_{eff} = \Gamma \delta n_{co}$. The apodisation profile, given by $v(z)$, has been introduced in this way so that the average index change is constant along the grating length. In the following, Γ, n_{eff} and δn_{eff} are indexed according to the propagating mode combinations. Thus Γ_{mn} represents the core confinement factor of the n and m modes.

The model is based on coupled-mode theory and describes the coupling between the forward-propagating core mode, the backward-propagating core mode, and N backward-propagating cladding modes [28] (see Figure 3.3). The following two approximations have been introduced: (*i*) no forward-propagating cladding modes are considered and (*ii*) the cladding mode cross-coupling is considered to take place exclusively through the forward-propagating core mode. This is justified by the fact that the coupling constant between core-cladding and cladding-cladding modes is much weaker than the corresponding core-core parameter so that only one scattering event is required (Born approximation) to completely describe this multimode interaction.

According to the coupled-mode theory [28, 44], the electric field, present in the fibre grating, can be expressed as a superposition of ideal modes. In this case only $N + 2$ modes are considered, so the electric field is given by

$$E(z) = E_f(z) + E_b(z) = A(z)e^{j\beta z} + B(z)e^{-j\beta z} + \sum_n C_n(z)e^{-j\beta_n z} \tag{3.3}$$

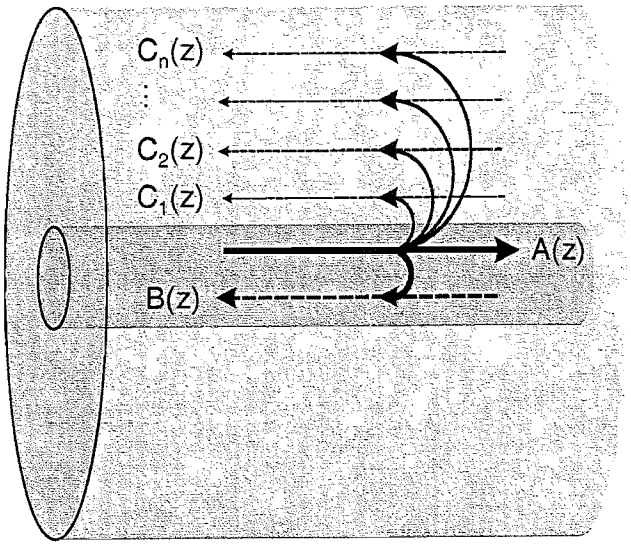

FIGURE 3.1: Schematic of the fibre modes considered in the model.

where $A(z)$ and $B(z)$ are the slowly varying amplitudes of the core forward- and backward-propagating modes, $C_n(z)$ is the n-th cladding backward-propagating mode ($n = 1, \ldots, N$), β and β_n are the propagation constants of the uncoupled waves. The presence of a refractive index perturbation causes the coupling between the modes, so that the change in amplitude of each mode along z depends on the perturbation Δn_{eff} (3.1) and on the amplitudes of all the other modes:

$$\frac{dA}{dz} = jAK_{00} + jBK_{00}e^{-j2\beta z} + j\sum_n C_n K_{n0} e^{-j(\beta_n+\beta)z} \tag{3.4a}$$

$$\frac{dB}{dz} = -jAK_{00}e^{j2\beta z} - jBK_{00} - j\sum_n C_n K_{n0} e^{-j(\beta_n-\beta)z} \tag{3.4b}$$

$$\frac{dC_n}{dz} = -jAK_{0n}e^{j(\beta+\beta_n)z} - jBK_{0n}e^{-j(\beta-\beta_n)} - j\sum_{m\neq n} C_m K_{mn} e^{-j(\beta_m-\beta_n)z}. \tag{3.4c}$$

The coupling coefficients $K_{mn}(z)$ are given, for the all mn-pairs present in (3.4), by

$$K_{mn}(z) = \sigma_{mn} + 2\kappa_{mn}(z)cos[Kz + \phi(z)] \tag{3.5}$$

as a function, then, of a "dc" coupling coefficient σ_{mn} (z-independent) and a "ac" coupling coefficient $\kappa_{mn}(z)$, namely

$$\sigma_{mn} = \frac{2\pi}{\lambda}\delta n_{eff,mn} \tag{3.6}$$

$$\kappa_{mn}(z) = \frac{v(z)}{2}\sigma_{mn}. \tag{3.7}$$

The system (3.4) can be simplified applying the synchronous approximation and ne-

glecting the effect of backward co-directional contributions in (3.4b) and (3.4c). The substitution

$$a(z) = A(z)e^{j(\delta_0 z - \frac{1}{2}\phi(z))} \tag{3.8a}$$

$$b(z) = B(z)e^{-j(\delta_0 z - \frac{1}{2}\phi(z))} \tag{3.8b}$$

$$c_n(z) = C_n(z)e^{-j(\delta_n z - \frac{1}{2}\phi(z))} \tag{3.8c}$$

leads to the following system

$$\frac{da}{dz} = j\hat{\sigma}_0(z)a(z) + j\kappa_{00}(z)b(z) + j\sum_n \kappa_{n0}(z)c_n(z) \tag{3.9a}$$

$$\frac{db}{dz} = -j\hat{\sigma}_0(z)b(z) - j\kappa_{00}(z)a(z) \tag{3.9b}$$

$$\frac{dc_n}{dz} = -j\hat{\sigma}_n(z)c_n(z) - j\kappa_{0n}(z)a(z). \tag{3.9c}$$

The wavenumber de-tuning coefficients δ_n and the local de-tuning coefficient $\hat{\sigma}_n(z)$ are given by

$$\delta_0 = \beta - \frac{\pi}{\Lambda_0} \tag{3.10a}$$

$$\delta_n = \beta_n - \frac{\pi}{\Lambda_0} \tag{3.10b}$$

$$\hat{\sigma}_n(z) = \delta_n + \sigma_{nn} - \frac{1}{2}\frac{d\phi}{dz}. \tag{3.11}$$

From the system (3.9) is clear that $\kappa_{mn}(z)$ assumes also the meaning of local coupling coefficient between the n-th forward-propagating mode and the m-th backward-propagating mode. The conservation of total power can be expressed as

$$\frac{d}{dz}\left[|a|^2 - |b|^2 - \sum_n |c_n|^2\right] = 0 \tag{3.12}$$

which, using (3.9) and taking into account that in a lossless structure κ is real, is satisfied when

$$\kappa_{0n} = \kappa_{n0}. \tag{3.13}$$

Introducing $N+1$ local reflection coefficients $r_0, r_1, \ldots, r_N$ and the local transmission coefficient $t_0(z)$, respectively defined as

$$r_0(z) = \frac{b(z)}{a(z)} \tag{3.14a}$$

$$r_n(z) = \frac{c_n(z)}{a(z)} \tag{3.14b}$$

$$t_0(z) = \frac{a(z)}{a(0)}, \tag{3.14c}$$

the system (3.9) can be re-written as:

$$\frac{dr_0}{dz} = -j2\hat{\sigma}_0(z)r_0(z) - j\kappa_{00}(z)[1 + r_0^2(z)] - jr_0(z)\sum_n \kappa_{n0}(z)r_n(z) \tag{3.15a}$$

$$\frac{dr_n}{dz} = -j[\hat{\sigma}_0(z) + \hat{\sigma}_n(z)]r_n(z) - j\kappa_{n0}(z)[1 + r_n^2(z)] - jr_n(z)\sum_{m\neq n} \kappa_{m0}(z)r_m(z) \tag{3.15b}$$

$$\frac{dt_0}{dz} = j\hat{\sigma}_0(z)t_0(z) + jt_0(z)\sum_n \kappa_{n0}(z)r_n(z). \tag{3.15c}$$

Observe that equations 3.15(a) and 3.15(b) are an extended version of the Riccati equation. From these equations it is obvious that the cladding-mode to cladding-mode coupling has been ignored. This is a second-order interaction and introduces small errors. The case without cladding-mode excitation ($\kappa_{n0} = 0$, $n = 1, 2, \ldots, N$) reverts equation 3.15(a) to the well known Riccati equation.

The system (3.15) is solved via integration with boundary conditions $t_0(0) = 1$ and $r_n(L) = 0$ for $n = \{0, \ldots, N\}$. Note that this is equivalent to the integration of (3.9) with boundary conditions $a(0) = 1$ and $b(L) = c_n(L) = 0$. The integration results in the expression of the grating reflection and transmission coefficients as a function of λ. Entering the grating from the "blue" end (c.f. Figure 3.2) the transmission coefficient t and reflection coefficient r can be obtained respectively as $r(\lambda) = r_0(0)$ and $t(\lambda) = t_0(L)$, while entering from the "red" the reflection coefficient ρ is obtained in the same way as r by reversing the chirp sign. The transmission coefficient is not affected due to reciprocity. From these coefficients, the grating transmissivity $T(\lambda)$ and reflectivity $R(\lambda)$ from the "blue"-"red" end can be calculated as $T(\lambda) = |t(\lambda)|^2$, $R(\lambda) = |r(\lambda)|^2$, $R(\lambda) = |\rho(\lambda)|^2$.

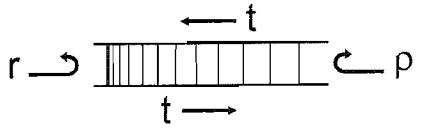

FIGURE 3.2: Schematic of the grating transmission and reflection coefficients t, r and ρ.

3.4 Study of the mode interaction

The theoretical model is first applied to demonstrate the interaction between cladding modes and core modes in an unapodised chirped grating, i.e. $v(z) = 1$ for every z in equation (3.1). For the sake of simplicity and better visualisation the coupling into one (Figures 3.3(a)-(c)) and two (Figures 3.3(d)-(f)) cladding modes only is considered. The grating parameters are shown in the figure caption. The first column in Figure 3.3 shows the reflectivity of the core and cladding modes when light is launched from the

"red" grating end, while the second column shows the corresponding spectra from the "blue" grating end. The third column gives the corresponding transmission spectrum. Figure 3.3(a) shows that the cladding mode spectrum (light blue line) overlaps with the main reflection band (red line) and affects its shape. However, when the grating is reversed (Figure 3.3(b)) the role of the modes is reversed too and as a result the cladding mode reflection spectrum is affected while the main reflection band remains intact. In the presence of two cladding modes (Figure 3.3(d)) a similar interaction is observed between cladding mode spectra with the shorter-wavelength reflection spectrum (dark blue line) affecting the longer-wavelength reflection spectrum (light blue line) and the combined effect passed on to the main reflection band (red line). As before, reversal of the grating results in a reversal of the role of the three modes (Figure 3.3(e)).

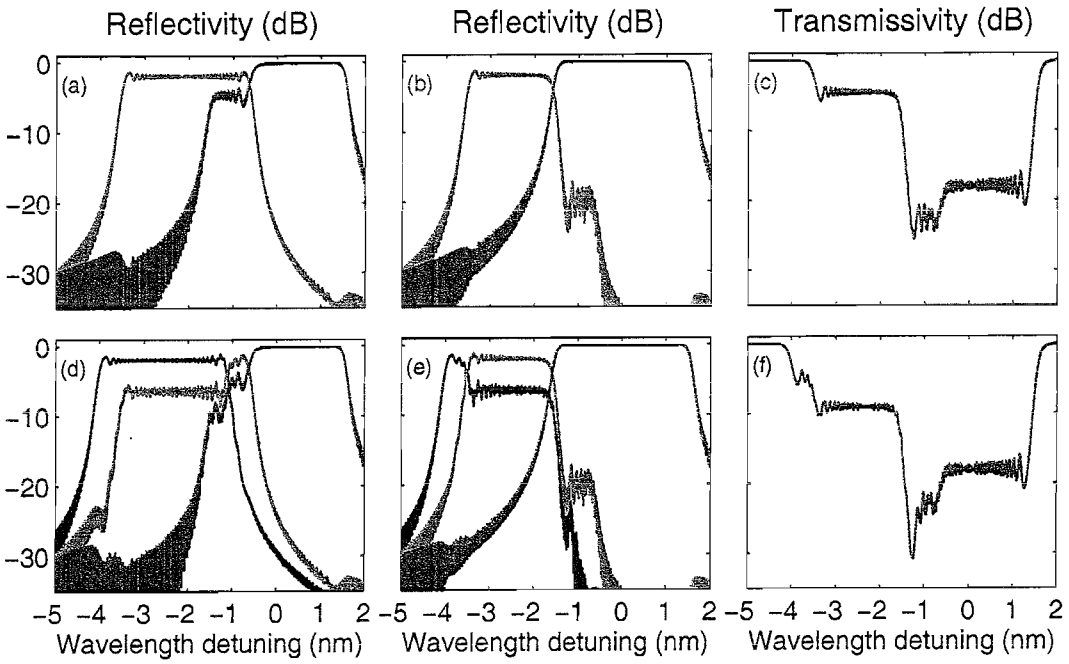

FIGURE 3.3: Spectral characteristics of an unapodised linearly chirped grating 5 cm long, with refractive index modulation 2.7×10^{-4} and chirp rate 0.6 nm/cm. (a-c) One cladding mode, (d-f) two cladding modes; main reflection spectra (red line), first cladding mode (light blue line), second cladding mode (dark blue line).

3.5 Equalisation of the reflectivity spectrum

The model was then used to study the possibility of equalising the reflection spectrum according to that reported by [39]. A 10 cm long grating has been considered, 40 percent apodised (raised sine apodisation profile) with a chirp rate of 0.44 nm/cm that results in ~23 dB of reflectivity. Three cladding modes were taken into account, located ~ 2 nm below the fundamental Bragg wavelength and separated by 0.5 nm. The cladding mode to core mode coupling constant ratios are 0.15, 0.20, and 0.25, respectively. These cladding modes' features closely resemble real fibre ones. In Figure 3.4 the reflection

spectrum (a) from the "blue" grating end $R = |r|^2$, reflection spectrum (b) from the "red" grating end $R = |\rho|^2$ and transmission spectrum (c) from both ends $T = |t|^2$ are shown. The loss induced on the short wavelength side of the reflection spectrum (b) is ~ 2 dB.

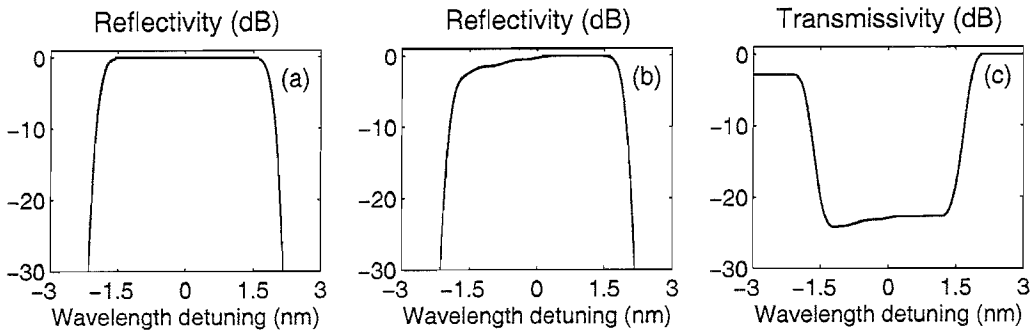

FIGURE 3.4: Reflection spectrum (a) from the "blue" grating end, (b) from the "red" grating end, (c) transmission spectrum from both ends.

The raised sine apodisation profile $v(z)$ used for all the calculations reported here is defined as

$$v(z) = \sin^2\left(\pi \frac{x}{L}\right) \text{ with } x = \begin{cases} \dfrac{zL}{2L_a} & \text{for } z < L_a \\ \dfrac{z - L + 2La}{2L_a} L & \text{for } z > L - L_a \\ 1 & \text{otherwise} \end{cases} \tag{3.16}$$

where $L_a = A_F L/2$, and A_F is the apodisation fraction. To perform the spectral equalisation the apodisation profile (3.16) has been multiplied by the function, written for the negative chirp case (i.e. entering from the "red" grating end), as

$$f(z) = \begin{cases} \gamma & \text{for } z \leq z_0 \\ \dfrac{(1-\gamma)(z - L + z_0)^2}{z_0^2} + \gamma & \text{for } z > z_0 \end{cases} \tag{3.17}$$

where z_0 is the location in the grating where the effect of cladding-mode loss disappears and γ is the relative strength of the grating in the "lossy" region $z < z_0$ [45]. To equalise the spectrum it is necessary to reduce the grating coupling constant at the "red" grating end. Since these grating sections are also responsible for the coupling with the cladding modes a loss reduction occurs at the same time. Figure 3.5(b) shows a magnified view of the reflection spectra obtained for different apodisation conditions, entering from the "red" end. The dashed line shows for comparison the unaffected spectrum entering from the "blue" end. The initial irregular and the final flattened spectra are shown in blue and red lines, respectively. The apodisation profile used to perform the equalisation is shown in Figure 3.5(a). The green and black lines show the spectra under sub- and

over-compensation, respectively. The corresponding apodisation profiles are also shown in Figure 3.5(a). The transmission spectra for all the cases are plotted in Figure 3.5(c). The grating profile has been lowered by up to 40 percent of the original value in order to perform the reflection spectrum equalisation, reducing the grating strength by ~ 8 dB, but maintaining the same dispersion characteristic.

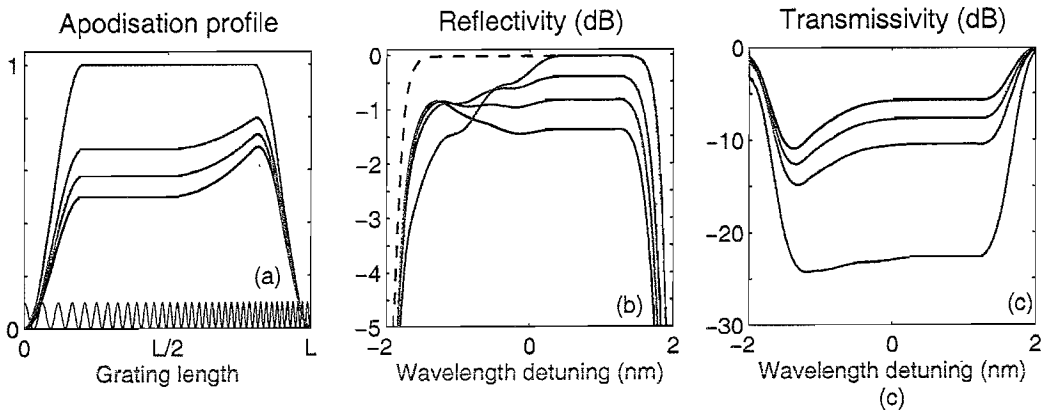

FIGURE 3.5: (a) Apodisation profiles; (b) reflection spectra obtained from the "red" grating end; (c) transmission spectra. The different colours refer to: the initial grating (blue), compensated grating (red), sub-compensated grating (green) and over-compensated grating (black); the dashed line in (c) represents the unaffected reflection spectrum when entering from the "blue" end.

Let's now consider the design of the apodisation profile, that results in the equalisation of the reflectivity spectrum, from the opposite perspective of increasing the grating coupling constant at the "blue" grating end, rather than reducing it at the "red" grating end. The blue line in Figure 3.6(a) represents the apodisation profile of the initial grating. The corresponding reflection and transmission spectra entering from the "red" grating end are plotted (in blue) in Figure 3.6(b) and (c), respectively. It is here assumed that $v(z) = 1$ corresponds to the maximum change in refractive index that can be induced in the fibre. In order to compensate the loss at the short-wavelength side of the reflection spectrum, the strength at the grating on the "blue" grating end is therefore enhanced. This is equivalent to say that the number of photons that go through the "lossy" region is increased, photons which due to coupling with the cladding modes are eventually lost. If the number of photons has been properly increased, the reflection spectrum is equalised (as shown by the red lines in Figure 3.6(a)-(c).

Given a certain grating strength, the number of photons available for the equalisation is represented by the transmissivity of the grating, while the photon deficit, that needs to be compensated by the available photons, is represented by the reflectivity loss. Clearly, the reflectivity loss depends on the ratio between the cladding/core mode coupling strength (i.e. $\kappa_{\text{cm}}/\kappa_{\text{core}}$). The blue line in Figure 3.7 represents the available photons (i.e. transmissivity) as a function of the grating strength. The stronger the grating, the smaller the number of photons available to compensate the short-wavelength loss. The three green lines correspond to the photon deficit for different values of cladding coupling strengths.

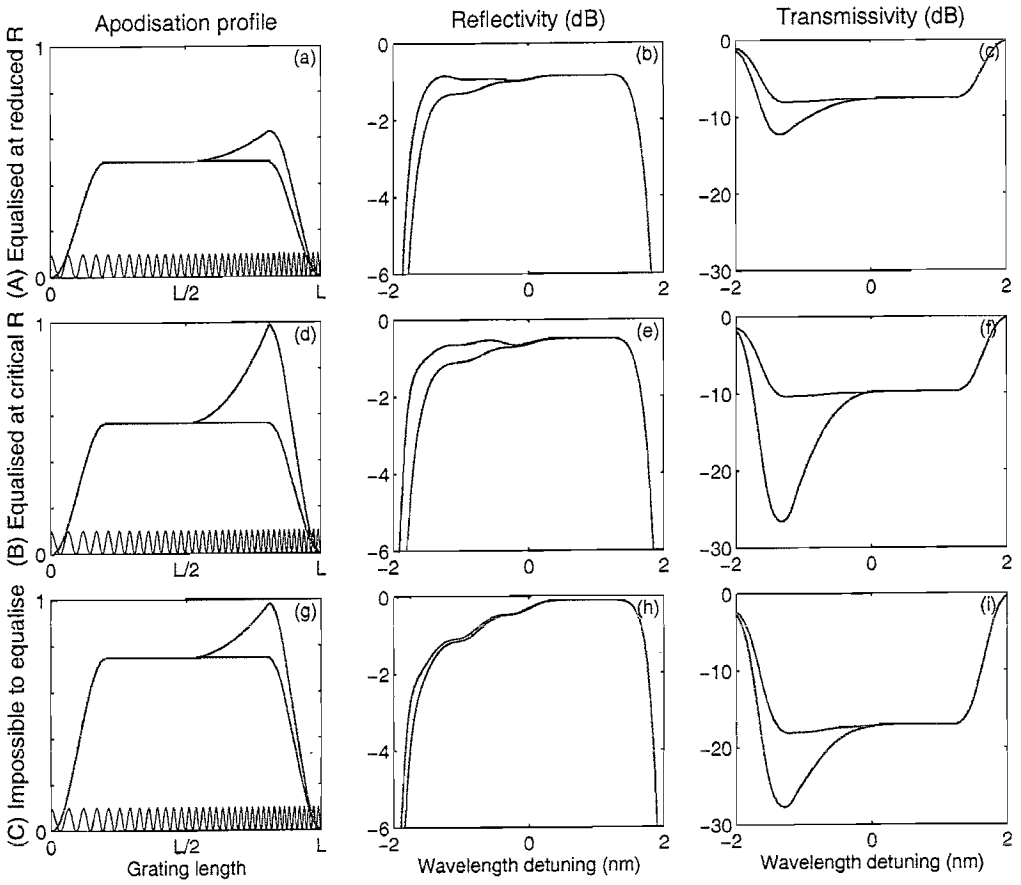

FIGURE 3.6: Apodisation profiles (first column), reflection spectra obtained from the "red" grating end (second column) and transmission spectra (third column) for a grating (A) equalised at reduced reflectivity (a-c), at (B) critical reflectivity (d-f) and (C) impossible to equalise (g-i). The different colours refer to: the initial grating (blue) and equalised grating (red).

The stronger the grating and the cladding coupling are, the larger the deficit (i.e loss) is. Three different scenarios can be encountered. First, when the number of available photons exceeds the photon deficit it is possible to equalise the reflection spectrum and this occurs within the white area in Figure 3.7. The case represented by the red triangle (A) corresponds to Figure 3.6(a)-(c) and equalisation is said to be obtained at the reduced reflectivity of 7.5 dB. Second, when the number of available photons equals the photon deficit the reflection spectrum can still be equalised. This case is represented by the red square (B) in Figure 3.7 and corresponds to Figure 3.6(d)-(f). The equalisation is obtained at the critical reflectivity of 9.5 dB. Third, when the photon deficit exceeds the number of available photons it is impossible to equalise the reflection spectrum and this occurs within the azure area in Figure 3.7. The example represented by the red circle (C) corresponds to Figure 3.6(g)-(i) and a reflectivity of 17 dB.

The graph in Figure 3.7 shows the fundamental limitation of using an apodisation profile to equalise the short-wavelength loss in chirped FBGs. In the case of relatively weak gratings the apodisation profile can be properly designed to provide enough photons to replace the ones lost through coupling to cladding modes, also when the coupling badly

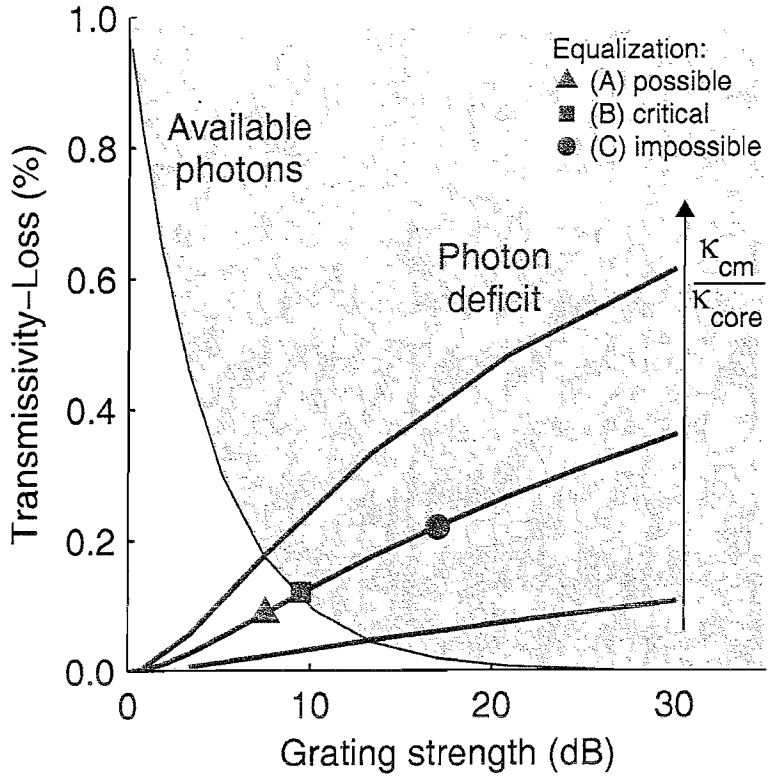

FIGURE 3.7: Graph representing the fundamental limitation of the loss equalisation process by means of apodisation profile.

affects the spectrum (i.e. when the cladding modes coupling strength is high). However in the case of strong gratings, both the number of photons lost into cladding modes increases and the number of photons available to compensate them decreases. This can easily lead to a situation in which it is impossible to equalise the reflection spectrum by means of redesigning the apodisation profile.

3.6 Conclusion

A full theoretical model that accounts for the effect of coupling modes on the performance of chirped FBGs have been presented here. The model reveals the dynamic interaction between successive cladding mode spectra and the main grating reflection spectrum under different launching conditions. The model is also used to study reflection spectrum equalisation by properly adjusting the apodisation profile. The fundamental limitation of this approach is also shown, it cannot be used to equalise strong gratings.

Part II

Microstructured optical fibres

Chapter 4

Holey fibres: Background

4.1 Introduction

4.1.1 History and background

Microstructured optical fibre (MOFs) are fibres typically made from a single material in which the guidance of light is obtained by structuring the fibre profile. The first examples of microstructured optical fibre dates back to 1973, and a fibre produced by Kaiser *et al.* [46, 47] is shown in Figure 4.1. The fibre consists of a small-diameter rod supported on a thin, polished plate in the centre of a larger-diameter protective tube, all made from fused quartz. The rod acts as the fibre core and is almost surrounded by air that acts as the fibre cladding. Thus this silica single material fibre guides light within the core by means of the refractive index difference between the silica core and the air cladding. The technology of the time allowed fabrication of doped-silica fibres, that is fibre structures consisting of a central glass core surrounded by a cylindrical glass cladding of lower refractive index (as current conventional fibre), but at the cost of very high loss values. The refractive index difference between the two glasses is obtained using different chemical compositions, but at the time the fabrication process of such a device did not allow impurities to be kept out of the glass. In particular, the concentration of OH impurity introduced during the fabrication process was significantly affecting the fibre transmission loss. Before 1968 the doped-silica fibre loss was of the order of 1000 dB/km, this was reduced to 20 dB/km at $0.8 - 0.85\,\mu$m in 1970 [48]. In 1972 Kaiser *et al.* [49] fabricated unclad round fibres from fused silica and measured a loss at $1.1\,\mu$m of 2.5 dB/km only in up to 32 m of unsupported length. The next step was structuring the pure silica fibre profile as in Figure 4.1 and, taking advantage of the purity of pure silica, allowing loss of the order of 3 dB/km at $1.1\,\mu$m to be achieved in 1974 [47]. In the same years single material MOFs were proposed as a low-loss alternative solution to doped-core fibres, the doping technologies have been significantly improved with the development of, amongst others, the outside vapour deposition process (OVD) in 1973,

modified chemical vapour deposition process (MCVD) in 1974 and vapour-phase axial deposition (VAD) in 1977 [50]. Thus the loss of single-mode doped-silica fibres was further reduced to 4 dB/km at 0.8–0.85 μm in 1973 [51] (fibre fabricated by OVD) and finally to 0.2 dB/km at 1.55 μm in 1979 [52] (single-mode fibre fabricated by MCVD). Once the transmission loss was lowered to an acceptable level, making doped-silica fibres was more attractive than making single-material structured fibres because the fabrication of the latter is more difficult and the fibre itself is less robust. Therefore the idea of MOF was set aside.

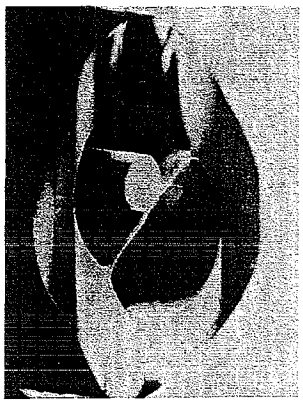

FIGURE 4.1: Single material fibre fabricated in 1974 by Kaiser and Astle [47].

The structuring of optical materials has been widely used since 1968 [53] to fabricate distributed feedback lasers, dielectric mirrors and Fabry-Perot filters. These devices rely on a 1D periodic or quasi-periodic structure, typically made of alternating layers of different dielectric materials. All these devices relies on the total reflection of optical wavelengths which fulfills the Bragg condition (see Part I).

In 1987 Eli Yablonovitch discovered an analogy between electrons and photons: in a periodic structure photons can in fact be described in terms of a band of structure just as electrons in a crystal [54]. The work of many researchers was then applied to convert the knowledge about semiconductors to optics, that is to study photonic crystal and photonic bandgap materials. Structuring optical materials with 3D periodic configurations can allow the formation of photonic bandgaps, the prohibition of wave propagation for specific band of wavelengths. When light is launched into the material, it cannot propagate if the light wavelength belongs to the bandgap due to Bragg diffraction within periodically arranged materials.

From 1995 the interest in microstructured optical fibres was renewed, with the proposal of a new structured fibre configuration: a single material fibre that contains a periodic arrangement of air holes that run along the fibre length [55], basically a 2D-extended periodic structure with out of plane light propagation. The first working example of MOF, shown in Figure 4.2, was fabricated at Southampton University by Knight *et al.* [56] in 1996. The central hole is missing, thus defining the fibre core. This fibre,

however, does not rely on the existence of a bandgap to guide the light, but on the reduced refractive index of the cladding, due to the presence of air holes, with respect to the central silica core. In this case, the way of structuring the single-material fibre resembles the fibre in Figure 4.1, produced more than 20 years before, in which light was guided in the silica core by the air cladding.

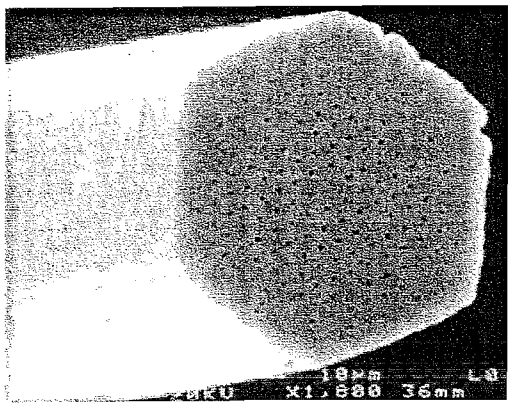

FIGURE 4.2: Endlessly single-mode single material fibre fabricated at Southampton University in 1996 by Birks *et al.* [55].

MOFs are made with materials (glass and air) with a refractive index contrast nearly two orders of magnitude higher than that used for conventional fibres and are characterised by a two dimensional microstructure. The presence of wavelength-scale holes in the transverse profile of a microstructured optical fiber can lead to novel optical properties (explained in Section 4.2) that cannot be achieved in more conventional forms of optical fibre and has widely motivated their study ever since 1995.

4.1.2 Guidance mechanisms

Light in microstructured optical fibres can be guided by two different guidance mechanisms: average-index and photonic bandgap effect. The average-index effect is characteristic of structures in which a solid core is surrounded by an arrangement of air holes that act as the fibre cladding, as in Figure 4.2. Light is basically guided by a modified form of total internal reflection. The effective refractive index of the cladding region is lower than that of the solid core due to the presence of the holes. Light can also be guided by randomly distributed air holes in the cladding [57].

Microstructured optical fibres can guide light by an alternative guidance mechanism if the air holes that define the cladding region are arranged on a periodic lattice. Periodic cladding structures can exhibit photonic bandgaps, and frequencies located within the bandgap cannot propagate within the cladding [55, 58]. By breaking the periodicity of the cladding (e.g. by adding an extra hole to form a low-index defect), it is possible to introduce a localised mode within this defect. Such a defect can act as the core, and

guide light within well-defined frequency windows. These photonic bandgap fibres can be designed to have transmission windows centred at near-infrared wavelengths [59].

Within this thesis, MOFs that guide light by means of the average index mechanism are considered.

4.1.3 Nomenclature

Historically, the first name used for MOF was photonic crystal fibre (PCF), used for both classes, because the periodic arrangement of the holes of the cladding region is an example of a photonic crystal [56]. Microstructured optical fibre (MOF) is a more general definition, since fibres with non periodic features have been produced, and should also be used to describe microstructured fibres with a doped core or any other variations if based on a microstructured fibre. In particular, air-silica microstructured fibre is sometimes used to refer to MOFs made of silica [60]. To distinguish the two guidance mechanisms, the index-guiding fibres are more generally called holey fibres (HFs) because their operation does not depend on having a periodic structure [61], while the others are quite obviously addressed as photonic bandgap fibre (PBGFs) [55]. Note that in the literature it is possible to find several of these terms addressing one or both kinds of MOF in a somewhat arbitrary way, but within this thesis, these definitions are used.

4.1.4 Fabrication

The vast majority of silica holey fibres produced to date have been fabricated using stacking techniques. Capillary tubes are stacked in a hexagonal configuration, and the central capillary can then be replaced with a solid silica rod, which ultimately forms the fibre core. This preform is then reduced in scale on a fibre drawing tower. This can either be done in a single step, or, if small-scale features are required in the final fibre, two scale reduction stages can be used. The parameters that characterise a HF profile are the hole-to-hole spacing (Λ), the hole diameter (d) and the number of rings of holes used to define the cladding region. In order to avoid the collapsing of the air-holes, the capillary end is sealed. The stacking procedure is a flexible one: holey fibres suitable for active devices can be made using a doped core rod, and multi-core fibres can be produced by introducing multiple rods into the stack. Although stacking is the principal technique that has been used to make holey fibre preforms thus far, other techniques have recently been demonstrated. Silica holey fibres have been made using sol-gel casting techniques [62], and the preform can also be extruded directly from bulk glass using glasses with low-softening temperatures [63]. Extrusion offers the prospect of fibre designs that could not be envisaged with stacking techniques (and vice versa). Both techniques allow the hole pattern, size and spacing to be altered independently and avoid the creation of interstitial holes. Although the arrangement of holes of HF can

be random, the holes are usually arranged in a hexagonal lattice (also named triangular lattice), both to have control of the optical properties of the final structure and for fabrication reasons. Honeycomb lattices are also used, mainly for photonic bandgap fibres [58].

4.2 Properties

In a conventional optical fiber, the light travels through the core by constantly reflecting from the cladding because the refractive index of the core is higher than that of the cladding. The light propagation is due to total reflection at the core/cladding interface, thus the optical fibre is said to guide light via total internal reflection. In a conventional step-index fiber with core radius ρ and core and cladding indices n_{co} and n_{cl}, the number of guided modes is determined by the normalised frequency V [30]:

$$V = \frac{2\pi\rho}{\lambda}\sqrt{n_{co}^2 - n_{cl}^2} \tag{4.1}$$

which must be less than 2.405 for the fiber to be single-mode. Thus conventional single-mode fibres, in which the core and cladding indices are only weakly wavelength dependent, are in fact multi-mode for light of sufficiently short wavelength λ.

Contrary to conventional fibres, in a HF the effective refractive index of the cladding is strongly dependent on the optical wavelength. This allows the fibre to be single-mode over a range of wavelengths not possible in conventional fibres. Qualitatively, as the wavelength decreases, the overlap between the mode and the holey-cladding region decreases, therefore the effective cladding index increases and the normalised frequency V is kept almost constant, as shown by the equation 4.1 which can be also applied to HFs [64]. This additional dispersion counteracts the explicit dependence of V on wavelength λ and so extends the single-mode range. If the fibre structure is designed to have $V < V_{\text{cut-off}}$, where $V_{\text{cut-off}}$ is the cut-off normalised frequency (equal to 2.405 for step-index fibres), the fibre is endlessly single-mode. The strong dependence of the cladding effective index on the wavelength also allows the HF optical properties to be tailored to values and combinations not possible in conventional fibres. The optical properties depend on the design of the arrangement of holes, on the scale of the structure too, and clearly on the material used to fabricate them. This allows more degrees of freedom in the fabrication of fibres with specific optical properties, with respect to conventional fibres.

The dispersion and polarisation properties of a HF can be particularly strongly influenced by the cladding configuration, particularly when the hole-to-hole spacing is small. Simply by scaling the dimensions of the features within the fibre profile, HFs can have mode areas ranging over three orders of magnitude [61]. Fibres providing tight mode confinement can be used as the basis for devices based on nonlinear effects [65], whereas

large mode area fibres allow high power operation [66, 67]. The large refractive index contrast also allows a new generation of high-precision measurements in optical frequency metrology [68]. In addition, these fibres can exhibit properties not readily attainable in conventional fibres, including the already mentioned broadband single-mode guidance [64], anomalous dispersion at wavelengths down to 550nm [69], novel fibre devices [70] and sensors [71] (based on evanescent field and a high percentage of field in the holes).

Also unlike conventional fibres, HF can be made of a single material, typically silica, although recently chalcogenide glasses [72] and polymers [73] have also been used. The core region can be doped either to help the guidance or to make use of the dopant properties. Both Yb^{3+} [74] and Ge [60] doped HFs have been reported, the former to realise an active device (laser), the latter to allow grating structures to be written in the core region.

Another characteristic not yet fully exploited, mainly for technology reasons, is the filling of the holes. For HF structures where the mode significantly overlaps with the holes-cladding region, filling the holes with a highly nonlinear material could enhance the effective nonlinearity of the fibre [65]. Active materials, such as polymers, have been infused into the relatively large air-holes of a silica doped-core HF, realising tunable grating filters and variable optical attenuator microstructured fibre devices [70].

4.2.1 Dispersion

A series of light pulses are used to transmit information in optical fibre systems. The fibre dispersion, when different from zero, induces a temporal broadening of the pulses which propagate along the fibre. This is due to the fact that the various frequency components of the signal propagating along the fibre have different propagation velocities within the physical medium (i.e. the fibre).

Physically, four mechanisms contribute to the total dispersion of an optical fibre:

1. multimode dispersion: present in multimode fibres only and due to the different group velocity of different modes
2. polarisation mode dispersion: present in birefringent fibres and due to the different group velocity of the two orthogonally polarised modes
3. material dispersion: caused by the frequency dependence of the refractive index of the material that the fibre is made of
4. waveguide dispersion: caused by the frequency dependent confinement of light in the waveguide structure, as explained at the beginning of Section 4.2.

In this thesis, only the dispersion of the HF fundamental mode has been calculated, thus the first mechanism has not been considered. Also, the dispersion of the fundamental mode of hexagonal lattice HFs is not affected by polarisation mode dispersion because the fundamental mode of the idealised structure is degenerate, as illustrated in detail in Section 4.2.5. Therefore the dispersion values present in the thesis are due to material and waveguide dispersions only. The material dispersion can be evaluated by using the Sellmeier equation [75] which defines the refractive index of the material as a function of the wavelength. Note that by using the Sellmeier equation, the material dispersion can be included in the calculation of the effective index of the mode of the fibre from the outset, and this has been done for all the calculations concerning HF structures.

Mathematically, the derivation of the fibre dispersion begins from the expansion of the mode propagation constant β in a Taylor series about the centre frequency ω_0 [75]:

$$\beta(\omega) = n_{eff}(\omega)\frac{\omega}{c} = \beta_0 + \beta_1(\omega - \omega_0) + \frac{1}{2}\beta_2(\omega - \omega_0)^2 + \cdots \tag{4.2}$$

where $n_{eff}(\omega)$ is the frequency dependent effective index, c is the velocity of light and

$$\beta_m = \left(\frac{d^m\beta}{d\omega^m}\right)_{\omega=\omega_0} \qquad \text{for } m = 0, 1, 2, \ldots. \tag{4.3}$$

The first three terms of the Taylor series can be related to three physical quantities. The phase velocity v_f of the pulse carrier wave at the centre frequency is expressed by:

$$v_f = \frac{\omega_0}{\beta_0} \tag{4.4}$$

whereas the pulse envelop moves at the group velocity v_g which is defined as

$$v_g = \left(\frac{d\omega}{d\beta}\right)_{\omega=\omega_0} = \beta_1^{-1} = c\left(n_{eff} + \omega\frac{dn_{eff}}{d\omega}\right)^{-1}. \tag{4.5}$$

Finally, the dispersion D is defined by

$$D = \frac{d\beta_1}{d\lambda} = -\frac{2\pi c}{\lambda^2}\beta_2 = -\frac{\lambda}{c}\frac{d^2 n_{eff}}{d\lambda^2} \tag{4.6}$$

where the last expression is the one that has been used in the thesis.

4.2.2 Nonlinear properties

Nonlinear effects in fibre can be used for a wide range of optical processing applications in telecommunications and beyond. Consequently, there is great interest in the development of fibres with high values of effective nonlinearity per unit length in order to reduce device lengths and the associated optical power requirements for fibre-based nonlinear optical devices.

There are three main classes of nonlinear effects observed in fibres, stimulated Brillouin scattering, stimulated Raman scattering, and optical Kerr effects [75]. The optical Kerr effect, which is the refractive index change that occurs due to high light intensities, leads to various secondary effects, such as self phase modulation, cross-phase modulation and four-wave mixing [75]. Examples include optical regeneration, wavelength conversion, optical demultiplexing, and Raman amplification.

Even though silica is not intrinsically a highly nonlinear material, its nonlinear properties can be utilised in silica optical fibres if high light intensities are guided within the core [75]. A commonly used measure of the nonlinearity of a fibre is the effective nonlinearity γ [75], given by

$$\gamma = \frac{2\pi}{\lambda}\frac{n_2}{A_{eff}} \tag{4.7}$$

where n_2 is the nonlinear coefficient of the material, A_{eff} is the effective mode area and λ the optical wavelength. For example standard SMF28 fibre has an A_{eff} of $\sim 90\,\mu\text{m}^2$ at 1550 nm, and since the n_2 of silica is $\sim 2.2 \times 10^{-20}$ m^2/W, γ is of the order of 1 W^{-1}km^{-1}. One way in which the nonlinearity of conventional silica fibres can be enhanced is to reduce the effective mode area by producing fibres with a smaller core diameter and higher index contrast. An higher index contrast corresponds to a larger numerical aperture, defined as $NA = \sqrt{n_{co}^2 - n_{cl}^2}$ where n_{co} are n_{cl} the refractive index of the fibre core and cladding, respectively. Okuno *et al.* [76] showed that by modifying the composition of a silica fibre and reducing the core diameter, values of γ as large as 20 W^{-1}km^{-1} can be achieved. In this example, the addition of Ge to the fibre core increases n_2 to $\sim 5.4 \times 10^{-20}$ m^2/W within the core and increases n_{co} to a value equal to ~ 1.03 of the refractive index of silica resulting in a larger NA of 0.37. Enhancing both NA and n_2 reduces the effective mode area to $\sim 11\,\mu\text{m}^2$. Using this enhanced NA and n_2, and assuming for simplicity a step-index fibre design, the largest γ that is possible is ~ 26 W^{-1}km^{-1} (corresponding to a core diameter of 2.4 μm and an effective mode area of $\sim 8\,\mu\text{m}^2$). To my knowledge, this result represents the largest NA and γ reported for a small-core conventional fibre. When even smaller core diameters are used, this NA becomes insufficient to confine the mode, and so the effective mode area increases, leading to smaller values of γ.

Silica holey fibres (HFs) can have a significantly larger NA than conventional silica fibre types because the cladding region can be mostly comprised of air. An example is shown in Figure 4.3. Making use of the large NA possible in these fibres, HFs can offer tighter mode confinement than conventional fibres. Hence HFs are attractive for nonlinear fibre devices [65]. Effective mode areas as small as $A_{eff} \sim 2.8\,\mu\text{m}^2$ have been achieved at 1550 nm corresponding to $\gamma \sim 60 \pm 10$ W^{-1}km^{-1} (Figure 6.1(b)) [77]. This is the best result in terms of nonlinearity reported to date in a silica fibre. In Section 6.3 it will be shown that pure silica HFs can be designed to have A_{eff} at least as small as $1.7\,\mu\text{m}^2$ at 1550 nm. Hence nonlinearities as high as $\gamma \sim 52$ W^{-1}km^{-1} are practical in these fibres, more than 50 times higher than in standard telecommunications fibre and 2 times higher

than the large *NA* conventional fibres described above.

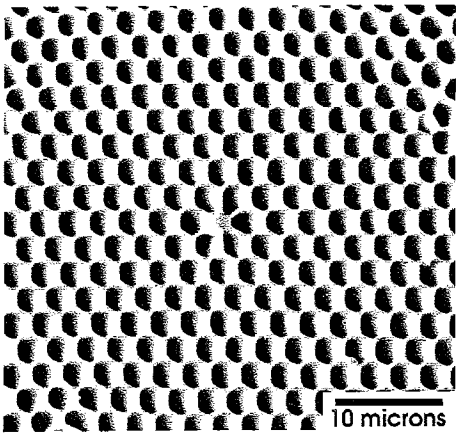

FIGURE 4.3: Typical small core silica holey fibre with 12 rings of regularly spaced air holes (only the central region is shown).

The mode propagating in a HF interacts both with glass and the air in the holes. However, air has a low nonlinearity ($n_2 \sim 3 \times 10^{-23}\,\mathrm{m^2W^{-1}}$ [78]), three orders of magnitude smaller than that of silica. The nonlinear effects in HFs are induced by the portion of the field located in the glass. In order to properly account for the overlap of the field with materials with different nonlinear characteristics, the usual definition of the effective nonlinear mode area A_{eff} given by Agrawal [75] as

$$A_{eff}^{\text{Agrawal}} = \frac{\left[\iint E_t(x,y)\cdot E_t^*(x,y)dxdy\right]^2}{\iint \left[E_t(x,y)\cdot E_t^*(x,y)\right]^2 dxdy} \tag{4.8}$$

has been modified here to give:

$$A_{eff} = \frac{n_2\left[\iint E_t(x,y)\cdot E_t^*(x,y)dxdy\right]^2}{\iint \tilde{n}_2(x,y)\left[E_t(x,y)\cdot E_t^*(x,y)\right]^2 dxdy} \tag{4.9}$$

where $\tilde{n}_2(x,y)$ is the nonlinear-index coefficient of the material at position (x,y), and n_2 is the nonlinear-index coefficient of the core region (to be used with $\gamma = \frac{2\pi}{\lambda}\frac{n_2}{A_{eff}}$). In a single-material HF with air holes, this expression removes the contribution to the predicted mode area, and hence to the effective nonlinearity, of any field located in the holes. Note that this is essential when the percentage of the field in the holes is significant, as for small-core HF structures.

Although these results indicate that HFs can dramatically enhance the achievable γ, the successful application of these fibres has been limited to date by loss, which is a consequence of the fact that these fibres are in an early stage of their development. This issue is discussed in the next section.

4.2.3 Confinement loss

The loss in HFs occurs for a variety of reasons: intrinsic material absorption, additional losses arising during the fabrication process (water contamination, absorption due to impurities, scattering, etc.) and confinement loss [79]. Fabrication-related losses can be reduced by careful optimisation of the fabrication process, as shown recently by NTT (the Nippon Telegraph & Telephone company) in Ref. [80], which reports a loss of 1 dB/km, and BlazePhotonics in Ref. [81], which reports a loss of 0.58 dB/km. The latter represents the lowest loss achieved so far in a HF. Confinement loss is an additional form of loss that occurs in single material HFs. In single-material HFs the core has the same refractive index as the material beyond the finite holey cladding region, and so every propagating mode is therefore intrinsically leaky. It has been proven that increasing the number of rings of air holes that surround the solid core, and thereby increasing the physical separation between the solid core and the external environment, reduces the confinement loss [79]. Thus confinement loss is determined by the geometry of the structure, and in Section 6.2 it is shown that it can contribute significantly to the loss for these fibres, unless care is taken with the fibre design. The propagation constant β of leaky modes is complex and the imaginary part of the propagation constant can be used to estimate the attenuation of the mode. The power loss at a position z along the fibre axis is given by $P(z) = P(0)e^{-2Im\{\beta\}z}$ where $P(0)$ is the initial modal power in the core [30].

4.2.4 Polarisation properties

In [82] one of the first full-vector calculations of the fundamental mode of HFs is presented. The fundamental mode is regarded as a polarisation-doublet, formed by two orthogonal states of almost-well-defined linear polarisation. The first higher order mode also appears as a multiplet, actually formed by four modes that are almost degenerate and that resemble the TE_01, TM_01 and HE_{21} (2-degenerate) modes of a conventional step-index fibre. Calculations of the HF spectrum show a tendency of the HF modes to be approximately arranged according to the multiplets of a step-index fibre. However, the paper also states that for the fundamental mode polarisation doublet, the two directions are not equivalent for the triangular distribution of holes characterising HF (or hexagonal lattice). As a result of this asymmetry, there is a breaking of the degeneracy of the fundamental polarisation doublet. Hence this paper predicts that idealised HFs with hexagonal hole arrangements exhibit form birefringence.

This form birefringence has been proved to be false in [83], according to an analysis of the fibre modes based on the group representation theory McIsaac [84] (this analysis is illustrated in detail in the following section). In the same paper [83], the multipole method has been applied to perform calculation of the HF modes and confirms the

absence of form birefringence. Recall that, as shown in Section 4.3 the multipole method also eliminates the false birefringence introduced by other methods which are based on a cartesian grid, as is the one used in [82]. The following section explains the proper theoretical symmetry classification of the hexagonal-lattice HF modes.

4.2.5 Symmetry and degeneracy

The group representation theory has been applied to study the symmetry-induced modal characteristics of uniform waveguides by McIsaac [84] in 1975. The hexagonal lattice HF has 6-fold rotational symmetry and at least one reflection plane, thus it must have 6-reflection planes and therefore belongs to the C_{6v} group. For a waveguide with C_{nv} symmetry, there are $n+1$ (n odd) or $n+2$ (n even) distinct mode classes. The modes in each class are either 2-fold degenerate, or non-degenerate. Any non-degenerate mode must exhibit the full symmetry of the structure, and any degenerate pair of modes must together reflect that symmetry. For a given mode class, a minimum waveguide sector can be assigned, which is the smallest sector sufficient to determine the fields of all the modes of the mode class, by applying the appropriate boundary conditions at either edge of the sector. For a C_{6v} waveguide, there are eight mode classes: four classes are degenerate and four form two degenerate pairs. Figure 4.4 shows the minimum sectors for the eight mode classes. The boundary lines of the minimum waveguide sector lie along one of the planes of reflection and on the sector boundaries either the tangential electric field (solid line) or the tangential magnetic field (dashed line) is zero. This proves that the idealised 6-fold symmetric fibre profiles are not birefringent [83]. Note that the modes of any waveguide with rotational symmetry of order $n > 2$ either exhibit the full waveguide symmetry and are non-degenerate or occur in degenerate pairs that support this symmetry only in combination. Thus, such symmetric waveguides are not birefringent, and only the intentional breaking of the symmetry does lead to birefringence [85, 86].

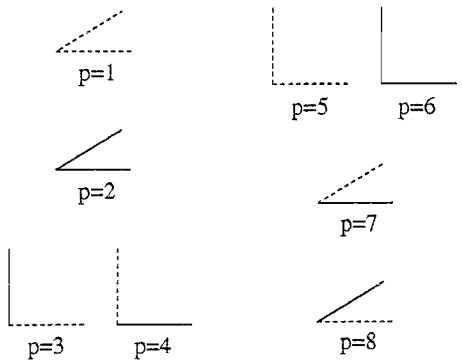

FIGURE 4.4: Minimum waveguide sectors for waveguides with symmetry C_{6v}. The non-degenerate mode classes, defined on a $\pi/6$ sector, are $p = 1, 2, 7$ and 8, whereas the 2-fold degenerate classes, defined on a $\pi/2$ sector, are $p = 3, 4$ and $p = 5, 6$. Solid and dashed lines represent zero tangential electric and magnetic field, respectively.

4.3 Modelling of MOFs

Several techniques have been adapted or developed to model the optical properties of MOFs. Although the high refractive index contrast between the glass and air requires full-vector methods, a qualitative description of the operation can be given by a scalar method based on analysis of the effective index of the cladding (effective index method). However, the high index contrast between air and glass and the presence of sub-wavelength details in the structure require a more complex method to be used to accurately predict the MOF optical properties. In the following, a wide range of techniques will be reviewed highlighting their applicability to model the fibre properties and their intrinsic limitations. Typically, many techniques complement one another and can be used in combination to have a complete picture of the MOF optical properties.

4.3.1 Effective index method

The effective index method has been first proposed and applied to the first working example of HF by Birks *et al.* [64]. The index-guidance of the HF is based on a modified total internal reflection. Thus, the HF can be equivalent to a conventional fibre with the refractive index of the core equal to that of the solid core region n_{co}, while the refractive index of the cladding must be properly defined according to the hole pattern. In order to do that, the fundamental mode of the infinite photonic crystal cladding when the core is absent, also named fundamental space-filling mode (FSM), is considered. Its propagation constant β_{FSM} is the maximum β allowed in the cladding. Consequently the effective index of the holey-cladding can be defined as $n_{eff} = \beta_{\text{FSM}}/k$, where $k = 2\pi/\lambda$. Similarly to conventional fibres, the propagation constant β of any propagating mode of the HF is therefore ascertained to be $kn_{co} > \beta > \beta_{\text{FSM}}$. The propagation constant of the FSM is determined by solving the scalar-wave equation in a cell region centred on one of the holes of the photonic crystal lattice. For a hexagonal lattice HF, the cell is hexagonal and has a diameter equal to Λ. Note that for the sake of simplicity, the hexagonal cell is then approximated to a circular one, a reasonable approximation if the holes are not too large [64]. This limits the accuracy of the results predicted by this approach in case of large holes. Note though that for structures with a significantly large air-filling fraction, the HF fibre can be considered equivalent to an air suspended rod [69].

Once the effective refractive index of the cladding n_{eff} is determined as a function of the optical wavelength, the study of the HF proceeds similarly to that of a conventional fibre. Note that, as mentioned above, the effective refractive index of the cladding has a strong dependance on the optical wavelength. The V-parameter, expressed by equation

(4.1) for conventional fibres, is more appropriately defined by Birks *et al.* [64] as

$$V_{eff} = \frac{2\pi}{\lambda}\Lambda\sqrt{n_{co}^2 - n_{eff}^2} \tag{4.10}$$

where the core radius is taken to be equal to Λ. After the Birks *et al.* [64] paper, there were several discussions about the proper definition of the HF core radius. For example for the structure analysed in [87], the core radius is approximately equal to 0.62Λ to 0.63Λ, in [88] it is taken to be 0.64Λ, and in [89] it is claimed to be 0.625Λ. As a matter of fact, the coefficient that multiplies Λ should be fixed according to the specific case. A comparison with predictions from other models can eventually help in the definition of this coefficient, reducing however the usefulness of this approach. The V-parameter is used to predict whether a HF structure is single-mode or not. Approximated dispersion and bending analysis has also been performed by means of the effective index method [90]. However, all the properties that strongly depend on the exact HF design, such as dispersion, birefringence or other polarisation properties, cannot be accurately predicted.

4.3.2 Plane wave technique

To analyse the modal properties of photonic bandgap guiding fibres it is necessary to calculate the photonic bandgaps of the full periodic structure and the modes allowed within the photonic bandgap by the defect(s). The plane wave method is the first method proposed to find a photonic bandgap in a photonic crystal, with an approach analogous to the finding of electronic bandgaps in semiconductor crystals [91]. For a full periodic structure, according to Bloch's theorem, the solution to the full-vector wave equation of the magnetic field can be written as a plane wave modulated by a periodic function with the same periodicity as the structure (Bloch function). The magnetic field is therefore expanded in a sum of plane waves such as

$$H_{\mathbf{k}} = \sum_G h_{\mathbf{k}-G} \exp(iG \cdot r) \tag{4.11}$$

where $\mathbf{k}$ represents the wave propagation vector of the mode and G is a lattice vector in the reciprocal space, describing the periodic structure. The position dependent dielectric constant $\varepsilon(r)$ is also expressed as a Fourier series expansion:

$$\frac{1}{\varepsilon(r)} = \sum_G V_G \exp(iG \cdot r) \tag{4.12}$$

where

$$V_G = \frac{1}{A_u}\int \frac{1}{\varepsilon(r)} \exp(-iG \cdot r)dr \tag{4.13}$$

and A_u is the area of the smallest region used to represent the periodic structure (unit cell). With these assumptions, the Maxwell's equations result in an eigenvalue equation where for a fixed wave vector $\mathbf{k}$ the frequencies of the allowed modes are found as eigenvalues [92]. In order to account for the presence of a defect in the otherwise periodic structure, a supercell with a periodically repeated defect must be considered instead of the unit cell. This approximation works if the supercell is large enough to uncouple the defects [93]. However, to achieve the required accuracy, the number of plane waves that must be retained in the expansion is of the order of 10 thousand or more. The inefficiency is mainly due to not taking advantage of the localisation of guided modes (contrary to the orthogonal functions techniques). This results in very large matrices and difficulties in the selection of the physically relevant eigenvalues. For example the study of a HF with elliptical holes performed in [94] requires 2^{16} basis functions and results in an accuracy of $\approx \pm 0.0003$ in the effective index. Another inefficiency of the approach is that the eigenvalues produce the frequency of the mode for a specified propagation constant. If the medium is dispersive the value of β needs to be modified for each frequency. Though simple to implement and use, this method has the draw back that the time taken for the calculation scales as the cube of the number of plane waves used and so rapidly becomes impractical as the complexity of the problem increases. Moreover, the plane wave expansion is based on a cartesian coordinate system, and if too few basis are retained, false-birefringence can be introduced in structures that have more than 2-fold symmetry and thus are not birefringent (see Section 4.2.5). Finally, the supercell imposes a periodicity to the structure of holes, therefore the modes found by this approach are bound and the confinement loss cannot be predicted (see Section 4.2.3). Despite these deficiencies, this technique has been widely used and applied to both kinds of MOF. It can also be used to model arbitrary HF profiles.

4.3.3 Beam propagation method (BPM)

The beam propagation method (BPM) uses a simple numerical algorithm to simulate the propagation of a coherent beam of light along a fibre [95]. An initial field profile is propagated using classical diffraction formulas for a short distance along the propagation axis and is then sent through a phase/amplitude mask. The properties of the mask are defined according to the fibre profile on the transverse axis. The process is repeated until one or more excited modes are stabilised. The medium between two masks is homogeneous, isotropic and has the average refractive index of the fibre. The modes are not solved explicitly and there is no guarantee that all the modes are found. This can be computationally inefficient, but any arbitrary fibre profile can be modelled by BPM. The BPM does not require a periodic arrangement of holes, and in the realistic case of a finite number of holes it can therefore predict the confinement loss. This results from the observation of the attenuation of the fields as the mode propagates. However, if the mode is slightly leaky, it must propagate for a long distance before the attenuation is

measurable. The BPM has been successfully applied to investigate the cladding modes of a Ge-doped core HF with a Bragg grating written in the fibre core [60] and to investigate the modes and the dispersive properties of a silica HF [96].

The imaginary-distance beam propagation method (ID-BPM) is a variation of the BPM. The conventional BPM is applied to the imaginary axis of the paraxial wave equation and gives the fundamental mode of a lossy optical waveguide and its complex effective index quite efficiently [97]. If the propagation distance is along an imaginary axis (i.e. z is substituted with iz), the phase oscillations turn into gain (i.e. $e^{i\beta z}$ is substituted with $e^{\beta z}$) and the fundamental mode, characterised by the largest propagation constant, is amplified the most. With optimised parameter sets, and especially with very large imaginary distances per propagation step, the fundamental mode can be determined within a few ID-BPM steps. The conventional BPM only obtains the fundamental mode if the structure is single-mode, and generally it takes longer to converge [98]. Higher order modes can be obtained by means of the ID-BPM using an orthogonalisation procedure to subtract contributions from lower order modes while performing the propagation [98].

4.3.4 Direct numerical analysis techniques

Several full-vector models for MOFs are based on an indirect, modal decomposition approach using sinusoidal functions (plane wave expansion method) [99], Hermite-Gaussian functions (localised function method) [61, 100], or cylindrical functions (multipole method) [101]. The first direct numerical analysis applied to HFs is the finite element method (FEM) by Brechet *et al.* [88], followed by the finite-difference time-domain method [102]. Direct approaches can treat arbitrarily shaped and arbitrarily arranged holes.

4.3.4.1 Finite element method (FEM)

According to the finite element method (FEM) [88], the classical Maxwell differential equations must be solved for a large set of properly chosen elementary subspaces, taking into account the condition of continuity of the fields. The fibre cross-section is divided in distinct homogeneous subspaces, resulting in a mesh of simple finite elements. To accurately model the fields, the subspaces closest to the fibre core are typically the smallest in dimension. Maxwell equations are then discretised for each element, resulting in a set of elementary matrices, that properly combined produce a global matrix system for the entire structure. Taking into account the condition of continuity of the fields at the boundary of each subspace, the effective index and the distribution of amplitudes and polarisations of the modes are numerically computed. Given the symmetries of the modes of a hexagonal lattice HF, it is possible to study only a quarter of the fibre profile, thus reducing the computational time required for the calculation. According to the mode, different boundaries conditions are imposed at the boundary of the quarter

region. The cladding effective index of the fundamental space-filling mode n_{FSM} can also be determined by applying the FEM to an elementary piece of the cladding that acts like a boundless propagation medium. For the calculation of n_{FSM}, contrary to the effective index method [64], this approach does not require any approximation. Single-mode behaviour, group velocity dispersion [88], modal birefringence [103] and confinement losses [104] have been analysed by means of the FEM. The technique is relatively inefficient computationally because the matrix size is proportional to the number of nodes and degrees of freedom. The choice of the subspace features is one of the critical parameters. Curvilinear subspaces can model curved boundaries with more accuracy and improve the computational efficiency [103]. The accuracy of the FEM depends also on the mesh discretisation. Recently a full-vectorial imaginary-distance beam propagation method based on a finite element scheme has been newly formulated and applied to the study of confinement loss in HFs [105]. It is possible to use nonuniform finite element meshes, and these meshes can be adaptively updated depending on the optical field distributions so that computational efficiency can be improved without degrading numerical accuracy. Moreover it produces the complex effective index of the modes, thus confinement loss can be readily predicted.

4.3.4.2 Finite-difference time-domain method (FDTD)

Expanding the fields on a discrete real-space lattice results in equations that can be rearranged into the form of a transfer matrix which relates the fields in one layer of the lattice to the fields in the next. This method scales not as the cube of the number of real space points (as the plane wave method), but rather as the square. The optimum scaling is a linear scaling with the system size and it is possible to achieve this by discretising Maxwell's equations not only spatially but also in the time domain. This technique is known as either the finite difference time domain method (FDTD) or the Order(N) method. Both time and memory requirements scale linearly with the system size [106]. The FDTD has been applied to the analysis of splice loss in HFs [107], tapered HFs [102] and dispersive properties of HFs [108]. It is possible to apply open boundary conditions in the FD methods and model leakage loss of guided modes, though complicated formulation and iterations are needed [108].

4.3.5 Orthogonal functions technique

Techniques like the plane wave method, first introduced to study perfectly periodical photonic crystals, deal with HFs (photonic crystal with defects) considering supercells and thus are very inefficient in the number of terms retained in the field expansions. Guided modes in HFs are localised in the fibre core. Thus modelling the field as a sum of functions localised near the core significantly reduces the number of functions that are needed to accurately represent the mode. The first scalar localised functions technique

was introduced by Mogilevtsev *et al.* [109] using orthogonal Hermite-Gaussian functions. The full vector version of the technique is presented in [100]. The Maxwell equations are reformulated as an eigenvalue problem for the propagation constant of the mode. The expansion coefficients contain overlap integrals between the localised functions and the distribution of refractive index of the fibre profile. The fibre profile can be represented as the sum of the perfectly periodic part (e.g. as a discrete Fourier series) and the part corresponding to the localised defect, allowing the integrals to be performed analytically. In [100] a second solution is proposed, that is to define a supercell, thus imposing a periodicity to the entire profile. The refractive index (ε and $\log\varepsilon$ in the paper) is therefore expanded in discrete Fourier series and the overlap integrals are performed analytically.

Another version of this approach is the hybrid approach presented in a scalar and full vector version by Monro *et al.* in [61] and [110], respectively. The hybrid approach describes the lattice of air holes with periodic functions (plane waves), while both the central index defect and the electric field are decomposed into localised Hermite-Gaussian functions [61]. This results in a very efficient method because different quantities are decomposed using functions chosen ad hoc, thus the number of terms retained in each expansion is relatively small. The coefficients of the decompositions are evaluated performing overlap integrals based on the decomposition functions. An advantage of using Hermite-Gaussians as localised functions is that their overlap integrals are analytically solvable, thus making the technique more efficient. For the fundamental mode of idealised periodic structures, only even order Hermite polynomials need to be used in the expansions. For HFs with asymmetric profiles or higher-order modes, both odd and even functions need to be included [111]. For more complex profiles, describing the localised core separately from air holes is no more advantageous, and the best combination of efficiency and accuracy is obtained by describing the entire refractive index distribution using a plane-wave expansion, using localised functions only for the modal fields [110]. The hybrid approach has been applied to HFs and used to model their dispersive properties and effective areas [61, 65], the effective area of and the role of interstitial holes in large air fraction HFs [110], HFs with random cladding distribution of the air holes [57], bend loss in large-mode HFs [67] and design requirements for effective field devices [71]. However, this approach cannot be accurate unless the refractive index is well represented. It can be applied to arbitrary fibre profile, but it cannot predict the confinement loss.

4.3.6 Multipole method

The multipole method is a multiple scattering technique time applied to the study of confinement loss in finite MOFs for the first time in [79]. The method allows confinement loss predictions because it does not use periodic boundary conditions and produces the

complex propagation constant. It can be applied to both holey and photonic bandgap fibres [112], with the only requirement of circular (at most elliptical) non-overlapping holes. All the previous techniques are based on a cartesian grid and typically predict a small degree of birefringence, that can be reduced (but not eliminated) by using a finer grid, even in the case of non-birefringent structures. The multipole method instead makes use of polar coordinate systems, thus the birefringence can be correctly calculated [83]. Moreover, the use of polar coordinate systems centred in each holes allows the method to be highly efficient since few terms are retained in the field expansions. Dispersive properties of HFs [113], polymer MOFs [73], modal cutoff in MOFs [114] and silica MOF with inclusions of a higher refractive index than silica [115] have also been studied by means of the multipole method. More details about the multipole method and its implementation will be given in Chapter 5. Here a general review of scattering techniques is presented.

Surprising or not, one of the earliest presentations of the basic features of multiple-scattering theory was given in the Avatamsaka Sutra (The Flower Ornament Scripture), an Indian Buddhist doctrine previous to the seventh century A.D., with the allegory of the Indra's Net. In the text the Indra's Net is described as: "Far away in the heavenly abode of the great god Indra, there is a wonderful net which has been hung by some cunning artificer in such a manner that it stretches out infinitely in all directions. In accordance with the extravagant tastes of the deities, the artificer has hung a single glittering jewel in each eye of the net, and since the net itself is infinite in dimension, the jewels are infinite in number. There hang the jewels, glittering like stars of the first magnitude, a wonderful sight to behold. If we now arbitrarily select one of the jewels for inspection and look closely at it, we will discover that in its polished surface there are reflected all the other jewels in the net, infinite in number. Not only that, but each of the jewels reflected in this one jewel is also reflecting all other jewels, so that there is an infinite reflecting process occurring" [116].

From a more scientific point of view, the question is how the infinite (and multiple) reflections that take place at each scatterer can be related in order to find a solution of the problem. The multiple scattering method has its origin in the works of Lord Rayleigh [117]. In this paper he developed a method for the solution of electrostatic problems involving lattices of spheres or arrays of cylinders. From that, methods in which field quantities are expanded in multipole expansions are called Rayleigh methods. The ingenious idea is to apply a field identity that relates the regular field in the vicinity of any scatterer to fields radiated by scatterers and external sources (also called Rayleigh identity). Originally applied to electrostatic problems for periodic systems, the technique has been adapted to dynamic problems involving both finite and periodic systems.

The multipole method has been applied to finite systems with applications in fiber optics since 1973 [118]. Both Wijngaard [118] and, more recently, Lo *et al.* [119] have considered the propagation of light along several parallel dielectric cylinders embedded in

a background uniform material. The applications involved were couplers and multicore optical fibres, thus at least one of the cylinders must have a refractive index larger than that of the background material, so that the models accounted for bound modes only. The findings of these and other publications [120, 121] allow the formulation by White *et al.* [101] of the multipole method which accounts for the propagation of leaky modes.

4.3.7 Fourier decomposition algorithm

Recently, a new technique that can model leaky (and bound) modes of arbitrary profile MOFs has been developed. The scalar algorithm is presented in [122] and the full vector in [123]. The Maxwell equation is reduced to an eigenvalue equation for the transverse magnetic field, so that the mode effective index appears in the eigenvalue. The algorithm is based on a polar-coordinate Fourier decomposition method with adjustable boundary conditions (ABC-FDM), capable of accurately determining the outward radiating fields. The MOF structure is enclosed in a circular computational domain. Outside the computational domain fields are expanded using modified Bessel functions of the second kind, that results in evanescent fields for bound modes and outward radiating fields for leaky modes. This expansion depends on the effective index only. Inside the domain fields are expanded using a set of complete basis functions, chosen to be a modified Fourier series for computational efficiency reasons. The Fourier series is modified by two adjustable parameters that allow any boundary condition to be satisfied. After setting an initial guess of the value of the effective index, the external field is determined and provides the boundary conditions for the internal field. A mode solver can find the internal field that satisfies these boundary conditions and generates an improved estimate of the effective index. The process is iterated using the new effective index value until required accuracy of the solution is reached. The Maxwell eigenvalue equation contains several inner products. Inner products that depend on basis functions only can be readily solved (and pre-tabulated) since they contain simple trigonometric functions. Inner products that depend on the structure can be done analytically if the holes are in the shape of annular sectors, otherwise they can be done numerically. However, the number of terms retained in the field expansions is small, thus the solution of the method is very efficient even in the case of numerically solved integrals. This algorithm has been applied to predict the confinement loss of HF structures with holes in the shape of an annular sector [122], circular and elliptical holes [123]. The use of a polar coordinate system allows the birefringence to be properly calculated, as already shown for elliptical holes HFs [123].

4.4 Conclusion

Holey fibres can have a significantly larger numerical aperture than conventional fibre types because the cladding region can be mostly comprised of air. When this is combined with a wavelength-scale core, HFs can provide tight mode confinement (i.e. small values of the effective mode area, A_{eff}). In such fibres, high light intensities are guided within the core. Thus even though silica is not intrinsically a highly nonlinear material [75], silica holey fibres can offer high effective fibre nonlinearities γ (see also Section 4.2.2). However, the successful application of these small-core HFs has been limited to date by loss, partly due to fabrication related losses, partly to confinement losses (see also Section 4.2.3) that can significantly affect the propagation of light when the scale structures is reduced. In the following chapters a study of the properties and limitations of these fibres is presented. The study is performed by means of the multipole method and Chapter 5 highlights the basic principles of the method and the way it has been implemented and used. Chapter 6 contains the study of confinement loss, effective area and dispersive properties of small-core HFs, whereas Chapter 7 presents the study of their modal properties, in particular of their polarisation properties. Finally Chapter 8 deals with the application of the multipole method to HF cases exempted from the small-core regime, highlighting the versatility of this method.

Chapter 5

Multipole method

5.1 Method outline

The multipole method is a multiple scattering technique, such that every inclusion part of the system is effectively regarded as a scatterer of light. As already mentioned in Section 4.3.6, this method was applied for the first time to the study of confinement loss in finite microstructured optical fibres in [79]. It has previously been successfully applied to two classes of microstructured optical fibres, both index-guiding HFs [79] and photonic bandgap fibres [112], to study their confinement loss, dispersive properties and modal cut-offs. The multipole method for microstructured optical fibres has been implemented as a full-vector modal approach, so that it can accurately represent the large refractive-index contrast present in MOFs. Here the physical and mathematical insight of the approach is outlined, according to the formulation given in White *et al.* [101] and Kuhlmey *et al.* [113].

The method can be applied to any microstructured optical fibre with an arbitrary arrangement of non-overlapping and circular inclusions or cylinders, as represented in Figure 5.1(a). These restrictions are imposed by the use of the Graf's addition theorem in the implementation of the model, as further discussed in section 5.4. The cylinders (indexed by l) are finite in number (N_c) and can have diameter d_l and refractive-index n_l. The inclusions are embedded in a uniform material of arbitrary refractive index n_e. The arrangement of cylinders is enclosed within a circular jacket of arbitrary refractive-index n_J. An arbitrary refractive index means that also complex values can be set for any part of the MOF structure, allowing for material gain or absorption to be considered. The jacket that surrounds the arrangement of cylinders has been introduced for a number of reasons. For the method to be mathematically rigourous, the fields should be zero at infinity in order to ensure the square integrability of the fields on the transverse plane, and this is enforced by the jacket. In addition, using a complex refractive index for the jacket allows the confinement loss to be estimated because the jacket absorbs the por-

tion of the mode that leaks. Hence this method produces complex values of the modal propagation constants β. Note that the choice of jacket radius r_J and its imaginary refractive index $\Im\{n_J\}$ should guarantee that the result of the calculation is insensitive to them. Thus the jacket needs to be placed reasonably far from the microstructured geometry and the its imaginary part needs to be small.

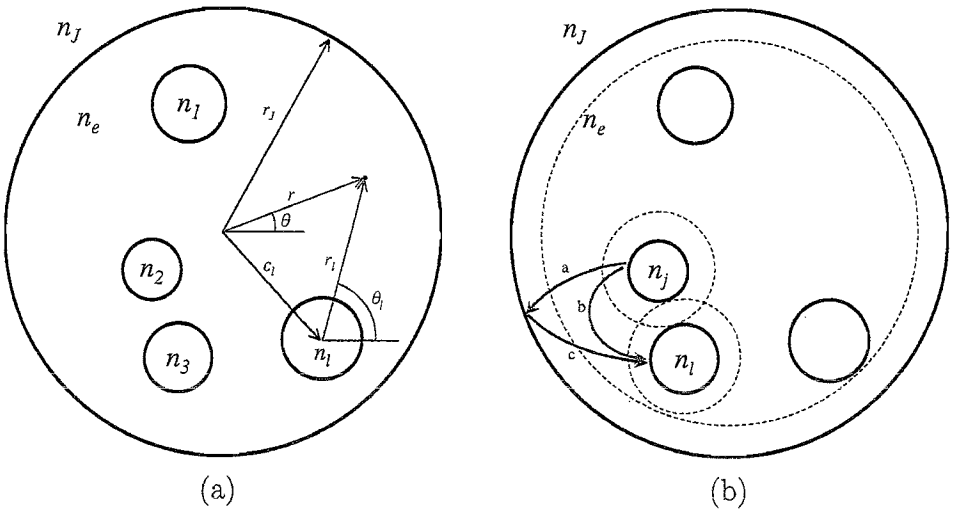

FIGURE 5.1: Schematic of the MOF geometry: (a) polar coordinate systems (in blue) and (b) field contributions (red arrows) and annular regions of validity for the local field expansions (dashed red lines) considered by the multipole method.

A physical picture of the multipole method is now given, followed by a brief summary of the formulation (explained in detail in the next paragraphs). At the boundary of each inclusion two different fields can be distinguished, the first transmitted through the boundary from beyond it, the second reflected from the boundary itself and coming from all the other inclusions. Therefore, even though no actual sources or sinks of fields are present, the boundary of each inclusion in the microstructured optical fibre is effectively a source of radiating fields. The problem is to find a relation between all these fields that effectively results from multiple reflections at the boundaries of each inclusion (scatterer). The essential idea of the multipole method, is to define a *field identity* that relates the field incident on each inclusion to the fields scattered from all the other inclusions; this identity is named *Rayleigh Identity* after Lord Rayleigh [117].

In summary, this method uses two different kinds of field expansions to represent the electromagnetic field. The first kind of field expansion (*local* expansion) is valid just outside each inclusion and expresses the field components that are incident on the inclusions and scattered away by the inclusions. The second kind of field expansion is valid throughout the different parts of the structure (i.e. inside the inclusions, outside the jacket and throughout the host uniform material). The one that is valid throughout the host uniform material (*global* expansion) is equal to the sum of all the field components scattered away by all the inclusions. At the boundary of each inclusion, the electromagnetic field must satisfy boundary conditions given by the Maxwell's equations. A relation

between the coefficients of expansions defined on the opposite side of a boundary can therefore be found. A second relation between the coefficients is found by applying the *Rayleigh Identity*. This finally results in a homogeneous system of algebraic equations in one of the coefficients only. The system can be expressed in the form of a matrix that depends on the propagation constant β of the mode propagating in the MOF. The problem of finding modes propagating in the structure is therefore reduced to finding the β that corresponds to a solution of the system.

The detailed mathematical formulation of the method is now presented. The coordinate systems used to implement it are shown in blue in Figure 5.1(a). $\mathbf{r} = (r, \theta)$ is the polar coordinate system of the jacket (global), while the polar coordinate system of each cylinder (local) is $\mathbf{r}_l = (r_l, \theta_l)$. The centre of each cylinder in the jacket coordinate system is $\mathbf{c}_l$. Each mode propagating in the MOF is defined by the electric and magnetic fields

$$\mathscr{E}(r, \theta, z, t) = \mathbf{E}(r, \theta) e^{j(\beta z - \omega t)} \tag{5.1a}$$

$$\mathscr{H}(r, \theta, z, t) = \mathbf{H}(r, \theta) e^{j(\beta z - \omega t)} \tag{5.1b}$$

where ω is the free-space angular frequency, β the complex mode propagation constant and the vectorial field are defined by $\mathbf{E} = (E_z, E_r, E_\theta)$, $\mathbf{H} = (H_z, H_r, H_\theta)$. The longitudinal components (E_z and H_z) of the electromagnetic field alone can be considered since the transverse components (E_r, E_θ and H_r, H_θ) can be calculated from the longitudinal via Maxwell equations [30], and these formulas are given in equations (5.32). The longitudinal field of the mode propagating in the MOF satisfies the Helmholtz equation

$$(\nabla^2 + (k_\perp)^2) V = 0 \tag{5.2}$$

where $V = E_z$ or $V = H_z$ and $k_\perp = \sqrt{k_0^2 n^2 - \beta^2}$ is the transverse wavevector component in the uniform material of refractive index n ($k_0 = 2\pi/\lambda$, with free-space wavelength λ). Note that the equation is valid in a homogeneous region free of sources thus, according to the field location, n equals the refractive index of the inclusions n_i, the uniform host material n_e or the jacket n_J.

To efficiently describe the fields of inclusions with cylindrical geometry the basis sets that yield cylindrical symmetry are chosen amongst all the possible basis sets that satisfies the Helmholtz equation. These basis sets are cylindrical harmonic functions centred on each inclusion and on the jacket. Considering now fields located in the uniform host material only, in the proximity of the l^{th} cylinder, the longitudinal electric field is expanded in terms of Bessel (J_m) and Hankel ($H_m^{(1)}$) functions using the local cylindrical coordinate centred at $\mathbf{c_l}$ (position of the cylinder), resulting in the following *local* expansion [101]

$$E_z(r_l, \theta_l) = \sum_{m=-\infty}^{\infty} \left[A_m^{El} J_m(k_\perp^e r_l) + B_m^{El} H_m^{(1)}(k_\perp^e r_l) \right] e^{im\theta_l} \tag{5.3}$$

where $k_\perp^e = \sqrt{k_0^2 n_e^2 - \beta^2}$ is the transverse wavevector component in the uniform host material. The superscript El of the coefficients A_m and B_m corresponds to the electric field of the l^{th} cylinder. The choice of functions used in the field expansion is justified by the characteristic of the field component that each function represents. The J_m terms are finite everywhere and represent the part of the field E_z incident on a cylinder that comes from all the other cylinders. The $H_m^{(1)}$ terms, which diverge towards the centre of the inclusion (i.e. the source) and die way with increasing distance from the source, represent the part of the field propagating away from the cylinder boundary. The local expansion (5.3) for each cylinder is a Fourier-Bessel expansion that satisfies the homogeneous Helmholtz equation (5.2) valid in a homogeneous region free of sources. Thus the local expansion is valid in an annular region around the cylinder that extends to the perimeter of the nearest cylinder, as shown by the dashed red line in Figure 5.1(b). Note that if the inclusions were overlapping each other, this annular region could not be defined because the region around the inclusion was not homogeneous. Thus, this also set the requirements of non-overlapping inclusions. A similar expansion can be written for the jacket as

$$E_z(r,\theta) = \sum_{m=-\infty}^{\infty} \left[A_m^{E0} J_m(k_\perp^e r) + B_m^{E0} H_m^{(1)}(k_\perp^e r) \right] e^{im\theta} \tag{5.4}$$

valid in an annular region inside the jacket, the region that extends from the jacket to the perimeter of the nearest inclusion, as shown by the dashed red line in Figure 5.1(b). The $H_m^{(1)}$ terms represent outgoing fields from all the inclusions, and the J_m terms waves that are reflected back towards the centre of the jacket from the jacket boundary.

To describe the field throughout the uniform host material, in which the inclusions are located, a *global* expansion needs to be introduced. According to Wijngaard [118], the field at any point within a material can be represented as superposition of outgoing waves from all source bodies within the material (i.e. all the inclusions and the jacket) [112]. This can be expressed in the form:

$$E_z(r,\theta) = \sum_{l=1}^{N_c} \sum_{m=-\infty}^{\infty} B_m^{El} H_m^{(1)}(k_\perp^e r_l) e^{im\theta_l} + \sum_{m=-\infty}^{\infty} A_m^{E0} J_m(k_\perp^e r) e^{im\theta}. \tag{5.5}$$

This global expansion is valid throughout the uniform host material (i.e. everywhere apart from the inclusions and the jacket, that act as sources) and demonstrations of its validity are given in [101, 119]. The expansion (5.5) contains outgoing waves ($H_m^{(1)}$ terms) from each cylinder (superscript l) and waves (J_m term) reflected back towards the centre of the jacket from the jacket boundary (superscript 0). The longitudinal component of the magnetic field is expanded using the same approach as for the electric field but with different expansion coefficients, labelled with the superscript H instead of E (i.e. A_m^{Hl}, B_m^{Hl}, A_m^{H0} and B_m^{H0} instead of A_m^{El}, B_m^{El}, etc.).

The local expansion for the field in the vicinity of each cylinder needs to be equated

with the global expansion for consistency, resulting in the following relation:

$$\sum_{m=-\infty}^{\infty} A_m^{El} J_m(k_\perp^e r_l) e^{im\theta_l} = \sum_{\substack{j=1 \\ j\neq l}}^{N_c} \sum_{m=-\infty}^{\infty} B_m^{Ej} H_m^{(1)}(k_\perp^e r_j) e^{im\theta_j} + \sum_{m=-\infty}^{\infty} A_m^{E0} J_m(k_\perp^e r) e^{im\theta} \tag{5.6}$$

where the term $\sum_m B_m^{El} H_m^{(1)}(k_\perp^e r_l) e^{im\theta_l}$, which is present in both expansions, cancels in (5.6). This relation is thus the mathematical expression of the *Rayleigh Identity* [117] described earlier. This expression ensures that the J_m (incident) parts of the field near cylinder l (A_m^{El}) result from the $H_m^{(1)}$ fields radiated (B_m^{Ej}) from all the other cylinders ($j \neq l$) and from the J_m fields back-reflected by the jacket (A_m^{E0}). Indeed, as shown by the red lines in Figure 5.1, the field radiated from the other cylinders can either arrive directly on the cylinder l (line b) or via back-reflection with the jacket (lines a and c). Note that the component related to line a, that is the outgoing $H_m^{(1)}$ fields radiated (B_m^{Ej}) radiated from all the cylinders j towards the jacket, does not explicitly appear in this equation (5.6). In the vicinity of the jacket, the field contributions approaching the jacket (from the inside) are given by the $H_m^{(1)}$ terms (B_m^{E0}) of the jacket local expansion (5.4), and must therefore be equal to the sum of the outgoing fields from all the cylinders, as defined by the following equation

$$\sum_{m=-\infty}^{\infty} B_m^{E0} H_m^{(1)}(k_\perp^e r) e^{im\theta} = \sum_{l=1}^{N_c} \sum_{m=-\infty}^{\infty} B_m^{El} H_m^{(1)}(k_\perp^e r_l) e^{im\theta_l}. \tag{5.7}$$

The cylindrical harmonic functions on the left hand side of equation (5.6) are expressed in the local coordinate system of the inclusion l, while functions on the right hand side are expressed in the local coordinate systems of the inclusions $j \neq l$ or in the global coordinate system of the jacket. To solve the problem it is necessary to translate the cylindrical harmonic functions on the right hand side into the coordinate system of the functions on the left hand side, that is the local coordinate systems of the inclusion l. In a similar way, the cylindrical harmonic functions on the left hand side of equation (5.7), that are expressed in the local coordinate systems of the inclusions l, must be transformed to the coordinate system of the functions on the left hand side that is the jacket coordinate systems. Three different changes of basis transformations are thus needed in total. These transforms between coordinate systems that are linearly translated one from the other can be performed by applying the Graf's addition theorem [124], as described below.

The general form of Graf's addition theorem states that a displaced cylinder harmonic function is a linear superposition of undisplaced cylinder harmonic functions. The geometrical meaning of this theorem is shown here with the support of Figure 5.2.

Consider a coordinate system placed in O, a second system Q displaced at a distance v from O, and a point P at a distance u from O and w from Q where the displaced/undis-

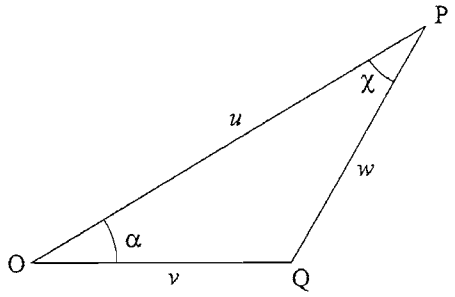

$$w = \sqrt{u^2 + v^2 - 2uv\cos\alpha}$$
$$u - v\cos\alpha = w\cos\chi$$
$$v\sin\alpha = w\sin\chi$$

FIGURE 5.2: Geometrical meaning of the Graf's addition theorem. O is the undisplaced point of view, Q is the displaced point of view and P is the observed point.

placed functions are evaluated. According to Graf's addition theorem, the displaced cylinder harmonic function $\mathscr{C}_m(w)$ is related to undisplaced cylinder harmonic functions $\mathscr{C}_{n+m}(u)$ via

$$\mathscr{C}_m(w)\begin{matrix}\cos\\ \sin\end{matrix}(m\chi) = \sum_{n=-\infty}^{\infty} \mathscr{C}_{n+m}(u)J_n(v)\begin{matrix}\cos\\ \sin\end{matrix}(n\alpha) \tag{5.8}$$

where $\mathscr{C}$ is a cylinder harmonic function and $|ve^{\pm i\alpha}| < |u|$ (note that when $\mathscr{C} = J$ and m is an integer or zero this restriction is unnecessary, thus equation (5.8) is always satisfied). The three forms of Graf's addition theorem that will be used in the following calculations, in order to evaluate in the most appropriate coordinate system the three field contributions indicated by the red lines in Figure 5.1, are reported here.

line a: The outgoing field from cylinder j is expressed in the jacket coordinate system (r, θ) via

$$H_m^{(1)}(k_\perp^e r_j)e^{im\theta_j} = \sum_{n=-\infty}^{\infty} H_n^{(1)}(k_\perp^e r_)J_{n-m}(k_\perp^e c_j)e^{in\theta - i(n-m)\arg\{\mathbf{c}_j\}} \tag{5.9}$$

and the conversion is valid for $u > v$, which is true in the vicinity of the jacket.

line b: The outgoing field from cylinder j is expressed in the coordinate system of cylinder l (r_l, θ_l) via

$$H_m^{(1)}(k_\perp^e r_j)e^{im\theta_j} = \sum_{n=-\infty}^{\infty} J_n(k_\perp^e r_l)H_{n-m}^{(1)}(k_\perp^e c_{lj})e^{in\theta_l - i(n-m)\arg\{\mathbf{c}_{lj}\}} \tag{5.10}$$

where $\mathbf{c}_{lj} = \mathbf{c}_l - \mathbf{c}_j$ and the conversion is valid for $u < v$, which is true in the vicinity of cylinder l.

line c: The field back-reflected by the jacket is expressed in the coordinate system of cylinder l via

$$J_m(k_\perp^e r)e^{im\theta} = \sum_{n=-\infty}^{\infty} (-1)^{n-m}J_n(k_\perp^e r_l)J_{n-m}(k_\perp^e c_l)e^{in\theta_l - i(n-m)\arg\{\mathbf{c}_l\}}. \tag{5.11}$$

Using the change of basis transformations just shown, equation (5.6), the *Rayleigh Identity*, can now be expressed entirely in the coordinate system of cylinder l. Let's start considering the second term on the right hand side of the equation, that is the field due to the jacket incident in the proximity of cylinder l (line c). By means of the change of basis transformation (5.11) this term is now represented by:

$$\mathbf{A}^{El0} = \mathcal{J}^{l0}\mathbf{A}^{E0} \tag{5.12}$$

where A_m^{El0} is the coefficient in the basis of cylinder l of the field radiated from the jacket and the vectorial notation $\mathbf{A}^{E0} = [A_m^{E0}] = [A_{-m}^{E0} \cdots A_{-1}^{E0} A_0^{E0} A_{+1}^{E0} \cdots A_m^{E0}]^T$ and $\mathbf{A}^{El0} = [A_m^{El0}]$ has been used (the superscript T indicates the matrix transpose operator). The quantity

$$\mathcal{J}^{l0} = [\mathcal{J}_{nm}^{l0}] = \left[(-1)^{n-m} J_{m-n}(k_\perp^e c_l) e^{i(m-n)\arg\{\mathbf{c}_l\}}\right] \tag{5.13}$$

expresses the change of basis. Next let's consider the first term on the right hand side of the equation (5.6), that is the field radiated from cylinder j and incident in the proximity of cylinder l (line b). By means of the change of basis transformation (5.10) this term is now expressed by

$$\mathbf{A}^{Elj} = \mathcal{H}^{lj}\mathbf{B}^{Ej} \tag{5.14}$$

where A_n^{Elj} is the coefficient in the basis of cylinder l for the field radiated from cylinder j and the vectorial notation $\mathbf{A}^{Elj} = [A_n^{Elj}]$ and $\mathbf{B}^{Ej} = [B_m^{Ej}]$ has been used. The change of basis is performed via $\mathcal{H}^{lj} = [\mathcal{H}_{nm}^{lj}]$ where

$$\mathcal{H}_{nm}^{lj} = H_{n-m}^{(1)}(k_\perp^e c_{lj}) e^{-i(n-m)\arg\{\mathbf{c}_{lj}\}} \tag{5.15}$$

and A_n^{Elj} is therefore defined as

$$A_n^{Elj} = \sum_m \mathcal{H}_{nm}^{lj} B_m^{Ej}. \tag{5.16}$$

Adding up the field contributions from all the cylinders, expressed by equation (5.14), and of the jacket (5.12) it is obtained

$$\mathbf{A}^{El} = \sum_{\substack{j=1 \\ j\neq l}}^{N_c} \mathcal{H}^{lj}\mathbf{B}^{Ej} + \mathcal{J}^{l0}\mathbf{A}^{E0} \tag{5.17}$$

that is valid in the annular region in the vicinity of cylinder l. Introducing the vector components for both the electric and magnetic field coefficients for cylinder l and the jacket, respectively, as $\tilde{\mathbf{A}}^l = \begin{bmatrix}\mathbf{A}^{El} \\ \mathbf{A}^{Hl}\end{bmatrix}$, $\tilde{\mathbf{B}}^l = \begin{bmatrix}\mathbf{B}^{El} \\ \mathbf{B}^{Hl}\end{bmatrix}$ and $\tilde{\mathbf{A}}^0 = \begin{bmatrix}\mathbf{A}^{E0} \\ \mathbf{A}^{K0}\end{bmatrix}$, $\tilde{\mathbf{B}}^0 = \begin{bmatrix}\mathbf{B}^{E0} \\ \mathbf{B}^{K0}\end{bmatrix}$, the equation for the electric field in the vicinity of cylinder l (5.17) and its magnetic field

equivalent can then be written in the general form

$$\tilde{\mathbf{A}}^l = \sum_{\substack{j=1 \\ j\neq l}}^{N_c} \tilde{\mathcal{H}}^{lj}\tilde{\mathbf{B}}^j + \tilde{\mathcal{J}}^{l0}\tilde{\mathbf{A}}^0 \tag{5.18}$$

where $\tilde{\mathcal{H}}^{lj} = \text{diag}(\mathcal{H}^{lj}, \mathcal{H}^{lj})$ and $\tilde{\mathcal{J}}^{l0} = \text{diag}(\mathcal{J}^{l0}, \mathcal{J}^{l0})$. Finally, combining equation (5.18) for all the cylinders results in

$$\mathcal{A} = \tilde{\mathcal{H}}\mathcal{B} + \tilde{\mathcal{J}}^{B0}\tilde{\mathbf{A}}^0 \tag{5.19}$$

where $\mathcal{A} = [\tilde{\mathbf{A}}^l]$, $\mathcal{B} = [\tilde{\mathbf{B}}^l]$ and $\tilde{\mathcal{H}} = [\tilde{\mathcal{H}}^{lj}]$, $\tilde{\mathcal{J}}^{B0} = [\tilde{\mathcal{J}}^{l0}]$.

As aforementioned, the outgoing field in the proximity of the jacket due to cylinder j (line a) can also be represented in the basis system of the jacket as:

$$\mathbf{B}^{E0l} = \mathcal{J}^{0l}\mathbf{B}^{El} \tag{5.20}$$

where B_m^{E0j} is the coefficient in the basis of the jacket for the outgoing field radiated from cylinder l and the vectorial notation $\mathbf{B}^{E0l} = [B_m^{E0l}]$ has been used. The term

$$\mathcal{J}^{0l} = [\mathcal{J}_{nm}^{0l}] = \left[J_{n-m}(k_\perp^e c_l)e^{-i(n-m)\arg\{c_l\}}\right] \tag{5.21}$$

expresses the change of basis transformation. Adding up the contribution of all the cylinders it is then obtained:

$$\mathbf{B}^{E0} = \sum_{l=1}^{N_c} \mathcal{J}^{0l}\mathbf{B}^{El} \tag{5.22}$$

that is equation (5.7) now expressed in the coordinate system of the jacket. Using the vector components for the electromagnetic field, equation (5.22) can be reduced to

$$\tilde{\mathbf{B}}^0 = \tilde{\mathcal{J}}^{0B}\mathcal{B} \tag{5.23}$$

where $\tilde{\mathcal{J}}^{0B} = [\tilde{\mathcal{J}}^{0l}]$. Note that $\tilde{\mathcal{H}}$, $\tilde{\mathcal{J}}^{B0}$ and $\tilde{\mathcal{J}}^{0B}$ are 2×2 block matrices composed of four sub-matrices equal in size and the elements of the off-diagonal sub-matrix are all equal to zero, so that:

$$\begin{bmatrix} \cdots\cdots & \\ \cdots\cdots & 0 \\ \cdots\cdots & \\ & \cdots\cdots \\ 0 & \cdots\cdots \\ & \cdots\cdots \end{bmatrix}$$

So far relations or field identities between each field component individually have been found, that is how the field in the vicinity of each cylinder is related to outgoing fields

from all the other cylinders and the jacket, and how the field in the vicinity of the jacket is related to outgoing fields from all the cylinders. It is now necessary to combine the contributions from each cylinder and from the jacket in order to build up a consistent description of the electric and magnetic fields from the local descriptions related to the different cylinders and the jacket. This is done by applying electromagnetic boundary conditions at the boundary of each inclusion and the jacket. The boundary conditions require the continuity of the tangential electric and magnetic field components at the boundary of each cylinder and of the jacket. Before this can be done, field expansions valid inside each cylinder and outside the jacket must be introduced. The following equation represents the *internal* expansion for the longitudinal electric field and is valid inside cylinder l ($r_l < d_l/2$)

$$E_z(r_l, \theta_l) = \sum_{m=-\infty}^{\infty} \mathbb{A}_m^{El} J_m(k_\perp^{(l)} r_l) e^{im\theta_l} \tag{5.24}$$

where $k_\perp^{(l)} = \sqrt{k_0^2 n_l^2 - \beta^2}$ and only bounded J_m terms are present since the field is finite everywhere. The *external* expansion, valid in the jacket ($r > r_J$), is

$$E_z(r, \theta) = \sum_{m=-\infty}^{\infty} \mathbb{B}_m^{E0} H_m^{(1)}(k_\perp^J r) e^{im\theta} \tag{5.25}$$

where $k_\perp^J = \sqrt{k_0^2 n_J^2 - \beta^2}$ and only $H_m^{(1)}$ terms, propagating away from the jacket boundary, are considered. Again, similar expansions can be written for the magnetic longitudinal field component (expansion coefficients $\mathbb{A}_m^{Hl}$ and $\mathbb{B}_m^{H0}$). The boundary conditions can be conveniently written in terms of reflection coefficients, producing a reflection matrix $\tilde{\mathbf{R}}^l$ for all the cylinders and $\tilde{\mathbf{R}}^0$ for the jacket [101]. Both the internal and external expansion coefficients $\mathbb{A}_m^{El}$ and $\mathbb{B}_m^{E0}$ can be expressed as a function of the local expansion coefficient for the cylinder (A_m^{El} and B_m^{El}) and the jacket (A_m^{E0} and B_m^{E0}) as:

$$\mathbb{A}_m^{El} = \frac{A_m^{El} J_m(k_\perp^e \frac{d_l}{2}) + B_m^{El} H_m^{(1)}(k_\perp^e \frac{d_l}{2})}{J_m(k_\perp^{(l)} \frac{d_l}{2})} \tag{5.26a}$$

$$\mathbb{B}_m^{E0} = \frac{A_m^{E0} J_m(k_\perp^e r_J) + B_m^{E0} H_m^{(1)}(k_\perp^e r_J)}{H_m^{(1)}(k_\perp^J r_J)} \tag{5.26b}$$

relations that straightforwardly derive from the continuity of the longitudinal components (i.e. from the equality of equations (5.24) and (5.3), and of equations (5.25) and (5.4), respectively). Thus the boundary condition equations relate the local expansion coefficients by means of the reflection coefficients as:

$$\tilde{\mathbf{B}}^l = \tilde{\mathbf{R}}^l \tilde{\mathbf{A}}^l \tag{5.27}$$

$$\tilde{\mathbf{A}}^0 = \tilde{\mathbf{R}}^0 \tilde{\mathbf{B}}^0. \tag{5.28}$$

Note that since the boundary conditions are referred to each cylinder separately $\tilde{\mathbf{R}}^l$ is a 2×2 block matrix, composed of four diagonal sub-matrices equal in size, and $\tilde{\mathbf{R}}^0$ is also a diagonal matrix. Combining equation (5.27) for all the cylinders results in

$$\mathcal{B} = \mathcal{R}\mathcal{A} \tag{5.29}$$

where $\mathcal{R} = \text{diag}[\tilde{\mathbf{R}}^l]$ is a diagonal matrix.

Equations (5.19), (5.23), (5.28) and (5.29) can now be combined to form a homogeneous system of equations that expresses the Rayleigh identity in terms of the coefficient $\mathcal{B}$ only

$$\mathcal{M}\mathcal{B} = 0 \qquad \text{where} \quad \mathcal{M} = \mathbf{I} - \mathcal{R}\left(\tilde{\mathcal{H}} + \tilde{\mathcal{J}}^{B0}\tilde{\mathbf{R}}^0\tilde{\mathcal{J}}^{0B}\right) \tag{5.30}$$

and $\mathbf{I}$ is the identity matrix. $\tilde{\mathcal{H}}$, $\tilde{\mathcal{J}}^{0B}$ and $\tilde{\mathcal{J}}^{B0}$ are translation matrices that express the change of basis transformations previously considered. Note that the $\tilde{\mathcal{H}}$ term in the matrix $\mathcal{M}$ describes direct cylinder to cylinder interactions, while the $\tilde{\mathcal{J}}^{B0}\tilde{\mathbf{R}}^0\tilde{\mathcal{J}}^{0B}$ term describes all indirect interactions between cylinders that take place via reflections ($\tilde{\mathbf{R}}^0$) at the jacket boundary. In the following, the matrix $\mathcal{M}$ is referred to as field identity matrix.

For a given material system, geometry and wavelength, the matrix $\mathcal{M}$ contains just one unknown, the mode propagation constants β of the propagating mode(s). If the MOF is multimode, as many values of β as the number of guided modes will satisfy the field identity (each value of β corresponding to a different guided mode). The propagation constant β is related to the effective index of the propagating mode n_{eff} via $\beta = k_0 n_{eff}$, thus in the following, depending on the context, either β or n_{eff} will be referred as the field identity unknown. By inspection, equation (5.30) indicates that non-trivial solutions occur when the determinant of the matrix $\mathcal{M}$ is zero (i.e. when $\mathcal{M}$ is singular). Since an absorbing jacket has been considered, this method yields complex values of β, and hence complex effective index values. The imaginary part of β can be used to estimate the attenuation of the leaky mode according to the power attenuation law $P(z) = P(0)e^{-2\Im\{\beta\}z}$, where $P(0)$ is the initial modal power [30]. The leakage due to the poor mode confinement can be calculated from the imaginary part of the effective index of the mode, via the following formula:

$$\mathcal{L}[\text{dB/m}] = \frac{2 \times 10^7}{\ln 10} \frac{2\pi}{\lambda[\mu\text{m}]} \Im\{n_{eff}\} \tag{5.31}$$

where $\mathcal{L}$ denotes the confinement loss.

After finding a value of β that results in $\mathcal{M}$ being singular, the null space or singular vector $\mathcal{B}$ corresponding to this solution is evaluated by performing a singular value decomposition. If the solution corresponds to a degenerate mode, according to the symmetry of the MOF structure as discussed in Section 4.2.5, more than one singular vector (two for 6-fold symmetry structures) can correspond to the same value of β. Note

that not all solutions to the singular value problem correspond to physical solutions for the fibre modes: see Section 5.2 for a more detailed discussion. The singular vector(s) $\boldsymbol{\mathcal{B}}$ of physical solutions corresponds to propagating solutions for β, and can be used to construct the associated longitudinal electric and magnetic field distributions. The transverse field components $\mathbf{E}_t = (E_r, E_\theta)$ and $\mathbf{H}_t = (H_r, H_\theta)$ can then be calculated from the longitudinal ones using Maxwell equations [30] as

$$E_r = \frac{i}{k^2n^2 - \beta^2}\left[\beta\frac{\partial E_z}{\partial r} + Z_0\frac{k}{r}\frac{\partial H_z}{\partial \theta}\right] \tag{5.32a}$$

$$H_r = \frac{i}{k^2n^2 - \beta^2}\left[-\frac{1}{Z_0}\frac{kn^2}{r}\frac{\partial E_z}{\partial \theta} + \beta\frac{\partial H_z}{\partial r}\right] \tag{5.32b}$$

$$E_\theta = \frac{i}{k^2n^2 - \beta^2}\left[\frac{\beta}{r}\frac{\partial E_z}{\partial \theta} - Z_0k\frac{\partial H_z}{\partial r}\right] \tag{5.32c}$$

$$H_\theta = \frac{i}{k^2n^2 - \beta^2}\left[\frac{1}{Z_0}kn^2\frac{\partial E_z}{\partial r} + \frac{\beta}{r}\frac{\partial H_z}{\partial \theta}\right] \tag{5.32d}$$

where $Z_0 = \sqrt{\mu_0/\epsilon_0}$ is the characteristic impedance of the free space. Once a solution for β for a given mode is found, the transverse field components can be used to calculate several useful physical quantities, like the effective mode area presented in Section 4.2.2, and the Poynting vector, defined as

$$S_z = \frac{1}{2}(E_r H_\phi^* - E_\phi H_r^*) \tag{5.33}$$

where * denotes the complex conjugate.

Note that in the case of silica MOFs, by using the Sellmeier equation [75] to define the refractive index of silica as a function of the operating wavelength, the material dispersion can be included in the calculation of the effective index of the mode from the outset.

5.2 Method implementation

The field identity (5.30) is an infinite system that must be truncated in order to find a numerical solution of the problem. The series of field expansions are truncated to the range $-M_{max} \leq m \leq M_{max}$, so that the total number of Bessel functions is $N_{bf} = 2M_{max} + 1$. When N_c cylinders are present in the fibre cross-section, the truncated field identity matrix $\boldsymbol{\mathcal{M}}$ is a square matrix with dimension $[2N_c(2M_{max}+1)] \times [2N_c(2M_{max}+1)]$. The accuracy of the solution is related to the number of terms retained in the truncated series, and in the following the convergence of the solution of the truncated matrix equation is described.

A non-trivial solution of the homogenous equation (5.30) occurs when the determinant of the matrix $\boldsymbol{\mathcal{M}}$ is zero (i.e. when $\boldsymbol{\mathcal{M}}$ is singular). The corresponding field vector(s)

$\mathcal{B}$ are therefore eigenvector(s) of the matrix $\mathcal{M}$ that have corresponding eigenvalue(s) equal to zero, more appropriately named singular vector(s) (or null space) and singular value(s) respectively. Since the numerical implementation of the model requires the matrix to be truncated, a non-trivial solution occurs when $\det(\mathcal{M})$ approaches zero, and the corresponding singular value(s) is much smaller than all the other eigenvalues.

The typical procedure followed to find the fundamental mode of a MOF is represented in the flowchart in Figure 5.3. The example of a HF comprised of 4 rings of hexagonally packed air holes, with hole-to-hole spacing Λ equal to 1.2 μm and hole diameter d equal to 1.08 μm ($d/\Lambda = 0.9$, see Figure 5.4) is considered in order to illustrate the algorithm. Note that the structure is 6-fold symmetric, therefore the mode can be either non-degenerate or 2-fold degenerate (see Section 4.2.5). For clarity, circled numbers have been introduced in the following text and in the flowchart to indicate the different parts of the procedure.

The first step is to define the field identity matrix $\mathcal{M}$ defined in (5.30). Thus the inputs to the model are the MOF geometry, the optical wavelength (here $\lambda = 1550$ nm), and the number of Bessel functions (here $M_{max} = 5$, so $N_{bf} = 11$) ①. The MOF geometry is defined by the coordinate location, dimension and refractive index of each cylinder, the refractive index of the glass matrix in which the holes are embedded (here undoped silica), and the jacket characteristics (that, as already mentioned must be defined in order to have a negligible impact on the solution). In this example the jacket radius r_J is taken to be 10 μm, the real part of the jacket refractive index is equal to that of silica, and its imaginary part $\Im\{n_J\}$ is 10^{-12}.

The only unknown now present in the field identity matrix $\det(\mathcal{M})$ is the effective index n_{eff}. Finding the modes of a MOF corresponds to finding the zeros, or local minima if the matrix is truncated, of the function $\det(\mathcal{M})$ as a function of the complex variable n_{eff}. Note that since the determinant of $\mathcal{M}$ is complex, in reality its absolute value $|\det(\mathcal{M})|$ must be minimised. For the cases under study, the imaginary part of the minimum is usually smaller than the real part, thus the real part of the minimum can be located setting the imaginary part to zero and then looking for the imaginary value that further minimises the function $|\det(\mathcal{M})|$. Thus, a lossless approximation ② of the MOF is first considered (i.e. $\Im\{n_{eff}\} = 0$). Since the propagation constant corresponding to the fundamental mode is the largest of all the possible modes, the function $|\det(\mathcal{M})|$ is calculated for different values of the real part of n_{eff} ($\Re\{n_{eff}\}$) ④ starting from the value n_i equal to the refractive index of silica (core region) ③ and then decreasing the value of $\Re\{n_{eff}\}$. The next n_{eff} value is obtained from the previous by subtracting an appropriate Δn. The scanning of the determinant is terminated when the first local minimum is found ⑤. Typically, from experience, steps of Δn of the order of 10^{-4} allow the minimum to be localised. If no minimum is found in this way it means that the value of the imaginary part of n_{eff} is not negligible, so that the lossless approximation fails. This can happen for modes that are poorly confined to the core and thus are very lossy.

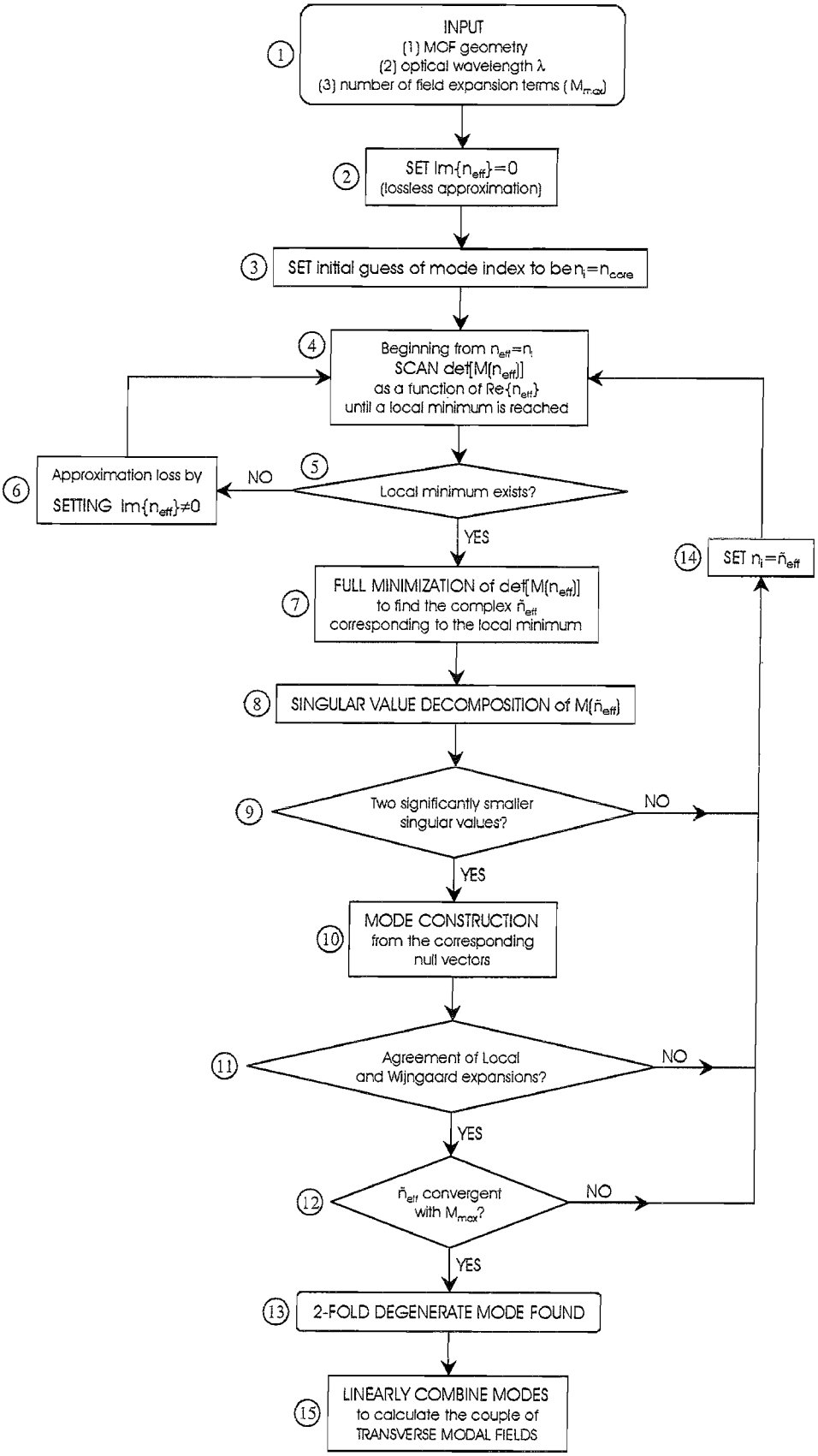

FIGURE 5.3: Flowchart for the search of the 2-fold degenerate fundamental mode of the MOF shown in Figure 5.4. The red circled numbers have been used in the text as reference to the different part of the flowchart.

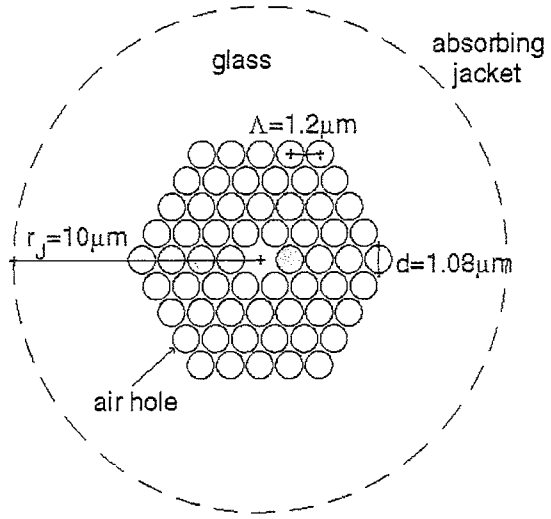

FIGURE 5.4: Geometry of the MOF studied in this section.

Therefore the same process must be repeated assigning a non-zero value to $\Im\{n_{eff}\}$ ⑥.

Once the local minimum in $|\det(\mathcal{M})|$ has been located, the precise value of the complex $\tilde{n}_{eff}$ corresponding to this minimum can be found via a minimisation routine ⑦. The minimisation of $|\det(\mathcal{M})|$ for complex values of n_{eff} is first performed for the real part of n_{eff} only (with $\Im\{n_{eff}\} = 0$, or equal to the value previously used to scan the determinant when the lossless approximation is not satisfied), and then for its imaginary part (with $\Re\{n_{eff}\}$ equal to the value just calculated). The routine is composed of two steps: bracketing the minimum and golden section searching of the minimum [125]. Bracketing the minimum of a function is an essential step in any one-dimensional minimisation routine. The minimum of a function f is known when there is a triplet of points $a < b < c$ (or $a > b > c$) such as $f(b) < f(a)$ and $f(b) < f(c)$. Thus the function f has a minimum in the interval (a, c) and the triplet of points (a, b, c) is said to bracket the minimum. Note that the bracketing of the minimum for the real part of n_{eff} is automatically determined when the local minimum is located ④, but it is not known for the imaginary part of n_{eff}. The second step of the minimisation routine basically consists of refining the bracketing interval until the distance between the two outer points of the triplet a and c is tolerably small, according to a previously set tolerance value. In order to refine the bracketing, a new trial point x between the two outer points of the triplet is introduced and the function f is evaluated here. The choice of x is made so that x lies in the larger of the two segments $|a - b|$ and $|b - c|$. For example, if the largest segment is $|b - c|$, according to the value of $f(x)$, the new triplet can be (a, b, x) or (b, x, c). In order to minimise the number of steps required to obtain the set tolerance, the choice of where x lies in the interval (b, c) is not such that x is equidistant from the two ends b and c, but such that $|x - b| = 0.61803\,|b - c|$ and $|x - c| = 0.38197\,|b - c|$. These fractions are those of the so-called golden section (thus the name of golden section searching for the minimisation routine), and guarantee a more efficient minimisation compared to equal

subdivisions. In order to improve the precision of the (complex) value of n_{eff}, the described minimisation process is always performed a second time setting $\Im\{n_{eff}\}$ to the value found at the end of the first iteration (which considered $\Im\{n_{eff}\} = 0$) .

Note that in practice the function $|\det(\mathcal{M})|$ initially decreases as the imaginary part of n_{eff} is decreased from a reasonably large value, until the local minimum is reached. If the function keeps decreasing even for the smallest computable values of $\Im\{n_{eff}\}$ (i.e. $\sim 10^{-14} - 10^{-15}$), it is possible that the local minimum corresponds to a real value of n_{eff}, such that the local minimum is not a physical solution (false minimum). However, if the MOF under study is characterised by negligible values of confinement loss, where negligible implies that the imaginary values are lower than those that can be represented by machine precision, a real value of n_{eff} can also be found. Also note that when the method is applied to the study of a bound mode, the imaginary part is zero. The procedure for determining whether the solution is a physical one is described next.

When the precise value of $\tilde{n}_{eff}$ corresponding to a local minimum of $|\det(\mathcal{M})|$ has been determined, a singular value decomposition (SVD) routine can be used to calculate the singular values and vectors of $\mathcal{M}(\tilde{n}_{eff})$ ⑧. Since physical solution(s) for the mode can only be non-degenerate or 2-fold degenerate (see Section 4.2.5), the singular value decomposition should produce one singular value (for non-degenerate modes) or two singular values (for 2-fold degenerate modes) that are significantly smaller than the others. If there are more than two significantly smaller singular values, the calculated $\tilde{n}_{eff}$ corresponds to a false minimum (i.e. to an unphysical solution) ⑨. Figure 5.5 reports the 1320 singular values for the minimum corresponding to the fibre under study, that is $\tilde{n}_{eff} = 1.2958442346151 + i3.6475 \times 10^{-11}$. The last two singular values, circled in red, are more than 10 orders of magnitude smaller than the others, which suggests that this is a genuine minimum (physical solution) that could correspond to the 2-fold degenerate fundamental mode.

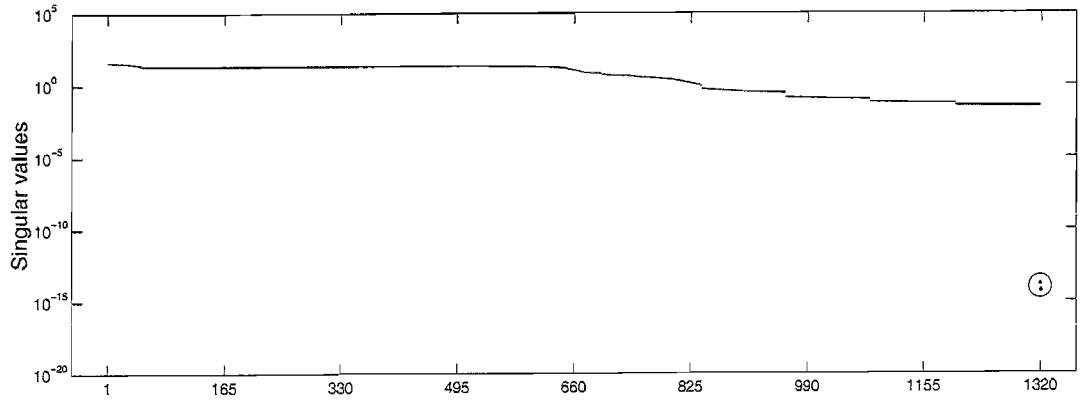

FIGURE 5.5: Singular values of the field identity matrix $\mathcal{M}$ evaluated for $\tilde{n}_{eff} = 1.2958442346151 + i3.6475 \times 10^{-11}$ and $M_{max} = 5$. The red circle indicates the two smallest singular values.

Using the singular vectors $\mathcal{B}$ associated with the two smallest singular values, the vector

components of the electric and magnetic fields of these degenerate modes can be calculated ⑩. The two modes are arbitrary linearly independent solutions of the problem and are plotted in Figure 5.6. They are described as arbitrary because no requirements about the mode features have been imposed. The single-peaked Poynting vector clearly indicates that $\tilde{n}_{eff}$ corresponds to the fundamental mode of the structure in each case. A careful analysis of the plots shows that this pair of modes does not reflect the 2-fold symmetry of the hexagonal structure. However, an appropriate linear combination of the two modes will result in the pair of modes that hold the 2-fold symmetry, as shown in the following. In order to conclude whether this value of $\tilde{n}_{eff}$ produces a genuine solution, it is necessary to verify two more things: the consistency of the different field expansions and the stability of the numerical solution.

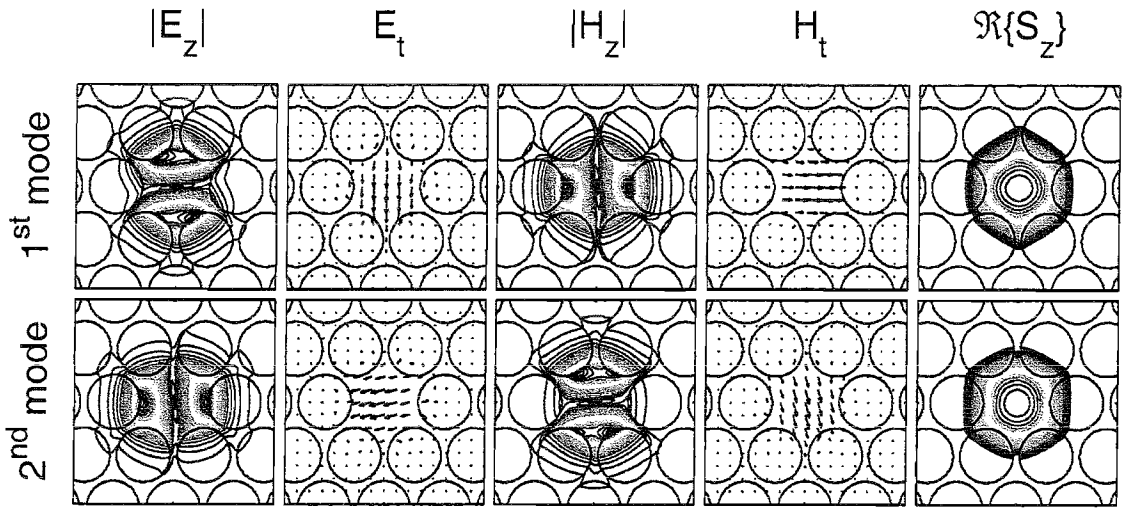

FIGURE 5.6: Electromagnetic field and Poynting vector of the arbitrary pair of modes, calculated for $\tilde{n}_{eff} = 1.2958442346151 + i3.6475 \times 10^{-11}$.

The agreement of the *local* and *global* (or Wijngaard) expansions ⑪ defined in equations (5.3) and (5.5) at the boundary of each cylinder is enforced by the Rayleigh identity when the correct value of n_{eff} is used, thus it is not guaranteed unless a physical solution is found. However, the agreement is perfect only for the untruncated field expansions ($M_{max} \to \infty$). Therefore any disagreement between the two expansions on the boundary of cylinders provides an indication of the accuracy of the choice of number of terms retained. Figure 5.7 shows the expansions (5.3) and (5.5) as a function of the angular position on the boundary of the cylinder shaded in red in Figure 5.4. The first and second columns represent, respectively, the real and imaginary part of the expansions; the third and fourth column the corresponding difference in magnitude of the local and global expansions (i.e the error term). Each of the six field components have been here reported. According to Kuhlmey *et al.* [113], when the two field expansions converge, the error term is dominated by the first neglected term in the expansion of order $m = M_{max} + 1$, where M_{max} is the order of the highest term retained in the expansion. Thus when the error term oscillates like $\exp\{i(M_{max} + 1)\theta\}$, enough terms have been included in

the expansions. The error terms in Figure 5.7, where $M_{max} = 5$ indeed exhibit 12 oscillations over a full period of 2π. However I don't find that this rule always applies, because there are cases in which the error term oscillates like $\exp\{i(M_{max}+1)\theta\}$ but the convergence of the two field expansions visually appears to be poor. Another measure

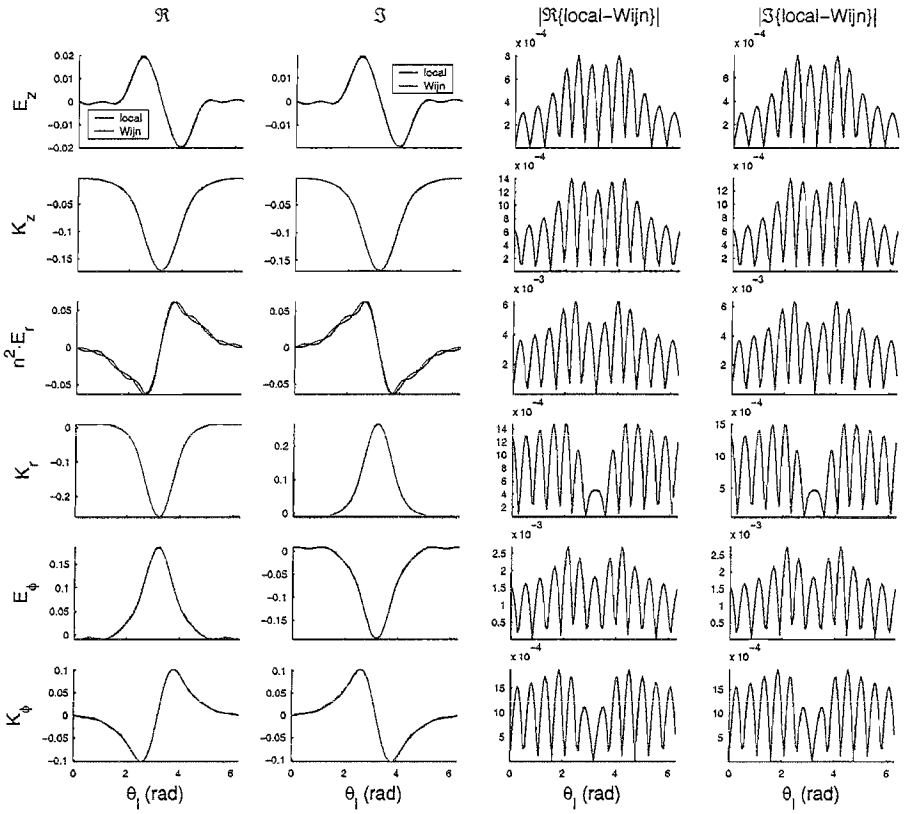

FIGURE 5.7: Field expansions agreement at the boundary of the cylinder marked in red in Figure 5.4 for the first mode shown in Figure 5.6, calculated for $\tilde{n}_{eff} = 1.2958442346151 + i3.6475 \times 10^{-11}$ and $M_{max} = 5$.

of the accuracy of the equality between the two expansions is expressed by the following parameter:

$$W = \frac{\int_{C_l} \left| E_z^{local}(\theta_l) - E_z^{Wijngaards}(\theta_l) \right| d\theta_l}{\int_{C_l} \left| E_z^{Wijngaards}(\theta_l) \right| d\theta_l}. \tag{5.34}$$

W expresses the relative integral error and for this case W is equal to 4×10^{-2}, a value that can be improved as shown in Section 5.3. From the plots in Figure 5.7, the $\tilde{n}_{eff} = 1.2958442346151 + i3.6475 \times 10^{-11}$ is clearly a genuine mode. Of course, the accuracy could have been improved retaining more terms as further discussed in Section 5.3. Note that the disagreement of the radial field components is even higher, as the graphs in the third row of Figure 5.7 show. The continuity of the radial component implies the use of the refractive index. The refractive index contrast is somehow modelled by the expansion, thus is not perfect when only a few terms are retained because sharp edges ideally require infinite terms to be completely described. This is also dependent on the optical wavelength: the smaller the optical wavelength is, the better the convergency of the method is.

The study of the convergence of the solution as the number of terms retained in the field expansions N_{bf} is increased is the final test of the validity of the solution ⑫. This criteria (which is satisfied by the case now under study) will be further discussed in Section 5.3.

Since the solution found for the fibre now under study verifies the agreement of the field expansions and the convergence with increasing terms retained in the expansions, $\tilde{n}_{eff} = 1.2958442346151 + i3.6475 \times 10^{-11}$ is the effective index of the 2-fold degenerate fundamental mode ⑬. As already mentioned when discussing the mode construction ⑩, the pair of modes calculated from the singular vectors $\boldsymbol{\mathcal{B}}$ associated with the two smallest singular values are two arbitrary linearly independent solutions because no requirements about the mode features have been imposed. Thus they need to be linearly combined in order to find the mode pair corresponding to one of the 2 degenerate classes allowed for by the symmetry of the structure (see Section 4.2.5) ⑮. In the literature both experimentally (from the first working example of this fibre [56]) and theoretically (from the first full vector analysis of MOFs [82]), the fundamental mode of hexagonal lattice HFs has been shown to have two perpendicular preferred polarisation axes. More precisely, the fundamental mode of this kind of structure is analogous to the HE_{11} pair of modes of a step-index circular fibre. Thus for this case, this piece of information can be used to decide a priori which class, of the 2 allowed for degenerate modes, the fundamental mode belongs to. For both the classes, the minimum sector angle is equal to $\pi/2$ and the sector boundaries must lie along one of the planes of reflection of the MOF structure as shown in Figure 4.4. For the sake of clarity, the two planes of reflection are chosen to correspond to the x- and y-axis. According to the class, either the tangential electric field or the tangential magnetic field is zero on the sector boundary. Since the electric field is orthogonal to the magnetic field, this implies that on the sector boundary either the longitudinal magnetic field or the longitudinal electric field must be zero, respectively. Therefore the degenerate mode classes corresponding to the fundamental mode should be the $p = 3, 4$ (see Figure 4.4), which allow one mode to be approximately "linearly polarised" along the x-axis and the other along the y-axis. Therefore, the pair of arbitrary modes need to be combined to obtain a pair of modes with the tangential electric field null along the x- and y-axis, respectively. To do that, a point Q along the y-axis where $E_z''(0, Q) \neq 0$ is chosen and this point is used to determine the coefficient of the first linear combination $\chi^{(x)} = -E_z'(0, Q)/E_z''(0, Q)$. The first mode is thus equal to $E_z^{(x)}(x, y) = E_z' + \chi^{(x)} E_z''$. Since its longitudinal electric field is null along the y-axis, $E_z^{(x)}(x, y)$ is linearly polarised along the x-axis. Similarly, the coefficient of the linear combination for the second mode is $\chi^{(y)} = -E_z'(Q, 0)/E_z''(Q, 0)$, where Q is now a point along the x-axis where $E_z''(Q, 0) \neq 0$. Thus $E_z^{(y)}(x, y) = E_z' + \chi^{(y)} E_z''$ is the second mode of the pair and is linearly polarised along the y-axis. The pair of transverse modes is shown in Figure 5.8.

Note that, looking again at the flowchart in Figure 5.3, if the $\tilde{n}_{eff}$ has not verified either

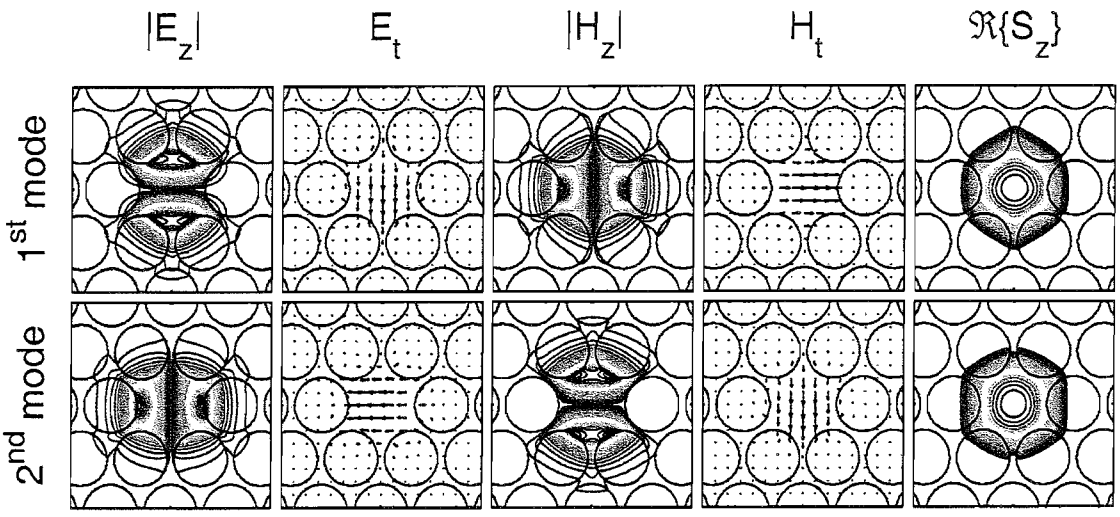

FIGURE 5.8: Electromagnetic field and Poynting vector of the transverse pair of modes, calculated for $\tilde{n}_{eff} = 1.2958442346151 + i3.6475 \times 10^{-11}$.

the agreement of the field expansions or the convergency with increasing terms retained in the expansions, the solution was not genuine. In this case the local minimum of $|\det(\mathcal{M})|$ is a false minimum, and the procedure must commence again, scanning the determinant ④ from $\tilde{n}_{eff}$ ⑭ downwards until another local minimum is localised and properly analysed.

In some HF cases characterised by a relatively small number of holes, as for example the modified triangular lattice HF shown in Figure 5.9(a), a more efficient procedure to localise the minimum corresponding to the fundamental mode can be followed. This structure is comprised of 9 air holes only. The 6 larger air holes have hole-to-hole spacing and diameter equal to 8 μm and 7.6 μm, respectively ($d/\Lambda = 0.95$), while the 3 interstitial holes have a diameter of 1 μm. As discussed in Section 5.4, the computational time scales with the square of the number of cylinders N_c^2. Given the relatively small number of holes within this structure, the calculation requires a significantly reduced computational time with respect to structures comprised of more air holes. Therefore the most efficient way of localising the fundamental mode minimum is to scan the magnitude of determinant of the field identity matrix $\mathcal{M}$ over a wide range of n_{eff} (starting from that of silica and setting $\Im\{n_{eff}\} = 0$). Using $M_{max} = 5$, the bottom curve on the graph in Figure 5.9(b) is obtained. Several local minima appear over the range in n_{eff} considered here. If the procedure explained above is followed (i.e. the examination of each minimum starting from the one with the largest n_{eff}) all these minima can be shown to be false. Next, the scan can be repeated over the same range of n_{eff} values, now retaining more terms in the expansion ($M_{max} = 9$), and the top curve on the graph in Figure 5.9(a) is obtained. All the local minima present in the previous scan appear also in the second one and should therefore be false. However a new local minimum, indicated by the arrow, emerges, which could correspond to a guided mode. Indeed, the analysis of this minimum confirms that this minimum corresponds to the fundamental

mode of the structure. Note that, as discussed in Section 5.3, the number of terms that are required in the expansion to achieve a reasonable degree of accuracy, varies according to the distance between, and the dimension of, the cylinders. The reason why the local minimum corresponding to the fundamental mode do not appear in the curve calculated for $M_{max} = 5$ is that, given the large dimension of the air holes, $M_{max} = 5$ was not sufficient to properly describe the MOF structure.

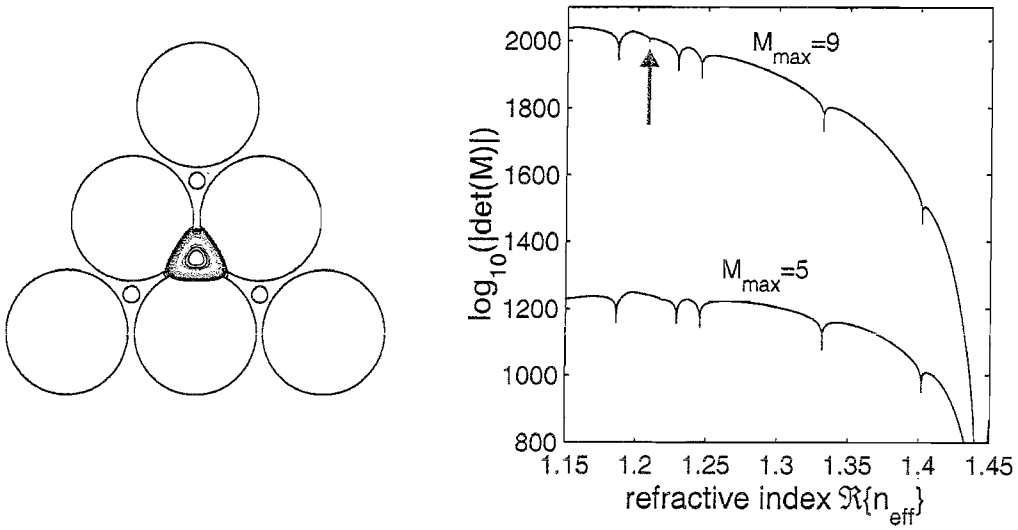

FIGURE 5.9: (a) Modified triangular lattice MOF with, superimposed, the Poynting vector of the fundamental mode; (b) Logarithm of $|\det(\mathcal{M})|$ as a function of the real part of the refractive index n_{eff} ($\Im\{n_{eff}\} = 0$), for $M_{max} = 5$ (bottom) and $M_{max} = 9$ (top). The red arrow indicates the local minimum corresponding to the fundamental mode.

Higher order modes of MOFs can be found following the procedure shown in the flowchart (Figure 5.3). Since such modes have propagation constants that are smaller than that of the fundamental mode, local minima of $|\det(\mathcal{M}(n_{eff}))|$ corresponding to higher order modes must be located at smaller n_{eff} than the fundamental mode minimum. For hexagonally-packed HF structures, according to the symmetry arguments presented in Section 4.2.5, higher order modes can either be non-degenerate or 2-fold degenerate. In the case of a 2-fold degenerate mode, the model results again in an arbitrary pair of modes that need to be linearly combined in order to obtain a pair of modes belonging to the classification reported in Section 4.2.5. Note that there are two different pairs of degenerate modes, thus different linear combinations need to be performed according to the appropriate degenerate mode class. In the case of a non-degenerate mode, only one of the singular values is significantly smaller than the others. Clearly, no linear combination needs to be performed in such cases. Note that according to the first vector analysis of hexagonal lattice HFs presented by Ferrando *et al.* [82], it is possible to classify the HF modes similarly to those of a conventional fibre. This might help in choosing the right linear combination for a pair of degenerate higher order modes, if all the previous modes have already been found.

Similar arguments apply to MOF structures that are not characterised by a 6-fold symmetry. The modified triangular lattice of the fibre in Figure 5.9 presents a 3-fold symmetry. According to the classification presented by McIsaac [84], such structures possess only 4 mode classes, composed of 2 non-degenerate classes and a 2-fold degenerate pair. In contrast, the fibre shown in Figure 8.1 does not possess any symmetry, thus all the modes are non-degenerate.

The process of locating the local minimum corresponding to the fundamental mode can be facilitated by using an estimate for n_{eff}. A reasonably good estimate allows the range of n_{eff} over which the function $|\det(\boldsymbol{\mathcal{M}}(n_{eff}))|$ needs to be evaluated to be significantly reduced. The most obvious case is when the MOF structure has already been studied for a limited number of Bessel functions (small M_{max}) and the same structure is analysed for higher values of M_{max} (e.g. to study the convergence or improve the quality of the solution). Checking the determinant for n_{eff} values nearby the one resulting from previous calculations provides an efficient starting point in this case. The same applies to the n_{eff} values obtained using different numerical methods, applied to the same MOF structure, like the beam propagation method or other such bound calculation. An estimate can also be extrapolated from the study of MOF structures characterised by the same scale. This approach has been widely used while performing the study presented in the following part of the thesis, to evaluate both the real and the imaginary part of n_{eff}. Moreover, it results that for the MOF scale structures under study here (i.e. small-core hexagonal lattice HFs), the value of $\Re\{n_{eff}\}$ is essentially independent of the number of rings of air-holes. Thus quick calculations for HFs comprised of just 2 rings of air-holes provide accurate starting estimates for predicting the properties of HFs comprised of more rings.

5.3 Solution accuracy and convergence

The convergence of the solution for the fundamental mode of the MOF structure presented in the previous section (Figure 5.4) is investigated here in detail. The solution is again calculated retaining different numbers of terms in the field expansions. The results are summarised in Table 5.1. Increasing M_{max}, it is clear that the value of n_{eff} converges. Moreover, increasing M_{max}, the accuracy of the equality between the local and global expansions is improved. This is shown by the decreasing of parameter W, defined by equation (5.34), that measure this accuracy.

Figure 5.10 shows the field expansions for the six choices of M_{max} made in Table 5.1. Note that the error terms oscillate more rapidly as M_{max} increases. From $M_{max} = 5$ onward, the number of oscillations is related to the first neglected term in field expansions (i.e. $\exp\{i(M_{max}+1)\theta\}$), implying that enough terms have been included and the solution is accurate.

M_{max}	$\Re\{n_{eff}\}$	$\Im\{n_{eff}\}$	W	$\Im\{Z\}$
3	1.2960958506153	$3.5721360 \times 10^{-11}$	1.1792×10^{-1}	1.80490
4	1.2958863171091	$4.2023025 \times 10^{-11}$	1.9152×10^{-2}	1.80418
5	1.2958442346151	$3.6475000 \times 10^{-11}$	4.0174×10^{-2}	1.80403
6	1.2958364054258	$3.7613404 \times 10^{-11}$	5.0320×10^{-3}	1.80401
7	1.2958360312080	$3.7517420 \times 10^{-11}$	9.6928×10^{-4}	1.80401
8	1.2958359820183	$3.7529643 \times 10^{-11}$	8.2506×10^{-4}	1.80401

TABLE 5.1: Fundamental mode properties as a function of M_{max} for the MOF shown in Figure 5.4.

According to Kuhlmey *et al.* [113], a second parameter used to evaluate the choice of M_{max} is Z, the value of the largest argument of Bessel functions on the boundary of the inclusions. Recall from Section 5.1 that inside the l^{th} inclusion the field is expanded using only the bounded Bessel functions $J_m(k_\perp^{(l)} r_l)$ (5.24). If the *internal* field expansion behaves as a electrostatic cylindrical multipole to leading order, then the solution rapidly converges with increasing function order m. Note that the largest argument of the Bessel functions in the series is $Z^{(l)} = k_\perp^{(l)}(n_{eff})d/2$, and is therefore related to the dimension of the inclusion via d. For the fibre under study all the inclusions have the same dimension d, thus $Z = Z^{(l)}$. For MOF structures comprised of inclusions of different dimensions it might be necessary to use a larger value of M_{max} for the larger cylinders. Note that since $k_\perp^{(l)}$ is a pure imaginary number, also the value of Z is imaginary, thus in Table 5.1

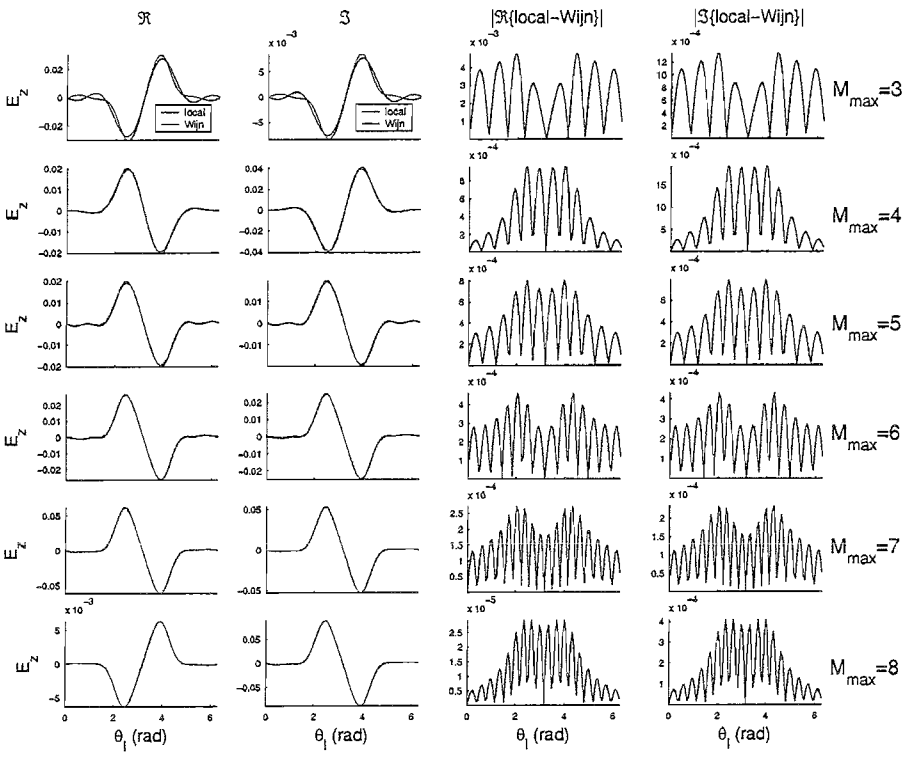

FIGURE 5.10: Expansions agreement as a function of M_{max} for the MOF shown in Figure 5.4.

the imaginary value $\Im\{Z\}$ is reported. The value of n_{eff} predicted by the multipole depends on the number of Bessel functions retained in the field expansions, thus the value of the parameter Z varies with M_{max}, as shown by Table 5.1. In Figure 5.11 the maximum value of $|J_m(Z)|$ (term of the field expansion) normalised to $|J_0(Z)|$ is plotted as a function of the Bessel function order m. The point corresponding to a certain value of m should be evaluated with the n_{eff} predicted by setting $M_{max} = m$. However, the dependance of $|J_m(Z)|$ on M_{max} (or n_{eff}) results to be weak, thus the curve plotted in Figure 5.11 can be evaluated by just considering the effective index resulting from one calculation (e.g. $M_{max} = 5$). This is due to the fact that, at least for the fibre under study, the value of n_{eff} is determined up to the third figure even when $M_{max} = 3$. The values marked with a dot have been actually retaining the proper number of Bessel functions. Considering 11 Bessel functions only (i.e. $M_{max} = 5$) implies that terms discarded are less than the 0.3% of the leading term. According to Kuhlmey *et al.* [113], M_{max} should clearly exceed (by a factor of ~ 1.5, empirically evaluated) the value of $\Im\{Z\}$ to guarantee the convergency of the solution. This is certainly true for all the choices of M_{max} reported in Table 5.1 for the fibre shown in Figure 5.4.

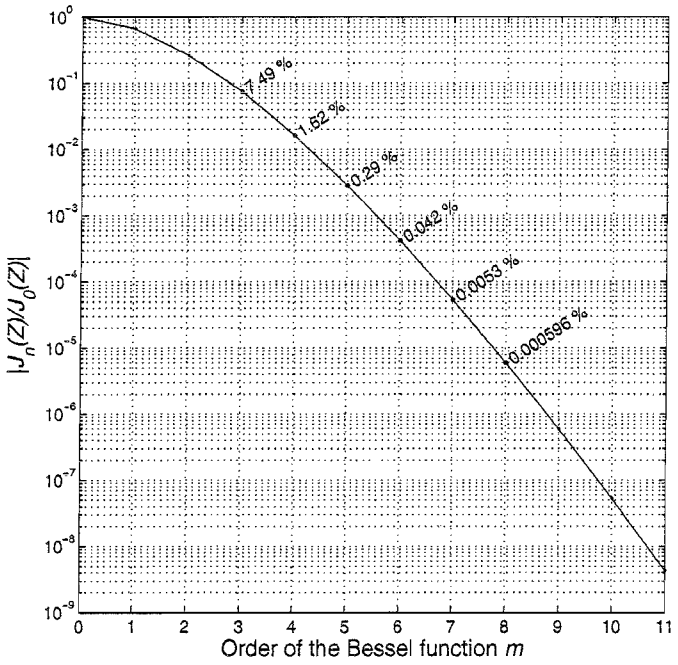

FIGURE 5.11: Evaluation of the values of the terms included in the *internal* expansion, that is $|J_m(Z)/J_0(Z)|$ as a function of m, for the MOF shown in Figure 5.4.

The dependance of this curve on the dimension of the air holes, for a range of structures holding the same scale as the example considered here, is shown in Figure 5.12. Note that Z is proportional to the dimension of the air holes d, and that the value of M_{max}, that is the number of Bessel functions that needs to be retained to obtain an accurate solution, should exceed the value of Z. Thus an accurate solution is obtained for large air holes retaining more Bessel functions than for small air holes.

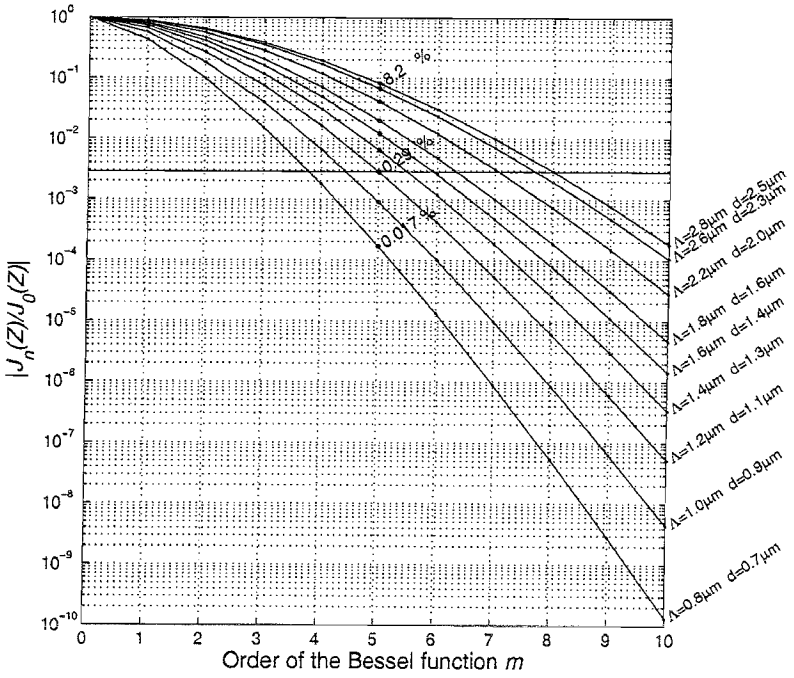

FIGURE 5.12: Evaluation of the values of the terms included in the *internal* expansion, that is $|J_m(Z)/J_0(Z)|$ as a function of m, for a range of MOF structures with air-filling fraction corresponding to $d/\Lambda = 0.9$.

This is also true when holes of different dimensions are present in the HF structure. For example, in [112, 113] the case of a photonic band MOF with a large air hole ($d \sim 13\,\mu$m) placed in the centre of a hexagonal lattice structure comprised of smaller air holes ($d \sim 4\,\mu$m, $\Lambda \sim 5.78\,\mu$m) is presented. In order to obtain a good agreement for the expansions at the boundary of the large air hole, a value of M_{max} equal to 19 needs to used, whereas $M_{max} = 5$ suffices to model the field at the boundary of the small air holes.

However, evaluating the largest argument of Bessel functions on the boundary of the inclusions Z is not always sufficient to test the convergence of the expansions. Depending on the structure design, the expansion coefficients can weight the Bessel functions in different ways, and an important parameter to take into account is not only the dimension of but also the distance between the air holes. In order to ascertain this, a comparison between the example of a small core HF (SCHF) presented here and a large mode HF (LMHF) characterised by 3 rings of hexagonally packed air holes with hole-to-hole spacing Λ equal to $12\,\mu$m (10 times larger then the SCHF one) and hole diameter d equal to $2.4\,\mu$m (more than twice as large as the SCHF one) is performed. The LMHF properties have been evaluated for an optical wavelength of $1.064\,\mu$m because this is a particularly useful application wavelength for this class of HFs. The predicted effective index for this LMHF is $n_{eff} = 1.44930894316107 + i1.2915368 \times 10^{-7}$, resulting in a value of $Z = 1.825$ only slightly larger than the SCHF one (~ 1.8), which should mean that a similar number of Bessel functions must be retained in the expansion to sufficiently describe the mode. Recall that $k_\perp^{(l)}(\lambda, n_{eff}) = \frac{2\pi}{\lambda}\sqrt{n_l^2 - n_{eff}^2}$, thus taking into account

the different λ and n_{eff}, it results that $k_{\perp}^{(l)}$ is equal to $\sim$ 3.34 for the SCHF and to $\sim$ 1.52 for the LMHF, counteracting the difference in air hole size of the two structures. However, this value of Z leads to values of $|J_m(Z)/J_0(Z)|$, reported in the small graph at the right in Figure 5.13, larger than the SCHF ones, which implies that the expansions for the LMHF should converge more slowly than the SCHF one as the number of terms retained in the expansions is increased. It results instead that for $M_{max} = 5$ the value of W (evaluating the agreement between the local and global expansions) for the LMHF is equal to 9.7669×10^{-8}, that is six orders of magnitude better than the SCHF case. This apparent inconsistency between the information given by Z and W about the expansions' convergence, can be explained considering also the expansion coefficients when evaluating the expansion terms. The function $|\mathbb{A}_m^{El} J_m(Z)/\max(\mathbb{A}_m^{El} J_m(Z))|$ has been evaluated as a function of m for both LMHF and SCHF for the same transverse mode configuration, i.e. the first mode shown in Figure 5.8. The results are reported in Figure 5.13 and clearly indicate that the LMHF expansions converge more rapidly than the SCHF. Note how, when a new higher order term is added to the expansion, the presence of the new term does not modify the value of previous term's coefficients, implying that in these two cases the expansion already describes the mode well.

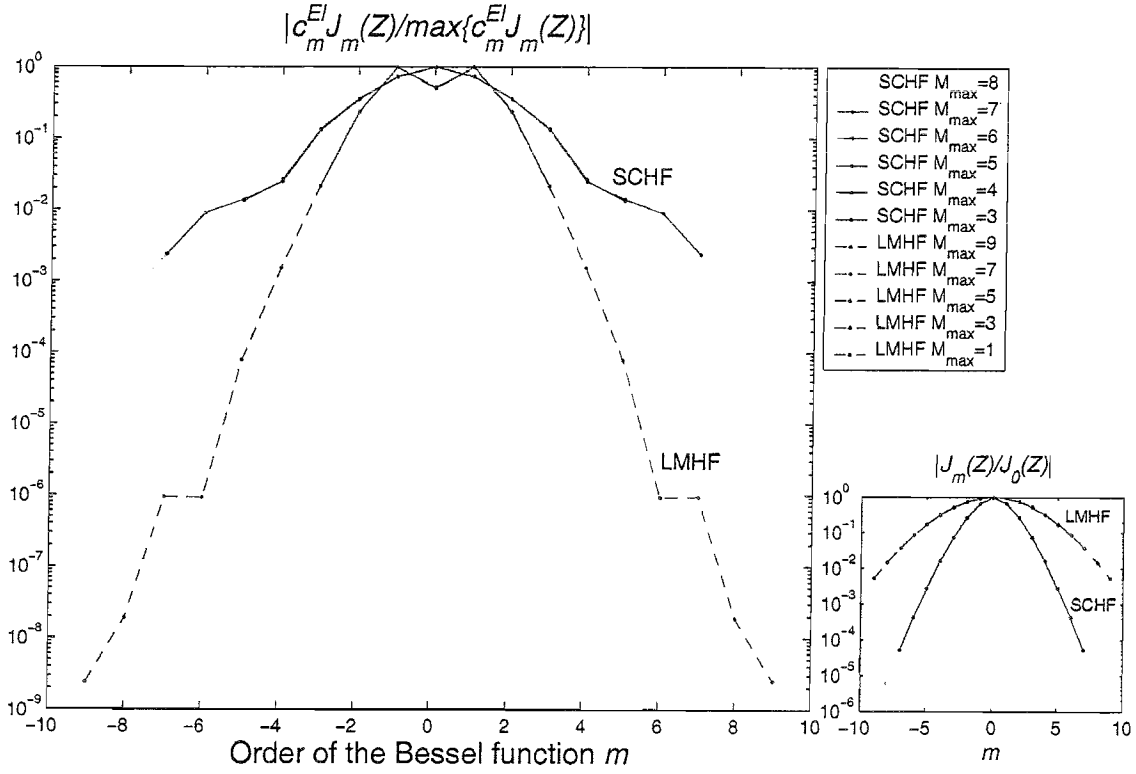

FIGURE 5.13: Evaluation of the values of the terms included in the *internal* expansion as a function of m, now weighted by the expansion coefficients, for the SCHF shown in Figure 5.4 and LMHF. Note that the expansion coefficients $\mathbb{A}_m^{El}$ are denoted by c_m^{El} in the figure.

Even though the apparently inconsistency between Z and W is here explained, the reason why the SCHF and the LMHF exhibit two different behaviours is not clarified

yet. This is clearly related to the significantly different distance between the holes of the two structures. A large interference between the contributions coming from the different holes when the holes are close to each other is expected, thus the convergency of the expansion is slower for the SCHF than for the LMHF. Let's therefore consider two cylinders only in both structures, marked A and B in Figure 5.14, and explore the expansions agreement in the host glass along the straight line that connects the two, denoted with the dashed line x in the same figure. Figure 5.14 also summarises the short-hand notation for the field expansions terms introduced in the following for the sake of this analysis. Recall that, for each inclusion, the local expansion (5.3) is valid in the annular region around each hole that extents to the perimeter of the nearest hole (dashed circle in the figure). Thus, along the black dashed line, the local expansions that refer to the two inclusions within both the regions of validity can be compared. The local expansion is composed by two distinct field contributions The first (J_m term) is the field converging on the cylinder l and is here named ψ^l_{conv}, the second ($H^{(1)}_m$ term) is the field diverging from the cylinder l, here named ψ^l_{div}. Thus, the local expansion referred to cylinder A is $E^A_{\text{local}} = \psi^A_{\text{conv}} + \psi^A_{\text{div}}$, and similarly defined for cylinder B (E^B_{local}).

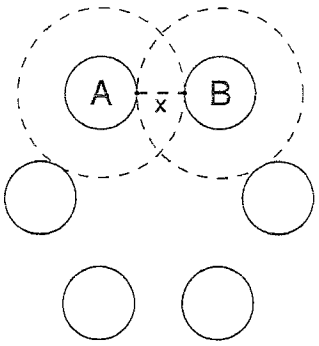

$\psi^A_{\text{conv}} =$ field converging on cylinder A, i.e. right hand side of (5.6)

$\Sigma\psi^{n\neq A}_{\text{div}} =$ sum of fields diverging towards A and coming from all the other cylinders, i.e. left hand side of (5.6)

$E^A_{\text{local}} =$ local expansion (5.3) for cylinder A valid in the marked annular region

$E_{\text{global}} =$ global expansion (5.5)

FIGURE 5.14: Schematic of the cylinder-to-cylinder interaction analysed in the text, along with the definition, referred to cylinder A, of the different field contributions considered in the analysis (similarly defined for cylinder B).

The agreement of the local and global expansions in the vicinity of each cylinder results in equation (5.6), that for cylinder A (B) now reads $\psi^A_{\text{conv}} = \Sigma\psi^{l\neq A}_{\text{div}}$ ($\psi^B_{\text{conv}} = \Sigma\psi^{l\neq B}_{\text{div}}$), an expression that equates the converging term to the diverging terms (in the actual calculation, also the field contribution back-reflected from the jacket, that appears in the right hand side of (5.6), has been included though it is not explicitly specified with the use of this short notation). The magnitude of the two sides of this equality are plotted as a function of the number of terms retained in the expansions (i.e. of the corresponding M_{max}) in the first column of Figure 5.15 for the SCHF and of Figure 5.16 for the LMHF. The second column of each figure reports the magnitude of the difference between the two functions. For the LMHF, even with few terms ($M_{max} \geq 3$) the agreement is almost perfect from the boundary till half way to the other hole. For the SCHF instead an almost perfect agreement is obtained only with ($M_{max} \geq 8$). This can be explained by the fact that the closer the holes are, the stronger the contributions from the near

cylinders perturb what would otherwise be a cylinder to cylinder relationship. For the LMHF the agreement of converging and diverging terms is relatively poor, especially when compared to the SCHF graphs, far from the cylinder boundary (improving though for increasing values of M_{max}). This is due to the perturbation, at large distance from the cylinder, of the converging term on the cylinder, as it is shown next.

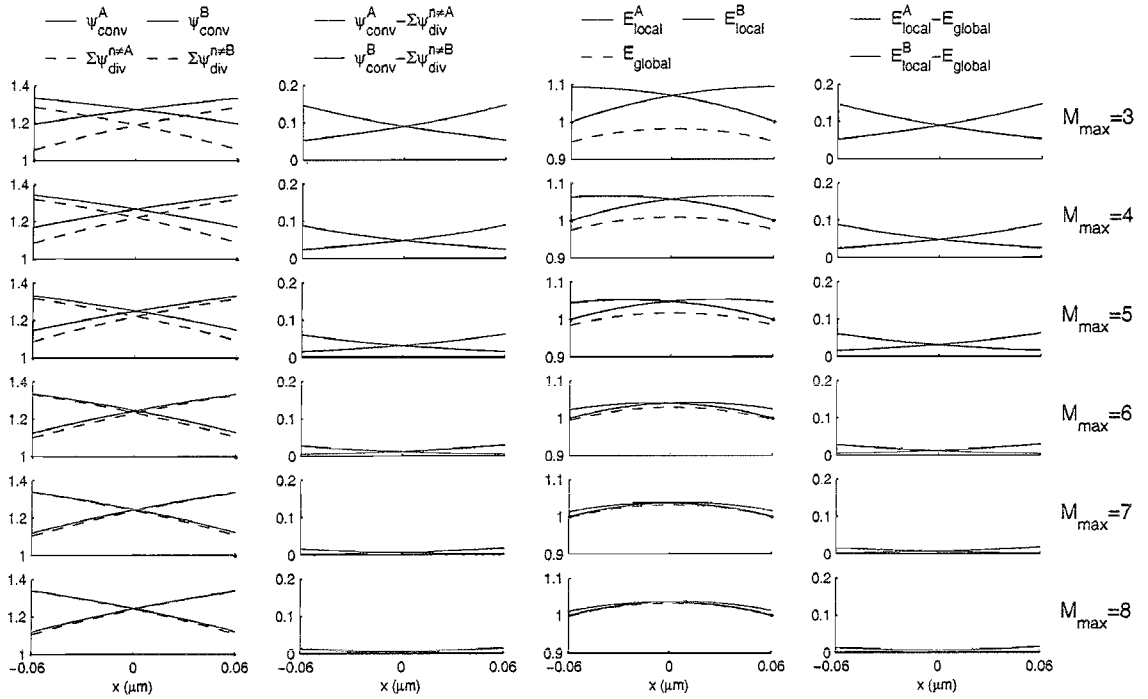

FIGURE 5.15: Spatial plot of the different field contributions used for the cylinder-to-cylinder interaction analysed in the text and referred to the SCHF. The two columns on the left show the agreement of equation (5.6) for cylinders A and B, whereas the two column on the right show the agreement of the global expansion (5.5) and the local expansions (5.3) for cylinders A and B. In each row the field contributions have been calculated for different M_{max} values, as indicated at the end of each row.

The third column of Figures 5.15 and 5.16 shown local expansions for cylinder A and B, defined as $E^A_{\text{local}} = \psi^A_{\text{conv}} + \psi^A_{\text{div}}$ and $E^B_{\text{local}} = \psi^B_{\text{conv}} + \psi^B_{\text{div}}$ respectively, and the global expansion (5.5) $E_{\text{global}} = \Sigma\psi^l_{\text{div}}$ that is the sum of all the diverging fields from all the cylinders (again, including the field back-reflected from the jacket). The magnitude of these functions have been plotted in the graphs, while the fourth column shows the magnitude of the difference between the two expressions. The local field of cylinder A is dominated in the half close to the boundary by the converging term ψ^A_{conv}, and in the half far from the boundary by the diverging term ψ^A_{div}. The global expansion, in the LMHF, lies exactly on the diverging terms coming from the two cylinders, behaviour that is hinted in the SCHF case where the diverging field from each cylinder is not the dominant, along the line that directly connects A to B, with respect to the ones from the other cylinders. When an infinite number of terms is considered it is expected that $E^A_{\text{local}} = E^B_{\text{local}} = E_{\text{global}}$.

Going back now to the analysis of the SCHF example, it has been ascertained that

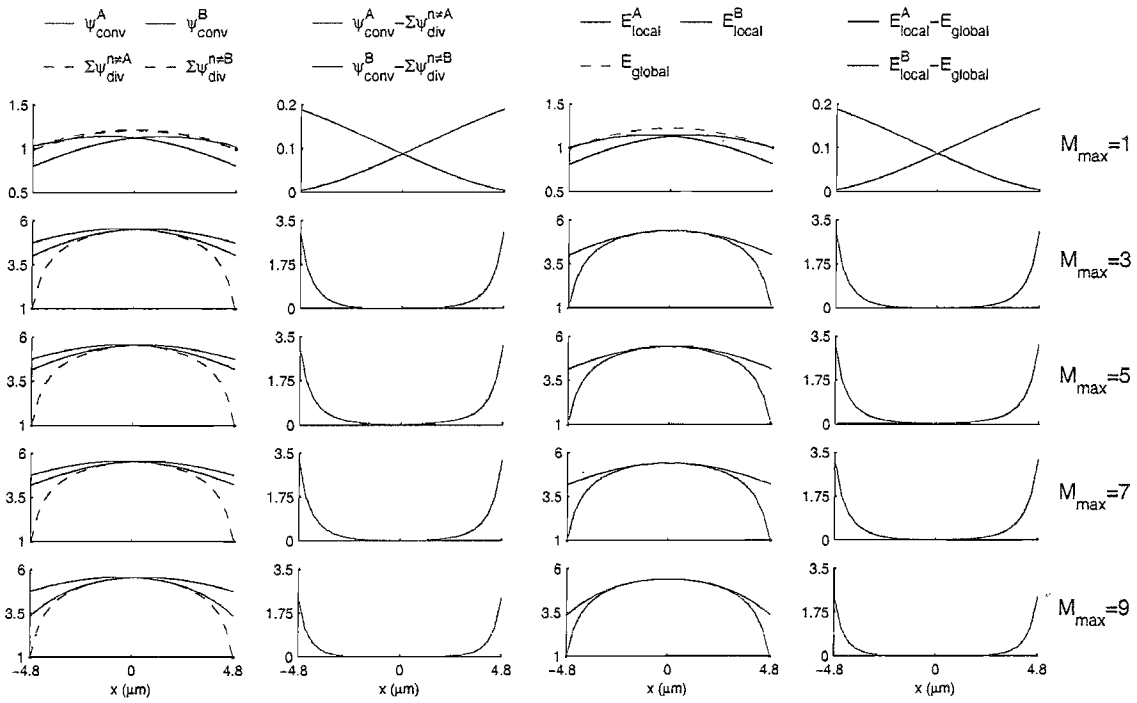

FIGURE 5.16: Spatial plot of the different field contributions used for the cylinder-to-cylinder interaction analysed in the text and referred to the LMHF. The two columns on the left show the agreement of equation (5.6) for cylinders A and B, whereas the two column on the right show the agreement of the global expansion (5.5) and the local expansions (5.3) for cylinders A and B. In each row the field contributions have been calculated for different M_{max} values, as indicated at the end of each row.

the number of Bessel functions related to M_{max} should be larger than 5 (value used to find the fundamental mode) to improve the agreement of the expansions. However, the convergence of the values of a range of physical properties which have a significant importance for the application of these fibres have also been checked. Table 5.2 reports the predicted values of confinement loss, effective nonlinear area as defined in equation (4.9), effective area according to Agrawal [75] and percentage of the fields in the holes, again for the six choices of M_{max}. Although the accuracy of the results improves using larger M_{max} than 5, these physically significant fibre parameters do not vary remarkably beyond the first 3 significant figures. Indeed the variation is less than the typically experimental error in physical measurements of these quantities. In this thesis a study of MOF structures of the same scale as this fibre will be presented, and all the calculations have been made with $M_{max} = 5$. This choice of M_{max} is therefore justified in terms of obtaining reasonable predictions of the fibre properties and reducing the computational time of the calculations (see following section).

5.4 Method discussion: advantages and disadvantages

The use of polar coordinate systems centred in every hole allows the symmetry properties of the structure to be accurately described. The idealised structures considered in the

M_{max}	$\mathcal{L}$ (dB/m)	A_{eff} (μm^2)	A_{eff}^{Agrawal} (μm^2)	PF_{holes} (%)
3	1.2577×10^{-3}	1.7551	1.7088	14.915
4	1.4796×10^{-3}	1.7598	1.7104	15.017
5	1.2843×10^{-3}	1.7593	1.7095	15.031
6	1.3244×10^{-3}	1.7592	1.7093	15.035
7	1.3210×10^{-3}	1.7592	1.7093	15.036
8	1.3214×10^{-3}	1.7592	1.7093	15.036

TABLE 5.2: Fundamental mode properties as a function of M_{max} for the MOF shown in Figure 5.4.

majority of the cases included in this thesis consist of hexagonally-packed rings of circular air holes. According to group theory [84], this kind of structure belongs to the C_{6v} symmetry group (6-fold rotational symmetry with at least one reflection plane), and so supports non-degenerate and 2-fold degenerate modes only (see Section 4.2.5). In addition, idealised 6-fold symmetric fibre profiles are not birefringent [83]. All these fibre characteristics are preserved by this model [83]. Moreover, the use of local polar coordinate systems makes this approach efficient [79]. As seen in the previous section, few terms need to be retained in the expansion to obtain an accurate solution.

The arrangement of inclusions can be arbitrary in terms of disposition, size and refractive index of the cylinder. The only requirement is for the inclusions to be circular and non-overlapping, due to the fact that the Graf's addition theorem, as described here, can only be applied to this kind of problem. An extension of the Graf's addition theorem for a rectangular array of elliptical holes has been performed [126] which expands the range of structures that can be investigated by means of the multipole method. This requirement, that yields the method ideally suited for ideal perfect MOFs, restricts the applicability of the method to imperfect real MOF structures. For real MOFs the solution is always an approximation because the holes are not perfectly circular, as in the case of the fibres shown in Figures 8.1 and 6.1. Note also that in a more regular fibre structure shown in Figure 4.3, the 6 air holes close to the core have a "drop" shape, while all the others have a hexagonal shape, and this is due to the extremely large air-filling fraction of the structure.

The computational time required to calculate one value of $|\det(\mathcal{M}(n_{eff}))|$ is plotted in the 3 graphs in Figure 5.17 as a function of the number of cylinder N_c, rings N_r and Bessel functions $N_{bf} = 2M_{max} + 1$. For large values of N_c and N_{bf}, the computational time is proportional to the square of the number of cylinders N_c and the square of the number of Bessel functions N_{bf}, as shown in Figure 5.17(a) and (c). Quadratic interpolation curves are superimposed on the data point in these figures. Note that the quadratic interpolation $t = O + aN_c^2 + bN_c$, where O, a and b are constant coefficients, is valid for high values of N_c. This scaling is determined by the fact that in order to implement this approach (i.e. build the field identity matrix) $N_c^2 N_{bf}^2$ loop executions are required. Recall

that, the size of the field identity matrix $\mathcal{M}$ is $[2N_c(2M_{max}+1)] \times [2N_c(2M_{max}+1)]$, that for the example thoroughly studied in this chapter is equal to 1320×1320. Note that for hexagonal lattice MOF the number of holes is related to the number of rings via $N_c = 6\sum_{n=1}^{N_r} n$, an expression that can be reduced to $N_c = 3N_r(N_r+1)$. Therefore the computational time is proportional to N_r^4, as shown by the forth-degree polynomial interpolation in Figure 5.17(b) that is directly derived from the quadratic interpolation of the N_c curve. This can lead to a limitation in the total number of holes that can be modelled, both in terms of computational time and also because of the memory required to store the matrix. The size of the matrix $\mathcal{M}$ for a range of examples is given in Table 5.3. Nevertheless, the multipole method is highly efficient when compared to conventional techniques because of the relatively small number of terms retained in the expansions and the efficiency resulting from the use of local coordinate systems, as highlighted at the beginning of this section (see also Section 4.3).

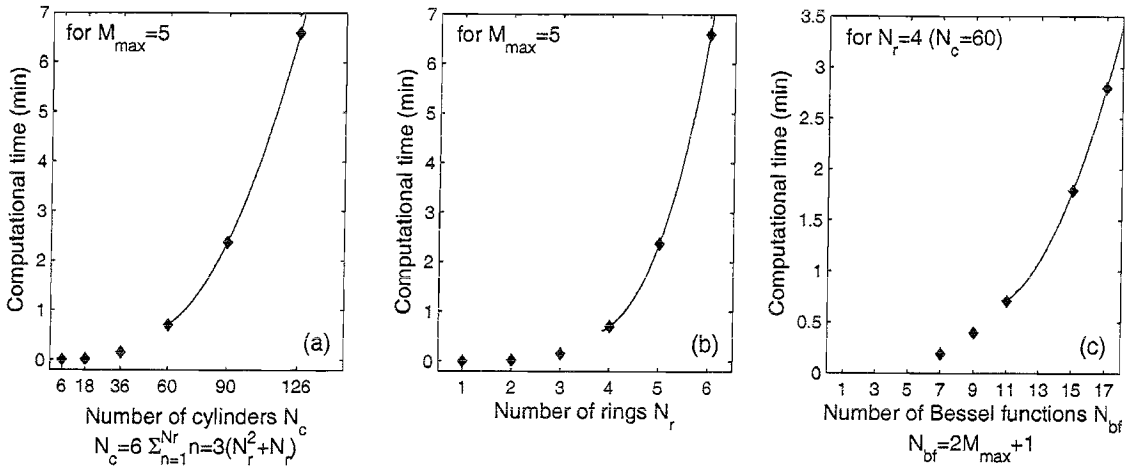

FIGURE 5.17: Computational time as a function of the number of: (a) cylinders (or holes) N_c; (b) rings of air holes N_r; (c) Bessel functions N_{bf}. The interpolation curves are quadratic for the (a) and (c), forth-degree polynomial for (b).

Number of rings N_r	Size of $\mathcal{M}$	Size in bytes
3	792×792	9.6 Mb
4	1320×1320	26.6 Mb
5	1980×1980	59.8 Mb
6	2772×2772	117.3 Mb
7	3696×3696	208.4 Mb

TABLE 5.3: Size of the field identity matrix $\mathcal{M}$ as a function of the number of rings of air holes, where $M_{max} = 5$ and each element of the matrix is a complex number expressed in double precision (i.e. the real and imaginary part require 8 bytes each).

The implementation of the multipole method presented here is not optimal because the process of localising local minima and the minimisation itself requires a lot of human intervention (steps from ② to ⑦ in the flowchart reported in Figure 5.3). However a

more engineered implementation of these steps would remarkably reduce the need for human intervention.

A possible improved implementation is discussed in [113] and consists of two steps. First, the function $|\det(\mathcal{M}(n_{eff}))|$ is computed over the region of interest, for complex values of n_{eff}. Second, the local minima found in this map of the determinant are used as initial points for a mixed zooming and modified Broyden algorithm, that is an iterative minimisation algorithm. All the local minima found in the first mapping are analysed by the Broyden algorithm, and if it fails a refined map is computed around the local minima (zooming), eventually finding new local minima and improving the values fed to the minimisation algorithm. In this way all the possible local minima are analysed, and when the minimisation algorithm converges a singular value decomposition is performed to verify if the solution is physical. Note that the localised mapping of the determinant has also been done in the method implementation performed here. Ideally, no human intervention will be needed any more in performing the localisation and analysis of the propagating modes.

In the case of MOFs holding a particular symmetry, like the 6-fold symmetric case discussed in Section 4.2.5, a further improvement of the method implementation in terms of computational time and memory allocation can be done [113]. Recall that for these structures each mode belongs to a certain class and is completely defined by a minimum sector. Only the coefficients corresponding to inclusions inside the minimum sector need to be specified, thus reducing the size of each matrix and also the computational time. A number of determinant maps equal to the number of possible mode configurations, that for the 6-fold symmetric case is equal to 6 (i.e. four non-degenerate and two 2-fold degenerate), need to be evaluated, but this is highly counteracted by the reduction in matrix size.

5.4.1 Numerical implementation issues

All the routines used in the implementation of the program are double-precision, thus the real and imaginary parts are defined by 8 bytes each. Therefore the effective index of the mode predicted by the method is expected to have an accuracy of $\sim 10^{-15}$, both on the real and imaginary part. In reality, especially in the case of MOFs characterised by a high value of confinement loss, the accuracy can be less.

The field identity matrix $\mathcal{M}(n_{eff})$ needs to be carefully conditioned to avoid under- and over-flows in calculating the determinant. Over-flow can occur when $n_{eff} \to n_e$ and thus $k_\perp^e$, related to the difference between the squared values of n_{eff} and n_e, approaches zero and the value of the determinant of $\mathcal{M}(n_{eff})$, due to the behaviour of the $J_m(k_\perp^e r)$ and $H_m^{(1)}(k_\perp^e r)$ terms, can consequently diverge. A proper scaling of the field identity can solve this problem [101] and the final matrix is said to be conditioned. However,

the conditioned matrix can now exhibit underflow, especially for large matrices (i.e. large M_{max} or many air holes). In order to avoid this, it is sufficient to multiply each element of the matrix by a factor s, thus increasing the determinant value of s^N, where $N = 2N_c(2M_{max} + 1)$ is the number of rows/columns of the matrix.

5.5 Conclusion

After careful consideration of the available methods for modelling MOFs, bearing in mind that the fibres under investigation in this part of the thesis are small-core HFs, the multipole method has been chosen. In this chapter the theory of the method is explained, highlighting the physical meaning of each part of the theory. Its implementation is then described and several numerical issues are discussed. The accuracy and convergence of the solution have also been analysed in detail. Note that the multipole method has also been validated against other methods, as illustrated in detail in Chapter 8. The multipole method can now be applied to the study of the properties of small-core holey fibres, a study that is presented in the following two chapters.

Chapter 6

Small-core holey fibres: Properties and trade-offs for practical designs

6.1 Introduction

Holey fibres (HFs) can have a significantly larger numerical aperture (NA) than conventional fibre types because the cladding region can be mostly comprised of air. When this is combined with a wavelength-scale core, HFs can provide tight mode confinement (i.e. small values of the effective mode area, A_{eff}). In such fibres, high light intensities are guided within the core. Thus even though silica is not intrinsically a highly nonlinear material [75], silica holey fibres can offer high effective fibre nonlinearities γ (see also section 4.2.2).

Effective nonlinearities as large as $\gamma \sim 60 \pm 10$ W^{-1}km^{-1} have been achieved at 1550 nm [77]. This is the best result in terms of nonlinearity reported to date in a silica fibre. In the following it is shown that pure silica HFs can be designed to have A_{eff} at least as small as 1.7 μm^2 at 1550 nm. Hence, considering $n_2 \sim 2.2 \times 10^{-20}$ m^2/W for silica, nonlinearities as high as $\gamma \sim 52$ W^{-1}km^{-1} are practical in these fibres, more than 50 times higher than in standard telecommunications fibre and 2 times higher than the large NA conventional fibres described in section 4.2.2. Note that this value is consistent with the experimental result presented above because of the uncertainty in the measurement of the value of n_2 for silica ($n_2 \approx 2.2 - 2.7 \times 10^{-20}$ m^2/W [75]).

Although these results indicate that HFs can dramatically enhance the achievable γ, the successful application of these fibres has been limited to date by loss, which is a consequence of the fact that these fibres are in an early stage of their development. The loss in HFs occurs for a variety of reasons: intrinsic material absorption, additional

losses arising during the fabrication process (water contamination, absorption due to impurities, scattering, etc.) and confinement loss [79]. Fabrication-related losses can be reduced by careful optimisation of the fabrication process, as shown recently by BlazePhotonics in Ref. [81], which reports a loss of 0.58 dB/km. This represents the lowest loss achieved so far in a HF. Confinement loss is an additional form of loss that occurs in single material fibres. In single-material HFs the core has the same refractive index as the material beyond the finite holey cladding region, and so every propagating mode is therefore intrinsically leaky. It has been proven that increasing the number of rings of air holes that surround the solid core, and thereby increasing the physical separation between the solid core and the external environment, reduces the confinement loss [79]. Thus confinement loss is determined by the geometry of the structure, and it is shown that it can contribute significantly to the loss for these fibres, unless care is taken with the fibre design.

The losses so far measured in real small-core HFs are typically of the order 50 dB/km [127], more than an order of magnitude larger than the best loss achieved by BlazePhotonics for a larger core design [81]. For example, Figures 6.1(a) and (b) shows two small-core fibres made at the ORC with similar effective mode areas ($A_{eff} = 2.6\,\mu m^2$ and $2.8\,\mu m^2$ at 1550 nm, respectively), values predicted from measurements of the effective nonlinearity γ (see Section 4.2.2). Fibre (a) has a cladding comprised of two rings of large air holes and the measured loss is 1 dB/m at 1550 nm. Fibre (b), made using the same fabrication procedure, but with the number of rings of large holes increased to four, has a measured loss of 0.04 dB/m. Since it is reasonable to assume that they both suffer similar absorption and scattering losses, it results that in the small-core regime, increasing the number of rings has served to reduce the fibre loss by improving the confinement of the mode. Thus confinement loss can significantly contribute to the total loss for these fibres. Note that the structural irregularities (such as the fact that the holes are not perfectly circular, the hole size is not constant and the lattice is not symmetrically structured) do not contribute significantly to the loss for the fibres shown here.

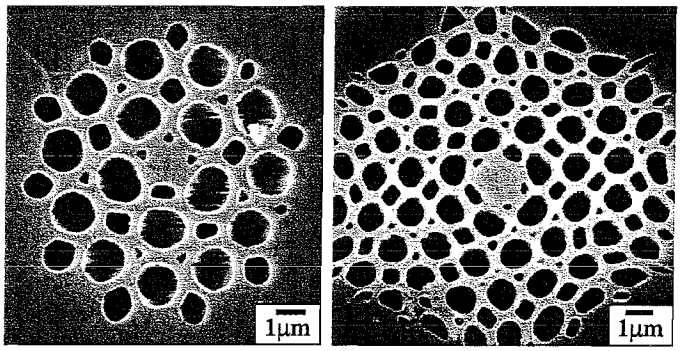

(a) (b)

FIGURE 6.1: Small core holey fibres with: (a) 2 rings of large air holes; (b) 4 rings of large air holes.

To make the fibre fabrication process practical, we ideally wish to limit the number of rings that are required. It is therefore important to be able to reliably calculate the confinement loss characteristics for these HFs. In this chapter the fibre designs that produce low-loss highly nonlinear fibres are identified. Note that although fibre loss limits the effective length of any nonlinear device, for highly nonlinear fibres, short lengths (<10 m) are typically required, and so loss values of the order of 1 dB/km can be readily tolerated.

The modified definition for the effective mode area defined by equation (4.9) is suitable for calculating the nonlinear properties of fibres comprising different material inclusions and is used to perform all calculations in this study. Unless otherwise stated, all calculations are performed for the fundamental mode at a wavelength of 1550 nm.

The multipole method is first applied to a HF structure containing 60 air holes. The fibre is shown in Figure 6.2 and in the following of the chapter is called fibre A. The hole-to-hole spacing (Λ) and the hole diameter (d) are equal to 1.2 μm and 1.08 μm respectively ($d/\Lambda = 0.9$). Using these small-scale core dimensions reduces the effective mode area to $\sim 1.8\,\mu m^2$ (equivalent to $\gamma \sim 50$ $W^{-1}km^{-1}$). The mode in Figure 6.2 is well-confined to the core region, and at these small scales an increased mode/air overlap occurs, which is reflected in the significantly lower real part of n_{eff} ($n_{eff} = 1.295844234615065 + i3.6475 \times 10^{-11}$). The predicted confinement loss for fibre A is ~ 1 dB/km, comparable with the total measured loss for the larger core NTT fibre, as shown in Table 6.1. Despite this, it is significantly lower than losses typically reported to date in small core HFs.

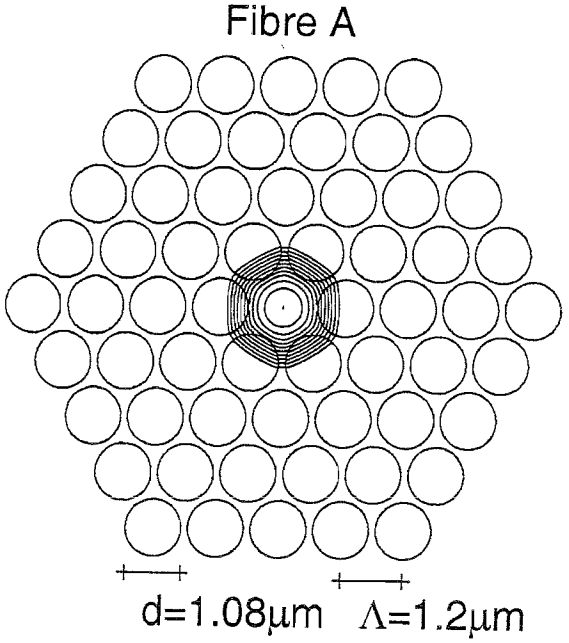

FIGURE 6.2: Fundamental mode (2-fold degenerate) of fibre A at 1550 nm: calculated Poynting vector (contours spaced by 2 dB).

Fibre	Λ (μm)	d (μm)	N_r	A_{eff} (μm^2)	Loss (dB/km)	Reference
NTT	2.8	1.7	4	-	1	OFC 2002 [80]
BlazePhotonics	4.2	1.85	≥ 5	-	0.58	ECOC 2002 [81]
A	1.2	1.08	4	~ 1.8	$\sim 1^{\dagger}$	

TABLE 6.1: Low loss HF examples. † confinement loss only.

Next, the multipole method is applied to the study of a range of small-core large air-filling fraction (highly nonlinear) HFs. The structures in the study contain between 1 and 5 rings of hexagonally-packed holes. Fibres with hole-to-hole spacings in the range $0.8\,\mu\text{m} < \Lambda < 1.8\,\mu\text{m}$ and hole diameters in the range $0.6\Lambda < d < 0.9\Lambda$, and thus the air-filling fraction of the cladding is $33\% < FF < 74\%$ ($FF = \frac{\pi}{2\sqrt{3}}\left(\frac{d}{\Lambda}\right)^2$) are considered. Some typical examples are shown in Figures 6.3(a) and (b). Note from Figs. 4.3 and 6.1 that this range of large air-filling fractions can be produced in practice. Within this study, it is useful to consider the extreme (theoretical) limit in which the air-filling fraction is 1. This structure is shown in Figure 6.3(c) and named jacketed air-suspended rod (JASR). It consists of a silica rod of diameter Λ fully suspended in air. The solid core is surrounded by a circular silica jacket placed at a distance of $(N_r + 0.5)\Lambda$ from the centre, where N_r is the number of rings of the holey fibre structure we wish to make a comparison with.

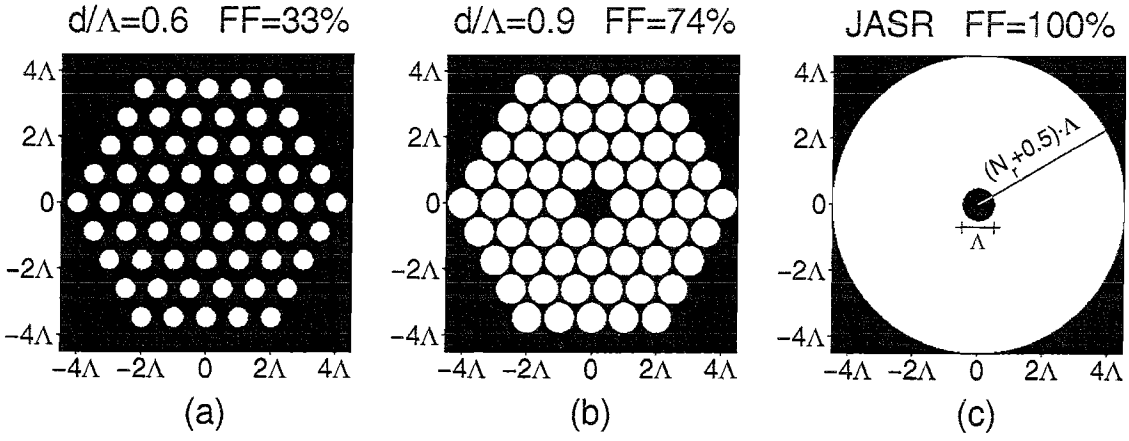

FIGURE 6.3: Typical structures considered in this study (dark regions are silica $n \sim 1.444$, white regions air $n = 1$). N_r is the number of rings of air holes, and is equal to 4 for the structures shown here.

The aim of the study is to optimise the design of highly nonlinear HFs without compromising the fibre performance in terms of confinement loss. First, the results concerning confinement loss only are presented (section 6.2), then the connection between loss and effective mode area is explored (section 6.3).

6.2 Confinement losses

The confinement loss at 1550 nm has been calculated for a range of fibre profiles. Consider typical HFs such as those shown in Figs. 6.3(a) and (b). The confinement loss as the structure's dimensions are scaled down in size is investigated here. Two competing effects might be expected to occur. Reducing the structure scale reduces the thickness of the silica bridges between the holes. If these bridges are small relative to the wavelength of light guided by the fibre, this might be expected to decrease the leakage along these bridges. At the same time, reducing the scale decreases the distance between the core and the solid silica region beyond the cladding ($N_r\Lambda + 0.5d$) which can cause the mode to be poorly confined.

In order to determine which effect dominates, let's calculate the confinement loss as a function of the hole-to-hole spacing (Λ) for different d/Λ ratios when 4 rings of hexagonally arranged holes are present, as shown in Figure 6.4. Using a bigger d/Λ (i.e. larger air holes) always reduces the loss for all values of Λ. This is unsurprising since the mode is always more tightly confined for larger air-filling fractions. However, regardless of the air-filling fraction, observe that confinement loss increases when Λ is reduced, and is the highest for the smallest-scale structures. In addition, note that for the smallest hole-to-hole spacings considered, the degree of improvement resulting from using larger d/Λ is reduced. To understand this trend, consider a structure in which the cladding is completely full of air such as in Figure 6.3(c). This jacketed air-suspended rod (JASR) corresponds to the limit of large air-filling fractions and thus represents the theoretical best case in terms of loss for a HF with a given hole-to-hole spacing and number of rings. Here the extent of the air region is chosen to be equivalent to a structure with 4 rings of holes (i.e. $N_r = 4$). The black line in Figure 6.4 represents the loss as a function of the rod size for a range of JASRs with $N_r = 4$. Observe that the confinement loss in the JASR is significantly larger at small rod sizes. When the JASR is scaled to small dimensions (small Λ), the physical extent of the cladding region is correspondingly reduced, because the cladding radius is equal to $(N_r + 0.5)\Lambda$. Observe that the JASR case removes the contribution to the confinement loss of light leaking along the silica bridges. Thus the result in Figure 6.4 demonstrates that at these small scales, the benefit that can be obtained by increasing the air-filling fraction is limited because the mode can "see over" the finite cladding structure. To validate the fact that JASR results are the lower bound of HF results, consider the point representing a HF with $d/\Lambda = 0.999$: although this is an unfeasible HF to fabricate in practice, it is useful because it represents the real theoretical limit for HF structures. As expected, this point is located between the HF and JASR loss curves.

Figure 6.5 shows again the confinement loss as a function of the hole-to-hole spacing (Λ), now for different numbers of rings and for a fixed air-filling fraction ($d/\Lambda = 0.9$). Regardless of the number of rings, observe that as the core size is reduced, the loss

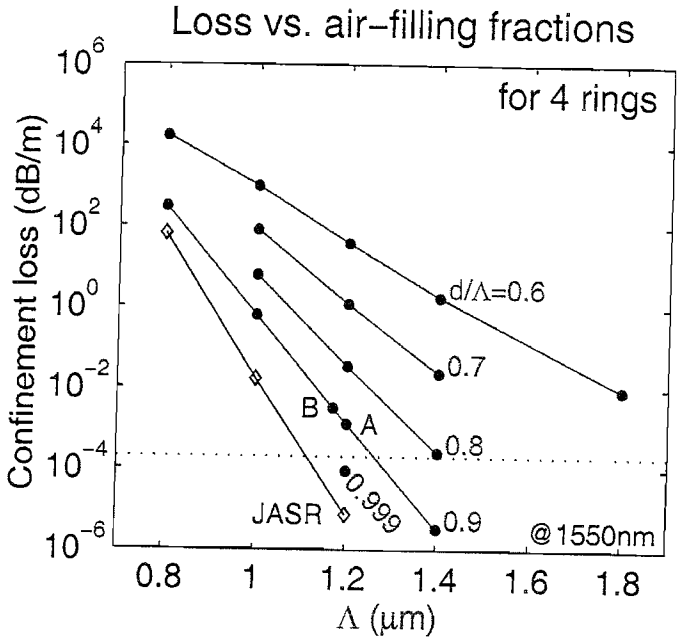

FIGURE 6.4: Confinement loss for different air-filling fractions as a function of the hole-to-hole spacing Λ. The black line corresponds to the case of a jacketed air-suspended rod (JASR) as defined in Figure 6.3(c). The dotted horizontal line represents the loss of conventional fibres (0.2 dB/km). Two fibres (A and B) are labelled for reference purposes.

increases. Again, unsurprisingly, increasing the number of rings also always decreases the loss because the holey cladding extends over a larger region. Also note that the degree of improvement resulting from using smaller Λ is reduced because the extent of the cladding region increases at a slower rate as extra rings are added. Hence it appears that in this small-core, large air-filling fraction regime the main confinement loss contribution is caused by the finite extent of the cladding structure, rather than leakage between the holes, and this is confirmed below.

Figure 6.6(a) shows the confinement loss as a function of thickness of the silica bridges between the holes (which is equal to $\Lambda - d$) for different d/Λ ratios (red lines) and hole-to-hole spacing Λ (green lines) when 4 rings of hexagonally arranged holes are present. Figure 6.6(b) shows the confinement loss as a function of the microstructured cladding extent (equal to $2(N_r\Lambda + 0.5d)$) for the same HF structures considered in Figure 6.4. For a given hole-to-hole spacing (green lines), as the air-filling fraction is increased, the thickness of the silica bridges is reduced and the HF cladding extent is increased. As expected, the loss decreases. Note that the increase of the cladding extent can be quite subtle, especially for the largest scale structures: increasing the air-filling fraction, for a given Λ, implies a limited scaling down of the structure. Therefore the difference in bridge thickness is what plays a role here. However, for a given air-filling fraction (red lines), as the structure is scaled down reducing the hole-to-hole spacing, both the thickness of the silica bridges and the HF cladding extent are reduced. Despite the reduction in thickness of the silica bridges, the confinement loss increases. The dominant

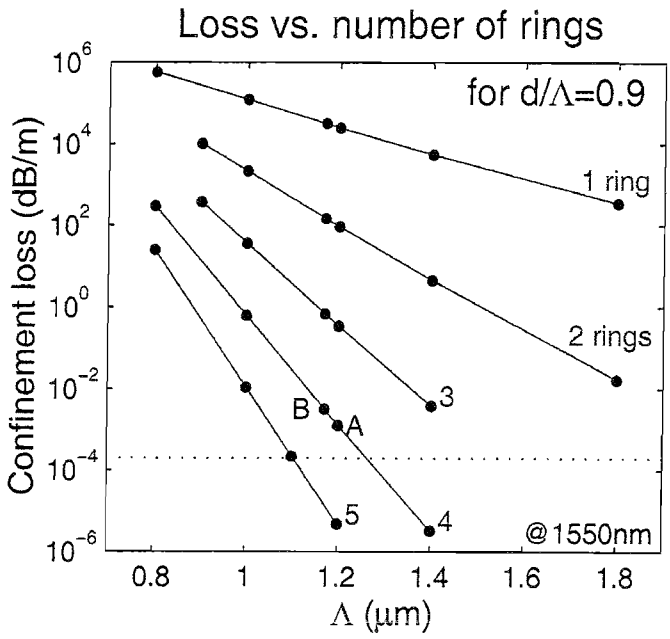

FIGURE 6.5: Confinement loss for different number of air holes rings as a function of the hole-to-hole spacing Λ. The dotted horizontal line represents the loss of conventional fibres (0.2 dB/km). Two fibres (A and B) are labelled for reference purposes.

contribution to the loss in the small-scale regime is hence given by the finite extent of the cladding and not to the reduction of the silica bridge thickness. Hence it results that in this regime, where the features that define the cladding are sub-wavelength, the main loss contribution is due to the finite extent of the cladding structure, rather than leakage between the holes.

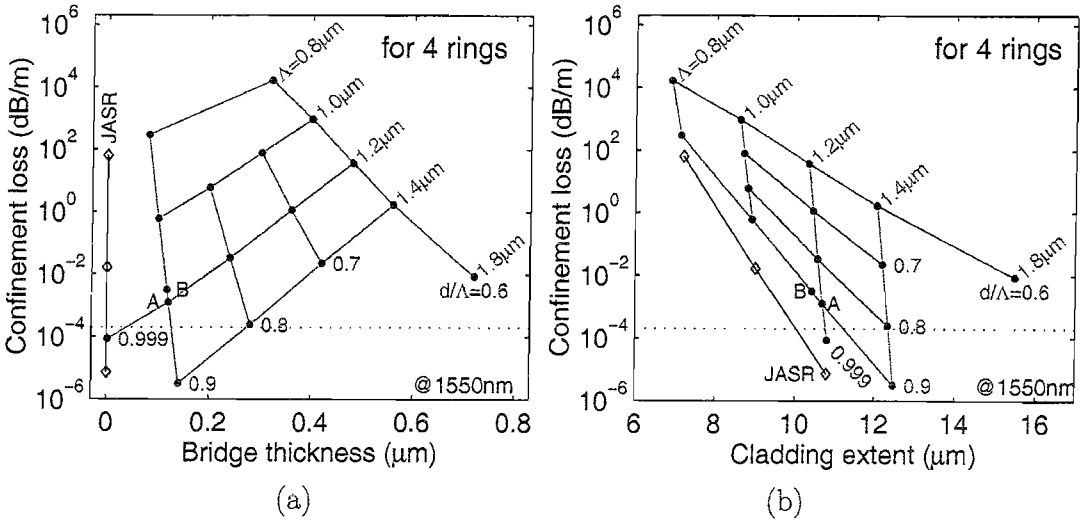

FIGURE 6.6: Confinement loss for different air-filling fractions (in red) and hole-to-hole spacing (in green) as a function of the silica bridge thickness (a) and the microstructured cladding extent (b). The black line corresponds to the case of a jacketed air-suspended rod (JASR) as defined in Figure 6.3(c). The dotted horizontal line represents the loss of conventional fibres (0.2 dB/km). Two fibres (A and B) are labelled for reference purposes.

Note that with careful design the confinement loss can be reduced to values comparable with, or less than, the loss of conventional fibres (0.2 dB/km), which is represented by the dotted line at the bottom of both figures. For example, adding one extra ring to fibre A is sufficient to lower the confinement loss below this level, from 1 dB/km to 0.01 dB/km.

6.3 Effective nonlinear mode area

Here the range of fibre profiles that lead to small effective mode areas, and hence high effective nonlinearities, is identified. In order to ascertain the range of effective mode areas that can be achieved in a given glass material, let's begin by modelling the extreme case of a silica rod of diameter Λ surrounded by air (as shown in Figure 6.3(c)). As the diameter of the rod is reduced, the mode becomes more and more confined, and the effective mode area decreases as shown by the black solid line in Figure 6.7. Once the core size becomes significantly smaller than the optical wavelength (here 1550 nm), the rod becomes too small to confine the light well and the mode rapidly broadens again. Hence, as shown in the figure, for a given optical wavelength there is a minimum effective mode area that depends on the refractive index of the rod only. For silica, Figure 6.7 shows that this minimum effective mode area is $\sim 1.45\,\mu\text{m}^2$, and that this occurs when the rod diameter Λ is $\sim 1.2\,\mu$m.

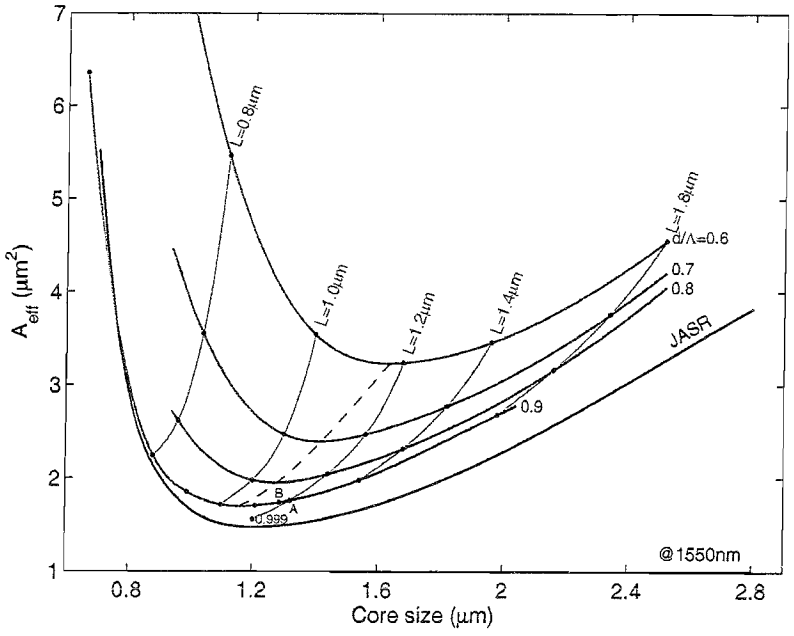

FIGURE 6.7: Effective mode area as a function of the effective core size (defined as $2\Lambda - d$). The black solid line represents the case of a silica jacketed air-suspended rod of diameter Λ (JASR) as defined in Figure 6.3(c). The black dashed line indicates the minimum effective area.

Figure 6.7 also shows the effective mode area as a function of the effective core size

(defined as $2\Lambda - d$) for a range of HFs with different air-filling fractions. These HF structures also exhibit a minimum effective mode area due to the same mechanism described above for the JASR. Unsurprisingly, the smallest effective mode area is achieved using the largest air-filling fraction ($d/\Lambda = 0.9$) that corresponds to the largest feasible refractive index contrast considered in this HF study, thus to the best confinement of the mode. [Note that structures characterised by a d/Λ ratio equal to ≈ 0.95 have been fabricated.] When $d/\Lambda = 0.9$, the minimum effective mode area value is $\sim 1.7\,\mu m^2$, only slightly larger than the value found for the air-suspended rod. This minimum value occurs when the hole-to-hole spacing Λ is $\sim 1\,\mu m$. Observe that for smaller air-filling fractions, the minimum point, indicated by the black dashed line in Figure 6.7, is shifted to larger core dimensions, which reflects the fact that for smaller air filling fractions, the index contrast between core and cladding is reduced. Note that the JASR curve crosses the HF curves at the left of the graph because the mode in the HFs can be confined somewhat by the silica bridges near the core. Apart from this crossing that occurs for very small core sizes, note that the JASR curve represents the theoretical lower bound in effective area for the HF curves. To confirm this, observe the point representing a HF with $d/\Lambda = 0.999$, which is located just above the JASR curve.

Now that the ultimate limit in mode area that is possible in silica fibres is known, let's explore whether it is possible to design fibres with small effective mode areas and reasonably low values of confinement loss. Figure 6.8 shows predictions for the loss as a function of the effective mode area for structures with a fixed hole-to-hole spacing Λ of $1.2\,\mu m$ and different d/Λ ratios. This particular hole-to-hole spacing has been chosen because it results in an effective mode area close to the theoretical limit (see Figure 6.7) and the loss can be reduced below the standard fibre value using just 5 rings of air holes (see Figure 6.5). Each curve in Figure 6.8 corresponds to a different number of rings. For a given d/Λ, as the number of rings is increased, the loss decreases, as shown previously. However, observe that the effective mode area remains remarkably constant regardless of the number of rings used. Effectively, although the tails of the mode significantly influence the mode's confinement loss, their impact on the effective mode area is minimal. Indeed, when just one ring of holes is considered, the effective mode area is only slightly larger than when two or more rings are present because the mode is not well confined. For this hole-to-hole spacing ($1.2\,\mu m$) increasing the air-filling fraction is clearly always advantageous both in terms of achieving small effective mode areas and low confinement losses regardless of the number of rings.

To gain an understanding of how the tradeoffs between confinement loss and effective mode area depend on the core dimensions, let's begin by considering structures with 2 rings of holes only. The curves in Figure 6.9(a) show the loss as a function of the effective mode area for four different values of the hole-to-hole spacing Λ. In Figure 6.9 the vertical lines at the left of the graphs represent the theoretical minimum effective mode area that can be achieved in an air-suspended structure (JASR with $N_r = \infty$).

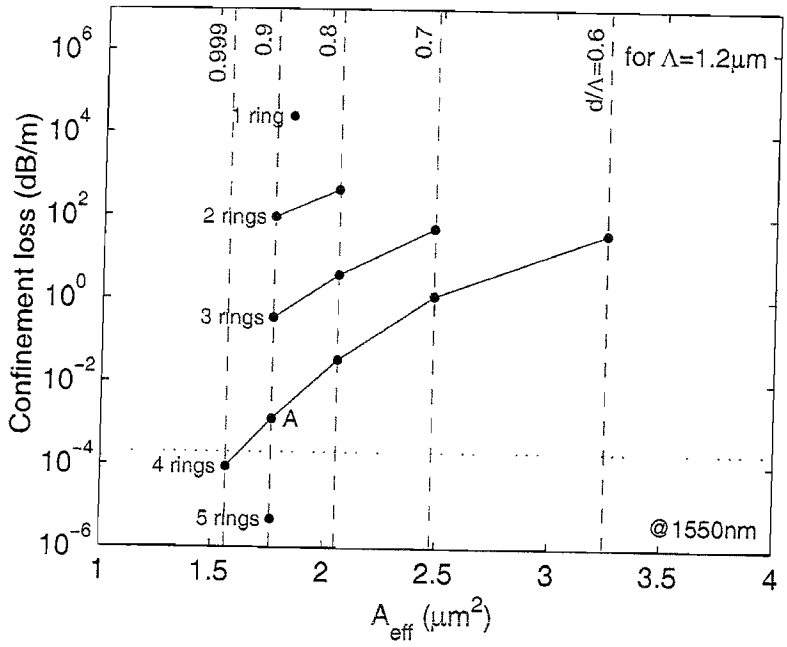

FIGURE 6.8: Confinement loss versus effective mode area for a fixed hole-to-hole spacing $\Lambda = 1.2\,\mu$m when different numbers of rings and different air-filling fractions are considered. The dotted horizontal line represents the loss of conventional fibres (0.2 dB/km).

The smallest hole-to-hole spacings are not plotted for smaller air-filling fractions because they correspond to high loss values except when many rings of holes are used. For all hole-to-hole spacings, larger air-filling fractions not only reduce the loss but also decrease the effective mode area. The solid symbols in Figure 6.9 correspond to the extreme case of a JASR, which represents the theoretical limit for the loss/area improvements that can be obtained by moving to larger air-filling fractions. The shaded region in the lower part of the graph therefore represents combinations of effective mode area and confinement loss that cannot be achieved unless more rings of holes are added. This is confirmed in Figure 6.9(b), which shows the effect of adding two more rings of holes.

Consider the fibre with the relatively small air-filling fraction $d/\Lambda = 0.6$ in combination with a large core size $\Lambda = 1.8\,\mu$m. The guided mode of this fibre is filamented in shape along the silica bridges, as shown in Figure 6.10(b). This is the reason why it has a large value of the effective mode area compared with the other fibres considered in Figure 6.9(b). The modes of the other fibres are more circular in shape, as the mode of fibre A also shown in Figure 6.10(a).

Figure 6.9(b) includes the case of hole-to-hole spacing of $\Lambda = 1\,\mu$m. Observe that increasing the air-filling fraction beyond $d/\Lambda = 0.9$ does not substantially reduce the achievable effective mode area in this case (although it does reduce the confinement loss). This can also be seen in Figure 6.7, since when $\Lambda = 1\,\mu$m, the curves for the JASR and the $d/\Lambda = 0.9$ fibre cross. This occurs because, as already mentioned, the presence of silica bridges near the core can help to confine the mode in this extreme regime.

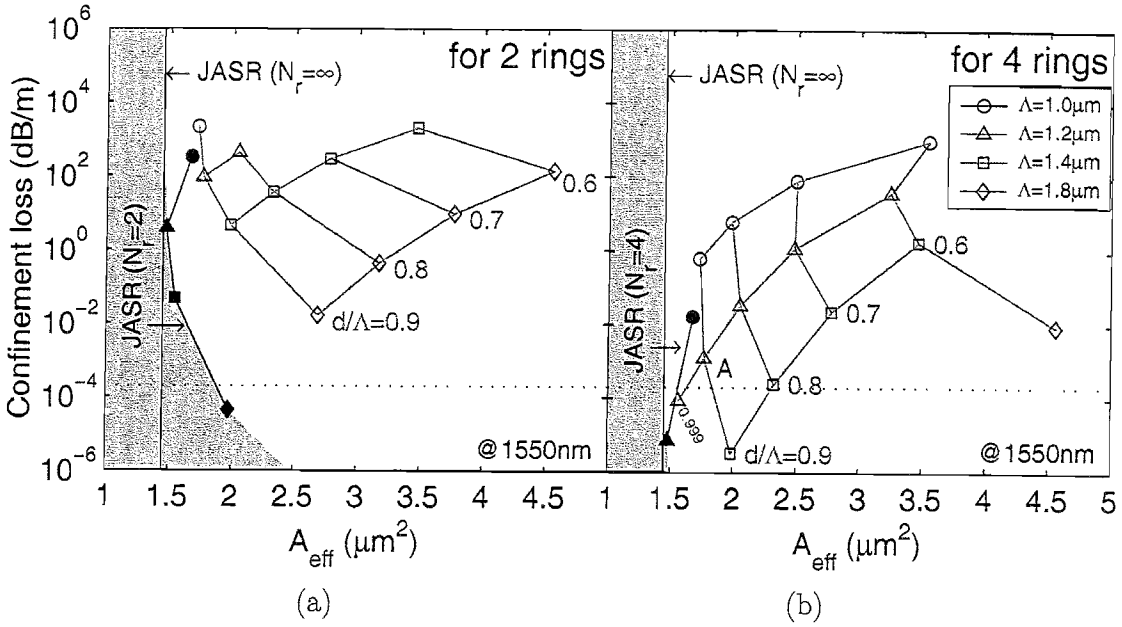

FIGURE 6.9: Confinement loss versus effective mode area for a range of Λ and d/Λ with a fixed number of rings. Solid symbols represent values for jacketed air-suspended rods. The dotted horizontal line represents the loss of conventional fibres (0.2 dB/km). The shaded region represents combinations of effective area and confinement loss that cannot be achieved using the specified number of rings.

Observe from Figure 6.9 that, regardless of the air-filling fraction, moving towards smaller core dimensions there is a clear a trade-off between achieving small effective mode area and low confinement loss in practical fibre design. Such graphs provide a useful practical design tool. Given an effective mode area required for a certain device and the magnitude of loss that can be tolerated (for a given device length) this representation can be used to choose a structure that minimises the fabrication difficulties (i.e. limits the number of rings that are required).

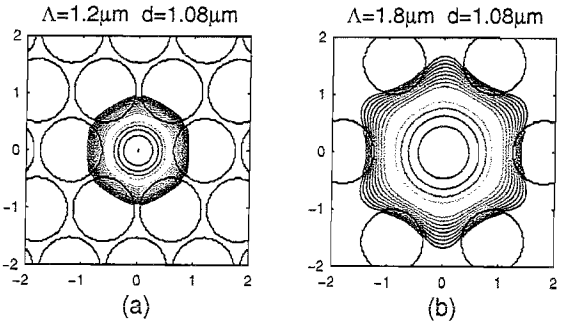

FIGURE 6.10: Fundamental mode (2-fold degenerate) at 1550 nm of two HF structures with the same hole size ($d = 1.08\,\mu$m) and different hole-to-hole spacing: (a) $\Lambda = 1.2\mu$m (fibre A) and (b) $\Lambda = 1.8\mu$m. The calculated Poynting vector is superimposed to the core region of the HF structure (contours spaced by 2 dB).

6.3.1 Higher refractive index glasses

Moving to glasses with a higher refractive index than silica, it is possible to access material nonlinearities that are orders of magnitude larger than that of silica. Some examples are shown in Table 6.2. Schott lead-glass SF57 has a refractive index of 1.8 at 1550 nm, and is 20 times more nonlinear than silica ($n_2(\text{SF57}) \sim 4.1 \times 10^{-19}$ m^2/W [128]). The chalcogenide glass As_2S_3 has a refractive index of ~ 2.4 at 1550 nm and is 100 times more nonlinear than silica glass ($n_2(As_2S_3) \sim 2 \times 10^{-18}$ m^2/W [129]). Note that for chalcogenide glasses the specific composition leads to different n and n_2 values.

Glass	n	n_2 (m^2/W)	λ_{meas} (μm)	Ref.
Silica	1.44	2.2×10^{-20}	1.55	[75]
SF57	1.81	4.1×10^{-19}	1.06	[128]
SF59	1.91	6.8×10^{-19}	1.06	[128]
As_2S_3	2.4	2.0×10^{-18}	1.55	[129]
GLS	2.41	2.16×10^{-18}	1.52	[130]

TABLE 6.2: Measured values of refractive index n and nonlinear coefficient n_2 for several optical glasses at the optical wavelength λ_{meas}.

High refractive index glasses are made of atoms with an atomic number (and therefore weight) larger than Si. The enhanced nonlinearity of high refractive index glasses is due to the increased electronic polarisation of the bound electrons that is present in heavier atoms. When light, i.e. electric field that oscillates at high frequency, propagates in a material, the field interacts with the bound electrons (that have a much smaller mass than the atoms) and results in a displacement of the electrons relative to the nucleus (electronic polarisation). The refractive index of the material is a measure of the electronic displacement (polarisation) that is directly proportional to the intensity of the light. The origin of the nonlinear response is related to unharmonic motion of the bound electrons. All media interact to some extent with light in a nonlinear manner but typically these nonlinear effects are too weak to be observed. The effect of electronic displacement (or polarisation) increases with the size of the atoms because the bound electrons are farther from the nucleus. Therefore, also their nonlinear response increases.

The relationship between linear and nonlinear electronic polarisation is expressed by an empirical rule introduced by Miller [131]. The electronic polarisation is expressed by the susceptibility coefficients $\chi^{(i)}$, where i defines the order, and each coefficient is a tensor of rank $i+1$ [75]. The linear susceptibility $\chi^{(1)}$ represents the dominant contribution and is related to the refractive index n via $\chi^{(1)} = n^2 - 1$. The third-order susceptibility $\chi^{(3)}$ is the lowest-order nonlinear effect present in silica and is related to the nonlinear coefficient n_2 via $n_2 = \frac{8}{3n}\Re\{\chi^{(3)}\}$. The empirically derived Miller's rule reveals the approximate relationship $\chi^{(3)} \propto [\chi^{(1)}]^4$, shown by the solid line in Figure 6.11. On the same graph, the

squares indicate the values of linear and third-order optical susceptibilities correspondent to the different glasses considered here. These values fit Miller's rule well.

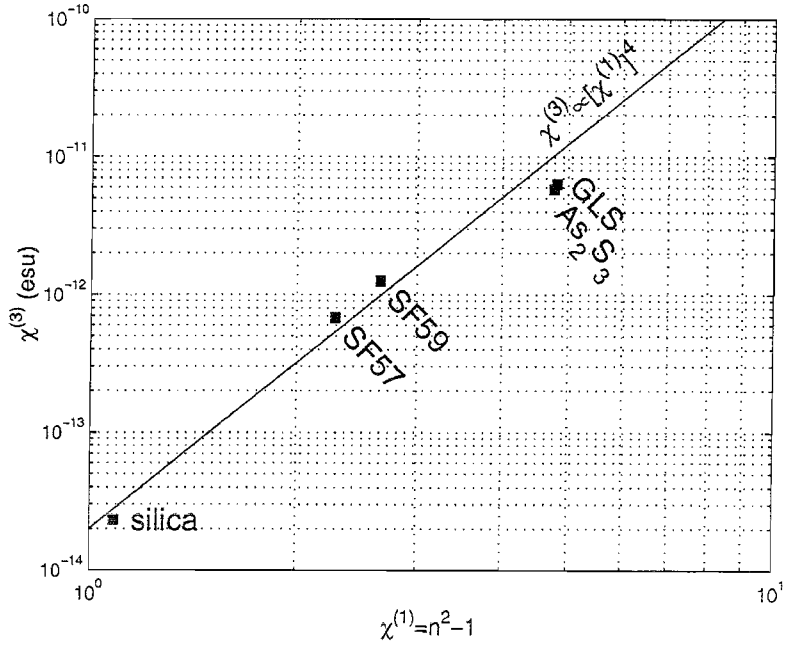

FIGURE 6.11: Relationship between linear and third-order optical susceptibilities for the glasses considered in Table 6.2. The line indicates the approximate relationship $\chi^{(3)} \propto [\chi^{(1)}]^4$, also known as Miller's rule.

In order to compare the mode confinement possible in glasses with different refractive indices, let's consider air-suspended rod (ASR) structures (i.e. JASR without the jacket). Figure 6.12 shows the effective mode area as a function of the rod diameter for a range of practically relevant (linear) refractive indices for the rod material. Unsurprisingly, for all rod sizes, the higher the refractive index, the smaller the achievable effective area. As already mentioned, at a given wavelength the minimum effective area depends on the refractive index only. Higher refractive index glasses can confine the mode well for smaller rod diameters, and thus the minimum effective area achievable is lower than for higher index glasses. This is also shown in Figure 6.13, where the minimum effective area and the rod size at which it is achieved are plotted as a function of the ASR refractive index.

For silica, the theoretical lower bound for the effective mode area is $\sim 1.45\,\mu\text{m}^2$. For the higher index SF57 glass, which has a refractive index of ~ 1.8, the minimum effective mode area is substantially reduced to $\sim 0.75\,\mu\text{m}^2$. Hence high nonlinearity glasses also offer substantial improvements in terms of mode confinement relative to silica. Note that it has been shown in section 6.3 that the minimum A_{eff} value achievable in realistic silica HFs ($\sim 1.7\,\mu\text{m}^2$) is only slightly larger than the theoretical limit, and similarly it is expected that the theoretical limit will provide a useful guide to the mode area possible in other glasses.

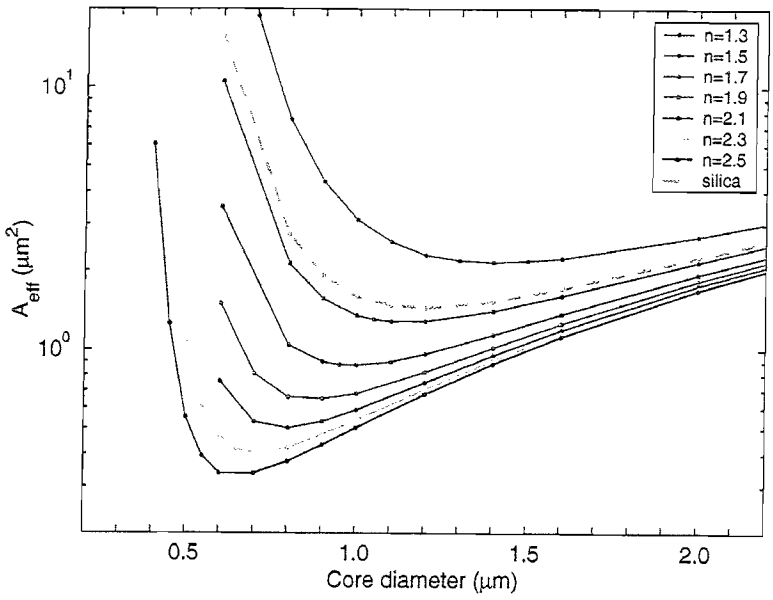

FIGURE 6.12: Effective mode area as a function of the core diameter for ASR with different refractive index materials.

Improvements in the achievable value of effective nonlinearities γ are therefore possible when a high index/highly nonlinear glass is combined with the tight mode confinement offered by an HF structure. Recently, using SF57 glass, HFs with a measured effective nonlinearity γ of 640 $W^{-1}km^{-1}$ have been produced [132], more than 600 times larger than standard silica fibres and 10 times larger than the theoretical limit for pure silica HF structures. For this SF57 fibre, the material nonlinearity (n_2) increases γ by a factor of 20 relative to silica, whereas the small mode area ($A_{eff} \sim 3\,\mu m^2$) provides a factor of $\sim$ 28 improvement. A further factor of 4 enhancement in nonlinearity should be achievable by using designs that reduce the effective mode area.

Figure 6.14 shows the maximum effective nonlinearity achievable at 1550 nm for ASR

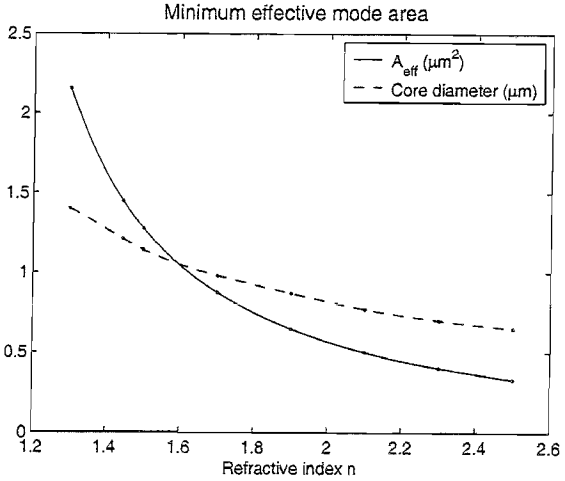

FIGURE 6.13: Minimum effective mode area and core size for ASR with different refractive index materials.

structures made of different glasses. In order to calculate these values, the minimum effective mode area achievable for ASRs made of the specific glass has been extrapolated from Figure 6.13. These values represent the (theoretical) upper bound limit for effective nonlinearities achievable with HF structures. For each glass, the value of n_2 used to calculate γ can be found in Table 6.2. When chalcogenide glasses (As_2S_3) are considered, a significant improvement, of three orders of magnitude in γ, can be obtained with respect to silica.

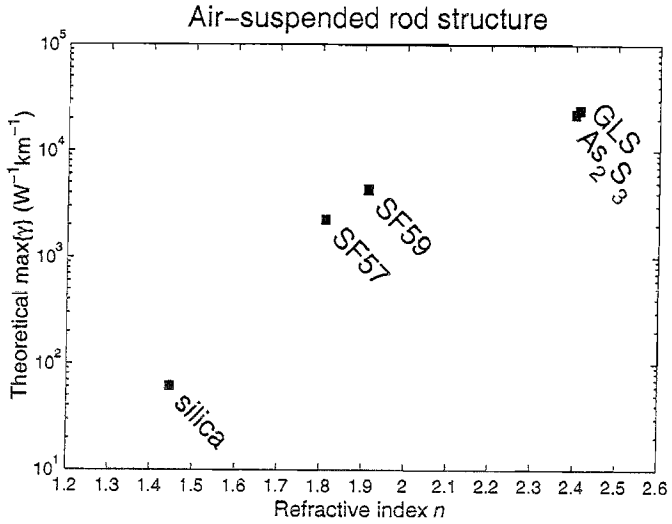

FIGURE 6.14: Maximum achievable effective nonlinearity γ for the glasses considered in Table 6.2.

The calculations performed so far, for the analysis of the effective nonlinearity for ASR structures made of different glasses, have assumed that the refractive index in the core is the linear refractive index of the material. However, another effect to be considered in highly nonlinear glasses, is the Kerr-induced change in the refractive index of the glass. The difference in refractive index caused by the propagation of light in the glass is proportional to the nonlinear coefficient n_2, e.g $\Delta n = n_2 |E|^2$ where E is the optical field distribution. From further calculations this effect, negligible for silica, appears to be negligible also for the high index glass considered here.

Besides the improvement in the achievable effective nonlinearities, let's now consider the impact on HFs confinement losses of the refractive index contrast being higher in these glasses than in silica. That is, is it always true that for the same HF design, the one fabricated with a high index glass will exhibit lower values of confinement loss than the one made of silica? Several effects must be taken into account. In ASR structures, higher refractive indices provide better confinement of the mode, as shown in Figure 6.12. However, when jacketed ASR, or similarly HF structures are considered, observe that the refractive index of the jacket, that causes the mode to be leaky, is also higher than that of silica. Thus, the higher refractive index jacket could counteract the increased confinement of light due to the central core. Moreover, in HF structures made of a high refractive index glass, the effect of the glass bridges could also have a bigger impact on

confinement losses than in silica HFs. Because the bridges are also characterised by a higher refractive index than silica, they could increase the leakage of the light between the air holes. All this could lead to confinement loss trends as a function of the core size/cladding extent different from the ones obtained in the case of silica structures. On the other hand, from the study of silica HFs, the higher the air-filling fraction is, i.e. the higher the refractive index contrast is, the larger is the improvement due to the addition of extra rings of air holes. Applying the same argument when comparing a high refractive index glass HF with a silica HF, it should result that the high refractive index glass HF should have a larger improvement than silica, in terms of confinement loss, when an extra ring of air holes is present.

To answer some of these questions the confinement loss as a function of the core diameter for JASR structures made of silica ($n \sim 1.44$) and SF57 ($n = 1.81$) are compared, as an example, and this is shown in Figure 6.15. The ASR jacket location is defined so that it is equivalent to 3 (dashed line) and 4 (solid line) rings of air holes. For all these designs, the higher refractive index glass JASR always exhibits a lower confinement loss than the corresponding silica one. As expected, the higher index glass structure also exhibits a larger improvement of confinement loss when the jacket extent is moved farther away from the core.

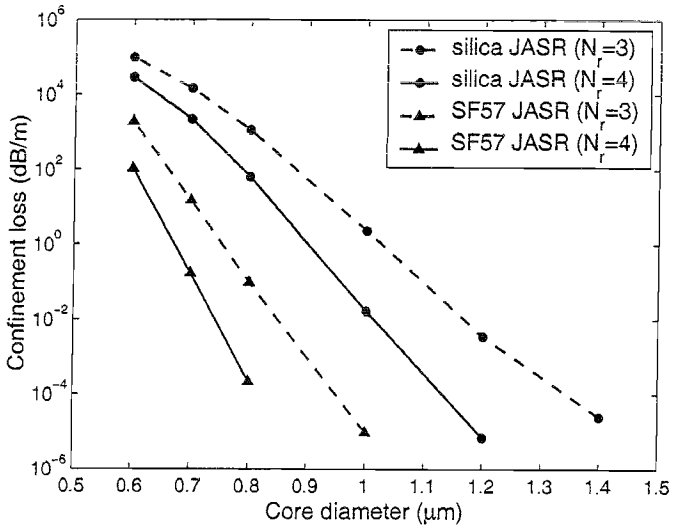

FIGURE 6.15: Confinement loss as a function of the core diameter for JASR structures with $N_r = 4$, for two different glasses: silica and SF57.

When considering high index glasses, it should be recalled that their material-related losses are typically larger than that of silica. Note that both the losses of the bulk glass and the processing losses are higher than that of silica, thus an improvement is needed both of the purification of the starting glass and of the consequent fabrication processes. Conventional fibre types made of chalcogenide glasses have resulted in 1550 nm values of transmission loss of 0.6 – 3 dB/m [129], 3-4 orders of magnitude larger than the 0.2 dB/km typical of conventional silica fibres. SF57 glass has a material loss in bulk of

$\sim$ 0.3 dB/m at 1530 nm [133]. The HF extruded from SF57, reported in [63, 134], has a transmission loss of 4 dB/m at 1550 nm, one order of magnitude larger than the bulk material loss. The increased loss is accounted for by the fabrication process of these fibres which is still in an early stage of development. Thus, the improvement of the fabrication process will allow smaller values of material related loss, both in bulk and later in the fibre fabrication. However it will never be possible to produce fibres with losses as low as conventional silica fibres due to the relatively high bulk losses in these glasses.

However, the enhanced effective nonlinearity resulting from the highly nonlinear properties of these glasses and the small effective areas achievable with HF fibre types, allow the length of the fibre required for device applications to be short. One useful figure of merit for the efficiency of the nonlinear process is the product IL_{eff} where I is the optical intensity and L_{eff} is the effective length of the interaction region [75]. The intensity I depends on the optical wavelength and incident optical power. In bulk material, the effective length L_{eff} depends on the focal region. In optical fibres, the extent of the propagating mode is defined by the fibre design, thus the interaction length L_{eff} is limited only by the material linear loss α (accounting for both linear absorption and scattering loss). L_{eff} is thus defined as $L_{eff} = (1 - \exp(-\alpha L))/\alpha$. Note that $L_{eff} \sim L$ if the linear loss is small ($\alpha L \ll 1$). If the material loss α is equal to 0.5 dB/m and a fibre length of 10 m is considered, the resulting effective length is $\sim$ 2 m. An order of magnitude reduction in the linear loss values, to $\sim$ 0.05 dB/m, allows 80% of the fibre length to be exploited.

6.4 Dispersion properties

In section 6.3 it is shown that it is possible to design high effective nonlinearity fibres with low confinement losses. It is shown here that by modifying the fibre profile, it is possible to tailor both the magnitude and the sign of the dispersion at 1550 nm to suit a range of device applications. For example, small-core fibres with (low) normal dispersion are advantageous for optical thresholding devices (because it reduces the impact of coherence degradation [135]), whereas anomalous dispersion allows soliton-based devices.

The dispersion for some of the structures considered in this study is calculated according to the definition given is Section 4.2.1, concentrating on the ones identified in the previous section as having the most desirable properties in terms of nonlinearity and loss. In Figure 6.16 the dispersion is plotted as a function of the hole-to-hole spacing Λ for a fixed large air-filling fraction ($d/\Lambda = 0.9$). The dispersion curves for one ($\circ$), two ($\triangle$), three ($\times$) and five ($\square$) rings of holes are shown on the graph. Observe from Figure 6.16 that the dispersion for a 1 ring structure differs significantly from a structure with 2 rings of holes, particularly for small hole-to-hole spacings. In addition

observe that structures with 2 or more rings of holes have effectively identical dispersion values. Recall from earlier that the mode area is similarly independent of the number of rings of holes once at least 2 rings of holes are used. It results that once at least 2 rings are used, the mode is well confined to the core, and adding further rings does not significantly impact the central part of the mode. Of course, adding further rings reduces the confinement loss, as discussed previously, by acting to reduce the power in the tails of the mode distribution beyond the cladding region. Note that the difference in dispersion between 1 and 2 ring cases is more marked for small hole-to-hole spacings because these structures have dimensions less than the wavelength of light, and so the 1 ring fibre provides relatively poorer confinement in this regime. The effective mode area as a function of the hole-to-hole spacing for two or more rings of holes and $d/\Lambda = 0.9$ is superimposed in Figure 6.16 from Figure 6.7 for reference purposes.

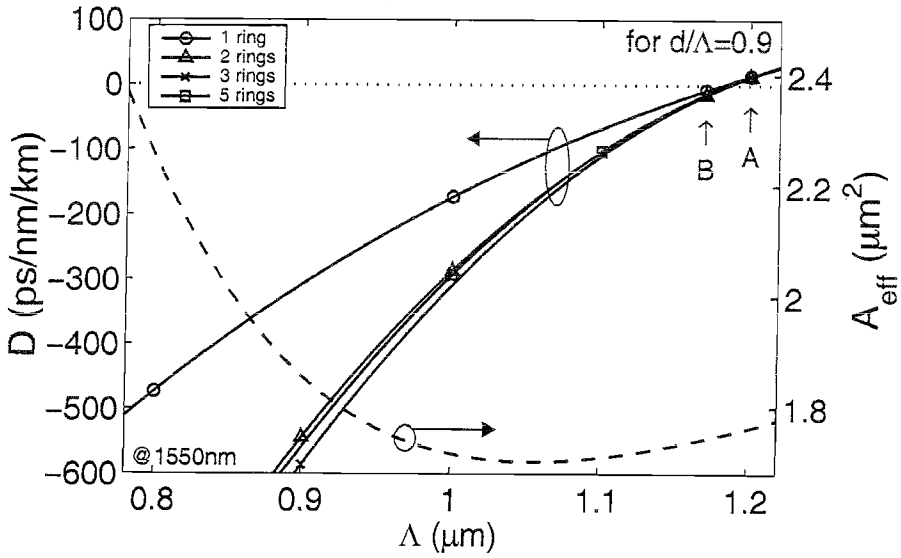

FIGURE 6.16: Dispersion and effective mode area at a wavelength of 1550 nm as a function of the hole-to-hole spacing Λ when different numbers of rings are considered for large air-filling fraction HFs.

For this fixed air-filling fraction ($d/\Lambda = 0.9$, $FF = 74\%$), the zero dispersion point for all curves is located near $\Lambda \sim 1.2\,\mu$m, whereas the minimum effective mode area point occurs for smaller structures, i.e. near $\Lambda \sim 1.05\,\mu$m (see the dashed line). Figure 6.16 shows that large normal values of dispersion are predicted for structures with $\Lambda < 1.05\,\mu$m.

For many nonlinear devices, low dispersion values are desirable, and so let's now concentrate on structures near the zero dispersion wavelength. Consider two examples on either side of the zero dispersion wavelength, fibre A (which was introduced earlier) and B both have $d/\Lambda = 0.9$ and 4 rings of air holes. Fibre A has a hole-to-hole spacing of $1.2\,\mu$m, whereas B has a slightly smaller hole-to-hole spacing of $1.17\,\mu$m. Fibre A has an anomalous dispersion of +14 ps/nm/km, whereas fibre B has a normal dispersion of −14 ps/nm/km. These structures both exhibit effective mode areas of approximately

$\sim 1.75\,\mu m^2$, only slightly larger than the smallest achievable mode area. Fibres A and B both have similar confinement losses (order of $\sim$ 1 dB/km). As already stated, the addition of another ring of air holes reduces the loss below the loss level of conventional fibres, but for the short fibre lengths typically required for nonlinear devices, the 4-ring loss level can be readily tolerated. Thus small-core HF can be used to produced efficient highly nonlinear devices characterised by near-zero values of dispersion, both normal and anomalous.

Moving towards smaller core dimensions, the normal dispersion increases, and hence fibre structures within this range could potentially be used for dispersion compensation. For example, as Figure 6.16 indicates, in order to compensate the dispersion of 1 km of standard SMF28 fibre ($D = +17$ ps/nm/km), just 2.8 m of a HF structure with a hole-to-hole spacing of $\Lambda \sim 0.9\,\mu m$ ($D = -600$ ps/nm/km) is required. Even using 5 rings of holes, the loss for this fibre is of the order of 1 dB/m, significantly larger than for the near-zero dispersion examples given above. At least 3 more rings of holes are necessary to reduce the HF loss below the loss value of standard fibres. Moreover, the effective mode area for this HF is $\sim 1.86\,\mu m^2$. Such small mode areas are undesirable for a dispersion compensation device because nonlinear effects would limit the bandwidth of the data stream that can be compensated.

The specific value of the air-filling fraction ($d/\Lambda = 0.9$) considered here was chosen for these first investigations of dispersion in small-core HFs because large air-filling fractions yield the highest effective nonlinearities. Further work is required to determine whether the same trade-offs between loss, nonlinearity and dispersion apply to structures containing less air (i.e. $d/\Lambda < 0.9$).

6.5 Conclusion

Using the multipole technique, a detailed numerical study of small-core microstructured silica fibres in order to optimise their design for operation at 1550 nm have been performed. Structures with large air-filling fractions (and hence small effective mode areas) were considered. It results that single-material silica structures can have an effective nonlinearity more than 50 times larger than that of standard telecommunications fibre. However, the simulations indicate that these highly nonlinear fibres can suffer from significant confinement loss unless certain rules are followed when designing the fibre profile, as summarised here. Utilising these rules, the confinement loss of small-core HFs can be reduced below the loss of standard fibres.

As shown in Figure 6.7, the hole-to-hole spacing (Λ) can be chosen to minimise the value of the effective area of the fundamental mode (A_{eff}), and this is true regardless of the air-filling fraction. However, the loss calculations indicate that it is not always desirable to use the structures with the smallest effective mode area, because they typically exhibit

higher confinement losses. A relatively modest increase in the structure scale in this small core regime can lead to dramatic improvements in the confinement of the mode without significantly compromising the achievable effective nonlinearity. Note that the loss can always be reduced by adding more rings of holes to the fibre cladding. In the limit of core dimensions that are much smaller than the wavelength guided by the fibre, many rings (>6) are required to ensure low-loss operation, which increases the complexity of the fabrication process.

The coupling of light into holey fibres with a small-core and a large NA is practically challenging when compared to fibres with a larger mode area. In order to achieve a good coupling efficiency using free space coupling, lasers with high spatial quality beams, to achieve small spot sizes, and high NA optics are required. In addition, without the use of tapers or couplers, the direct splicing of conventional fibre types to these fibres becomes impractical due to mode mismatch. Note that these issues are also important for highly nonlinear conventional fibres, but because HFs can achieve smaller mode areas than conventional fibre types, the coupling of light in holey fibre types can be more challenging.

The multimode behaviour has not been studied for these regime of HFs. It has been calculated that silica ASR structures are single mode for a core size smaller than $\sim 1.2\,\mu$m, and few-moded for the rest of the scale range considered here. These HF structures, which cladding refractive index depends on the wavelength and is always larger than 1 (air refractive index) for the presence of the silica bridges, are expected to be effectively single mode for core sizes larger than $\sim 1.2\,\mu$m, thus all over the identified range of interest for device application. Note that the higher order modes of a HF structure are usually more separated in terms of propagation constant than conventional (weakly guiding) fibre ones.

For a complete understanding of these HF structures, it is also necessary to consider the polarisation properties for this range of fibre designs. The study of these properties, presented in the following chapter, indicates that, unsurprisingly, polarisation effects can be extreme in the small core regime. Of particular interest, the polarisation extinction ratio degrades significantly when the core dimension is sub-wavelength, which can have a major impact on device performance.

In this study only the properties of the fundamental modes of these HFs have been considered. To estimate which of the fibres in the study are single mode, the V number for a silica JASR has been calculated. It results that these structures are single mode when the core diameter is smaller than $\sim 1.2\,\mu$m, and are at most few-moded for the largest dimensions considered here. HFs have an effective cladding refractive index that is always larger than 1 and so will be single mode for core sizes somewhat larger than $1.2\,\mu$m. Thus for all of the device applications identified in these chapter, the fibres are single mode. All these important issues regarding modal properties are discussed further

in Section 7.2.

The dispersive properties of the structures have also been analysed in order to determine which designs provide the most suitable dispersion for a range of different fibre device applications. It results that when the air-filling fraction is large ($d/\Lambda = 0.9$, $FF = 74\%$), the zero-dispersion wavelength lies close to 1550 nm (within the 3rd telecommunications window) for structures that have an effective mode area just 3% larger than the minimum achievable area. Conveniently, this promises the development of devices with low dispersion values (both anomalous and normal) with near-optimum effective nonlinearity and reasonably low confinement loss (<1 dB/km). Structures that yield the minimum effective mode area exhibit a large normal dispersion of the order of -300 ps/nm/km. Decreasing the scale further results in even larger values of normal dispersion. As described in Section 6.4, such structures are of potential interest for dispersion compensation. However, as mentioned previously, penalties in terms of loss occur in this regime, and so many rings of holes will be required to make a practical device.

Interestingly, when at least two rings of holes are present, the effective mode area of the structure is essentially independent of the number of rings. This is useful because it allows quick (but remarkably accurate) calculations of the modal properties of any structure to be performed considering just two rings of holes. Once the basic properties have been calculated in this way, the confinement loss can always be reduced by adding more holes, and indeed the loss decays exponentially with the number of rings of holes. Exploiting this fact, it is possible to extrapolate the loss calculations for structures with 1, 2 and 3 rings of holes to predict the confinement loss for structures with more rings (which are computationally intensive to calculate directly using the multipole method).

The calculations performed here indicate that the effective nonlinearity (γ) achievable in pure silica HFs can be as high as 52 $W^{-1}km^{-1}$. One way of enhancing the nonlinearity further is by doping the solid core. Doping with Ge, for example, can increase the value of n_2 by a factor of ~ 2. This technique has previously been exploited for conventional fibres [76] as discussed in section 4.2.2. The preforms of most HFs fabricated to date have been made by stacking silica capillary tubes around a solid silica rod, which ultimately forms the core. HFs with doped cores can be fabricated by replacing the silica rod with a doped rod, and both Yb^{3+} [74] and Ge [60] doped HFs have been reported.

Moving to glasses with a higher refractive index than silica, it is possible to access material nonlinearities that are orders of magnitude larger than that of silica. Note that it is here shown that the minimum A_{eff} value achievable in realistic silica HFs is only slightly larger than the theoretical limit, and similarly it is expected that the theoretical limit will provide a useful guide to the mode area possible in other glasses. If so, the effective nonlinearity achievable with chalcogenide HFs can be three order of magnitude larger than that achievable with silica HFs.

Chapter 7

Small-core holey fibres: Fundamental limits

7.1 Introduction

In the previous chapter it is ascertained the fundamental limits of highly nonlinear small core holey fibres in terms of achievable nonlinearity. The issue of reduction of the confinement loss, which can become a significant penalty as the scale structure is reduced compared to the optical wavelength, has also been addressed. The dispersive properties for a range of structures, which are of great relevance for device applications, were also analysed. Consideration of all these factors allow us to calculate the optimal design for specific practical nonlinear devices. However another practical consideration is the integration of highly nonlinear small core HFs with existing technologies. Although it is possible to splice holey fibres with conventional fibre types [136], the mode mismatch between small core HFs and standard telecommunications fibres tends to make this impractical. For laboratory-based device demonstrations, free-space coupling has generally been used to launch light into small core HFs. Ultimately, any commercial development of nonlinear devices based on small core HFs will require new techniques for providing low-loss interconnection to existing systems. In either case, it is important to understand the fundamental limits on the efficiency with which light can be coupled into these extreme fibres.

7.2 Modal properties

The optical properties of small-core HFs in terms of their coupling efficiency and polarisation properties are investigated here. As a first approximation let's first chose to study these properties by applying a formulation that can be correctly adopted only in

the case of weakly guiding fibres (thus ignoring the fact that HFs are in fact characterised by a high numerical aperture and a complex fibre refractive index profile). More appropriate approaches that allow a more exact analysis of the problem are described in Section 7.3, where the extent of validity of the "approximated" approach and the difficulties of performing a more exact analysis is also highlighted. Therefore all the results contained in this section should at this stage be regarded as a preliminary study on the modal properties of HFs.

The modal characteristics at 1550 nm for a range of small core, high *NA*, pure silica HFs with 4 rings of hexagonally arranged holes are investigated here. Structures with Λ ranging from 0.8 to 2.8 μm and d/Λ of 0.6 and 0.9 were considered.

The idealised 6-fold symmetric HFs considered within this study have fundamental modes that are 2-fold degenerate, that is they are a pair of orthogonally polarised modes with the same propagation constant [85] (see Section 4.2.4). These modes are quasi-linearly polarised, meaning that the polarisation of the field varies across the mode profile, resulting in a slightly curved vector field diagram. The multipole method allows us to calculate this degenerate pair of fundamental modes, and any linear combination of these solutions is also a mode. For the following analysis, it is chosen the linear combination that results in a circular field distribution and transverse electric fields that are approximately linearly polarised along the x-axis and y-axis, labelled mode (1) and (2) respectively.

7.2.1 Percentage of the field in the holes

For some of the designs considered in this paper, the microstructured fibre core is smaller than the optical wavelength, and so its fundamental mode overlaps significantly with the air holes. Calculating this degree of overlap provides a useful way of understanding how the mode properties depend on the fibre structure. For this purpose let's define PF_{holes}, which is the percentage of the transverse modal field located in the air-holes (regardless of the mode polarisation). In Figure 7.1 PF_{holes} is plotted as a function of the hole-to-hole spacing (Λ) for two different air-filling fractions ($d/\Lambda = 0.6$ and $d/\Lambda = 0.9$). For structures with Λ larger than the wavelength (1550 nm), decreasing the structure scale increases the mode/air overlap slightly. However, once Λ is smaller than 1550 nm, it is clear that the mode/air overlap increases dramatically. Unsurprisingly, using a larger air-filling fraction results in higher values of PF_{holes} [137].

7.2.2 Coupling efficiency

For the smallest hole-to-hole spacings (Λ) considered in this study, the fine silica bridges that surround the core are substantially sub-wavelength in scale. For example, when

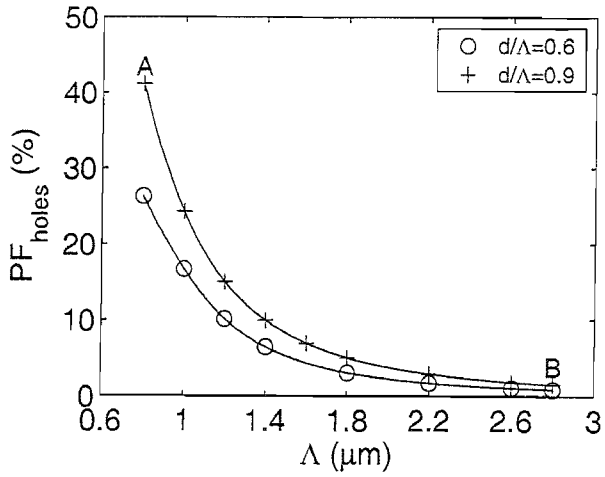

FIGURE 7.1: Percentage of the transverse electric field in the air holes (PF_{holes}) for a range of HF structures.

$\Lambda = 1.2\,\mu m$ and $d/\Lambda = 0.9$, the thickness of these bridges is 120 nm ($\approx 0.078\lambda$). Hence at first sight one might expect the mode to be less filamented along the silica bridges for the smallest-scale fibre structures, and thus more similar to a Gaussian profile in shape. For this reason, better coupling with the Gaussian profile mode of a conventional fibre (or a free space beam) might be anticipated.

In order to test this assumption the mode coupling between the HF mode linearly polarised along the x-axis (i.e. mode (1)) and a Gaussian electric field linearly polarised along the x-axis is calculated here. The mode coupling efficiency CE_x is defined to be:

$$CE_x = \frac{\left|\iint E_x(x,y)\cdot E_0^*(x,y)dxdy\right|^2}{\iint E(x,y)\cdot E^*(x,y)dxdy \iint E_0(x,y)\cdot E_0^*(x,y)dxdy} \tag{7.1}$$

where E_x and $E_0 = \exp\{-(x^2+y^2)/w^2\}$ are the transverse electric field distributions along the x-axis of the HF under study and of a Gaussian field respectively. The full width at half maximum of the mode intensity for this Gaussian profile is $FWHM = w\sqrt{2\ln 2}$. For any choice of Gaussian width (w), CE_x represents the fraction of the power of the linearly polarised Gaussian field that is coupled into the HF mode. In order to determine the optimal coupling that is possible in the HFs, w is chosen numerically in order to maximise CE_x. The coupling loss (CL_x) can be determined from CE_x via

$$CL_x[dB] = -10\log_{10}(CE_x). \tag{7.2}$$

Hence the best coupling is achieved when CL_x is minimised. [Note that when considering the mode coupling between the HF mode and a Gaussian electric field linearly polarised along the y-axis, a similar formula is used simply by substituting the transverse electric field distributions along the x-axis with the one along the y-axis. When the y-axis is considered, results similar to the ones presented in the following, and calculated for the

x-axis, have been obtained.]

Figure 7.2 shows the minimum coupling loss in dB for a range of HF structures along with the choice of Gaussian beam *FWHM* that results in the optimum coupling for each HF (solid lines). Regardless of the air-filling fraction, as the HF scale dimension is reduced, the coupling loss increases (Figure 7.2(a)). Note that this is unexpected with regards to previous discussions about mode filamentation. The two fibre cases, with $d/\Lambda = 0.9$, at the extremes of the range of Λ under study are now considered. The two cases are labelled in the following as fibre A and fibre B, and are characterised by a hole-to-hole spacing Λ equal to $0.8\,\mu$m and $2.8\,\mu$m, respectively. For fiber A, which has an effective mode area of $A_{eff} \approx 2\,\mu\text{m}^2$, the minimum coupling loss is 1.2 dB (corresponding to 75% coupling efficiency), where for fibre B, which has a mode area of $\approx 5\,\mu m^2$, the coupling loss is reduced to 0.2 dB ($\approx$ 95% coupling efficiency). The trend observed for the coupling loss in Figure 7.2(a) is clearly related to the behaviour of the air/mode overlap (Figure 7.1). Note from the graphs that the air-filling fraction has more impact on the air/mode overlap than it does on the coupling loss. This occurs because the field is always somewhat curved along the silica bridges, and so the relatively thicker silica bridges that can be found for the smaller air-filling fractions compensates for the reduced mode/air overlap. This is evident from the close-up view of the transverse electric fields shown in Figure. 7.3. Compare in particular the two cases at the left of the figure, that are fiber A and the fibre with the same hole-to-hole spacing as fiber A but with a smaller $d/\Lambda = 0.6$. Figure 7.2(b) also shows that for the smallest structures, the spot sizes of the Gaussian beams that lead to optimal launch conditions are sub-wavelength and the coupling with sub-wavelength Gaussian beams is impractical. Hence in practice the coupling loss would degrade more at small structure scales than Figure 7.2(a) suggests, and so these predictions should be viewed as a upper bound on the coupling efficiency.

The dashed lines in Figure 7.2(a) show the coupling loss between mode (1) and a Gaussian beam, ignoring the contribution from the mode polarisation, and thus describe the contribution to the coupling loss purely due to the mode shape. This contribution increases significantly for the smallest structures, and so the principal reason for the coupling degradation is the non-Gaussian mode shape that results when a significant fraction of the light is located in the holes. The loss difference between the solid and dashed lines in Figure 7.2(a) reflects the deviation from linearity of the holey fibre mode. The effect of the mode polarisation on the coupling loss worsens for small-scale HFs, and to understand this trend, consider again Figure 7.3, which shows a close-up view of the transverse electric field for the smallest and largest scale structures from Figure 7.2 (fibres A and B respectively, the two graphs at the bottom of Figure 7.3). Figure 7.3 shows that for each structure, the field is essentially linearly polarised throughout the core region. For the largest fibre (B), the mode overlap with the air holes is negligible. In contrast, observe that in the smallest structure (A), the mode extends further within the air holes, and in the holes, the field curvature becomes significant. Hence the deviation

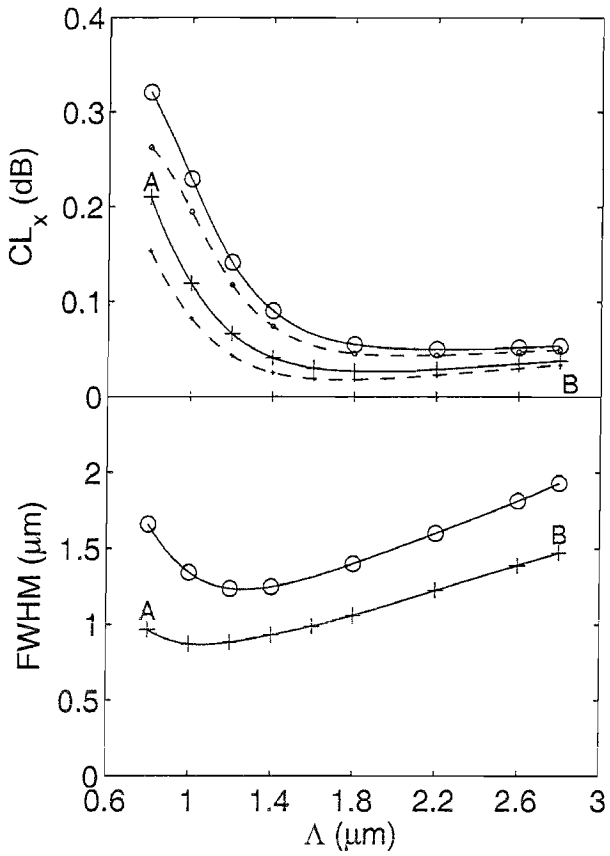

FIGURE 7.2: (a) Mode coupling in dB and (b) full width at half maximum of the Gaussian beam that optimises the coupling of a linearly polarised Gaussian beam (solid lines) and non-polarised (dashed lines) into the HF fundamental mode, for a range of HF structures. Note that the optimal FWHM is essentially the same for both coupling into the linearly polarised and non-polarised Gaussian beam.

from linearity of the field in the air holes overwhelms any filamentation effects, which explains why the coupling with a linearly polarised Gaussian beam is poorer when the scale structure is decreased.

Figure 7.3 also shows the field for a jacketed air-suspended rod (JASR) with equivalent dimensions to fibre A (upper right graph). The modal field exhibits less deviation from linear polarisation than fibre A, even though a significant fraction of the mode is also located in air. This difference is attributed to the different shape of the core/cladding boundary. Hence it should ultimately be possible to improve the coupling to small effective area holey fibres using more sophisticated cladding designs to modify the shape of the core/cladding boundary.

7.2.3 Polarisation extinction ratio

The results given above indicate that the field curvature in the air holes can have a significant practical impact for small scale HF structures. The implications of this field

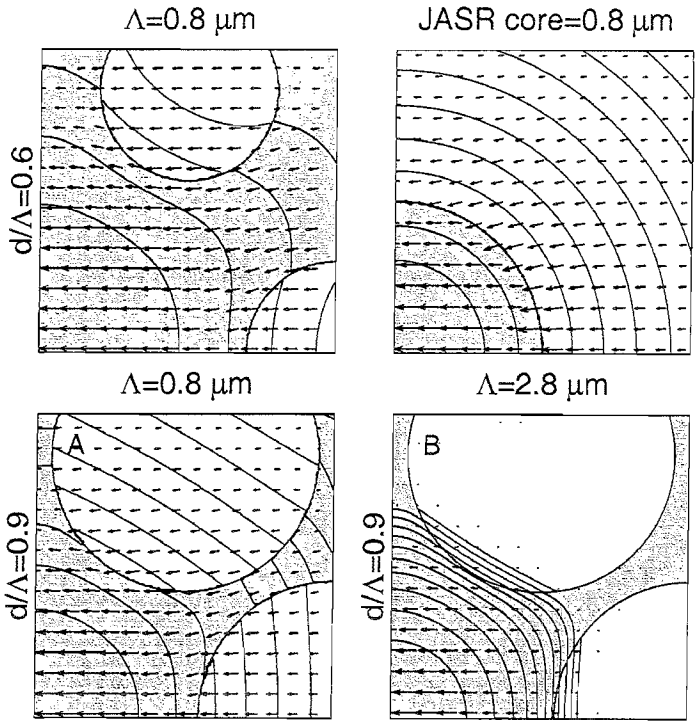

FIGURE 7.3: Vector diagrams of the transverse electric field for three different HF structures (including fibre A and B) and the JASR equivalent to fibre A. Shading denotes silica regions (thus the bottom left corner of each box corresponds to the centre of the fibre). The contours represent the Poynting vector in dB.

curvature for practical devices are now further explored. Although it is known that highly nonlinear HFs are typically birefringent, one related quantity of interest that has not previously been explored in any detail is the polarisation extinction ratio. For many applications, a large extinction ratio is crucial to avoid problems related to walk-off effects from light coupled into the orthogonal mode. The polarisation extinction ratio is defined in the usual way to be:

$$ER_x[dB] = 10\log_{10}\frac{P_{\max}}{P_{\min}} \tag{7.3}$$

where $P_{\max}$ ($P_{\min}$) is the maximum (minimum) power that can be transmitted through a linear polariser positioned at the output of the fibre when linearly polarised light is launched onto one of the principal axes of the fibre, considered in the following to be the x-axis of the fibre.

The function $L_\alpha^{(n)}$ is the overlap between a linear polariser oriented in the α direction and the mode (n), defined by:

$$L_\alpha^{(n)} = \frac{\iint E_\alpha^{(n)}(x,y)\cdot E_\alpha^{(n)*}(x,y)dxdy}{\iint E^{(n)}(x,y)\cdot E^{(n)*}(x,y)dxdy} \tag{7.4}$$

and the function $CE_\alpha^{(n)}$ to be the coupling efficiency between mode (n) and a Gaussian

beam E_0 polarised in the α direction, defined by

$$CE_{\alpha}^{(n)} = \frac{\left|\iint E_{\alpha}^{(n)}(x,y) \cdot E_0^*(x,y)dxdy\right|^2}{\iint E^{(n)}(x,y) \cdot E^{(n)*}(x,y)dxdy \iint E_0(x,y) \cdot E_0^*(x,y)dxdy} \tag{7.5}$$

an expression that is the general version of equation (7.1). Equations (7.4) and (7.5) represent the output and input functions of the considered optical system, respectively.

The maximum power $P_{\max}$ is obtained when the output linear polariser is oriented along the x-axis. The contribution to $P_{\max}$ from mode (1) is expressed by $CE_x^{(1)}L_x^{(1)}$ and the contribution from mode (2) by $CE_x^{(2)}L_x^{(2)}$, hence

$$P_{\max} = CE_x^{(1)}L_x^{(1)} + CE_x^{(2)}L_x^{(2)}. \tag{7.6}$$

Similarly, the minimum power $P_{\min}$ is obtained when the output linear polariser is oriented along the y-axis. The contribution to $P_{\min}$ from mode (1) is expressed by $CE_x^{(1)}L_y^{(1)}$ and the contribution from mode (2) by $CE_x^{(2)}L_y^{(2)}$, hence

$$P_{\min} = CE_x^{(1)}L_y^{(1)} + CE_x^{(2)}L_y^{(2)}. \tag{7.7}$$

For the ideal case of a linearly-polarised mode, it is possible to avoid launching any light into the orthogonal mode, and so $ER_x = \infty dB$. In real fibres, any field curvature reduces the values of ER_x that can be achieved. The polarisation extinction ratio can be readily measured experimentally (and does not require an optimal coupling configuration).

In Figure 7.4 the extinction ratio is plotted for a range of HF structures. The extinction ratio worsens significantly for the smallest-scale structures, which reflects the increasing deviation from linear polarisation for the modes of these fibres. At first, it appears that the extinction ratio is independent of the air-filling fraction (d/Λ). However, by plotting

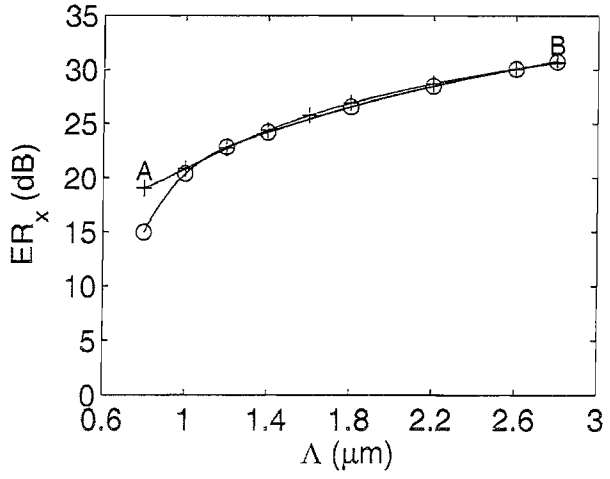

FIGURE 7.4: Polarisation extinction ratio in dB for a range of HF structures.

the extinction ratio as a function of the effective mode area (see Figure 7.5) it is clear that the use of larger filling fractions leads to fibres with smaller mode areas without worsening the extinction ratio. In other words, for a specified mode area, the fibre with larger air-filling fraction has a higher extinction ratio. Note that larger air-filling fractions also produce fibres with lower confinement loss. Hence highly nonlinear HFs with large d/Λ reduce the impact of coupling, polarisation and coupling penalties in this sub-wavelength core regime.

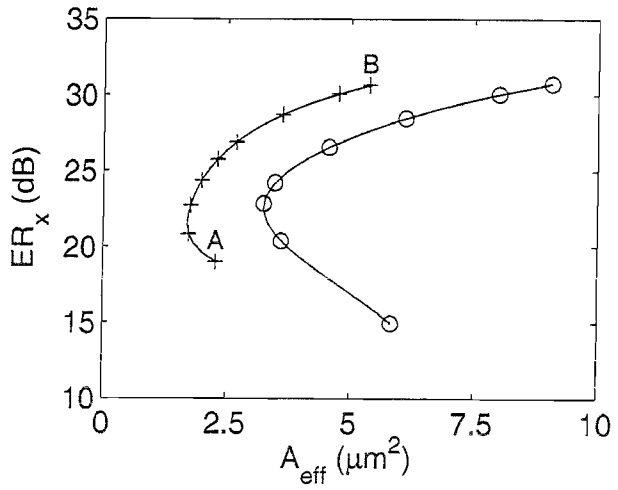

FIGURE 7.5: Polarisation extinction ratio in dB as a function of the effective nonlinear area for a range of HF structures.

The actual calculations of each component indicate that the expressions for the maximum and minimum powers can be simplified when $CE_x^{(1)} \gg CE_x^{(2)}$, which occurs when the two modes are effectively quasi-linearly polarised along the orthogonal axis. It is straightforward to see that, under this assumption, the maximum power (7.6) is reduced to

$$P_{\max} \simeq CE_x^{(1)} L_x^{(1)} \tag{7.8}$$

and that expresses the fact that the main contribution to $P_{\max}$ comes from mode (1). Under the same assumption, the minimum power (7.7) can also be reduced to

$$P_{\min} \simeq CE_x^{(1)} L_y^{(1)} \tag{7.9}$$

showing also that the main contribution to $P_{\min}$ comes from mode (1). The simplification of the $P_{\min}$ definition is at first sight less straightforward than that of the $P_{\max}$ definition, because obviously $L_y^{(2)} > L_y^{(1)}$. However, notice that the definition of $CE_\alpha^{(n)}$, when compared to the definition of $L_\alpha^{(n)}$, effectively involves square values of the field integrals, so the difference in magnitude between $CE_x^{(1)}$ and $CE_x^{(2)}$ is considerably larger than that between $L_y^{(2)}$ and $L_y^{(1)}$. Thus the term $CE_x^{(1)} L_y^{(1)}$ is larger than $CE_x^{(2)} L_y^{(2)}$ even though

$L_y^{(2)} > L_y^{(1)}$. The extinction ratio expression is therefore reduced to

$$ER_x \simeq 10 \log_{10} \frac{L_x^{(1)}}{L_y^{(1)}} \tag{7.10}$$

and is thus related to the modal linear polarisation of mode (1) only, in other words to how well linearly polarised the mode is. This approximation holds for the largest scale cases presented in this study, in particular for the cases with $\Lambda \gtrsim 1.2\,\mu$m. As the scale of the structure is reduced below this value, the exact ER_x expressed by equation (7.3) becomes smaller than the approximated ER_x expressed by equation (7.10), because the two modes are less well linearly polarised along the orthogonal axis and the contribution originating from mode (2) cannot be neglected. Note also that when this approximation holds, the extinction ratio is effectively independent of the field incident on the fibre.

7.3 Exact calculation of the modal properties

As already mentioned, the results so far presented have been derived making various simplifying assumptions that are no longer valid as the structural scale of the fibre is reduced. When considering the excitation of a guided mode through the facet of the fibre, the incident field $(\mathbf{E}_{\text{inc}}, \mathbf{H}_{\text{inc}})$ is scattered into different field components, one of which is the guided mode $(\mathbf{E}^{(1,2)}, \mathbf{H}^{(1,2)})$, however other of the various different propagating and radiative modes can also being excited. The coupling efficiency is defined as the ratio between the power that is launched in the guided mode under study and the total incident power.

It is therefore needed to isolate the portion of the incident field that effectively couples into the fundamental mode. In order to do that, reciprocity can be used and the problem can be reversed, thus calculating first the field radiated from the fibre facet when the guided mode arrives at it. It is known that the *optimum coupling* into the guided mode occurs when a field $(\mathbf{E}_{\text{opt}}, \mathbf{H}_{\text{opt}})$ with the same characteristic of the radiated mode is coupled into the fibre. Therefore, the ratio between the power carried by the guided mode and the total power carried by the field $(\mathbf{E}_{\text{opt}}, \mathbf{H}_{\text{opt}})$, which corresponds to the field radiated from the same guided mode, defines the *optimum coupling efficiency* CE_{opt}. However, a generic incident field $(\mathbf{E}_{\text{inc}}, \mathbf{H}_{\text{inc}})$ will achieve a coupling efficiency CE that is less than the optimum coupling efficiency CE_{opt}, and the measure of such reduction in coupling efficiency is given by the mismatch between the optimum and incident fields. Thus the coupling efficiency CE for a *non-optimum incident field* is expressed by [138]

$$CE = CE_{\text{opt}} \frac{\left| \iint \mathbf{E}^*_{\text{opt}} \times \mathbf{H}_{\text{inc}} \cdot \mathbf{n} dx dy \right|^2}{\left| \iint \mathbf{E}_{\text{opt}} \times \mathbf{H}^*_{\text{opt}} \cdot \mathbf{n} dx dy \iint \mathbf{E}_{\text{inc}} \times \mathbf{H}^*_{\text{inc}} \cdot \mathbf{n} dx dy \right|} \tag{7.11}$$

where the vector $\mathbf{n}$ is normal to the facet.

Note that for weakly guiding fibres, the impedance relationship $\mathbf{E}_t \simeq \pm Z\mathbf{n} \times \mathbf{H}$ holds, where $\mathbf{E}_t$ is the transverse component of $\mathbf{E}$ and Z denotes the waveguide impedance. In such a case equation (7.11) can be reduced to

$$CE \simeq CE_{\text{opt}} \frac{\left| \iint \mathbf{E}^*_{\text{opt},t} \cdot \mathbf{E}_{\text{inc},t} \cdot dxdy \right|^2}{\iint |\mathbf{E}_{\text{opt},t}|^2 dxdy \iint |\mathbf{E}_{\text{inc},t}|^2 dxdy}. \tag{7.12}$$

Note also that when the fibre profile at the facet is relatively uniform, the radiated field (thus the optimum coupling field $(\mathbf{E}_{\text{opt}}, \mathbf{H}_{\text{opt}})$) has essentially the same form as the guided mode $(\mathbf{E}^{(1,2)}, \mathbf{H}^{(1,2)})$. This implies two things: CE_{opt} reduces to the Fresnel transmission formula at the interface of materials with different refractive index (thus at the silica/air interface it is equal to 96%), and, more importantly, the integrals in equation (7.12) can be done directly between the incident field and the guided mode. All these approximations lead to the coupling efficiency formulation used in the analysis presented in Section 7.2.2, where equation (7.1) can be derived from equation (7.12), by neglecting the Fresnel transmission (note that $CE_{\text{opt}} \sim 1$ when considering fiber-to-fiber coupling) and by replacing the optimum coupling field $(\mathbf{E}_{\text{opt}}, \mathbf{H}_{\text{opt}})$ with the fundamental mode $(\mathbf{E}^{(1,2)}, \mathbf{H}^{(1,2)})$.

The analysis presented in Section 7.2.2 (that involves several simplifications valid for weakly guiding fibre with a relative uniform profile) has been used to predict preliminary results on coupling properties of small-core HFs since the exact analysis (7.11) requires the knowledge of the field radiated from the fibre facet and this field that cannot be evaluated by means of the multipole method. To calculate the field radiated from the fibre facet it should also be considered that a portion of the guided mode is also back-reflected and coupled into the back-propagating guided mode and other back-propagating and radiative modes. An analytical solution of this problem, considering also the complex HF profile, is not straightforward, although the field radiated from the HF facet can in principle be numerically calculated with the beam propagation method.

As pointed out already in Section 7.2.2, the spot sizes of the Gaussian beams that achieve the best coupling efficiency are sub-wavelength. This, apart from being impractical, also means that the assumption of a simple Gaussian beam incident at the fibre facet is no longer valid. The process of tightly focusing a linearly polarised Gaussian beam by means of a high-NA lens, results in a beam that is no longer Gaussian and which also can become significantly depolarised. That is, when a linearly polarised (e.g. along the x-axis) Gaussian beam is tightly focused by a high-NA lens, the resultant beam exhibits significant E_y and E_z components. An integral solution of the focal field of a tightly focused plane wave was derived by Richards and Wolf [139] in 1959, and this approach has been extended only recently to a tightly focused Gaussian beam (actually by L. Novotny) [140]. Such an integral solution can be solved numerically, but the simulation can be computationally intensive. Moreover, the focal field depends on the spot size of the Gaussian beam incident on the lens, and on lens characteristics (focal length and

NA). Similar sub-wavelength spot sizes can be produced by different combinations of these parameters and that result in different field profiles. Note also that there is not a clear (analytical) definition of the spot size of the focal field.

An alternative way of calculating tightly focused Gaussian beams was presented by Barton and Alexander [141] in 1989, which although less accurate than the integral solution, especially when the spot size is sub-wavelength, results in a faster implementation. Their approach is based on a fifth-order corrected expression for the Gaussian field and allows calculation of the field components in a closed analytical form as a function of the parameter s defined as:

$$s = \frac{1}{2\pi}\frac{\lambda}{w} \tag{7.13}$$

where λ is the optical wavelength and w the Gaussian beam waist radius. This formulation involves a series expansion in even powers of the parameter s, that is stopped at the third term for a fifth-order correction. Clearly the larger s is (i.e. the tighter the focus is), the slower the convergence of the series is and more terms should be included to accurately represent the solution. The spot size values resulting from the coupling analysis presented in Section 7.2.2 are in the range 0.75–1.65, thus s varies between 0.15 and 0.33, which corresponds to an average percentage error of the fifth-order correction that is less than $\sim 2\%$. Thus using the fifth-order corrected Gaussian fields in the calculation of the coupling efficiency should allow us to predict with reasonable accuracy the impact of tight focusing for the smallest scale structures considered here.

The impact of the non-Gaussian mode profiles on polarisation extinction ratio also needs to be considered as the structural scale is reduced. As previously mentioned if it is assumed that an x-polarised Gaussian beam is tightly focused by a high-*NA* lens to efficiently couple light into the fibre, the field that is actually coupled into the fibre becomes depolarised with tight focusing, therefore the coupling of light into the y-polarised mode (i.e. $CE_x^{(2)}$) should increase with respect to the previous analysis. Therefore a further degradation of the extinction ratio values is expected, especially for the smallest scale structures. The use of the fifth-order correction for a Gaussian beam to assess the magnitude of this effect is currently under investigation.

7.4 Conclusion

The results presented in this chapter represent the first study ever done of the fundamental limits on the efficiency with which light can be coupled into small core HFs. These results highlight some practical penalties associated with the use of small core HFs. For structures with core dimensions that are smaller than the optical wavelength, it is shown that the achievable coupling decreases and the polarisation extinction ratio is reduced. Since these small structures are required to achieve large normal dispersion in silica HFs [142], these penalties will pose a challenge for the successful realisation

of HF-based devices for dispersion compensation. Similarly, since the coupling/polarisation/loss penalties become significant for fibres with a substantial air/mode overlap, they will impact the development of any devices that exploit evanescent field effects in these fibres [137].

For other devices such as those used for optical data regeneration and switching, wavelength conversion and Brillouin and Raman-based devices, it is possible to design fibres that represent an acceptable compromise between nonlinearity and these penalties. For example, for a fibre with $\Lambda = 2.2\,\mu$m and $d/\Lambda = 0.9$, the extinction ratio is > 20 dB, the coupling loss can be < 0.5 dB and the effective area is still small ($A_{eff} \sim 4\,\mu\text{m}^2$). Hence the effective fibre nonlinearity is still high ($\gamma \sim 30$ W^{-1}km^{-1} compared to the values that can be achieved using conventional fibre types. Such fibres reduce the typical power length product requirements of devices based on nonlinear effects to the 10 W.m level. In the future, by combining the higher material nonlinearity possible in compound glasses with the mode confinement offered by HF structures[134], it should ultimately be possible to realise sub-(W.m) devices.

Chapter 8

Multipole method: Examples of applications

In the following chapter examples of the application of the multipole method are presented. First, the method is tested in order to validate it. The method is then applied to the analysis of several MOF cases that do not form part of the study of small core HFs, presented in the following two chapters, because these cases concern different structure regimes or designs. Motivations related to the analysis of each case are given.

8.1 Testing of the multipole method

Firstly, the implementation of the multipole method was tested against previous results reported in the literature. The multipole method was then applied to the study of a range of fabricated MOFs, and its findings compared with available experimental results. The agreement of the multipole method with other prediction techniques is then discussed.

8.1.1 Testing against previous results

The implementation of the multipole method, presented in Chapter 5, is based on the formulation given in White *et al.* [101] and Kuhlmey *et al.* [113]. The method implementation used for the work presentedin this thesis has therefore been validated against all the results given in White *et al.* [101]. Perfect agreement with the solutions found for the MOF structure present in the paper was obtained, for all the figures reported there. From this, it can be concluded that the method has been implemented correctly. Note also that both [79] and [113] present studies of the confinement loss of HF structures performed by means of the multipole method, but for structural scales larger than that considered in this thesis (i.e. small-core regime).

8.1.2 Testing against experimental results

In order to be proved to be valid any theoretical method needs to be compared to experimental results. A comparison between the measured values of loss and effective area for three different HFs is here performed.

The first fibre has been fabricated at the ORC and is a small-core HF, which is the class of HFs studied in Chapters 6 and 7, and the same fibre has been already introduced in Chapter 6, see Figure 6.1(a). Figure 8.1(a) shows the surface topography of the small-core HF ($\sim 1.25\ \mu$m core diameter) obtained by scanning the cleaved fibre end using an atomic force microscopy (AFM) [143]. Note that this fibre contains just two rings of large holes surrounding the core. The measured effective area is $2.8\,\mu\text{m}^2$ at 1550 nm [144]. The measured fibre loss at 1550 nm is $\sim$ 1 dB/m, considerably more than in similar fibres with more rings of holes, such as the fibre shown in Figure 6.1(b) which has a loss of 0.04 dB/m. Here an AFM image of the fibre is used because it provides a precise knowledge of the dimensions and topography of the finest structural details of the fibre profile. In order to apply the multipole method, the circular holes arrangement reported in Figure 8.1(b) has been chosen to match to the real HF structure. In this approximated structure, some of the interstitial and outer holes have been neglected for simplicity, and so it is expected that this approach should somewhat overestimate the confinement loss and the effective area. The Poynting vector of the calculated fundamental mode at 1550 nm for the approximated HF is also shown in Figure 8.1(b). The resulting effective index is $n_{eff} = 1.318854368247964 + i3.6072222 \times 10^{-7}$, that corresponds to a loss of $\sim$ 12.7 dB/m and an effective area of $\sim 2.4\mu\text{m}^2$. Despite the approximation in the modelled structure, the predicted value for the effective area is relatively close to the measured one of $2.8\,\mu\text{m}^2$. Although it is expected that this could be made to agree more closely with observations if more small holes were included to improve the representation of the structure in this model, these estimates show that this method can provide a useful guide to the magnitude of the confinement losses in these structures. This has been recently confirmed by Koshiba and Saitoh [145] where a full-vector FEM has been applied to study the same fibre. According to [145], accounting for the presence of interstitial holes does significantly reduce the confinement losses, because they increase the air-filling fraction. In the same paper modelling of the fibre with the same hole arrangement reported in Figure 8.1(b) but allowing for the actual noncircular shape of the holes has also been performed. The result confirms that replacing circular holes with the actual noncircular holes does not affect significantly the confinement loss calculation.

The method was then tested for the low-loss holey fibre presented by NTT in Tajima *et al.* [80]. The fibre cladding is comprised of 60 air holes, hexagonally-packed into 4 rings. Contrary to the previous case, this HF presents almost circular air holes. The hole diameter d is $1.7\,\mu$m and the hole-to-hole spacing Λ is $2.8\,\mu$m (and so $d/\Lambda \sim 0.6$). The multipole method predicts an effective mode index n_{eff} of $1.422361568456178 + i2.9 \times$

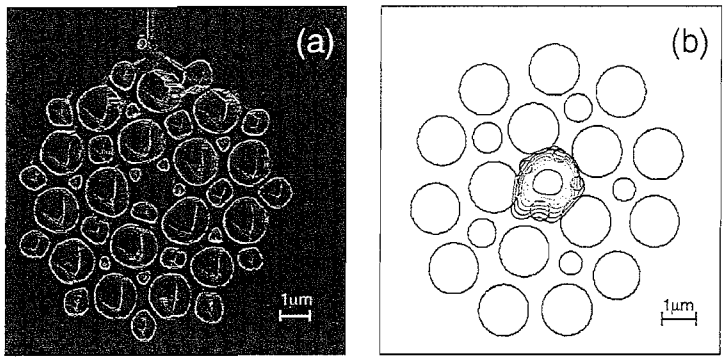

FIGURE 8.1: (a) AFM surface topography of a HF with 1.25 μm core; (b) arrangement of circular holes corresponding to the previous real HF and calculated Poynting vector in dB (contours spaced 2 dB) of the fundamental mode at 1550 nm.

10^{-14}. The predicted effective mode area is $\sim 9\,\mu m^2$. Note that this value is comparable with the smallest effective mode area achieved in conventional fibre ($\sim 11\,\mu m^2$). The predicted confinement loss for the fundamental mode at 1550 nm is $\sim 10^{-3}$ dB/km, consistent with, and significantly smaller than, the total measured loss of 1 dB/km reported in Ref. [80]. Hence even though the fabrication, scattering and material-related losses have been reduced dramatically in this fibre relative to previous fibres, they still dominate the confinement loss here.

BlazePhotonics Ltd. recently presented a fibre with a loss of 0.58 dB/km at 1550nm [81]. The HF has a hole diameter d of 1.85 μm and hole-to-hole spacing Λ of 4.2 μm (and so $d/\Lambda \sim 0.44$). They determined that 0.18 dB/km of the total loss was due to Rayleigh loss (or scattering from particles loss, that is the fundamental limit for loss) and 0.13 dB/km to OH^- absorption. The excess loss (0.27 dB/km) that remains unaccounted for has been primarily attributed to scattering at the air/glass interfaces due to nanometre-scale surface roughness. Table 8.1 reports the predicted values of the effective index and confinement loss of this fibre design using structures with different numbers of rings. Since for 4 rings the confinement loss is predicted to be still larger than the excess loss, these results indicate that the fibre must have at least 5 rings. The results in Table 8.1 indicate that for 5 or more rings the contribution of the confinement loss to the excess loss becomes negligible (the confinement loss for the 5 rings structure is 7.1×10^{-3} dB/km). The analysis of the different loss contributions performed on this fibre in [81] have therefore correctly ignored the confinement loss contribution.

8.1.3 Testing against other methods

In Ref. [79] the multipole method was tested against the beam propagation method (BMP). Good agreement was found between the multipole method and the vector BPM in both the real and the imaginary parts of the effective mode index n_{eff}.

Testing the multipole method against the orthogonal function technique [61, 110] is here

Number of rings	$\Re\{n_{eff}\}$	$\Im\{n_{eff}\}$	$\mathcal{L}$ (dB/km)
1	1.436197380970710	7.8754847×10^{-5}	2.8×10^{6}
2	1.436202669564560	5.6330104×10^{-7}	2.0×10^{4}
3	1.436202773109870	3.9731529×10^{-9}	1.4×10^{2}
4	1.436202774050850	$2.8035070 \times 10^{-11}$	9.9×10^{-1}
5	1.436202774058195	2.0108×10^{-13}	7.1×10^{-3}
6	1.436202774058251	$\sim 9 \times 10^{-16}$	3.4×10^{-5}

TABLE 8.1: Effective index and confinement loss of the BlazePhotonics fibre structure for different numbers of rings.

performed for large mode HFs. The results are presented in Section 8.4 of this chapter.

8.2 Effect of relative location of two circular rings of air-holes

The effect of the relative position of two circular rings of air-holes on the confinement loss is under investigation here. Since the extent of the cladding region does not vary, the confinement loss is expected to be affected by the presence of glass routes, created by the relative position of the two rings, which can allow the light to be guided out of the core region.

The multipole method has been applied to study a structure with two rings of air holes, where the rings have a circular shape. As shown in Figure 8.2(a), the inner ring has 6 holes equally spaced at a distance of 1.8 μm from the centre of the structure, while the outer ring is comprised of 18 holes located at a distance of 3.6 μm from the centre (so that $\Lambda = 1.8\mu$m and $d/\Lambda \simeq 0.72$). The outer ring is rotated with respect to the inner ring, in order to evaluate the effect of the relative location of the two circular rings on the total confinement. Figure 8.2(b) shows the difference in the real part of the effective index as a function of the dephasing between the two rings. The corresponding values of confinement loss are plotted in Figure 8.2(c). As expected, the loss is minimum when the holes of the outer ring are aligned with the silica bridges of the inner ring, because this alignment counteracts the leakage of the light along the bridges.

8.3 Effect of interstitial holes

The presence or absence of interstitial holes in MOFs can now largely be controlled during fibre fabrication. The interstitial holes can be eliminated by sealing each capillary before performing the stacking into the desired design. The interstitial holes are retained

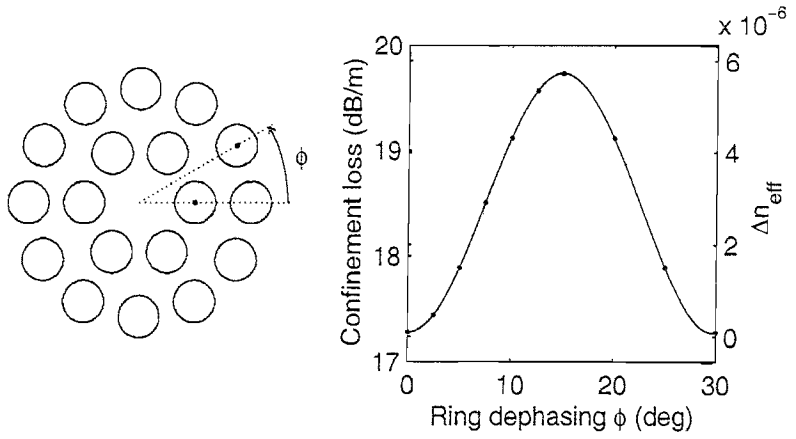

FIGURE 8.2: (left) Schematic of the mutual rotation between two circular rings of air holes, where ϕ represents the dephasing between the two rings; (right) Confinement loss (left axis) and difference in effective index (right axis) as a function of the dephasing angle ϕ.

if the sealing is not performed and their size can be controlled by varying the temperature and pressure conditions during the drawing of the fibre.

In Monro *et al.* [110] the effect of interstitial holes is studied for a HF structure with hole-to-hole spacing Λ equal to $3.2\,\mu$m and air-filling fraction equivalent to a $d/\Lambda \sim 0.6$. The small interstitial holes are present between the larger air holes over the entire structure. Given their location, it might be expected that the interstitial holes will act on the tails of the propagating mode, improving its confinement. This can also be confirmed by the analysis presented in Section 8.2 where it is shown that the confinement improves when the outer air-holes are aligned to the silica bridges created by inner air-holes. As expected, Ref. [110] shows that when the size of the interstitial holes is increased from zero, the mode area decreases.

Here, the effect of the interstitial holes on a smaller scale design than that considered in [110] is under investigation. In particular, consider a HF structure comprised of 4 rings of air holes and characterised by $\Lambda = 1\,\mu$m and $d = 0.9\,\mu$m. Only six interstitial holes of dimension $d_i = 0.1\,\mu$m are considered, first located close to the core and then between the first and second ring of larger air holes, as shown in Figures 8.3(b) and (c) respectively. In this way, it can also be ascertained, for this small-core regime, the impact on the mode of the different locations of the interstitial holes within the HF structure.

The results are summarised in Table 8.2. Despite the tiny dimension of the interstitial holes compared to the optical wavelength ($\lambda = 1.55\,\mu$m, thus $d_i \sim 0.065 \times \lambda$), their presence affects the mode. In the first case (b), where the interstitial holes are present very close to the core, both the effective area and the confinement loss increases when compared to the case in which the interstitial holes are absent, shown in Figure 8.3(a). The second case (c) results in smaller effective area and confinement loss values. There-

fore it seems that when the interstitial holes are located close to the core they somehow push out the light rather than confining it more tightly. However, this is strictly related to the small scale of the overall structure and the sub-wavelength dimension of the interstitial holes, which act as a perturbation of the mode confinement. For larger hole-to-hole spacing, as reported in Monro *et al.* [110], the presence of interstitial holes close to the core improves the confinement of the mode, as for case (c).

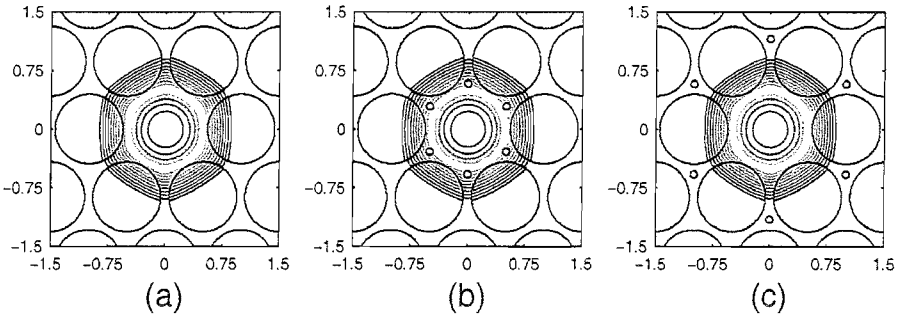

FIGURE 8.3: Small core HF without interstitial holes (a), with interstitial holes located close to the core (b) and between the first and second ring of air holes (c). Contours of the Poynting vector in dB of the fundamental mode are superimposed to each structure.

Fig. 8.3	$\Re\{n_{eff}\}$	$\mathcal{L}$ (dB/m)	A_{eff} (μm^2)	A_{eff}^{Agrawal} (μm^2)	PF_{holes} (%)
(a)	1.2519591173638	0.63	1.72	1.61	24.3
(b)	1.2438882803565	0.99	1.75	1.61	26.4
(c)	1.2516104712842	0.61	1.71	1.60	24.1

TABLE 8.2: Predicted properties of the fundamental mode for the three HF cases shown in Figure 8.3.

8.4 Large mode area holey fibres

Large mode holey fibres (LMHFs) have been successfully analysed by applying the scalar version of the orthogonal functions technique (OFT) [61, 110]. It is, in general, not necessary to apply the vector version of this approach when the MOF exhibits a low numerical aperture and the structure scale is large compared to the wavelength, because the resulting mode is essentially transversal. Comparing predictions for LMHFs computed by the orthogonal function technique and the multipole method can therefore lead to a further validation of the multipole method.

The first example studied here by means of the multipole method is a hexagonal lattice structure characterised by a hole-to-hole spacing Λ of 8.87 μm and air holes diameter d of 2.3 μm. These structural parameters corresponds to a fabricate HF and have been measured with scanning probe microscopy [143], the same technique used for the fibre presented in Section 8.1.2 and described there. The effective mode area A_{eff} of

$\Lambda(\mu m)$	$d(\mu m)$	N_r	$\Re\{n_{eff}\}$	$\Im\{n_{eff}\}$	$\mathcal{L}$ (dB/m)
8.87	2.3	3	1.45677486042102	1.0125821×10^{-8}	~ 0.87
8.87	2.3	4	1.45677486585686	3.64791×10^{-10}	~ 0.031
10.00	2.593	3	1.45682479679682	7.464727×10^{-9}	~ 0.64
10.00	2.593	4	1.45682480076638	2.62019×10^{-10}	~ 0.023

TABLE 8.3: Multipole method predictions at 633 nm for LMHFs with $d/\Lambda = 0.2593$.

the fundamental mode of this fibre at an optical wavelength of 633 nm has also been measured via scanning probe microscopy and with standard knife-edge techniques [146], which both estimated $A_{eff} \sim 90\,\mu m^2$. This result was in disagreement with a prediction computed via the orthogonal function technique, according to which A_{eff} $140\,\mu m^2$. The value of the effective mode area of the fundamental mode predicted by the multipole method is under investigation here, in order to understand whether the orthogonal functions technique is somehow failing or the real HF structure is different from the modelled one. Even though the real fibre is comprised of 7 rings of air holes, only structures with 3 and 4 rings of air holes have been considered for the sake of reducing the computational time. This can be done because, due to the large scale of the structure compared to the optical wavelength, the confinement losses are small and the mode is already well confined for a reduced number of rings. The fundamental mode characteristics are summarised in Table 8.3 (first two rows). Both the designs lead to an effective area of the order of $147\,\mu m^2$, implying that the mode is well confined despite the limited number of rings considered here. Note also that the first nine figures of the real part of the effective index are exactly the same, as shown in the table. The result is compatible with the OFT prediction of $140\,\mu m^2$, whereas it is 39% larger than the measured one. Therefore it results that the real fibre is somehow different from the modelled one, not in terms of the structural characteristic (i.e. Λ and d) finely described by the AFM image, but of the material characteristics. Indeed it has subsequently been proven that the heat treatment of the glass resulted in a non-uniformity of the material refractive index.

Table 8.3 also reports a second HF design characterised by the same d/Λ ratio of 0.2593 and a larger hole-to-hole spacing of $\Lambda = 10\,\mu m$. This second case has been computed to ascertain the degree of increase of the propagation constant as a function of the scale of the structure in the regime where $\lambda/\Lambda << 1$. This analysis was then performed at a wavelength of $1.064\,\mu m$ (that is the emission wavelength of Nd-glass based power-lasers) for which a wider range of results computed via OFT was already available. Large mode area HF structures comprised of 3-4 rings of air-holes, with an air-filling fraction corresponding to $d/\Lambda = 0.2$ and hole-to-hole spacing equal to 7 and $12\,\mu m$ are considered. The predictions obtained via the multipole method are summarised in the upper half of Table 8.4, whereas the ones computed via the orthogonal functions technique are shown in the lower half. Considering that the OFT was used in its scalar version and applied on an infinite cladding HF structure, the fact that the effective indexes agree up to the fifth

$\Lambda(\mu m)$	$d(\mu m)$	N_r	$\Re\{n_{eff}\}$	$\Im\{n_{eff}\}$	$\mathcal{L}$ (dB/m)
7.00	1.400	3	1.44871772881362	6.0192484×10^{-7}	~ 30.87
7.00	1.400	4	1.44871819573661	6.3421836×10^{-8}	~ 3.25
7.00	1.400	5	1.44871824686663	6.711785×10^{-9}	~ 0.34
12.00	2.400	3	1.44930894316107	1.2915368×10^{-7}	~ 6.62
12.00	2.400	4	1.44930903720589	1.1133351×10^{-8}	~ 0.57
12.00	2.400	5	1.44930904563108	9.62294×10^{-10}	~ 0.049
7.00	1.400	-	1.44871855725142	-	-
12.00	2.400	-	1.44929614308265	-	-

TABLE 8.4: Predictions at $1.064\,\mu m$ for LMHFs with $d/\Lambda = 0.2$, computed with the multipole method (upper half of the table) and the orthogonal functions technique (lower half).

figure is a very good result. For the smallest scale structure, the effective areas predicted via multipole method and via OFT are equal to $\sim 127\,\mu m$ and $\sim 123\,\mu m$, respectively; whereas for the largest scale structure they are equal to $\sim 344\,\mu m$ and $\sim 313\,\mu m$. The agreement between the results produced by the two methods is again good. Figure 8.4 shows a comparison between the cross sections of the transverse field E_t along the two main axes of the fibre for the fundamental mode predicted by the two methods. The agreement between the mode profiles calculated by the two methods is almost perfect in the core region and the profiles slightly differ only on the tails of the mode, consistent with the good agreement between the effective indexes and the effective mode areas.

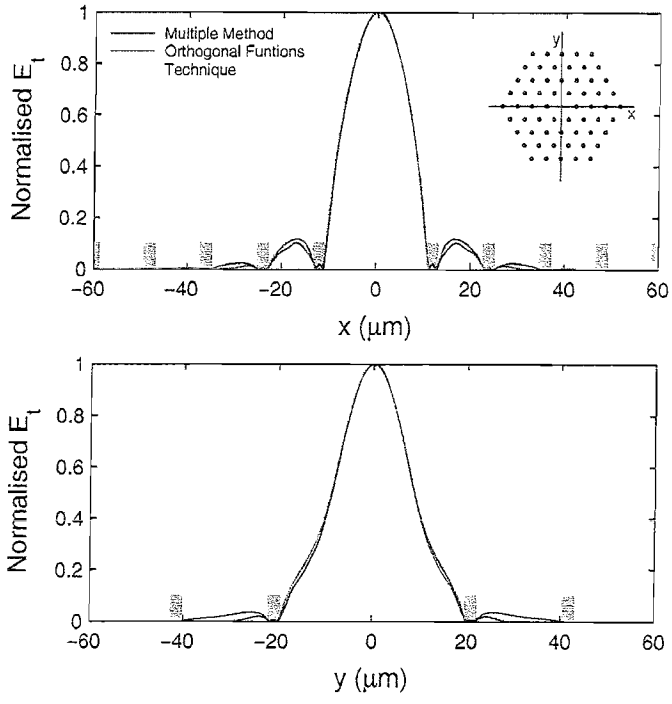

FIGURE 8.4: LMHF $\Lambda = 12$ - $d/\Lambda = 0.2$ at $1.064\,\mu m$.

8.4.1 Fundamental space-filling mode

The effective refractive index of the MOF cladding strongly depends on the optical wavelength, as mentioned already in Section 4.2. The effective cladding index can be used to determine whether the fibre is single- or multi-mode, and also in bend loss calculations. For periodic lattice HFs, the cladding index has always been estimated by calculating the fundamental space-filling mode (FSM) of the periodic lattice of the HF, i.e. replacing the HF core with an air hole and thus considering the cladding to be infinite. The effective index of the FSM is considered to be the effective cladding index of the HF. Several methods can be used to calculate the FSM, such as the plane wave technique [99], and some of them rely on the study of the unit cell of the periodic lattice, such as the beam propagation method or the fully analytical vector approach presented in Midrio *et al.* [147] which approximates the hexagonal unit cell with a circular one.

However, HFs are actually comprised of a finite number of air holes, and practical HFs are preferably made with a limited number of air holes. Thus the effective index of the FSM estimated with the assumption of an infinite cladding extent could not be accurate. The multipole method can be applied to the study of the fundamental space-filling mode for HF structures comprised of a finite number of air holes, again replacing the core with an air hole. A hexagonal lattice (large mode) HF is considered here, characterised by 3 rings of air holes, a hole-to-hole spacing Λ of $12\,\mu$m and an air hole diameter d of $4.8\,\mu$m (thus $d/\Lambda = 0.4$), and analysed at a wavelength of 1064 nm. Figure 8.5 shows the arrangement of holes that act as the cladding of this fibre, along with the transverse electric intensity distribution of the fundamental mode of this structure (i.e. the FSM of a finite extent lattice) predicted by the multipole method. The mode profile is essentially zero within the air holes and is somehow localised into the central part of structure, due to the finite extent of the periodic lattice. Note that the FSM for an infinite periodic structure is essentially zero within the air holes but is clearly not localised. The mode is a two-degenerate mode with polarisation characteristics similar to that of the HE_{11} mode for a conventional fibre.

In order to analyse how the effective cladding index, calculated in this way, is affected by the cladding dimension, the calculation is repeated for the same scale structure but with a different number of rings of air holes. Figure 8.6 shows that the effective cladding index increases as more rings are added to the structure. This curve is expected to converge towards the effective index of the FSM calculated for the infinite lattice. Indeed, for all the cases considered here, it always results that the effective index value predicted for the FSM of the infinite lattice is larger than that predicted by the multipole method for a finite lattice. This convergency can be easily visualised when considering that when the cladding extent is increased, the mode spreads more and becomes less localised to the central part of the structure.

The multipole method can be used to study the single/multimode behaviour of HF

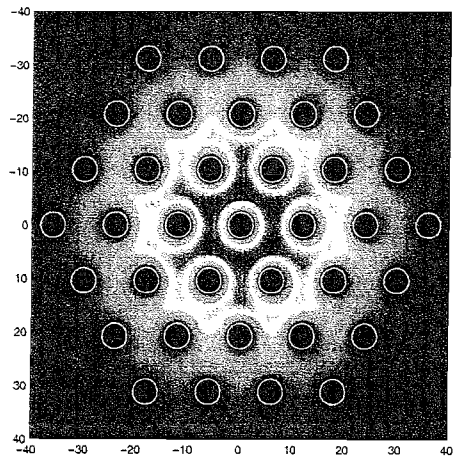

FIGURE 8.5: Cladding profile corresponding to a HF comprised of 3 rings of air holes. The transverse electric intensity distribution of its fundamental mode is superimposed to the structure profile.

structures. Figure 8.7 shows the scan of the determinant of the field identity matrix $|\det(\mathcal{M}(n_{eff}))|$ for the HF previously presented (black line) and its corresponding cladding (red line), as a function of the real part of the effective index n_{eff}. Each subfigure refers to a different number of rings. The derivative of the function $|\det(\mathcal{M}(n_{eff}))|$ is actually plotted on the graphs, in order to better highlight the presence of local minima. A point of discontinuity in the derivative of the function indicates the presence of a local minimum in the function. In the curves plotted in Figure 8.7, this point of discontinuity appears as a "glitch" on an otherwise smooth curve. The glitch (labelled FM in the figure) on the black curve located at the largest n_{eff} is the HF fundamental mode. Note that no glitches are present on the red curve at that position, because the HF fundamental mode is clearly not a mode of the corresponding cladding structure. The glitch (labelled FSM in the figure) on the red curve located at the largest n_{eff} corresponds to fundamental mode of the cladding structure. If the fibre is multimode, other glitches appears on the HF (black) curve at n_{eff} values included between n_{eff}(FSM) and n_{eff}(FM). In the case presented here, the fibre is single-mode. It results that to have an indication on the single-modality of the fibre, it is usually enough to analyse the HF

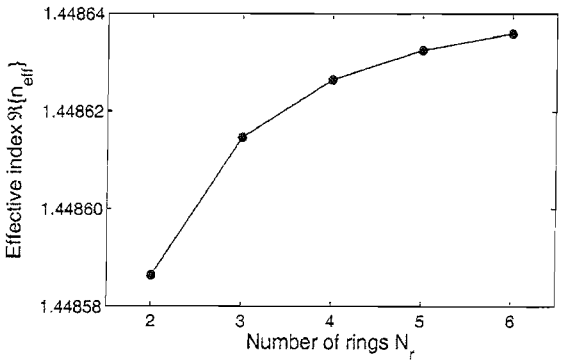

FIGURE 8.6: Effective cladding index as a function of the number of rings.

structure comprised of 2 rings of holes only (recall from Section 5.4 that the computational time required by the multipole method scales as the fourth-power of the number of rings, in a hexagonal lattice, and considering 2 rings only results in a relatively quick calculation). However, it also results that a fibre can be just multi-mode for 2 rings and single-mode when more rings are considered.

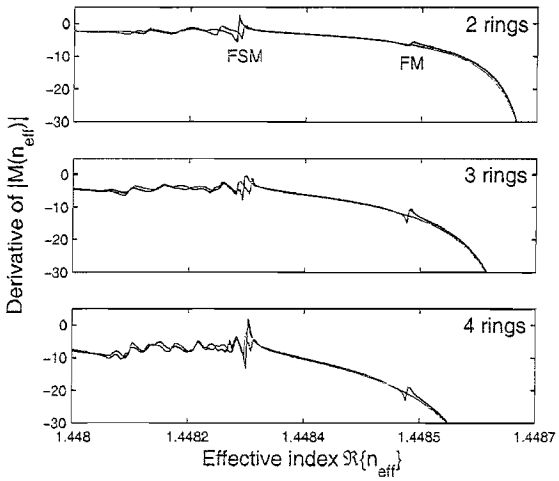

FIGURE 8.7: Derivative of function $|\det(\mathcal{M})|$ as a function of $\Re\{n_{eff}\}$ for a HF structure (black line) and the corresponding cladding structure (red line). Three different number of rings are considered, as indicated in each sub-figure. FM indicates the position of the fundamental mode of the HF structure, whereas FSM indicates the position of FSM (i.e the effective cladding index).

8.5 Solid holes (SOHO) microstructured optical fibres

A new MOF design has recently been fabricated at the ORC by Feng *et al.* [148]. It consists of a usual HF structure in which the holes have been filled with a low refractive index glass and has therefore been named SOHO (solid holes) fibre. Two glasses with similar thermal properties were chosen for this purpose. It is essential that the two glasses have similar softening and melting temperature in order to allow the microstructured material to be kept as it is during all the steps of the fibre fabrication process. The background glass is SF6 whereas for the inclusions the LLF1 glass has been used, they are characterised by a refractive index of 1.76444 and 1.5347 at 1530 nm, respectively [133]. In order to fabricate the MOF, rod-in-tube composites were first fabricated, the rod consisting of the lower refractive index glass (LLF1). The composite rods were then stacked together in a hexagonal lattice, with the central part made of a rod of the high refractive index glass (SF6) to form the core of the fibre.

The main problem of using capillaries, as in single material HF, is the collapsing of the air-holes during the fibre drawing, that is usually avoided by sealing the end of the capillaries, as discussed in Section 4.1.4. However, even with sealing, the geometry can change under the drawing process. Thus, the use of solid "holes" should result in more

$\Lambda(\mu\text{m})$	$d(\mu\text{m})$	d/Λ	N_r	$\Re\{n_{eff}\}$	$\Im\{n_{eff}\}$	$\mathcal{L}$ (dB/m)
4.00	1.144	0.286	2	1.75964843990176	4.0396586×10^{-5}	~ 1.420
4.00	1.144	0.286	4	1.75968287145702	6.4078192×10^{-7}	~ 22.6
4.00	2.000	0.5	2	1.75715497146709	3.2445199×10^{-7}	~ 11.4
4.00	2.000	0.5	4	1.75715501728467	9.287×10^{-12}	$\sim 3.27 \times 10^{-4}$
4.00	3.200	0.8	2	1.75247212693672	3.55×10^{-13}	$\sim 1.25 \times 10^{-5}$

TABLE 8.5: Predictions for SOHO fibres at 1550 nm.

perfect structures and help to maintain almost circular inclusions. The background glass should also fill the interstitial spaces between the tubes. As a side effect, because of the circular inclusions, the multipole method will ideally yield very reliable predictions for the optical properties of SOHO fibres. This can be an important issue when optimisation of the fibre design for a particular application is required.

Since this is a new class of MOFs, predictions for the confinement losses of several structures need to be done in order to give guidelines for the fabrication of a design not affected by this kind of loss. Calculations are performed here at 1550 nm for MOF structures characterised by a hole-to-hole spacing Λ of $4\,\mu$m, a range of d/Λ of $0.286-0.8$ and 2 to 4 rings of holes, as reported in Table 8.5. This range was chosen because these ratios have been fabricated into rod-in-tube mono-structures. Note that although the refractive index contrast of the two glasses is smaller than the silica-air combination, which might be expected to lead to a worse mode confinement, the refractive index of the background glass (SF6) is higher than silica, that might instead lead to a better mode confinement. Thus the confinement of the SOHO fibre compared to a single-material silica HF results from a trade-off between these two effects. Observe also that the nonlinear index of SF6 is approximately 10 times higher than that of silica, thus this MOF design potentially leads to higher value of effective nonlinearity γ.

Figure 8.8 shows the confinement loss as a function of the number of rings for the SOHO fibre cases studied here. The confinement loss values for the silica HF presented in Section 8.1.2 (low-loss fibre made by BlazePhotonics) have also been plotted on the graph (dashed line) for comparison, because this HF is characterised by a scale structure similar to the SOHO cases, i.e $\Lambda = 4\,\mu$m and $d/\Lambda \sim 0.44$. For these SOHO fibre cases, despite the reduced refractive index contrast, the degree of improvement as extra rings of inclusions are added seems to be only slightly worse than the silica HF case. However, comparison with silica HF predictions reported in [113] shows that the degree of improvement, when the air-filling fraction is increased, is significantly reduced for the SOHO structure, therefore the higher refractive index glass does not counteract enough the reduced mode confinement offered by the lower refractive index contrast.

In order to ascertain what values of effective nonlinearity can be achieved with a SOHO fibre design, an step-index fibre design is considered here. This design represents the

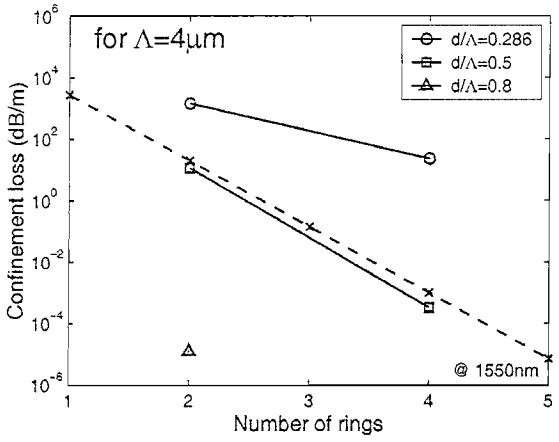

FIGURE 8.8: Confinement loss as a function of the number of rings for the SOHO fibre cases reported in Table 8.5. The dashed line represents the silica HF presented in Section 8.1.2, characterised by $\Lambda = 4\,\mu$m and $d/\Lambda \sim 0.44$.

ultimate limit of a SOHO design, where the cladding inclusions fill up all the cladding region and thus provide the largest possible *NA*s. The core and the cladding are made of SF6 and LLF1, respectively. The solid line in the inset of Figure 8.9 shows the effective nonlinear area as a function of the core diameter, calculated by applying the effective area definition (4.9) which accounts for the presence of glasses with different nonlinear properties. The nonlinear coefficients of the two glasses considered here are $n_2(\text{SF6}) = 2.2 \times 10^{-19}$ m^2/W and $n_2(\text{LLF1}) = 2 \times 10^{-20}$ m^2/W [133]. The curve in Figure 8.9 represents a lower bound of the effective area achievable with a SOHO MOF design. The minimum effective area is $\sim 1.7\,\mu$m^2 corresponding to a core diameter of $\sim 1.2\,\mu$m. The effective nonlinearity corresponding to the minimum effective area is $\gamma \sim 520$ W^{-1}km^{-1}, more than 500 times higher than in standard telecommunications fibre (which, as discussed in Section 4.2.2, has a $\gamma \sim 1$ W^{-1}km^{-1}). On the same graph is also reported the case of a silica ASR, showing how the confinement of the mode is similar despite the use of materials with different refractive indexes. However, the gain in effective nonlinearity γ, due to the fact that SF6 glass is ten time more nonlinear than silica, is remarkable, as shown by the main graph in Figure 8.9 where the effectively nonlinearity γ is plotted as a function of the core diameter for the two cases air/silica and LLF1/SF6. The triangle indicates the fundamental mode of the 2 rings SOHO fibre with $d/\Lambda = 0.8$ reported in Figure 8.8, the case which exhibits the lowest loss amongst the ones considered here. The effective core size of the fibre, defined as $2\Lambda - d$, is equal to $4.8\,\mu$m. The multipole method predicts for this fibre an effective nonlinear area of the order of $\sim 12.8\,\mu$m^2, which corresponds to an effective nonlinearity of ~ 70 W^{-1}km^{-1}.

As it is shown in Chapter 6, the maximum nonlinearity achievable with a silica single material HF is of the order of ~ 52 W^{-1}km^{-1}, smaller than the one achieved by this particular SOHO fibre and ten times smaller than the maximum achievable with the two glasses MOF here presented. Note that in both cases, the maximum nonlinearity is obtained for a similar core sizes. However, for this scale structure, the confinement loss

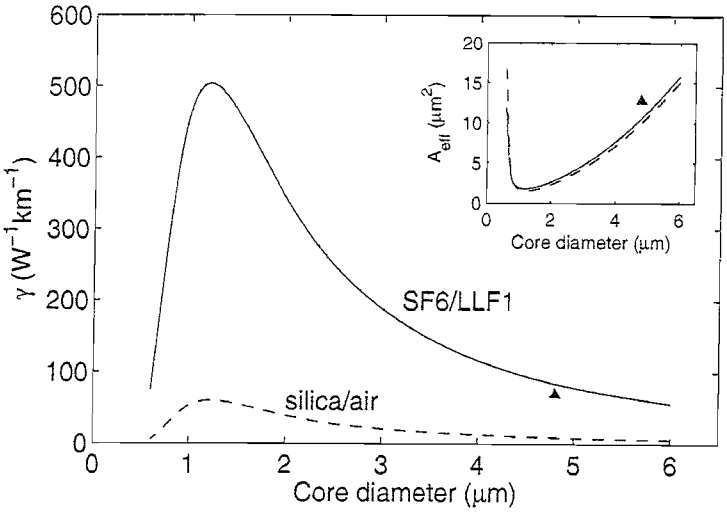

FIGURE 8.9: Effective nonlinearity (inset: effective nonlinear area) as a function of the core size for LLF1/SF6 step-index fibres (solid line) and silica air-suspended rod structures (dashed line). The triangle represents the case of a 2 rings SOHO fibre with $d/\Lambda = 0.8$ (also shown in Figure 8.8).

penalties for the SOHO design might be more severe than for single material silica HFs, as previously discussed.

8.6 Conclusion

In this chapter it is shown that the multipole method can be successfully validated against previous results present in the literature (i.e. predicted by the a different implementation of the multipole method), experimental results relative to several fabricated HF structures (including small-core silica HFs) and results predicted by other techniques (in particular, by the orthogonal function technique [61, 110]). It is also shown the large versatility of the multipole method, by successfully applying the method to the analysis of a wide range of fibre geometries and materials.

Chapter 9

Conclusion and future work

In this thesis several theoretical models have been applied to the study of "microstructured materials" in order to: ascertain the properties of different designs, give an insight into the physical mechanisms involved and eventually highlight the fundamental limitation of a certain design. In particular, fibre Bragg gratings (FBGs) and microstructured optical fibres (MOFs) have been considered. The main findings of the work are summarised and possible future works are illustrated in the following.

Part I of this thesis deals with the effect of losses on FBGs. First, the effect of background loss on uniform FBGs is considered. The FBG writing process induces, in addition to refractive index changes, an increase in the propagation mode background losses. The level of background losses depends on the fibre type, photosensitisation process and writing conditions. The interaction between a uniform refractive index and a uniform loss grating with the same spatial periodicity is analysed by means of the coupled mode theory [1, 18]. It is shown how the loss pattern affects the features and symmetry of the FBG reflection, transmission and loss spectra according to the value of the de-phasing between the index and loss patterns. Even in the case of symmetric spectra, the presence of background losses limits the maximum attainable peak reflectivity. In the case of modulated background losses this maximum reflectivity depends on the de-phasing between the two patterns. It is also demonstrated that the resultant spectral asymmetry can be explained by considering the overlap between the standing-wave intensity distribution and the periodic loss pattern. It would be interesting to analyse the effects of background losses on more complicated grating designs, such as apodised and chirped gratings. The case of an apodised, unchirped grating is expected to be affected in a way similar to the uniform, unchirped FBG case. The main contribution to the spectra asymmetries however originates from the central (stronger) part of the grating only. The case of chirped gratings looks more interesting, because light at different optical wavelengths is back-reflected at a different position within the grating length. The longer the light travels along the grating, the more the background loss affects it. An asymmetry in the reflection spectrum is therefore expected, asymmetry that depends on which grating

end the light is launched into. A spatial-averaging effect is also expected to take place owing to the gradual change of the underlying grating periodicity. This is expected to reduce the impact of the loss on the reflection spectrum, when compared to the worst case where the field distribution inside the grating is always in phase with the modulated loss pattern. Due to the spatial-averaging effect, the transmission spectrum is not expected to show any asymmetry. The impact of the periodic loss on the transmission spectrum becomes equivalent to the averaged constant background loss.

Next, the effect of cladding mode losses on linearly chirped FBGs used as dispersion compensators, thus launching the light from the long-wavelength end of the grating, has been considered. The chirping of the FBG results in a spectral overlap of the resonant coupling of the forward-propagating core mode to a particular backward-propagating cladding mode. A new extension of the standard coupled-mode theory has been developed here to study the resultant mode dynamics. Coupling of light into cladding modes results in a loss on the short-wavelength side of the reflection spectrum that affects the performance of the dispersion compensator. A technique to equalise the spectrum by means of a properly designed apodisation profile is also analysed [39]. This technique consists of making the grating stronger on the short-wavelength side, so that more photons are available in the lossy region and the resultant reflection spectrum is flattened. The fundamental limitations of this approach is here derived. According to the strength of the cladding modes that interact with the core mode, there is a limit in the maximum strength of the grating that can be equalised. When the grating strength is above this limit, it is physically impossible to equalise the reflection spectrum, because there are not enough photons available to compensate for those lost. The apodisation profile should be targeted to the particular fibre used to fabricate the dispersion compensator. However the extended coupled-mode theory used here results in significantly time consuming simulations. Thus it is not advisable to use this approach to optimise the apodisation profile according to the fibre characteristics. Inverse scattering techniques based on the layer-peeling algorithm [149] allow the synthesis of Bragg gratings with complex spectral responses in reasonable simulation times. The standard layer-peeling algorithm requires the knowledge of the desired reflection spectrum, and consequently reconstructs the grating profile layer after layer. However, in the presence of cladding modes, the "desired" reflection spectrum of each cladding mode is also required, and clearly this information is not available (since this depends on the grating profile, which has not been identified yet). Only an iterative solution is therefore possible and this has recently been developed at the ORC by Ghiringhelli and Zervas [150].

Part II of this thesis deals with modelling the properties of microstructured optical fibres. In particular, a detailed study on highly nonlinear silica holey-fibres for applications at 1550 nm is presented. After a careful consideration of the available modelling techniques and their advantages, the multipole method first demonstrated by White *et al.* [101], Kuhlmey *et al.* [113] is chosen to perform this study, and a considerable part of the work

has been dedicated to the implementation of the method, as described in Chapter 5. The multipole method is chosen for a variety of reasons, such as the fact that it allows the calculation of complex values of the propagation constant of the mode, that is that it allows the prediction of the confinement loss of the mode. The multipole method is also highly efficient, when compared to other methods, because it makes use of polar coordinate systems centred in each air-hole, thus few terms are retained in the field expansions. In addition, the use of polar coordinate systems avoids the introduction of any false birefringence.

Even though silica is not intrinsically a highly nonlinear material [75], silica holey fibres (HFs) can provide high effective fibre nonlinearities γ when the large numerical apertures possible in these fibres are combined with a wavelength-scale core. It results that effective nonlinearity more than 50 times larger than that of standard telecommunications fibre can be achieved in silica single-material holey fibres. However, at such small scale structure, holey fibres can suffer from significant confinement loss unless certain rules are followed when designing the fibre profile. Utilising these rules, the confinement loss of small-core HFs can be reduced below the background loss of standard fibres (0.2 dB/km). It results that in this regime the main contribution to confinement loss comes from the finite extent of the cladding region more than the leakage of light between the (sub-wavelength) silica bridges. Thus the loss can always be reduced by adding more rings of holes to the fibre cladding (albeit with an increase in fabrication complexity).

In the small-core regime, it results that regardless of the air-filling fraction the effective mode area (effective nonlinearity) can be minimised (maximised) by a certain value of the hole-to-hole spacing. However, this occurs at a scale structure where the confinement loss penalties can become significant. In particular, for the largest air-filling fractions, the core dimension which achieves the maximum effective nonlinearity is sub-wavelength. Although on one hand, the loss can always be reduced by adding more rings of holes to the fibre cladding, on the other hand, for ease of fabrication, we wish to limit the number of rings of air-holes that need to be stacked in the fibre preform. There is a clear trade-off between achieving small effective mode area and low confinement loss in practical fibre design. Graphs providing useful guidelines when choosing the design parameters for a particular device performance (i.e. required effective nonlinearity and magnitude of loss that can be tolerated) are presented in the thesis. Another useful finding is that, when at least two rings of holes are present, the effective mode area of the structure is essentially independent of the number of rings. Quick but remarkably accurate calculations of the modal properties of any structure can be performed considering just two rings of holes. Once the basic properties have been calculated in this way, the confinement loss can always be reduced by adding more holes.

Fibre device applications also require particular sign and magnitude of fibre dispersion. The dispersive properties of small-core HFs for the range of structures included in this study which achieves the largest nonlinearities (air-filling fraction equal to 74%, i.e.

$d/\Lambda = 0.9$) have been analysed. It results that the zero-dispersion regime at 1550 nm is achieved for scale structures that have an effective mode area just 3% larger than the minimum achievable area. This allows devices with low dispersion values (both anomalous and normal) to exploit the fibre designs with near-optimum effective nonlinearity and reasonably low confinement loss (<1 dB/km). An anomalous dispersion allows soliton-based devices, whereas a low normal dispersion is required to improve the performances of optical thresholding devices. A large normal dispersion of the order of -300 ps/nm/km can be achieved at the structural scale that maximises the effective nonlinearity, and further decreasing the scale of the structure makes even larger values of normal dispersion available for dispersion compensation devices. However, as mentioned previously, penalties in terms of loss occur in this regime, and so many rings of holes will be required to make a practical device.

The coupling of light into holey fibres with a small-core and a large *NA* is practically challenging when compared to fibres with a larger mode area. In order to achieve a good coupling efficiency using free space coupling, lasers with high spatial quality beams, to achieve small spot sizes, and high *NA* optics are required. In addition, without the use of tapers or couplers, the direct splicing of conventional fibre types to these fibres becomes impractical due to mode mismatch. Note that these issues are also important for highly nonlinear conventional fibres, but because HFs can achieve smaller mode areas than conventional fibre types, the coupling of light in holey fibre types can be more challenging.

For a complete understanding of these HF structures, it is also necessary to consider the polarisation properties for this range of fibre designs. Our studies indicate that, unsurprisingly, polarisation effects can be extreme in the small core regime. Of particular interest, the polarisation extinction ratio degrades significantly when the core dimension is sub-wavelength, which can have a major impact on device performance. However it results that, for a specified mode area, the fibre with larger air-filling fraction has a higher extinction ratio. Note that larger air-filling fractions also produce fibres with lower confinement loss. Hence highly nonlinear HFs with large d/Λ reduce the impact of confinement loss, polarisation and coupling penalties in this sub-wavelength core regime.

Note that the analysis of the coupling and polarisation properties of small-core HFs presented in Chapter 7 was performed by applying a formulation that is no longer valid as the structural scale of the fibre is reduced. In particular, it is not considered that an initially linearly polarised Gaussian beam, when tightly focused by a high-*NA* lens, can become significantly depolarised and its shape is no longer Gaussian. A more accurate approach to study the problem is currently under investigation, as discussed in Section 7.3, and a further degradation of the extinction ratio values, especially for the smallest scale structures, is expected.

The natural progression of the study on highly nonlinear HFs consists in considering

fibre made with glasses with a higher refractive index than silica. Using such materials it is possible to access material nonlinearities that are orders of magnitude larger than that of silica. Recently, using SF57 glass, HFs with a measured effective nonlinearity γ of 640 $W^{-1}km^{-1}$ have been produced [132], more than 600 times larger than standard silica fibres and 10 times larger than the theoretical limit for pure silica HF structures. In the thesis a preliminary study on such glasses is indeed presented, but air-suspended rod structures only have been considered to date. The fabrication of HFs made of highly nonlinear glasses with low-softening temperatures (such as SF57) is so far performed via direct extrusion of the preform, thus the final fibre is comprised of non-circular holes. In this case the multipole method cannot be successfully applied to the study of these designs. Given the small-scale of the fibre structures the confinement loss can still be a significant penalty in the performances of the device. Thus models that can give confinement loss predictions for non-circular holes designs must be considered, such as the beam propagation method and the Fourier decomposition algorithm, in order to perform an accurate study of their optical properties, especially when targeted to a particular device application. However, the extrusion of highly nonlinear glasses can also be used to fabricate capillary elements, which are then stacked to form a traditional HF lattice. In this case the resulting fibre is comprised of circular air holes and the multipole method can be applied to study these designs. Regardless of the particular fibre design, the results of the study on small-core silica HFs presented in this thesis will also provide a useful guide to the analysis of small-core HFs made of highly nonlinear glasses.

List of publications

V. Finazzi and M. N. Zervas, "Effect of periodic background loss on grating spectra," in *Applied Optics*, vol. 41, no. 12, pp. 2240–2250, April 2002.

V. Finazzi and M. N. Zervas, "Cladding mode losses in chirped fibre Bragg gratings," in *Proceedings BGPP*, Stresa, Italy, June 2001, Optical Society of America, OSA Technical Digest, paper BThB4.

V. Finazzi and T. M. Monro, "Modelling confinement loss in practical small-core holey optical fibres", in International Workshop on Nonlinear Photonic Crystals - Danish Technical University, Lyngby, Denmark, October 2001.

V. Finazzi, T. M. Monro, and D. J. Richardson, "Confinement loss in highly nonlinear holey optical fibres," in *Proceedings OFC*, Anaheim, California, March 2002, Optical Society of America, OSA Technical Digest, paper ThS4.

V. Finazzi, T. M. Monro, and D. J. Richardson, "Small core silica holey fibers: Nonlinearity and confinement loss trade-offs," in *Journal of the Optical Society of America B*, vol. 20, no. 7, pp. 1427–1436, July 2003.

V. Finazzi, T. M. Monro, and D. J. Richardson, "The role of confinement loss in highly nonlinear silica holey fibers," in *Photonics Technology Letters*, vol. 15, no. 9, pp. 1246–1248, September 2003.

V. Finazzi, T. M. Monro, and D. J. Richardson, "Fundamental properties of small core holey fibres," in *Proceedings ECOC-IOOC*, Rimini, Italy, September 2003, paper We1.7.6.

X. Feng, T. M. Monro, P. Petropoulos, V. Finazzi, and D. W. Hewak, "SOHO (solid holey) fiber," in *Proceedings ECOC-IOOC*, Rimini, Italy, September 2003, paper We1.7.2.

Bibliography

[1] H. Kogelnik. Coupled wave theory for thick hologram gratings. *The Bell Syst. Tech. J.*, 48(9):2909–2947, November 1969.

[2] H. Kogelnik and C. V. Shank. Coupled-wave theory of Distributed Feedback Lasers. *J. Appl. Phys.*, 43(5):2327–2335, May 1972.

[3] K. O. Hill, Y. Fujii, D. C. Johnson, and B. S. Kawasaki. Photosensitivity in optical fiber waveguides: Applications to reflection filter fabrication. *Appl. Phys. Lett.*, 32(10):647–649, May 1978.

[4] R. M. Atkins, P. J. Lemaire, T. Erdogan, and V. Mizrahi. Mechanisms of enhanced UV photosensitivity via hydrogen loading in germanosilicate glasses. *Electron. Lett.*, 29(14):1234–1235, July 1993.

[5] F. Bilodeau, B. Malo, J. Albert, D. C. Johnson, K. O. Hill, Y. Hibino, M. Abe, and M. Kawachi. Photosensitization of optical fiber and silica-on-silicon/silica waveguides. *Opt. Lett.*, 18(12):953–955, June 1993.

[6] G. Meltz, W. W. Morey, and W. H. Glenn. Formation of Bragg gratings in optical fibers by a transverse holographic method. *Opt. Lett.*, 14(15):823–825, August 1989.

[7] K. O. Hill, B. Malo, F. Bilodeau, D. C. Johnson, and J. Albert. Bragg gratings fabricated in monomode photosensitive optical fiber by UV exposure through a phase mask. *Appl. Phys. Lett.*, 62(10):1035–1037, March 1993.

[8] M. J. Cole, W. H. Loh, R. I. Laming, M. N. Zervas, and S. Barcelos. Moving fibre/phase mask-scanning beam technique for enhanced flexibility in producing fiber gratings with uniform phase mask. *Electron. Lett.*, 31(17):1488–1490, August 1995.

[9] M. J. Cole. *Fibre Bragg Gratings for Dispersion Compensation.* Mini-thesis, University of Southampton, Southampton, SO17 1BJ, February 1997.

[10] C. R. Giles. Lightwave applications of fiber Bragg gratings. *J. Lightwave Tech.*, 15(8):1391–1404, August 1997.

[11] K. O. Hill and G. Meltz. Fiber Bragg grating technology fundamentals and overview. *J. Lightwave Tech.*, 15(8):1263–1276, August 1997.

[12] Y. J. Chen, A. W. Snyder, and D. N. Payne. Twin core nonlinear couplers with gain and loss. *IEEE J. Quantum Electron.*, 28(1):239–245, January 1992.

[13] Special issue on fiber gratings, photosensitivity, and poling. *J. Lightwave Tech.*, 15(8):1263–1512, August 1997.

[14] A. V. Kavokin and M. A. Kaliteevski. Light-absorption effect on Bragg interference in multilayer semiconductor heterostructures. *J. Appl. Phys.*, 79(2):595–598, January 1996.

[15] Y. Boucher. Influence of a localized scattering center upon the spectral characteristics of a distributed-feedback structure. *IEEE Phot. Tech. Lett.*, 9(11):1454–1456, November 1997.

[16] P. St. J. Russell. Bloch wave analysis of dispersion and pulse propagation in pure distributed feedback structures. *J. Mod. Opt.*, 38(8):1599–1619, May 1991.

[17] T. Fessant and Y. Boucher. Additional modal selectivity induced by a localized defect in quarter-wave-shifted DFB lasers. *IEEE J. Quantum Electron.*, 34(4): 602–608, April 1998.

[18] D. A. Cardimona, M. P. Sharma, V. Kovanis, and A. Gavrielides. Dephased index and gain coupling in Distributed Feedback Lasers. *IEEE J. Quantum Electron.*, 31(8):60–66, January 1995.

[19] D. Johlen, F. Knappe, H. Renner, and E. Brinkmeyer. UV-induced absorption, scattering and transition losses in UV side-written fibers. In *Proc. OFC '99*, OSA Technical Digest, pages 50–52, San Diego, California, February 1999. Optical Society of America, OSA. paper ThD1.

[20] V. Grubsky, D. S. Starodubov, and J. Feinberg. Photochemical reaction of hydrogen with germanosilicate glass initiated by 3.4–5.4-eV ultraviolet light. *Opt. Lett.*, 24(11):729–731, June 1999.

[21] M. Scalora, M. J. Bloemer, A. S. Pethel, J. P. Dowling, C. M. Bowden, and A. S. Manka. Transparent, metallo-dielectric, one-dimensional, photonic band-gap structures. *J. Appl. Phys.*, 83(5):2377–2383, March 1998.

[22] M. J. Bloemer and M. Scalora. Transmissive properties of Ag/MgF_2 photonic band gaps. *Appl. Phys. Lett.*, 72(14):1676–1678, April 1998.

[23] R. B. Bylsma, D. H. Olson, and A. M. Glass. Photochromic gratings in photorefractive materials. *Opt. Lett.*, 13(10):853–855, October 1988.

[24] R. S. Cudney, R. M. Pierce, G. D. Bacher, and J. Feinberg. Absorption gratings in photorefractive crystals with multiple levels. *J. Opt. Soc. Am. B*, 15(8):1326–1332, June 1991.

[25] M. Liphardt and S. Ducharme. Measurement of the photorefractive grating phase shift in a polimer by an ac phase-modulation technique. *J. Opt. Soc. Am. B*, 15 (7):2154–2160, July 1998.

[26] M. Gehrtz, J. Pinsl, and C. Bräuchle. Sensitive detection of phase and absorption gratings: phase-modulated, homodyne detected holography. *Appl. Phys. B*, 43(2): 61–77, June 1987.

[27] L. Dong, W. F. Liu, and L. Reekie. Negative index gratings formed at 193 nm excimer laser. *Opt. Lett.*, 21(24):2032–2034, December 1996.

[28] T. Erdogan. Fiber grating spectra. *J. Lightwave Tech.*, 15(8):1277–1294, August 1997.

[29] D. I. Babic and S. W. Corzine. Analytic expressions for the reflection delay, penetration depth, and absorbance of quarter -wave dielectric mirrors. *IEEE J. Quantum Electron.*, 28(2):514–524, February 1992.

[30] A. W. Snyder and J. D. Love. *Optical Waveguide Theory.* Chapman and Hall, 1996.

[31] J. M. Bendickson, J. P. Dowling, and M. Scalora. Lightwave applications of fiber Bragg gratings. *Phys. Rev. E*, 53(4):4107–4121, April 1996.

[32] M. Centini, C. Sibilia, M. Scalora, G. D'Aguanno, M. Bertolotti, M. J. Bloemer, C. M. Bowden, and I. Nefedov. Dispersive properties of finite, one-dimensional photonic band gap structures: Applications to nonlinear quadratic interactions. *Phys. Rev. E*, 60(4):4891–4898, October 1999.

[33] P. Yeh, A. Yariv, and C.-S. Hong. Electromagnetic propagation in periodic stratified media. i. general theory. *J. Opt. Soc. Am.*, 67(4):423–438, April 1977.

[34] A. Yariv and P. Yeh. Electromagnetic propagation in periodic stratified media. ii. birefringence, phase matching, and x–ray lasers. *J. Opt. Soc. Am.*, 67(4):438–448, April 1977.

[35] F. Ouellette. Dispersion cancellation using linearly chirped Bragg grating filters in optical waveguides. *Opt. Lett.*, 12(10):847–849, October 1987.

[36] V. Mizrahi and J. E. Sipe. Optical properties of photosensitive fiber phase gratings. *J. Lightwave Tech.*, 11(10):1513–1517, October 1993.

[37] T. Erdogan. Cladding-mode resonances in short and long period fiber grating. *J. Opt. Soc. Am. A*, 14(8):1760–1773, August 1997.

[38] Y. Koyamada. Analysis of core-mode to radiation-mode coupling in fiber Bragg gratings with finite cladding radius. *J. Lightwave Tech.*, 18(9):1220–1225, September 2000.

[39] M. Durkin, M. Ibsen, R. I. Laming, and V. Gusmeroli. Equalisation of spectral non-uniformities in broad-band chirped fibre gratings. In *Proc. BGPP*, OSA Technical Digest, pages 231–3, Williamsburg, Virginia, October 1997. Optical Society of America. Paper BMG16.1-3.

[40] T. Komukai and M. Nakazawa. Efficient fiber gratings formed on high NA dispersion shifted fibers. In *Eur. Conf. Opt. Commun.*, volume 1, pages 31–34, Brussels, Belgium, September 1995. Paper MoA3.3.

[41] E. Delevaque, S. Boj, J. F. Bayon, H. Poignat, J. Le Mellot, and M. Monerie. Optical fiber design for strong gratings photoimprinting with radiation mode suppression. In *Proc. OFC*, OSA Technical Digest, San Diego, California, February 1995. Optical Society of America. Postdeadline paper PD5.

[42] L. Dong, L. Reekie, J. L. Cruz, J. E. Caplen, J. P. de Sandro, and D. N. Payne. Optical fibers with depressed claddings for suppression of coupling into cladding modes in fiber Bragg gratings. *IEEE Phot. Tech. Lett.*, 9(1):64–66, January 1997.

[43] M. N. Zervas, M. Ibsen, and R. I. Laming. Short-wavelength, transmission-loss suppression in fiber Bragg gratings. In *Proc. BGPP*, OSA Technical Digest, pages 39–41, Williamsburg, Virginia, October 1995. Optical Society of America. Paper BSuC4-1.

[44] H. Kogelnik. *Theory of Optical Waveguides*, chapter in Guided-Wave Optoelectronics, T. Tamir, pages 7–88. Springer-Verlag, 1988.

[45] M. K. Durkin. *Advanced Fibre Bragg Gratings: Application to Dispersion Compensation.* PhD thesis, University of Southampton, Southampton, SO17 1BJ, December 1999.

[46] P. Kaiser, E. A. J. Marcatili, and S. E. Miller. A new optical fiber. *The Bell Syst. Tech. J.*, 52(2):265–269, February 1973.

[47] P. Kaiser and H. W. Astle. Low-loss single-material fibers made from pure fused silica. *The Bell Syst. Tech. J.*, 53(6):1021–1039, July–August 1974.

[48] F. P. Kapron, D. B. Keck, and R. D. Maurer. Radiation losses in glass optical waveguides. *Appl. Phys. Lett.*, 17(10):423–425, November 1970.

[49] P. Kaiser, A. R. Tynes, A. H. Cherin, and A. D. Pearson. Loss measurements of unclad optical fibers. In *Topical meeting on integrated optics-guided waves, materials and devices*, pages 187–191, Las Vegas, Nevada, February 1972. Optical Society of America. Paper WA4.

[50] T. Li. Advances in optical fiber communications: an historical perspective. *IEEE J. Sel. Areas Commun.*, 1(3):356–372, April 1983.

[51] D. B. Keck, R. D. Maurer, and P. C. Schultz. On the ultimate lower limit of attenuation in glass optical waveguides. *Appl. Phys. Lett.*, 22(7):307–309, April 1973.

[52] T. Miya, Y. Terunuma, T. Hosaka, and T. Miyashita. Ultimate low-loss single-mode fibre at 1.55 μm. *Electron. Lett.*, 15(4):106–108, February 1979.

[53] Zh. I. Alferov, V. M. Andreev, V. I. Korol'kov, E. L. Portnoi, and D. N. Tret'yakov. Coherent radiation of epitaxial heterojunction structures in the AlAs–GaAs system. *Soviet Phys. Semiconductors*, 20(2):1545–1547, October 1968.

[54] E. Yablonovitch. Inhibited spontaneous emission in solid-state physics and electronics. *Phys. Rev. Lett.*, 58(20):2059–2062, May 1987.

[55] T. A. Birks, P. J. Roberts, P. St. J. Russell, D. M. Atkins, and T. J. Shepherd. Full 2–D photonic bandgaps in silica/air structures. *Electron. Lett.*, 31(22):1941–1943, October 1995.

[56] J. C. Knight, T. A. Birks, P. St. J. Russell, and D. M. Atkins. All–silica single–mode optical fiber with photonic crystal cladding. *Opt. Lett.*, 21(19):1547–1549, October 1996.

[57] T. M. Monro, P. J. Bennett, N. G. R. Broderick, and D. J. Richardson. Holey fibers with random cladding distributions. *Opt. Lett.*, 25(4):206–208, February 2000.

[58] R. F. Cregan, B. J. Mangan, J. C. Knight, T. A. Birks, P. St. J. Russell, P. J. Roberts, and D. C. Allan. Single–mode photonic band gap guidance of light in air. *Science*, 285:1537–1539, September 1999.

[59] J. Broeng, T. Søndergaard ans S. Barkou, P. Barbeito, and A. Bjarklev. Waveguidance by the photonic bandgap effect in optical fibres. *J. Opt. A: Pure Appl. Opt.*, 1(4):477–482, July 1999.

[60] B. J. Eggleton, P. S. Westbrook, R. S. Windeler, S. Spälter, and T. A. Strasser. Grating resonances in air–silica microstructured optical fibers. *Opt. Lett.*, 24(21): 1460–1462, November 1999.

[61] T. M. Monro, D. J. Richardson, N. G. R. Broderick, and P. J. Bennett. Holey optical fibers: an efficient modal model. *J. Lightwave Tech.*, 17(6):1093–1102, June 1999.

[62] R. T. Bise, R. S. Windeler, K. S. Kranz, C. Kerbage, B. J. Eggleton, and D. J. Trevor. Tunable photonic band gap fiber. In *Proc. OFC*, OSA Technical Digest,

pages 466–468, Anaheim, California, March 2002. Optical Society of America. Paper ThK3.

[63] K. M. Kiang, K. Frampton, T. M. Monro, R. Moore, J. Tucknott, D. W. Hewak, and D. J. Richardson. Extruded single-mode non-silica glass holey optical fibres. *Electron. Lett.*, 38(12):546–547, June 2002.

[64] T. A. Birks, J. C. Knight, and P. St. J. Russell. Endlessly single–mode photonic crystal fiber. *Opt. Lett.*, 22(13):961–963, July 1997.

[65] N. G. R. Broderick, T. M. Monro, P. J. Bennett, and D. J. Richardson. Nonlinearity in holey optical fibers: measurement and future opportunities. *Opt. Lett.*, 24(20):1395–1397, October 1999.

[66] J. C. Knight, T. A. Birks, R. F. Cregan, P. St. J. Russell, and J.-P. de Sandro. Large mode area photonic crystal fibre. *Electron. Lett.*, 34(13):1347–1348, June 1998.

[67] J. C. Baggett, T. M. Monro, K. Furusawa, and D. J. Richardson. Comparative study of large–mode holey and conventional fibers. *Opt. Lett.*, 26(14):1045–1047, July 2001.

[68] R. Holzwarth, Th. Udem, T. W. Hänsch, J. C. Knight, W. J. Wadsworth, and P. St. J. Russell. Optical frequency synthesizer for precision spectroscopy. *Phys. Rev. Lett.*, 85(11):2264–2267, September 2000.

[69] J. C. Knight, J. Arriaga, T. A. Birks, A. Ortigosa-Blanch, W. J. Wadsworth, and P. St. J. Russell. Anomalous dispersion in photonic crystal fiber. *IEEE Phot. Tech. Lett.*, 12(7):807–809, July 2000.

[70] B. J. Eggleton, C. Kerbage, P. Westbrook, R. S. Windeler, and A. Hale. Microstructured optical fiber devices. *Opt. Express*, 9(13):698–713, December 2001.

[71] T. M. Monro, W. Belardi, K. Furusawa, J. C. Baggett, N. G. R. Broderick, and D. J. Richardson. Sensing with microstructured optical fibres. *Meas. Sci. Technol.*, 12(7):854–858, July 2001.

[72] T. M. Monro, Y. D. West, D. W. Hewak, N. G. R. Broderick, and D. J. Richardson. Chalcogenide holey fibres. *Electron. Lett.*, 36(24):1998–2000, November 2000.

[73] M. van Eijkelenborg, M. Large, A. Argyros, J. Zagari, S. Manos, N. A. Issa, I. M. Bassett, S. C. Fleming, R. C. McPhedran, C. M. de Sterke, and N. P. Nicorovici. Microstructured polymer optical fibre. *Opt. Express*, 9(7):319–327, September 2001.

[74] K. Furusawa, T. M. Monro, P. Petropoulos, and D. J. Richardson. Modelocked laser based on Ytterbium doped holey fibre. *Electron. Lett.*, 37(9):560–561, April 2001.

[75] G. P. Agrawal. *Nonlinear Fiber Optics.* Academic Press, New York, 1989.

[76] T. Okuno, M. Onishi, T. Kashiwada, S. Ishikawa, and M. Nishimura. Silica-based functional fibers with enhanced nonlinearity and their applications. *IEEE J. Sel. Top. Quant.*, 5(5):1385–1391, September–October 1999.

[77] W. Belardi, J. H. Lee, K. Furusawa, Z. Yusoff, P. Petropoulos, M. Ibsen, T. M. Monro, and D. J. Richardson. A 10 Gbit/s tuneable wavelength converter based on four-wave mixing in highly nonlinear holey fibre. In *Proc. ECOC*, Copenhagen, Denmark, September 2002. Postdeadline paper PD1.2.

[78] D. N. Nikogosyan. *Optical and laser-related materials.* Wiley, Chichester, 1997.

[79] T. P. White, R. C. McPhedran, C. M. de Sterke, L. C. Botten, and M. J. Steel. Confinement losses in microstructured optical fibers. *Opt. Lett.*, 26(21):1660–1662, November 2001.

[80] K. Tajima, K. Nakajima, K. Kurokawa, N. Yoshizawa, and M. Ohashi. Low-loss photonic crystal fibers. In *Proc. OFC*, OSA Technical Digest, pages 523–524, Anaheim, California, March 2002. Optical Society of America. Paper ThS3.

[81] L. Farr, J. C. Knight, B. J. Mangan, and P. J. Roberts. Low loss photonic crystal fibre. In *Proc. ECOC*, Copenhagen, Denmark, September 2002. IEEE. Postdeadline paper PD1.3.

[82] A. Ferrando, E. Silvestre, J. J. Miret, and P. Andrés. Vector description of higher–order modes in photonic crystal fibers. *J. Opt. Soc. Am. A*, 17(7):1333–1340, July 2000.

[83] M. J. Steel, T. P. White, C. Martijn de Sterke, R. C. McPhedran, and L. C. Botten. Symmetry and degeneracy in microstructured optical fibers. *Opt. Lett.*, 26(8):488–490, April 2001.

[84] P. R. McIsaac. Symmetry–induced modal characteristics of uniform waveguides – I: Summary of results. *IEEE Trans. Microwave Theory Tech.*, MTT–23(5):421–429, May 1975.

[85] M. J. Steel and Jr. R. M. Osgood. Elliptical–hole photonic crystal fibers. *Opt. Lett.*, 26(4):229–231, February 2001.

[86] A. Ortigosa-Blanch, J. C. Knight, W. J. Wadsworth, J. Arriaga, B. J. Mangan, T. A. Birks, and P. St. J. Russell. Highly birefringent photonic crystal fibers. *Opt. Lett.*, 25(18):1325–1327, September 2000.

[87] M. Koshiba. Full-vector analysis of photonic crystal fibers using the finite element method. *IEICE Trans. Electron.*, E85-C(4):881–888, April 2002.

[88] F. Brechet, J. Marcou, D. Pagnoux, and P. Roy. Complete analysis of the characteristics of propagation into photonic crystal fibers, by finite element method. *Opt. Fiber Tech.*, 6(2):181–191, April 2000.

[89] T.A. Birks, D.Mogilevtsev, J.C. Knight, P.St.J. Russell, J. Broeng, P.J. Roberts, J.A. West, D.C. Allen, and J.C. Fajardo. The analogy between photonic crystal fibers and step index fibers. In *Proc. OFC*, OSA Technical Digest, pages 114–116, San Diego, California, February 1999. Optical Society of America. Paper FG4.

[90] A. Bjarklev, J. Broeng, K. Dridi, and S. E. Barkou. Dispersion properties of photonic crystal fibres. In *Proc. ECOC*, pages 135–136, Madrid, Spain, September 1998.

[91] K. M. Ho, C. T. Chan, and C. M. Soukoulis. Existence of a photonic bandgap in periodic dielectric structures. *Phys. Rev. Lett.*, 65(25):3152–3155, December 1990.

[92] J. Broeng, D. Mogilevstev, S. E. Barkou, and A. Bjarklev. Photonic crystal fibers: A new class of optical waveguides. *Opt. Fiber Tech.*, 5(3):305–330, July 1999.

[93] R. D. Meade, A. M. Rappe, K. D. Brommer, J. D. Joannopoulos, and O. L. Alerhand. Accurate theoretical analysis of photonic band-gap materials. *Phys. Rev. B*, 48(11):8434–8437, September 1993.

[94] M. J. Steel and R. M. Osgood. Polarization and dispersive properties of elliptical-hole photonic crystal fibers. *J. Lightwave Tech.*, 19(4):495–503, April 2001.

[95] M. Mansuripur, E. M. Wright, and M. Fallahi. The beam propagation method. *Opt. & Photon. News*, 11(7):42–48, July 2000.

[96] J. K. Ranka, R. S. Windeler, and A. J. Stentz. Optical properties of high–delta air–silica microstructure optical fibers. *Opt. Lett.*, 25(11):796–798, June 2000.

[97] D. Yevick and B. Hermansson. New approach to lossy optical wave-guides. *Electron. Lett.*, 21(22):1029–1030, October 1985.

[98] R. Scarmozzino, A. Gopinath, R. Pregla, and S. Helfert. Numerical techniques for modeling guided–wave photonic devices. *IEEE J. Sel. Top. Quant.*, 6(1):150–162, January–February 2000.

[99] A. Ferrando, E. Silvestre, J. J. Miret, P. Andrés, and M. V. Andrés. Full–vector analysis of a realistic photonic crystal fiber. *Opt. Lett.*, 24(5):276–278, March 1999.

[100] D. Mogilevtsev, T. A. Birks, and P. St. J. Russell. Localized function method for modeling defect modes in 2–D photonic crystals. *J. Lightwave Tech.*, 17(11): 2078–2081, November 1999.

[101] T. P. White, B. T. Kuhlmey, R. C. McPhedran, D. Maystre, G. Renservez, C. M. de Sterke, and L. C. Botten. Multipole method for microstructured optical fibers. I. Formulation. *J. Opt. Soc. Am. B*, 19(10):2322–2330, October 2002.

[102] G. E. Town and J. T. Lizier. Tapered holey fibers for spot–size and numerical–aperture conversion. *Opt. Lett.*, 26(14):1042–1044, July 2001.

[103] M. Koshiba and K. Saitoh. Numerical verification of degeneracy in hexagonal photonic crystal fibers. *IEEE Phot. Tech. Lett.*, 13(12):1313–1315, December 2001.

[104] D. Ferrarini, L. Vincetti, M. Zoboli, A. Cucinotta, and S. Selleri. Leakage properties of photonic crystal fibers. *Opt. Express*, 10(23):1314–1319, November 2002.

[105] K. Saitoh and M. Koshiba. Full-vectorial imaginary-distance beam propagation method based on a finite element scheme: Application to photonic crystal fibers. *IEEE J. Quantum Electron.*, 38(7):927–933, July 2002.

[106] A. J. Ward and J. B. Pendry. A program for calculating photonic band structures, Green's functions and transmission/reflection coefficients using a non-orthogonal FDTD method. *Comput. Phys. Commun.*, 128(3):590–621, June 2000.

[107] J. T. Lizier and G. E. Town. Splice losses in holey optical fibers. *IEEE Phot. Tech. Lett.*, 13(18):794–796, August 2001.

[108] Z. Zhu and T. Brown. Full-vectorial finite-difference analysis of microstructured optical fibers. *Opt. Express*, 10(17):853–864, August 2002.

[109] D. Mogilevtsev, T. A. Birks, and P. St. J. Russell. Group–velocity dispersion in photonic crystal fibers. *Opt. Lett.*, 23(21):1662–1664, November 1998.

[110] T. M. Monro, D. J. Richardson, N. G. R. Broderick, and P. J. Bennett. Modeling large air fraction holey optical fibers. *J. Lightwave Tech.*, 18(1):50–56, January 2000.

[111] T. M. Monro, N. G. R. Broderick, and D. J. Richardson. Exploring the optical properties of holey fibers. In *NATO Summer School on Nanoscale Linear and Nonlinear Optics*, Erice, Sicily, July 2000.

[112] T. P. White, R. C. McPhedran, L. C. Botten, G. H. Smith, and C. M. de Sterke. Calculations of air-guided modes in photonic crystal fibers using the multipole method. *Opt. Express*, 9(13):721–732, December 2001.

[113] B. T. Kuhlmey, T. P. White, G. Renservez, D. Maystre, L. C. Botten, C. M. de Sterke, and R. C. McPhedran. Multipole method for microstructured optical fibers. II. Implementation and results. *J. Opt. Soc. Am. B*, 19(10):2331–2340, October 2002.

[114] B. T. Kuhlmey, R. C. McPhedran, and C. M. de Sterke. Modal cutoff in microstructured optical fibers. *Opt. Lett.*, 27(19):1684–1686, October 2002.

[115] T. P. White, R. C. McPhedran, C. M. de Sterke, N. M. Litchinitser, and B. J. Eggleton. Resonance and scattering in microstructured optical fibers. *Opt. Lett.*, 27(22):1977–1979, November 2002.

[116] J. Korringa. Early history of multiple scattering theory for ordered systems. *Phys. Rep.*, 238(6):341–360, March 1994.

[117] Lord Rayleigh. On the influence of obstacles arranged in rectangular order upon the properties of a medium. *Phil. Mag.*, 34:481–502, 1892.

[118] W. Wijngaard. Guided normal modes of two parallel circular dielectric rods. *J. Opt. Soc. Am.*, 63(8):944–949, May 1973.

[119] K. M. Lo, R. C. McPhedran, I. M. Bassett, and G. W. Milton. An electromagnetic theory of dielectric waveguides with multiple embedded cylinders. *J. Lightwave Tech.*, 12(3):396–410, March 1994.

[120] L.-M. Li and Z.-Q. Zhang. Multiple-scattering approach to finite-sized photonic band-gap materials. *Phys. Rev. B*, 58(15):9587–9590, October 1998.

[121] D. Felbacq, G. Tayeb, and D. Maystre. Scattering by random set of parallel cylinders. *J. Opt. Soc. Am. A*, 11(9):2526–2538, September 1994.

[122] L. Poladian, N. A. Issa, and T. M. Monro. Fourier decomposition algorithm for leaky modes of fibres with arbitrary geometry. *Opt. Express*, 10(10):449–454, May 2002.

[123] N. A. Issa and L. Poladian. Vector wave expansion for leaky modes of microstructured optical fibres. *J. Lightwave Tech.*, 21(4):1005–1012, April 2003.

[124] M. Abramowits and I. A. Stegun. *Handbook of mathematical functions.* Dover, New York, 1965.

[125] W. H. Press, S. A. Teukolsky, W. T. Vetterling, and B. P. Flannery. *Numerical Recipes in C: The Art of Scientific Computing.* Cambridge University Press, second edition, 1992.

[126] J. G. Yardley, R. C. McPhedran, N. A. Nicorovici, and L. C. Botten. Addition formulas and the Rayleigh identity for arrays of elliptical cylinders. *Phys. Rev. E*, 68(5):6068–6090, November 1999.

[127] Z. Yusoff, J. H. Lee, W. Belardi, T. M. Monro, P. C. Teh, and D. J. Richardson. Raman effects in a highly nonlinear holey fiber: amplification and modulation. *Opt. Lett.*, 27(6):424–426, March 2002.

[128] S. R. Friberg and P. W. Smith. Nonlinear optical-glasses for ultrafast optical switches. *IEEE J. Quantum Electron.*, 23(12):2089–2094, December 1987.

[129] M. Asobe. Nonlinear optical properties of chalcogenide glass fibers and their application to all-optical switching. *Opt. Fiber Tech.*, 3(2):142–148, April 1997.

[130] J. Requejo-Isidro, A. K. Mairaj, V. Pruneri, D. W. Hewak, M. C. Netti, and J. J. Baumberg. Self refractive non–linearities in chalcogenide based glasses. *J. Non-Cryst. Sol.*, 317(3):241–246, March 2003.

[131] R. W. Boyd. *Nonlinear optics.* Academic Press, 1992.

[132] P. Petropoulos, T. M. Monro, H. Ebendorff-Heidepriem, K. Frampton, R. C. Moore, H. N. Rutt, and D. J. Richardson. Soliton-self-frequency-shift effects and pulse compression in an anomalously dispersive high nonlinearity lead silicate holey fiber. In *Proc. OFC*, OSA Technical Digest, Atlanta, Georgia, March 2003. Optical Society of America. Postdeadline Paper PD03.

[133] *Schott Optical Glass Catalog.*

[134] T. M. Monro, K. M. Kiang, J. H. Lee, K. Frampton, Z. Yusoff, R. Moore, J. Tucknott, D. W. Hewak, H. N. Rutt, and D. J. Richardson. High nonlinear extruded single-mode holey optical fibers. In *Proc. OFC*, OSA Technical Digest, pages 315–317, Anaheim, California, March 2002. Optical Society of America. Postdeadline paper PD-FA9.

[135] N. Nakazawa, H. Kubota, and K. Tamura. Random evolution and coherence degradation of a high-order optical soliton train in the presence of noise. *Opt. Lett.*, 24(5):318–320, March 1999.

[136] P. J. Bennett, T. M. Monro, and D. J. Richardson. Toward practical holey fiber technology: fabrication, splicing, modeling, and characterization. *Opt. Lett.*, 24 (17):1203–1205, September 1999.

[137] T. M. Monro, D. J. Richardson, and P. J. Bennett. Developing holey fibers for evanescent field devices. *Electron. Lett.*, 35(14):1188–1189, July 1999.

[138] C. Vassallo. *Optical Waveguide Concepts.* Elsevier, 1991.

[139] B. Richards and E. Wolf. Electromagnetic diffraction in optical systems. II. Structure of the image field in an aplanatic system. *Proc. Roy. Soc. A*, 253(1274): 358–379, December 1959.

[140] Ji-Xin Cheng, A Volkmer, and X. Sunney Xie. Theoretical and experimental characterization of coherent anti-Stokes Raman scattering microsopy. *J. Opt. Soc. Am. B*, 19(6):1363–1375, June 2002.

[141] J. P. Barton and D. R. Alexander. Fifth-order corrected electromagnetic field components for a fundamental gaussian beam. *J. Appl. Phys.*, 66(7):2800–2802, October 1989.

[142] T. A. Birks, D. Mogilevtsev, J. C. Knight, and P. St. J. Russell. Dispersion compensation using single–material fibers. *IEEE Phot. Tech. Lett.*, 11(6):674–676, June 1999.

[143] C. W. J. Hillman, W. S. Brocklesby, T. M. Monro, W. Belardi, and D. J. Richardson. Structural and optical characterisation of holey fibres using scanning probe microscopy. *Electron. Lett.*, 37(21):1283–1284, October 2001.

[144] P. Petropoulos, T. M. Monro, W. Belardi, K. Furusawa, J. H. Lee, and D. J. Richardson. 2R–regenerative all–optical switch based on a highly nonlinear holey fiber. *Opt. Lett.*, 26(16):1233–1235, August 2001.

[145] M. Koshiba and K. Saitoh. Polarization-dependent confinement losses in actual holey fibres. *IEEE Phot. Tech. Lett.*, 15(5):691–693, May 2003.

[146] M. Artiglia, G. Coppa, P. Di Vita, M. Potenza, and A. Sharma. Mode field diameter measurements in single-mode optical fibres. *J. Lightwave Tech.*, 7(8): 1093–1102, August 1989.

[147] M. Midrio, M. P. Singh, and C. G. Someda. The space filling mode of holey fibers: An analytical vectorial solution. *J. Lightwave Tech.*, 18(7):1031–1037, July 2000.

[148] X. Feng, T. M. Monro, P. Petropoulos, V. Finazzi, and D. W. Hewak. SOHO (solid holey) fiber. In *Eur. Conf. Opt. Commun.*, Rimini, Italy, September 2003. Paper We1.7.2.

[149] R. Feced, M. N. Zervas, and M. A. Muriel. An efficient inverse scattering algorithm for the design of nonuniform fiber Bragg gratïngs. *IEEE J. Quantum Electron.*, 35(8):1105–1115, August 1999.

[150] F. Ghiringhelli and M. N. Zervas. Inverse scattering design of fiber Bragg gratings with cladding mode losses compensation. In *Proc. BGPP*, OSA Technical Digest, Monterey, California, September 2003. Optical Society of America. Paper TuD2.